UNIVERSITA' DEGLI STUDI DI MODENA E REGGIO EMILIA
Dipartimento di Scienze Fisiche, Informatiche e Matematiche

DOTTORATO DI RICERCA IN PHYSICS AND NANO SCIENCES

MICROFLUIDIC DEVICES INTEGRATED INTO ORGANIC ELECTRONICS BIOSENSORS

Relatore:

Prof. Andrea Alessandrini

Tesi di Laurea di:

Gulseren Deniz Saygin

Correlatore:

Prof. Fabio Biscarini

Correlatore:

Dr.Pierpaolo Greco

Anno Accademico 2021-2022

This project has received funding from the European Union's Horizon 2020 research and innovation programme under the Marie Sklodowska-Curie grant agreement no. 813863.

Relatore: PROF. DR. ANDREA ALESSANDRINI

Department of Physics, Computer Science and Mathematics
University of Modena and Reggio Emilia
Via Campi, 103 I-1125 Modena, Italy
Tel: +39 059 205 5297
Fax: +39 059 205 5651
e-mail: andrea.alessandrini@unimore.it

Correlatore: PROF. DR. FABIO BISCARINI

Life Science Department
University of Modena and Reggio Emilia
Via Campi, 103 I-1125 Modena, Italy
Tel: +39 059 205 8587
Fax: +39 059 205 5410
e-mail: fabio.biscarini@unimore.it

Correlatore: DR. PIERPAOLO GRECO

Department of Neuroscience and Rehabilitation
University of Ferrara
Via Fossato di Mortara, 18, 44121 Ferrara, Italy
e-mail: pierpaolo.greco@unife.it

To my beloved family

Considerate la vostra semenza:

Fatti non foste a viver come bruti
Ma per seguir virtute e canoscenza

La Divina Commedia, Inferno
Dante Alighieri (1265-1321)

ABSTRACT:

The electrolyte-gated organic field effect transistors (EGOFET) are commonly used in biosensing applications due to the ultrasensitive sensing mechanism. The potential of the gate electrode is sensitive to antigen binding at surface bound recognition sites, which is capacitively coupled to the transistor channel. Even the low amount target biomolecules can cause a shift of the gate electrode workfunction, inducing a change in the Electrical Double Layers (EDLs) near the semiconductor-electrolyte interface.In this PhD thesis, I present applications of multi gate EGOFET architectures integrated with microfluidic devices exploiting diffusion in laminar flow mixer. The gradient of concentration affects the EGOFET electrical characteristics, providing an insight of the kinetics of surface functionalization reactions, oligonucleotide probe-target hybridization or antigen-protein binding reactions.

The reported results indicate that multi gate EGOFET can be used as an electroanalytical tool for monitoring self-assembly monolayers (SAM) on top of gold thin electrodes sputtered on flexible polymeric substrates. The possibility to control the self-assembled monolayer formation is achieved by means of the diffusion interface within the microfluidic streams. For this purpose, we integrate the microfluidic mixer with EGOFET device by means of an electrolyte bridge. The mixer performance is validated with UV Spectroscopy with different biomolecules.

The diffusion interface between concurrent streams of solutions generates a concentration gradient along the H-mixer main channel, which affects the kinetics of thiols self-assembly upon the array of electrodes patterned on the lower boundary of the microfluidics. The study was pursued with four short chain alkanethiol moieties (3-mercapto-1-propanol, 6-mercapto-1-hexanol, 8-mercapto-1-octanol, 9-mercapto-1-nonanol) at flow rates ranging from 2 µl/min to 50 µl/min. The 6,13-Bis(triisopropylsilylethynyl)pentacene (TIPS-pentacene) EGOFET was biased by a gate sweep in between -0.1 V and -0.6 V, with a fixed drain-source potential of -0.2 V. The drain-source current was recorded in the nA to µA range, showing a decrease correlated with the axial position of the gate electrode along the microfluidic channel. The initial gate electrodes in the array kept the same transfer curves as immersed in the PBS electrolyte, while those along the stream were influenced by thiol diffusion, leading to drain-source current lower than 50%.

Multi gate EGOFET architecture with microfluidic chamber has been used to perform biorecognition with oligonucleotides probe-target pairs, showing high sensitivity response. MicroRNAs (miRNA) are classified as important biomarkers for cancer such as glioblastoma, lung and breast cancers. Innovative diagnostic devices not only aim at early diagnosis but also at more

effective variant screening and therapy selection. In the present thesis I include the results of the research work on the dual gate/common channel organic transistor architecture designed for quantifying the concentration of one of the strands of miRNA-21 in solution, an important biomarker of glioblastoma The device allows one to measure the differential response with respect to a sensing gate and a reference gate electrode, both immersed in the electrolyte above the transistor channel. Hybridization with oligonucleotide in the picomolar regime induced a reduction of the current flowing through the transistor channel. The device response signal is reported at various gate voltages, being the sensitivity of the biosensor maximized in the sublinear regime, with a limit of detection as low as 35 pM. We describe the dose curves with an analytical function derived from a thermodynamic model of the reaction equilibria relevant in our experiment and device configuration and we show that the apparent Hill dependence on analyte concentration with exponent between 0.5 and 1 emerges from the interplay of the different equilibria. The binding free energy characteristic of the hybridization on the device surface is found to be approximately 20% lower with respect to the reaction in solution, hinting to partially inhibiting effect of the surface and presence of competing reactions.

A planar gate EGOFET-microfluidic integration has been tested for the quantification of α-synuclein, whose aggregation represents a critical event in the pathogenesis of neurological diseases, such as Parkinson.. The microfluidics integrated organic transistor was optimized for the detection of amounts of α-synuclein in the range from 0.25 pM to 25 nM. In our device, the single planar gate electrode is the effective sensing element and has been functionalised with anti-(α-synuclein) antibodies using two different strategies strategy: i) an amino-terminated self-assembled monolayer activated by glutaraldehyde, and ii) the His-tagged recombinant protein G. In both approaches, comparable sensitivity values were achieved, featuring very low limit of detection values at the sub-pM level. The microfluidics engineering is central to achieve a controlled functionalization of the gate electrode and avoid contamination or physisorption on the organic semiconductor. The demonstrated sensing architecture might represent a promising label-free tool to explore *in-vitro* protein aggregation that takes place during the progression of neurodegenerative illnesses.

Keywords: Organic Electronics, Electrolyte-gated organic field effect transistors (EGOFETs), Self-assembled monolayers (SAM), microfluidic mixer, diffusion

SOMMARIO:

I transistor a effetto di campo organico con elettrolita (EGOFET) sono usati sempre più frequentemente nelle applicazioni di biosensoristica a causa della sensibilità accresciuta dall'amplificazione del transistor. Il potenziale dell'elettrodo di gate è sensibile al legame dell'antigene nei siti di riconoscimento legati alla superficie dell'elettrodo. Inoltre questo potenziale è accoppiato capacitivamente al canale del transistor. Anche una ridotta concentrazione di biomolecole target vicine all'elettrodo di gate può causare uno spostamento amplificato della funzione di lavoro dell'elettrodo di gate, inducendo un cambiamento nel doppio strato elettrico (EDL) vicino all'interfaccia semiconduttore-elettrolita. In questa tesi di dottorato, presento applicazioni di architetture EGOFET multi gate integrate con dispositivi di microfluidica che sfruttano la diffusione nei mixer a flusso laminare. Il gradiente di concentrazione influenza le caratteristiche elettriche di EGOFET, fornendo un'idea della cinetica delle reazioni di funzionalizzazione della superficie, dell'ibridazione sonda-target dell'oligonucleotide o delle reazioni di legame antigene-proteina.

I risultati riportati indicano che l'EGOFET multi-gate può essere utilizzato come strumento analitico per il monitoraggio di monostrati di molecole (SAM) autoassemblati su elettrodi a film sottile d'oro ottenuti per deposizione in vuoto su substrati polimerici flessibili. La possibilità di controllare la formazione del monostrato autoassemblato è ottenuta tramite l'interfaccia di diffusione esistente fra i flussi microfluidici. A tale scopo integriamo il mixer microfluidico con il dispositivo EGOFET tramite un ponte elettrolitico. Le prestazioni del mixer sono state validate con la spettroscopia UV con diverse biomolecole.

L'interfaccia di diffusione tra flussi simultanei di soluzioni genera un gradiente di concentrazione lungo il canale principale del mixer ad H, che influisce sulla cinetica dell'autoassemblaggio dei tioli sull'array di elettrodi presenti sul confine inferiore della microfluidica. Lo studio è stato realizzato con quattro composti di alcantiolo a catena corta (3-mercapto-1-propanolo, 6-mercapto-1-esanolo, 8-mercapto-1-ottanolo, 9-mercapto-1-nonanolo) con flussi compresi tra 2 µl /min a 50 µl/min. Il transistor organico con semiconduttore 6,13-Bis (triisopropylsililethynyl) pentacene (TIPS-pentacene) è stato polarizzato da un gate sweep compreso tra -0,1 V e -0,6 V, con un potenziale drain-source fisso di -0,2 V. La corrente drain-source è stata registrata nell'intervallo da nA a µA, che mostra una diminuzione correlata alla posizione assiale dell'elettrodo di gate lungo il canale microfluidico. Gli elettrodi di gate iniziali nell'array mantenevano le stesse curve di trasferimento

immerse nell'elettrolita PBS, mentre quelli lungo il flusso erano influenzati dalla diffusione del tiolo, portando a una corrente di drain-source inferiore al 50%.

L'architettura EGOFET multi-gate con camera microfluidica è stata utilizzata per eseguire il bioriconoscimento con coppie sonda-bersaglio di oligonucleotidi, mostrando una risposta ad alta sensibilità. I microRNA (miRNA) sono classificati come importanti biomarcatori per il cancro come il glioblastoma, i tumori del polmone e della mammella. I dispositivi diagnostici innovativi non mirano solo alla diagnosi precoce, ma anche a uno screening più efficace delle varianti e alla selezione della terapia. Nella presente tesi includo i risultati del lavoro di ricerca sull'architettura del transistor organico dual gate/common channel progettata per quantificare la concentrazione di miRNA-21 in soluzione, un importante biomarcatore del glioblastoma. Il dispositivo consente di misurare la risposta differenziale rispetto ad un gate di rilevamento e ad un elettrodo di gate di riferimento, entrambi immersi nell'elettrolita al di sopra del canale del transistor. L'ibridazione con oligonucleotide in range di concentrazione picomolare ha indotto una riduzione della corrente che scorre attraverso il canale del transistor. Il segnale di risposta del dispositivo è riportato a varie tensioni di gate, essendo la sensibilità del biosensore massimizzata nel regime sublineare, con un limite di rilevamento di 35 pM. Nella tesi sono descritte le curve di dose con una funzione analitica derivata da un modello termodinamico degli equilibri di reazione rilevanti nel nostro esperimento e nella configurazione del dispositivo e mostriamo che l'apparente dipendenza di Hill dalla concentrazione di analita con esponente compreso tra 0,5 e 1 emerge dall'interazione dei diversi equilibri . L'energia libera di legame caratteristica dell'ibridazione sulla superficie del dispositivo risulta essere inferiore di circa il 20% rispetto alla reazione in soluzione, suggerendo un effetto parzialmente inibente della superficie e la presenza di reazioni concorrenti.

Un'integrazione planare EGOFET-microfluidica è stata testata per la quantificazione dell'α-sinucleina, la cui aggregazione rappresenta un evento critico nella patogenesi di malattie neurologiche, come il Parkinson. Il transistor organico integrato con microfluidica è stato ottimizzato per il rilevamento di quantità di α-sinucleina nell'intervallo da 0,25 pM a 25 nM. Nel nostro dispositivo, il singolo elettrodo di gate planare è l'elemento sensibile ed è stato funzionalizzato con anticorpi anti-(α-sinucleina) utilizzando due strategie diverse: i) un monostrato autoassemblato con terminazione amminica attivato dalla glutaraldeide e ii) la proteina ricombinante con etichetta His G. In entrambi gli approcci sono stati raggiunti valori di sensibilità comparabili, caratterizzati da valori limite di rilevabilità molto bassi a livello sub-pM. Lo studio della microfluidica è fondamentale per ottenere una funzionalizzazione controllata dell'elettrodo di gate ed evitare la contaminazione o il fisisorbimento sul semiconduttore organico. L'architettura di

rilevamento dimostrata potrebbe rappresentare un promettente strumento label-free per esplorare l'aggregazione proteica in vitro che avviene durante la progressione delle malattie neurodegenerative.

Parole chiave: Elettronica organica, Transistor ad effetto di campo organico con elettrolita (EGOFET), Monostrati autoassemblati (SAM), Mixer microfluidico, Diffusione

TABLE OF CONTENTS

CHAPTER 1

ORGANIC ELECTRONICS AND MICROFLUIDICS

1.1 Introduction

In the following chapter, I will introduce the research aim of my PhD work. The integration of microfluidic devices with organic electronics was my research topic in the BORGES – Biosensing with Organic Electronics, which is Marie Curie Skłodowska Project. It belongs to European Training Network (MSCA-ITN-ETN). I will explain the main important themes and aspects of my PhD work. Firstly, I will briefly discuss the importance and relevance of the biosensors in todays modern world. Starting from the first applications up to the state-of-the-art, I will explain Bioelectronics in details. Later, I will focus on Bioelectronics with Organic Electronics and their importance in this PhD thesis. Lastly, I will describe the microfluidic devices, its history and state of art devices. Most importantly, I will give some examples from the literature for the microfluidics and their integration to the biosensors.

1.2 Importance of biosensors in today healthcare

COVID –19 caused a global pandemic in recent years. In these times, it is needed to have fast diagnostic tools that shows if the patients have COVID or not. The traditional methods like Polymerase Chain Reaction (PCR) take long time to get results and they require lab facilities and expertise. So the importance and need of the biosensors and point of care devices are understood better. Fast rapid COVID tests like Lateral Flow Test (LFT) reduced the workload of the hospitals to an incredible extent, since they are low-cost, portable and easy to use. However, these type of disposable biosensors could lack the high sensitivity, considering the test can give false negative or false positive. Overall, the LFT meets many other criteria for a good biosensor such as affordability, portability, ease of use, high selectivity and specificity.

Biological sensor or also known as biosensor is a biochemical and analytical sensing device, which transduces signals when the analyte interacts with biorecognition components connected with the transducing components [1]. They are used for the disease detection and monitoring, drug discovery, food safety and environmental issues [2]. Specially, they are quite important for early diagnosis and its progression and treatment for certain diseases such as cancer [7]. One of the first example of the biosensors was from 19^{th} century where the electrodes were used for pH measurement [3]. In 1950s, Leland C. Clark, Jr invented the Clark electrode, a device used to measure oxygen level in blood and in various tissue cells of body parts. Clark's device was inserted into the blood vessels for continuous measurement and recording of oxygen level [4]. He is considered as "father of the biosensors". In 1962, Clark Jr developed a device to detect level of

glucose content in blood [5]. This turned to be one of the most successful biosensor up to this day is the glucose sensor.

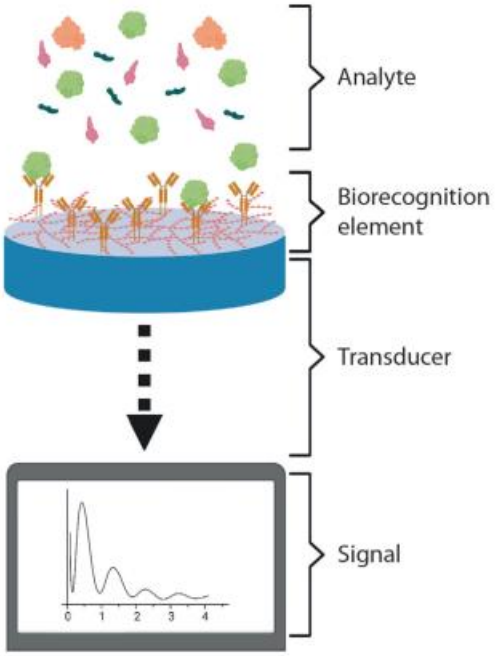

Figure 1.1: Schematics of a biosensor [6].

Monitoring and controlling the blood sugar levels throughout the day for the people with diabetes are quite important since the chronic disease could develop severe side effects and cause irreversible damages. For the biosensor, sensing are done with the biological samples such as blood, saliva, plasma or sweat. This choice depends on the application, targeted biomarkers and signal transmission. The signal is generated when the biorecognition occurs between the biorecognition element and the analyte leading to the detection. The transducer helps in the detection of the physical parameter change or chemical reaction output to an electrical signal or an optical signal. In order to develop a complete sensing platform, it is necessary that the biosensor should have been integrated with microfluidics to improve the fluid manipulation or processing.

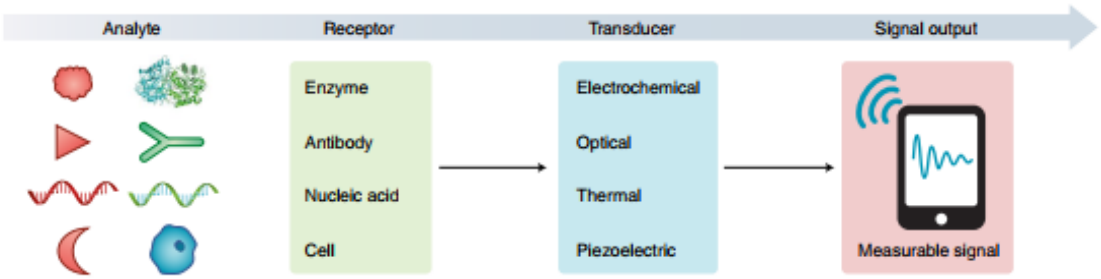

Figure 1.2: Components of a biosensor and operation principles [18].

1.3 Bioelectronics

The bioelectronics refer to the combination of the biological matter and electronics. It is a multidisciplinary field that is associated with the biomedical engineering, the microbiology, the genetic engineering and the molecular engineering. Bioelectronics have been closing the gap between the biological field and the electronics and build communication between them. They are valuable for early detection of diseases, diagnosis, and treatment or rehabilitation. They improve the life quality and the health of the individual. In the bioelectronics, the signal from the biological process should be be transferred to the electronic part, contrarily the stimulation of a biochemical reaction or process should be transferred as well to the electronic device. Some important factors that influence the device performance are the signal generation, processing, transmission and its digitalization from the electronics perspective whereas the signal transmission efficiency, signal strength and the type of material used for device are the sources of limitation in the bioelectronics [15].

In the end of 18^{th} century, Luigi Galvani conducted an experiment with the frog legs where he connected the frog legs on a lightning rod. The frog leg twitched as the current passed through. It was evident that the frog leg reacted when current passed through the tissues. This discovery is one of the most important fundamental discovery and development in the field of bioelectronics [8, 9]. It led to the development of numerous devices like pacemaker [10, 11], cochlear implant [12] and deep brain simulations [16]. A pacemaker is a device to control and regulate the working of the human heart [13]. It controls the hearth rate and rhythm by sending electrical impulses to the muscles surrounded to the heart [14]. The mechanism is based on the same mechanism discovered by Luigi Galvani. The first implementation of the pacemaker was successfully done in 1958. The

evolution of the pacemaker could be seen Figure 1.3. With the advancements in technology and material science, the bioelectronics have been evolving from hard electronics to soft electronics.

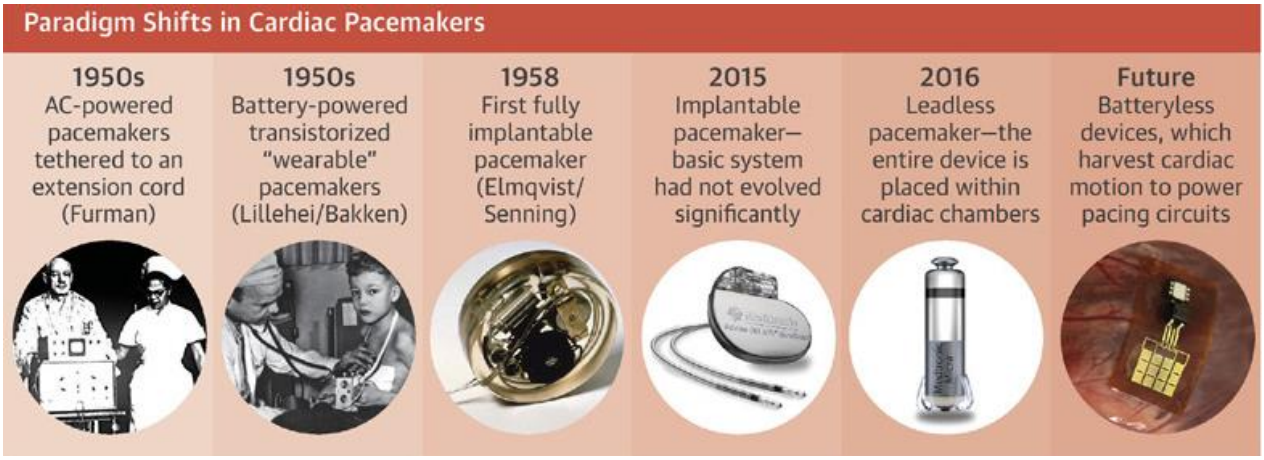

Figure 1.3: An overview of the history of cardiac pacing [11].

Another important example from bioelectronics is the amperometric glucose sensor; a device that can measure the blood sugar level in non-hospitalized environment In the amperomentric glucose sensor, an enzyme named Glucose oxidase (GOD) is the commonly used and Glucose concentration in blood is the analyte, which needs to be measured. Glucose oxidase enzyme starts to catalyse the oxidation reaction of glucose with oxygen. It produces gluconolactone and hydrogen peroxide (H2O2) as a result. The increase in H2O2concentration reduces the oxygen concentration. This is directly proportional to the glucose concentration where quantifiable reading can be derived on the output. [17].

To monitor the body to measure physical performance or stamina aside from glucose monitoring has been gaining lots of interest. The ease of use, flexibility, high performance and affordability are few reasons that the wearable sensors become favored, especially in the sports industry. The wearable sensors attach to the human body, take sweat or tear as a sample in micro volume. They are often used to measure the status of hydration levels, heartbeat and other performance characteristics [18]. One of the main advantage of the wearable sensors is the usage of the microliter volume of solution that can be analyzed. However, the sweat rate, concentration and composition are the factors that could influence the wearable sensor performance [19].

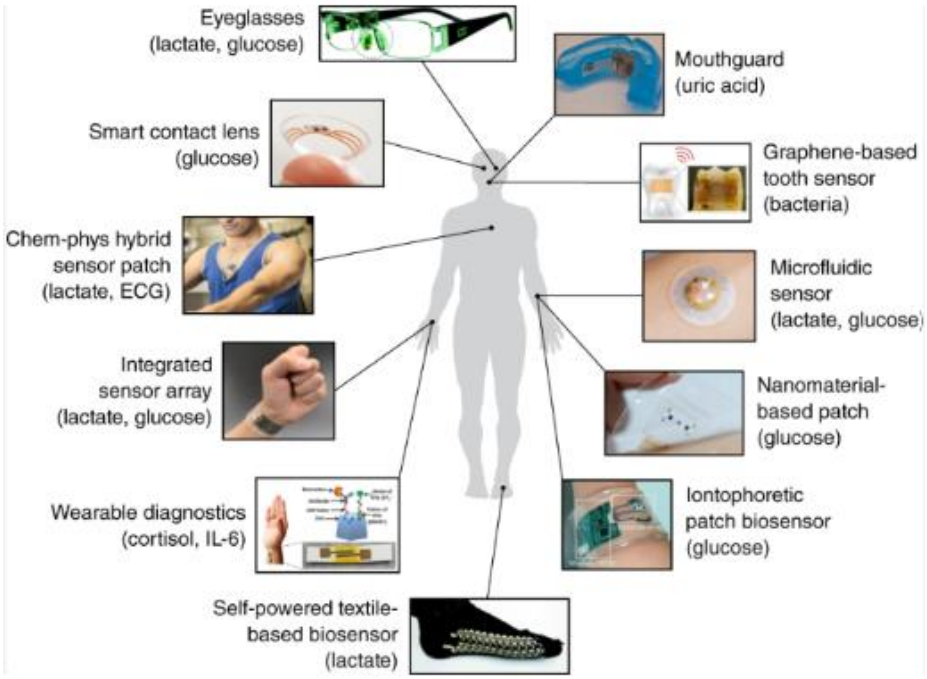

Figure 1.4: Examples of wearable sensors for different applications [18].

1.4 Organic Electronics

Bioelectronics have been aiming to overcome the challenges when it comes to closing the gap between the electronics and the biological specimens. One of the most challenges is to decrease the impedance of biological interfaces with electronics. The other challenge is compatibility between electronics and the surrounding biological environment. Here, the field of Organic Electronics arises.

The name organic originates from the usage of carbon based π-conjugated small molecules and polymers, whereas traditional electronics are silicon-based. In late 19th century, Henry Letheby discovered the conductive properties of polyaniline, an organic polymer. Since then the organic polymers have been used as a source of conductivity [20]. Compared to the silicon-based electronics, organic electronics have advantages such as low-cost fabrication, flexibility and low temperature processing, which makes them suitable for disposable devices such as biosensors. However, materials research is focused on developing organic semiconductors with accpetable performance, since they are still not comparable with inorganic FETs in terms of carrier mobility and operating frequency, and their subthreshold swing is often much higher [44]. Improving the

device performance is possible with the doping process of the organic polymers [22, 23]. One of the most commonly used organic polymer in organic electronics is Polyacetylene. Hideki Shirakawa and coauthors successfully doped polyacetylene and improved the electrical conductivity of the organic polymer [21]. This led to the extensive development of technologies related to organic semiconductors. They won Noble prize for their work in 2000 for their work.Organic field effective transistor (OFET) [24, 25], Organic light emitting diode (OLED) [26, 27], Organic solar cell (OSC) [28], and organic photoelectrochemical cell (PEC) [29] are some of the examples of organic electronics used in different applications.

In the OFET devices, conjugated polymers are used as organic semiconductors for the conducting channel. They create an interface between electronic and biological systems and have to capability to interact with ions and water molecules of the biological system. One of the biggest advantages is that they make use of circuitry and signal amplification already developed for electronic applications[30, 31]. With organic electronics, it is possible to measure weak biochemical signals. Moreover, organicdevices tend to be more biocompatible than devices based on inorganic materials, in particular rigid silicon-based [32]. Organic electrochemical transistor (OECT) and Electrolyte-gated Organic Field-Effect Transistors (EGOFET) are most developed and commonly used in biological applications. Both of them belong to class of transistors called electrolyte gated transistors (EGTs) in which the electrolyte acts as a dielectric. This makes these devices compatible with aqueous environments [35]. PEDOT: PSS based OECTs are used as ion or enzymatic or immune sensors [34-39]. Other examples could be seen in Figure 1.6.

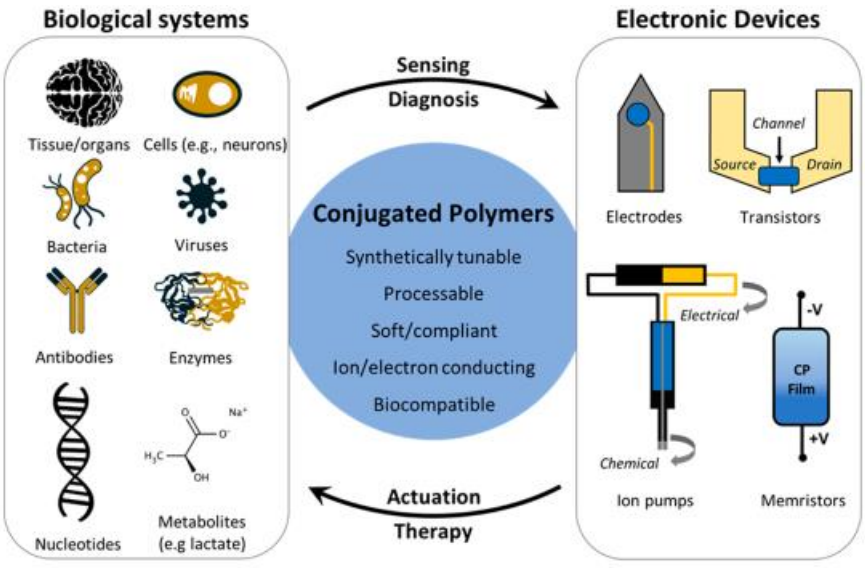

Figure 1.5: Schematic presentation of the relations between the biological system and electronics [33].

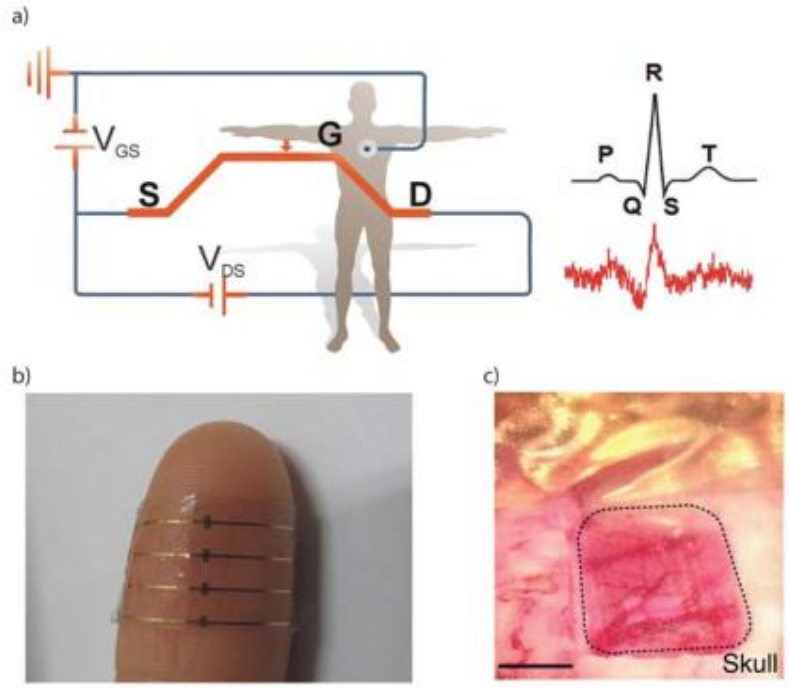

Figure 1.6: Few example of OECTs in the different applications a) Electrocardiogram (ECG) recording with an OECT operated in direct contact with the skin. b) Photograph of the device showing its transparency and adaptability when attached to human skin [38] c) Optical micrograph of the electrocorticographic (ECoG) probe placed over the somatosensory cortex, with the craniotomy surrounded by dashed lines. Scale bar: 1 mm [39].

1.4.1 Electrolyte-Gated Organic Field-Effect Transistor (EGOFETs)

Field-Effect Transistors (FETs) are three or four terminals semiconducting devices that can amplify and control the electronic signals, as they are transferred through the device from input to output terminals [44]. FETs act like an ON/OFF switch. When the transistor is on, the gate voltage is applied and the current flows. Likewise, when no gate voltage is applied, it is switched off and the current stops. Three terminals are three metallic electrodes known as Source (S), Drain (D) and Gate (G). The fourth terminal is known as Body (B) and not every FETs have this terminal.

The Gate (G) is separated from Source (S), Drain (D) electrodes by a thin solid insulating layer known as dielectric. Different types of dielectrics can be used like oxides or polymers. In the silicon-based FETs, mostly silicon oxide is used as the dielectric. Depending on the location of the Gate electrode, FETs have different architectures like top-gate or bottom gate architecture. Likewise, depending on the location of the Source and Drain electrodes, the device architecture

changes: top Source-Drain contacts (top-contacts) and bottom Source-Drain contacts (bottom-contacts). The field-effect transistors use the electric field to control the flow of current. When the voltage is applied at the Gate; it modifies the charge carrier density in the semiconductor layer and it forms a conducting channel between the Source and Drain. Based on the semiconductor type, the charge carrier could be either electrons or holes [41]. Field effect is capacitance related, which is very sensitive to surface changes. For example, the presence of guest molecules over one of the gate/dielectric or dielectric/semiconductor interface would result in a shift of the conductance of the semiconductor [44].

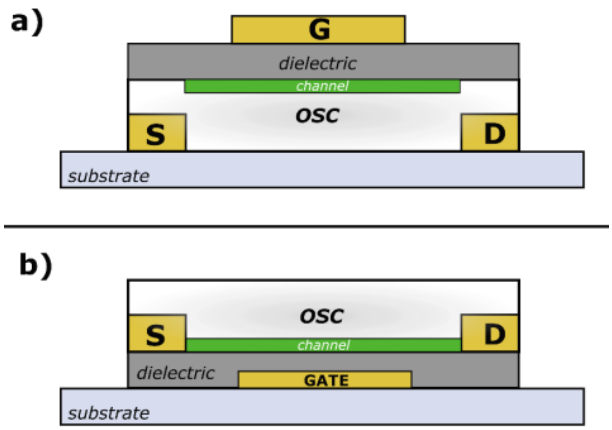

Figure 1.7: a) Different classifications of FET: a) bottom-contacts with top gate electrode, b) bottom-gate contact with top Source-Drain electrodes [43].

Organic Field-Effect Transistor (OFETs) have the same configuration and the working mechanism of the traditional FETs but an organic semiconducting material are adopted for the conduction path. When the negative gate voltage is applied to the Source and Drain for p-type semiconductor, the holes are injected from Source and the current flows inside the channel. The free holes in the conducting channel are shifted towards the dielectric-semiconductor interface to compensate for an equivalent negative charge at the gate dielectric interface. The first OFET was made by Tsumura *et al.*, in the year of 1986. [44].

The most commonly used organic semiconductors (OSC) are terthiophene and α-sexithiophene, P3HT (Poly (3-hexylthiophene)), Perlyene derivatives, Pentacene and TIPS-Pentacene (6,13-Bis(triisopropylsilylethynyl)Pentacene**)** [45]. For p-type semiconductors, the electron donating organic semiconductors involving the highest occupied molecular orbital (HOMO) level are good

candidates, while electron- accepting ones with low HOMO levels are used as an n-type semiconductor [44].

In OFETs, between the organic semiconductor channel and the gate, a solid dielectric like silicon dioxide (SiO2) or PMMA (Poly (methyl methacrylate)) has been used. In Electrolyte-Gated Organic Field-Effect transistors (EGOFETs), the solid dielectric is substituted by a liquid dielectric medium like PBS buffer [45, 47]. Using a liquid dielectric results in much higher capacitance (≈101-102 $\mu F/cm^2$) and low biasing voltage properties (< 1V) [48]. These features make EGOFET suitable candidate for biosensors, specially the device operates in a liquid environment and it is possible for the biomolecules to bind with the bio receptors. [43, 49–55].

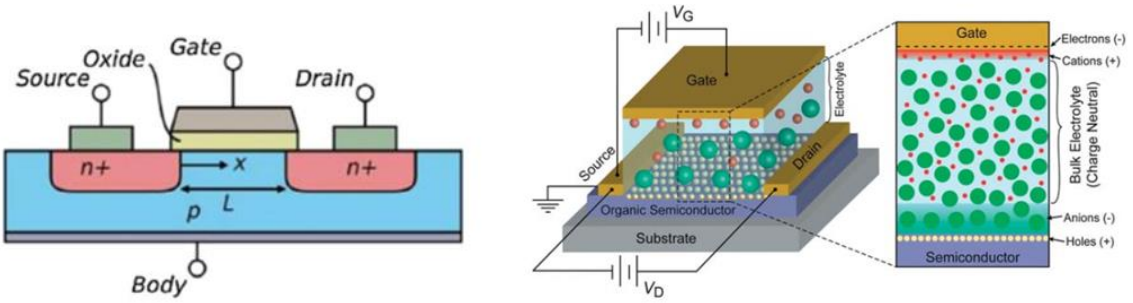

Figure 1.8: a) Schematics of silicon-based field effect transistor (FET) [41] b) Device structure and working principle of an electrolyte-gated organic field-effect transistor. The gate voltage (V_G) and the drain voltage (V_D) are applied relatively to the grounded source electrode. The gate voltage V_G causes ions migration within the electrolyte layer, resulting in the formation of EDLs at the gate–electrolyte and electrolyte semiconductor interfaces [37, 42].

The device turns on when the negative potential is applied between Gate and Source electrodes for p-type semiconductor. The electrons at the gate electrode surface produces the accumulation of cations at the Gate-electrolyte interface, whereas, the accumulation of anions at the electrolyte-semiconductor interface produces the accumulation of the holes at the top layer of the semiconductor, which modulates the hole transport inside the semiconductor channel [44, 56-58].

Electrical Double Layer (EDL) forms at the interface at electrolyte-gate and electrolyte-semiconductor for even very low operating potentials. It is very sensitive to interfacial changes and responsible for the modulation of the output current I_{DS} of the device. EDL consists of the two layers Helmholtz layer (HL) and Diffusion layer (DL). In the Helmholtz layer, the ions are arranged in a monolayer and the Diffusion layer is set as a region of highly concentrated ions (cations and anions), based on the potentials applied to the gate [48]. The concentration of ions in the Diffusion layer decreases with the increased distance from the interface. The thickness of the EDL is in the range of the sub-nanometer (nm) length scale and looks like a parallel plate capacitor having a thin layer of dielectric polarized solvent molecules separating them. The capacitance is higher at the EDL due to the small distance between the charged layers [56, 58]. The low potentials (< 1V) are sufficient to produce a high field at the interface, whereas the field stays constant in the bulk resulting in very low capacitance due to the increase of distance. The output current changes when the capacitance changes with respect to the interfacial changes with the target analyte in the solution. [44, 56].

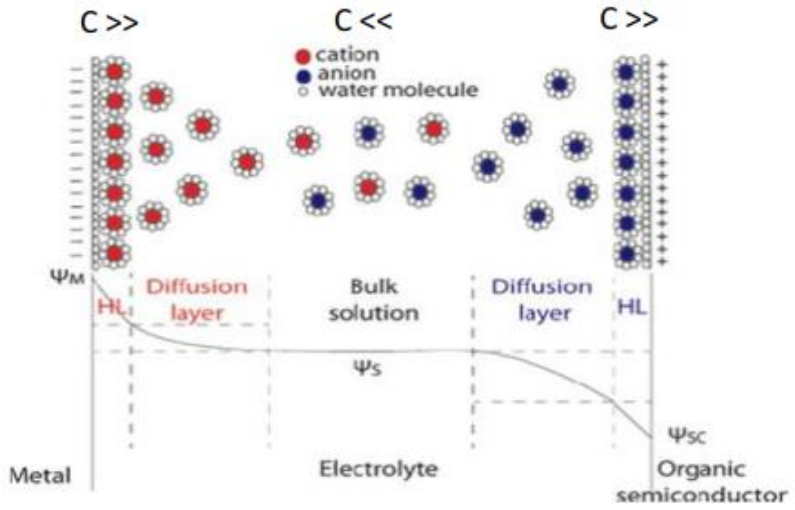

Figure 1.9: Ion distribution across the EDL and potential drop inside the electrolyte solution [44, 46].

EGOFET device can be operated in two regimes; Linear regime and Saturation regime (Equation 1.1 and 1.2). In the equation, the W and L are the width and length of the channel, while C is the capacitance of the insulating layer. By the electrical characterization of the EGOFET, parameters such as μ (carrier mobility in the channel specific to the semiconductor) and V_{th} (threshold voltage, which is the minimum voltage necessary to turn on the device) can be extracted and used as figures of merit, while performing sensing [46,59].

For biosensing applications, the EGOFET device operates under the linear regime, since the device conducts and dI_{DS}/dV_{DS} is maximum. In the saturation regime, the conducting path is completely filled with the charge carrier and the current reaches the saturation. When the device reaches the saturation, it enters the pinch-off state and acts like an OFF switch.

$$I_{DS} = \frac{W}{L} \mu C (V_{GS}-V_{Th}-V_{DS}/2)V_{DS} \text{ , for } |V_{DS}| << |V_{GS}-V_{Th}| \quad \text{(Linear Regime)} \quad \text{(Eq. 1.1)}$$

$$I_{DS} = \frac{W}{2L} \mu C (V_{GS}-V_{Th})^2 \text{ , for } |V_{DS}| >> |V_{GS}-V_{Th}| \quad \text{(Saturation Regime)} \quad \text{(Eq. 1.2)}$$

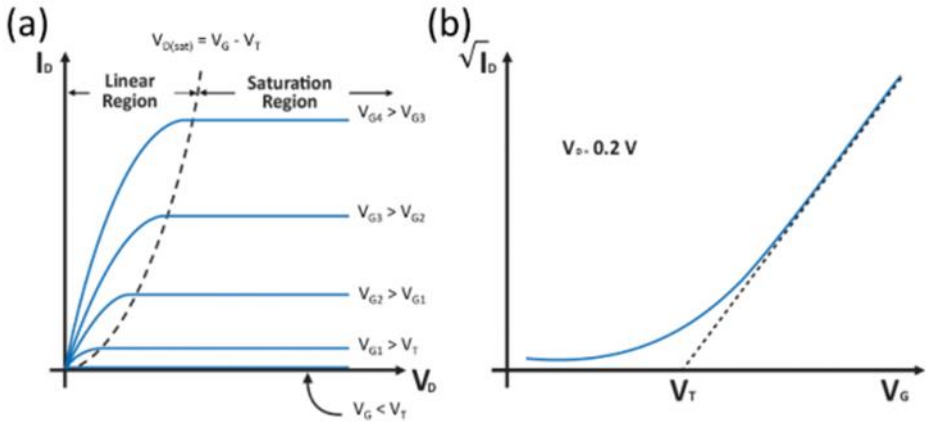

Figure 1.10: a) Output and b) transfer curves of a generic n-type transistor [48].

In the next segment, I will give some examples of EGOFET-based biosensors for detecting different biomarkers like protein and nucleic acids. One of the first DNA EGOFET sensor was first reported by Kergoat *et al* [60]. The EGOFET device was based on Poly(3-hexylthiophene) (P3HT) and phosphate buffer saline (PBS, pH 7.2) solution as the dielectric medium. Platinum (Pt wire) was used as a gate electrode and the device was operated below 1V.

P3HT has carboxylic acid moieties that was used to perform covalent ODN (oligonucleotide) grafting. With the DNA hybridization with 100nM concentration, the gate voltage was shifted between 40 to 60mV in the negative values, which attribute to the negative charges carried by the DNA backbones. The importance of Debye length, which could screen negative charges of the DNA, can be analyzed with other experiments by using buffers having various ionic strengths [44, 60].

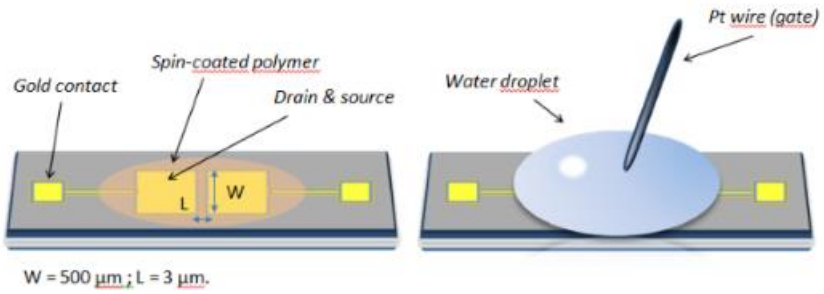

Figure 1.11: Schematic view of P3HT based EGOFET device for DNA detection [60].

Another example of P3HT based EGOFET biosensor is for the protein (streptavidin) detection [61]. The semiconducting channel was based on a copolymer of P3HT, P3HT- COOH and biotinylated P3HT acting as an active sensing platform. The -COOH group reduces a non-specific interaction. Additional pre-treating the polymer surfaces with 1-octanol, reduced the non-specific interaction . Biotin-streptavidin couples were used for detection due to their very low dissociation constant. The transfer curve shows, no effect on human serum albumin exposure, whereas the Drain-Source current decreases due to streptavidin exposure [61].

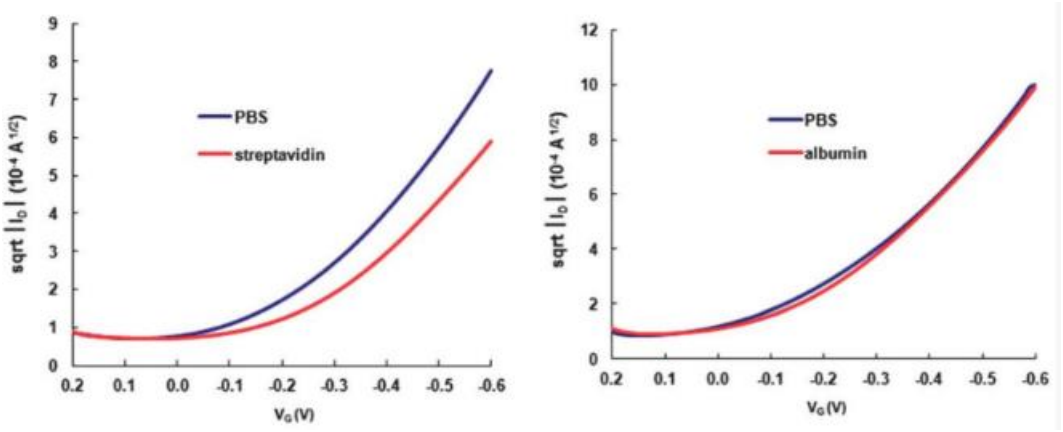

Figure 1.12: Transfer curves at saturation for P3HT:P3HT-COOH: P3HT-biotin based transistors treated with 1-octanol before and after incubation with proteins [61].

In order to study the transduction mechanism of EGOFET device, Palazzo *et al*. investigated the sensitivity as a function of the Debye's length, the receptor charge, and the distance at which the binding event takes place [62]. For this purpose, experiments were performed phospholipid film with biotin/avidin andantigen/antibody interactions (C-reactive protein (CRP) and anti- CRP, respectively) which were immobilized on the semiconductor layer. The device was successfully able to detect binding events occurring at distances that are 30 times the Debye's length value from the transistor electronic channel. The transduction mechanism of the biorecognition was explained by the capacitance changes at the electrolyte/OSC interface rather than by electrostatic effects of the charges carried by the target molecule [62].

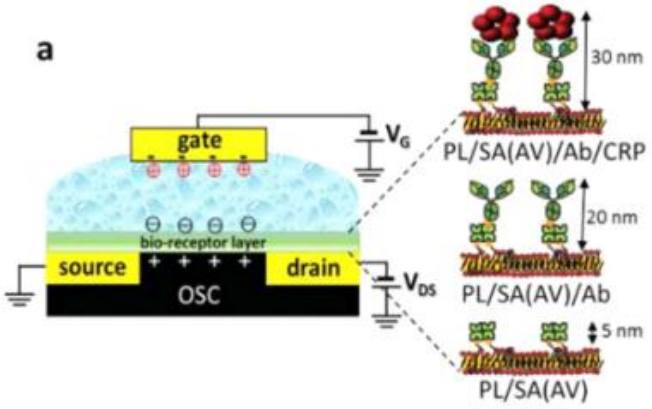

Figure 1.13: Schematic view with different thicknesses of the bioreceptor layer [62].

Magliulo et al. used biotin-labeled phospholipids, in order to form a streptavidin binding layer [63]. To minimize the penetration of ions from electrolyte to OSC surface, the phospholipid bilayer thin film was used on top of the semiconductor layer. This approach led to EGOFET compatible with the immobilization of the probes in or onto the phospholipid bilayer. The sensing mechanism depends once again on the capacitive changes in EGOFET at the phospholipid bilayer together involving the

charge carrier of streptavidin. This path led to a new way for preparing immunosensors, since a phospholipid bilayer could be functionalized with any bioreceptors.

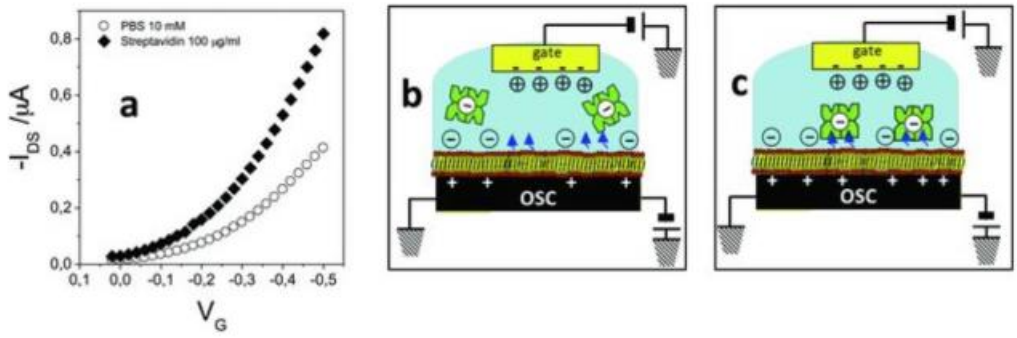

Figure 1.14: a) Transfer characteristics of the biotin-functionalized phospholipid bilayer-EGOFET in PBS, pH 7.4 (open symbols) and streptavidin (full symbols) solutions. b,c) Diagram for the rationale leading to the I_{DS} current increase [63].

In the EGOFET, not only the semiconductor layer could be functionalized but also the Gate electrode. For the detection of dopamine, the Gate electrode (Au) acted as a sensing area and it was functionalized with a self-assembled monolayer of cysteamine and 4-formylphenyl boronic acids. The transduction mechanism is based on the modulation of capacitive changes of the electrical double layer formed at the Gate/electrolyte interface. The transfer curve of the device changes, when the dopamine bonded with boronic acid, thus the work function of the gold electrode changes together with the gate capacitance changes [53].

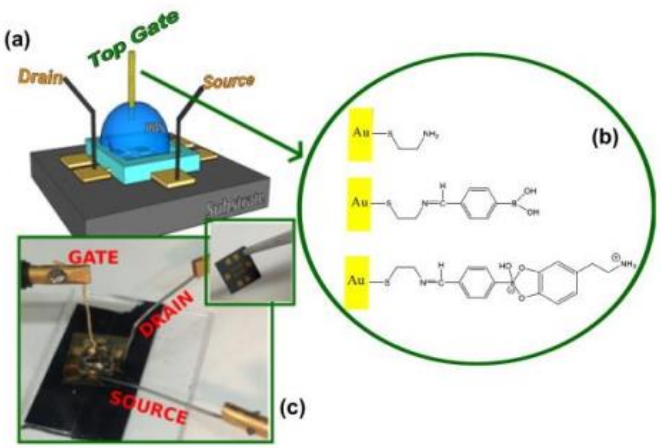

Figure 1.15: a) Schematic picture of the test pattern integrated with a poly(dimethylsiloxane) pool for confining a droplet of phosphate buffer solution (PBS). b) The SAM steps are (1) cysteamine, (2) 4-formylphenyl boronic acid and (3) dopamine. c) Picture of the device [53].

Another example of the gate functionalization of EGOFET is for the detection of Interleukin (IL)-6, which is a multifunctional cytokine. Its level in blood increases with infections, cancer and inflammation. Two different bioreceptors monoclonal antibodies and peptide aptamers are used for the detection of protein (IL-6). The results were compared for both the strategies, which were employed with two different EGOFETs. Antibodies were functionalized on the gate surface of one EGOFET biosensor and aptamer on the gate surface of the second EGOFET biosensor. When two EGOFET biosensor results were compared, where both leads to the limit of detection about 1 pM concentration of IL-6 [64].

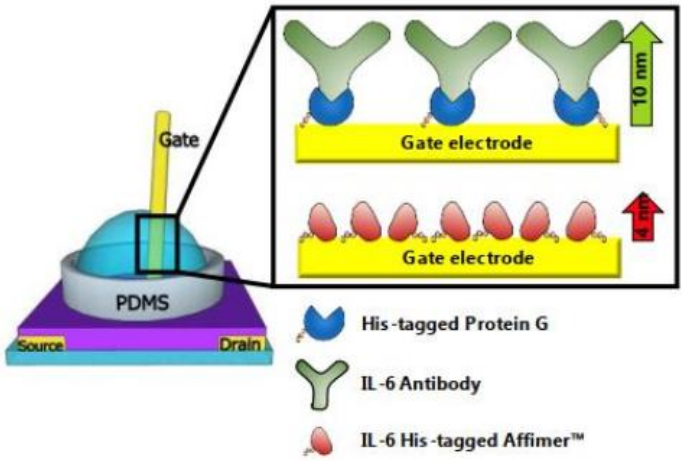

Figure 1.16: Schematic experimental setup; Source, Drain and Gate electrodes, the PDMS pool, the organic semiconductor layer on the quartz substrate and the electrolyte (left) and the two gate functionalization strategies (right): IL-6 Antibodies are immobilized on the gate surface through His-tagged Protein G, while anti-IL-6 Affimers are directly immobilized on the gold surface by means of the His-tag [64].

Another example of the gate functionalization is for the label free detection of (TNF- α). It is another inflammatory cytokine. TNF -α Antibody was immobilized on the gate electrode by using His-tag protein G. The target analyte Tumor Necrosis Factor (TNF) was detected with the limit of detection of 100 pM. High selectivity of the target analyte was achieved in PBS solutions containing different concentrations of Bovine Serum Albumin (BSA) [65].

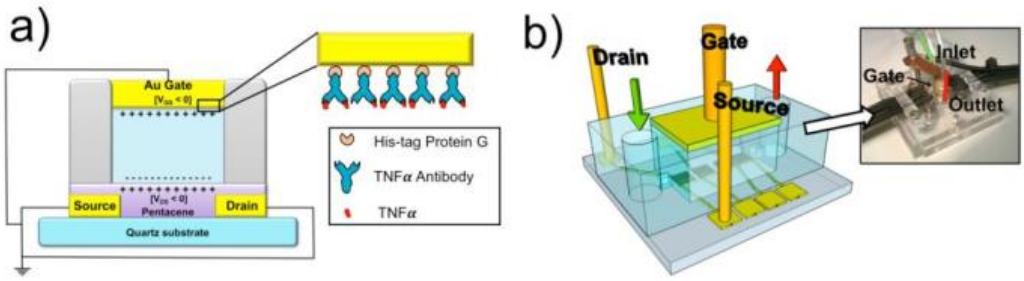

Figure 1.17: a) Schematics of the EGOFET device with the functionalized gate. b) Schematic drawing of the microfluidics and a photo of the experimental setup with the electrical connections and fluidic inlets [65].

1.5 Microfluidics

Microfluidics is the science and technology of systems that process or manipulate small amounts of fluid such as nano or micro litres by using channels with dimensions of tens to hundreds of micrometres [66]. They have been used in various application areas like chemical and biological analysis, clinical diagnostics, and drug development [66, 68, 69, 70].

One of the first microfluidic device was a miniaturized gas chromatography (GC) system, which was developed by Terry et al. [67]. Since then, many researches have been conducted with microfluidics [71, 72, 73,74]. They have many advantages such as low-cost fabrication and fast prototyping. Other advantages are low volume of reagents and waste during analysis within shorter time. Due to the miniaturization, the weight and volume of these devices are decreased and they became lightweight. This led to the portability of microfluidic devices [66, 76].

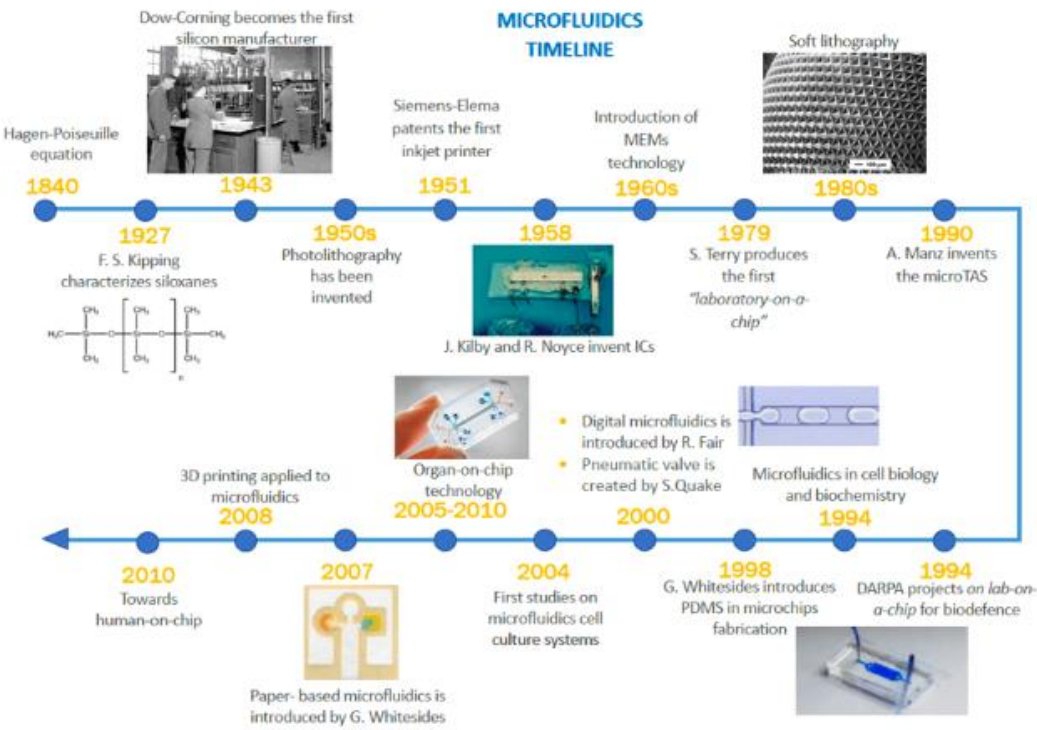

Figure 1.18:Chronological order: a) Poly (dimethyl siloxane) (PDMS)chemical structure, b) Dow Corning is founded in Midland (1943) to work on silicones c) the first working germanium IC created by Jack Kilby (1958), d) SEM image of a patterned PDMS microstructure obtained by replica molding [80], e) a PDMS microfluidic chip, f) digital microfluidics for manipulation and control of discrete droplets and bubbles, g) an example of organ-on-chip, a device that allows cells to be seeded in order to recreate the microenvironment and microarchitecture of a specific human tissue or organ, h) a paper-based microfluidic device can be used as low-cost, portable diagnostic tool, resulting to be particularly useful in emergency conditions and in resource-limited areas. [79].

For the fabrication of the microfluidic devices, the photolithography and etching were used which were known from the microelectronics (MEMS). In addition, the first materials used for microfluidics came from microelectronics too such as glass and silicon, which are expensive and requires high cost processing techniques in cleanrooms [77]. With the discovery of Poly (dimethyl siloxane) (PDMS), new fabrication techniques such as soft lithography made possible to fabricate quickly prototypes of the microfluidics [75, 78]. PDMS is an inexpensive and flexible material and optically transparent down to wavelength of 230 nm. Therefore, it is compatible with many optical methods for detection. Moreover, it is biocompatible with the cells because it is impermeable to water and permeable to gases. Another advantage of PDMS over glass and silicon is the easiness with which it can be fabricated and bonded to other surfaces [78, 85].

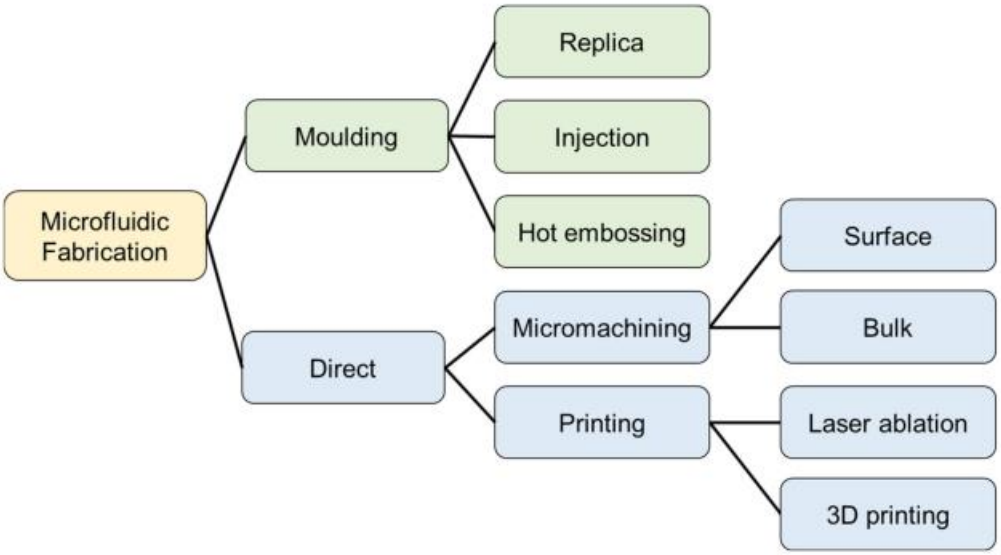

Figure 1.19: Main methods used for the manufacturing of microfluidics [81].

Each fabrication technique has its own advantages like high resolution or low-cost fabrication. With photolithography and printing, one can achieve tens of micrometre (μm) or less, whereas the replica moulding resolution is mostly dependent on the fabrication technique used for the master. The photolithography requires clean room facilities, whereas the others do not require. Due to this, cost per device has been much lower. Another aspect to consider is manufacturing time. For replica moulding, this can take several hours or days, whereas with 3D printers and the photolithography, the process is much quicker. With 3D printers, it is possible to have 3D structures compared to the photolithography.

However, only with replica moulding, one can achieve large-scale production for the microfluidic devices. More information about the fabrication of microfluidic devices could be found in Chapter 2.

1.5.1 Theoretical background of microfluidics

To manipulate and control the fluid in the microchannels, it is important to understand the physics at the microscale level. When the dimension of system decreases, gravity becomes less important. Since the microfluidics are in micro or nanoscale range, the viscous forces become dominant compared to the gravity [82]. The Reynolds number (Re) is a dimensionless number, which represents the ratio of inertial forces over viscous force and characterizes the flow in the channels [76, 82].

$$\mathrm{Re} = \frac{Inertial\ Forces}{Viscous\ Forces} = \frac{\rho \cdot v \cdot L}{\mu} \qquad \text{(Eq. 1.3)}$$

In the equation 1.3, ρ is the fluid density (kg/m^3) and *v* is the average flow speed (m/s). L is the characteristic length scale of the channel (m), and μ is the kinematic viscosity of the fluid (Pa.s). If Re is above 4000, inertial forces dominate the flow, which leads to turbulence. If Re is less than 2000, viscous forces dominate the flow. This flow characteristic is defined as laminar flow [82, 83]. Due to the dimension of micro channels, the Reynold number has low value typically *Re* <1. In laminar flow, when the two flow streams come together, they flow parallel and flowing on top of each other without mixing due to the lack of turbulence [82]. The only mixing occurs by cause of diffusion of molecules across the interface between the fluid.

The fluid flow inside of the microfluidic channel is described by Navier-Stokes equation for incompressible Newtonian liquid. The equation expresses mathematically the conservation of mass and the conservation of momentum for Newtonian fluids. It can be considered as the balance of the forces, which act on each single fluid element [85]. In the Navier –Stokes equation, V represents the fluid velocity, ρ is fluid density, p is the pressure, μ is the viscosity of the fluid and F is the body forces per unit volume.

$$\rho \frac{\partial \mathrm{v}}{\partial \mathrm{t}} + \rho(V.\nabla)V = -\nabla \mathrm{p} + \mu\nabla^2 V + F \qquad \text{(Eq. 1.4)}$$

More information about the fluid dynamics and Navier-Stokes equation could be found in Chapter 4.

1.5.2 Integration of microfluidics to point of care diagnostic devices

With the recent event like COVID -19 pandemic, the need for low-cost, sensitive, user-friendly, robust diagnostic devices has been increased. The state of art methods like PCR, ELISA and other immunoassays are time consuming and require many sample preparation steps. The integration of the microfluidics with a sensing unit could improve requirements matching performing all the sample preparation steps, assay, detection and analysis in small volume quantities. However, this integration could be challenging, since there are important parameters to consider like material and process compatibility [81]. The chosen materials for the fluidics and the sensing units should be compatible and must not interfere with each other during the biological reaction and the detection. In the following, I will give some examples of the integration of microfluidics with different sensing units.

Surface Plasmon Resonance (SPR) is an optical detection method, which is employed with gold coated quartz substrates integrated with microfluidic channels and immobilized antibodies for the detection of target analytes [86,87]. The sensing mechanism of SPR depends on the detection of a refractive index change at the metal surface which is functionalized with probes molecules (e.g., antibodies) [87]. Frasconi et al. demonstrated the use of an Eco Chemie Autolab SPR system for the immunological detection of cortisol and cortisone in saliva and urine. They used polycarboxylate-hydrogel-based coatings for antibody immobilization onto gold disks, and showed a detection limit of less than 10 µg/L, sufficiently sensitive for both clinical and forensic use [87,91].

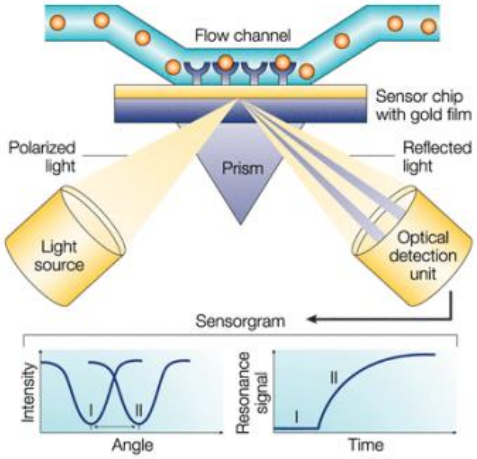

Figure 1.20: Setup of a microfluidic SPR biosensor. The configuration encompasses a light source, a prism and a detector, all coupled to a metal-coated sensor microfluidic chip. SPR detection involves variation in the refractive index in the immediate vicinity of the metal layer of the sensor chip [87].

Peng Lin et al. achieved the integration of microfluidics with the organic electrochemical transistors (OECT). In their work, the organic electrochemical transistor based on on a poly(3,4-ethylenedioxythiophene):poly(styrene sulfonic acid) (PEDOT:PSS) was integrated in a flexible microfluidic system for DNA detection. The OECT was fabricated on flexible polyethylene terephthalate (PET) substrates and integrated in a microfluidic channel formed with PDMS bound on the top. For label-free DNA detection, the single-stranded (ss) DNA probes were immobilized on the surface of Au gate electrodes and then the devices were used to detect complementary DNA targets at concentrations as low as 1 nM. The detection limit of the DNA sensor was extended to 10 pM when the hybridization of DNA was enhanced by applying an electric pulse to the gate electrode in the microfluidic channel [88].

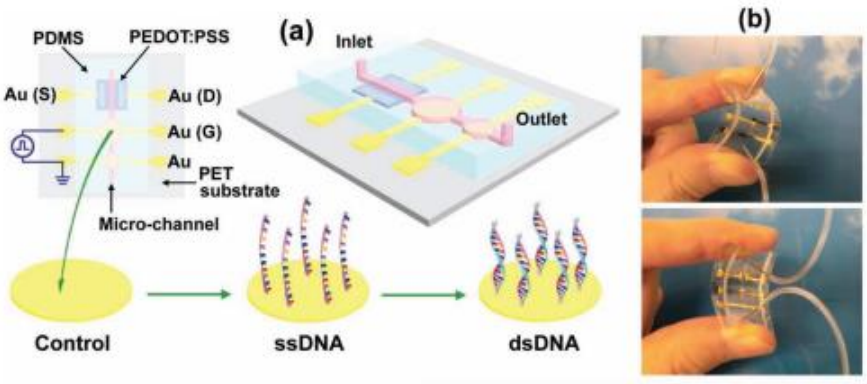

Figure 1.21: a) Schematic diagram of an OECT integrated in a flexible microfluidic system. The device is characterized before and after the modification and the hybridization of DNA on the surface of Au gate electrode. b) Photographs of a device bent to both sides [88].

A.M. Pappa et al. showed another example of the integration of an organic electrochemical transistor (OECT) microarray with a pumpless finger-powered microfluidic to detect three clinically relevant biomarkers, glucose, lactate, and cholesterol in human saliva. This integration led to an easy-to-handle platform potentially extended to any type of enzymatic biosensors [89].

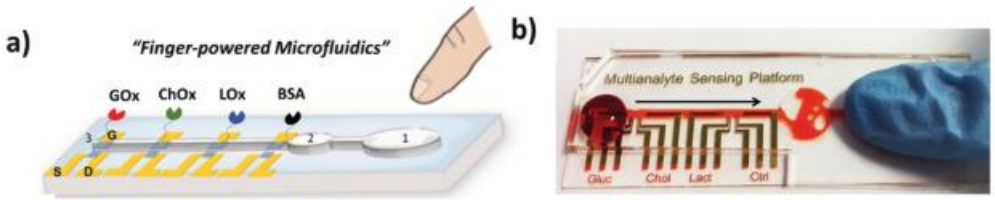

Figure 1.22: Selective multi analyte detection in complex media using the OECT array. a) Schematic illustration of the biosensing multiplatform with the embedded "finger-powered" PDMS microfluidic showing the 1) activation "button," 2) the liquid reservoir and 3) the punched inlet. b) Photograph of the actual device used for the measurements, showing a red-colored solution that was pressure-driven from the inlet through the sensing areas, as indicated by the arrow [89].

For continuous monitoring of glucose, A.C. Fernandes et al. demonstrated the sensor integration in microfluidic platform. The platform was compatible with different sensor formats by enabling their replacement and was built in order to be highly flexible. It made possible to achieve the electrochemical and other sensor technologies like optical sensing together by using the predefined pockets for sensor integration. With the integrated mixing chamber, the samples could be diluted, or it may be further used as a reaction chamber for the screening of biocatalysts, as an inactivation chamber or as a labeling unit, by mixing the sample stream with a fluorescent or magnetic marker, depending on the sensing approach chosen [90].

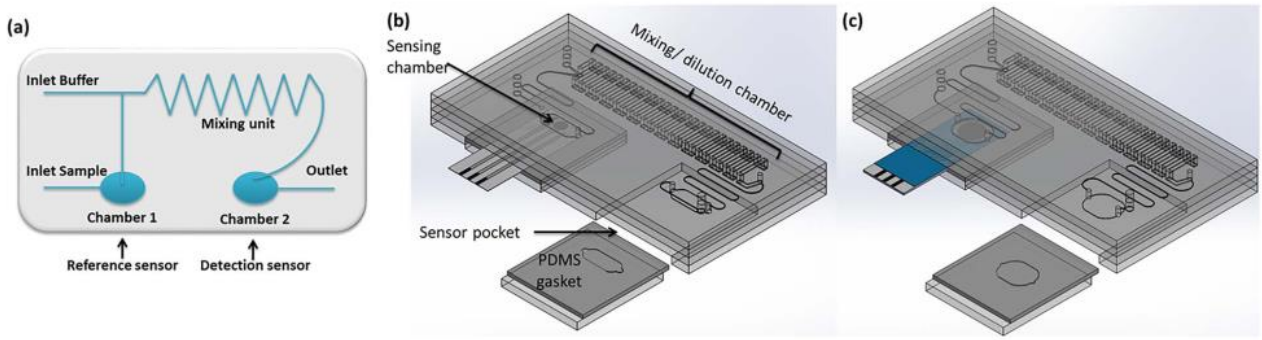

Figure 1.23: Schematics of the developed platform, highlighting the different elements and the sensor positions and SolidWorks 3D representation of the assembled microfluidic platform with one integrated IS-C SPE [90].

1.6 Aim of Thesis

My PhD thesis aims to fabricate and integrate the novel label-free biosensors for different analytes with microfluidic devices. Developing new strategies for integrating organic electronic biosensors with microfluidics are crucial to develop diagnostic devices working in hospital environment or outside health-care. Organic electronic biosensors are ultra-high sensitivity devices and are stable under low-voltage operations. The low-cost fabrication and the freedom to use flexible biocompatible plastic foils for the sensors and microfluidics are one of the few reasons, which make them attractive tools for investigating physiological conditions and for providing solutions such as label-free diagnostics at point of care, minimally invasive implant for neural recordings and stimulation and device-assisted loco-regional treatments. These are the objectives and the aims of Marie Curie Sklodowska Action "BORGES-Biosensing with Organic Electronics" European Training Network (MSCA-ITN-ETN, grant agreement no. 813863)**,** which I was involved as an Early Stage Researcher.

In Chapter 2, Materials and Methods are reported for designing and fabricating low-cost and portable EGOFETs on a flexible substrate and disposable microfluidics. The laser lithography is used to fabricate EGOFETs with different geometries (different W/L ratios) on a range of polymeric substrates and disposable microfluidics with adhesive tape. Different types of 3D printers are compared and reported for producing masters and mechanical clamps for microfluidic elastomeric

devices. Various printing techniques like screen, inkjet and aerosol jet printing have been compared and explained.

In Chapter 3, I report about the characterization techniques employed to assess the electrical performance of the organic transistors. Electrochemistry methods were used to investigate the reproducibility of the functionalization protocol with oligonucleotide probes and thiol based self-assembled monolayers. With the UV-Spectroscopy, the performance of the microfluidic mixers was assessed and validated.

In Chapter 4, I present the design choices and the numerical simulations for the microfluidic devices. All simulations were accomplished for fluid dynamics with COMSOL Multiphysics®. The Laminar Flow and Transport of Diluted Species Interface were used for the simulations of the microfluidic mixers. The geometry optimization of H-cell microfluidic mixer was studied for achieving serial dilution of the biological samples. Additionally, the different flowrates were investigated for manipulating the diffusion gradient inside of the mixer.

In Chapter 5, I show examples for the integration of microfluidic devices with EGOFET for different applications. For the electroanalytical application, I integrate the microfluidic mixer with EGOFET through the electrolyte bridge to monitor the formation of self-assembly monolayers (SAM) on top of gold gates. The mixer helps with the formation of SAM on the gates with diffusion gradient inside of microfluidic channel. The developed diffusion gradient controls the thiol based monolayer formation on gold gates. With the multi-gate EGOFET architecture, this formation has been monitored and electrically characterized. The work function of metallic gate changes due to the SAM formation and is therefore reflected on the transfer properties of the EGOFET. The output current is decreasing in correlation with the axial position of the gate along the microfluidic channel. For biosensing applications, the microfluidics are integrated for detection of IL-1b with the collaboration of BORGES consortium. Another example is IL-6 biosensor; Extended Gate-OECT has been integrated with microfluidics with multiple chambers. Lastly, an integration of microfluidics with EG-FET with a plasmonic fiber optic gate is shown.

In Chapter 6, label-free detection for miRNA with the dual gate EGOFET architecture is presented for different analyte concentrations. For studying the bio recognition events and extracting the kinetic constant for validation of the results, a new reactions model has been proposed to analyse the dose curves of the EGOFET biosensor.

1.7 References

[1] Mehrotra P. Biosensors and their applications – A review. J Oral Biol Craniofac Res 2016;6 (2):153–59.

[2] Freitag R. Applied biosensors. Current Opinion in Biotechnology 1993; 4(1):75–79.

[3]Hughes WS. THE POTENTIAL DIFFERENCE BETWEEN GLASS AND ELECTROLYTES IN CONTACT WITH THE GLASS. J Am Chem Soc American Chemical Society 1922; 44(12):2860–67.

[4] Clark LC, Wolf R, Granger D, et al. Continuous recording of blood oxygen tensions by polarography. J Appl Physiol 1953; 6(3):189–93.

[5] Yoo EH, Lee SY. Glucose biosensors: an overview of use in clinical practice. Sensors (Basel). 2010; 10 (5):4558-76.

[6] Burtscher B. et al. Sensing Inflammation Biomarkers with Electrolyte-Gated Organic Electronic Transistor. Advanced healthcare materials vol. 10, 20, 2021: e2100955.

[7] Selvaraj M. et al. Label free detection of miRNA-21 with electrolyte gated organic field effect transistors (EGOFETs). Biosensors and Bioelectronics Vol. 182, 2021: 113144.

[8]Piccolino M. Luigi Galvani's path to animal electricity. Comptes Rendus Biologies 2006; 329(5):303–18.

[9]Piccolino M. Visual Images in Luigi Galvani's Path to Animal Electricity. Journal of the History of the Neurosciences Routledge 2008; 17(3):335–48.

[10]Arzuaga P. Cardiac pacemakers: past, present and future. IEEE Instrumentation Measurement Magazine 2014; 17(3):21–27.

[11]Mulpuru S.K. et al., Cardiac Pacemakers: Function, Troubleshooting, and Management: Part 1 of a 2-Part Series. J. Am. Coll. Cardiol. 2017; 69 (2):189-210.

[12] Lenarz T. Cochlear implant - state of the art. GMS Curr Top Otorhinolaryngol Head Neck Surg. 2018

[13]DiFrancesco D. Pacemaker Mechanisms in Cardiac Tissue. Annu Rev Physiol Annual Reviews 1993; 55(1):455–72.

[14] Ouyang H, Liu Z, Li N, et al. Symbiotic cardiac pacemaker. Nature Communications Nature Publishing Group 2019; 10(1):1821.

[15] Irisawa H. Comparative physiology of the cardiac pacemaker mechanism. Physiological Reviews American Physiological Society 1978; 58(2):461–98.

[16] Krauss, J.K., Lipsman, N., Aziz, T. et al. Technology of deep brain stimulation: current status and future directions. Nat Rev Neurol 2021;17, 75–87.

[17]Foulds NC, Lowe CR. Enzyme entrapment in electrically conducting polymers. Immobilisation of glucose oxidase in polypyrrole and its application in amperometric glucose sensors. J Chem Soc, Faraday Trans 1 The Royal Society of Chemistry 1986; 82(4):1259–64

[18] Kim J, Campbell AS, Ávila BE-F de, et al. Wearable biosensors for healthcare monitoring. Nature Biotechnology Nature Publishing Group 2019; 37(4):389–406.

[19] Ates, H.C., Nguyen, P.Q., Gonzalez-Macia, L. et al. End-to-end design of wearable sensors. Nat Rev Mater 7 2022; 887–907.

[20] Rasmussen SC. The Early History of Polyaniline: Discovery and Origins. Substania 2017; 1(2):99–109.

[21]Rasmussen SC. Conjugated and Conducting Organic Polymers: The First 150 Years. ChemPlusChem 2020; 85(7):1412–29.

[22]Di Lauro, M. et al. Liquid-Gated Organic Electronic Devices Based on HighPerformance Solution-Processed Molecular Semiconductor. Adv. Electron. Mater. 3, 2017; 1–6.

[23]Campos, A., Zhang, Q., Ajayakumar, M. R., Leonardi, F. & Mas-Torrent, M. High Performance Organic Field-Effect Transistors with Solid and Aqueous Dielectric Based on a Solution Sheared Sulfur-Bridged Annulene Derivative. Adv. Electron. Mater. 2017; 1700349, 1–10.

[24] Kotlowski C. et al. Electronic biosensing with flexible organic transistor devices. Flex. Print. Electron. 3, 2018; 034003.

[25]Torsi L. et al. Organic field-effect transistor sensors: a tutorial review. Chem. Soc. Rev., 2013; 42, 8612-8628.

[26] Guo F, Karl A, Xue Q-F, et al. The fabrication of color-tunable organic light-emitting diode displays via solution processing. Light: Science & Applications Nature Publishing Group 2017; 6(11):e17094–e17094.

[27] Geffroy B, Roy P le, Prat C. Organic light-emitting diode (OLED) technology: materials, devices and display technologies. Polymer International 2006; 55(6):572–82.

[28] Chen L.X. Organic Solar Cells: Recent Progress and Challenges. ACS Energy Lett. 2019; 4, 10, 2537–2539.

[29] Yu, J.M., Lee, J., Kim, Y.S. et al. High-performance and stable photoelectrochemical water splitting cell with organic-photoactive-layer-based photoanode. Nat Commun 11, 2020; 5509.

[30]Simon D.T., Gabrielsson EO, Tybrandt K, et al. Organic Bioelectronics: Bridging the Signaling Gap between Biology and Technology. Chem Rev American Chemical Society 2016; 116(21):13009–41.

[31]Berggren M. et al. In Vivo Organic Bioelectronics for Neuromodulation Chemical Reviews 2022; 122 (4), 4826-4846.

[32]Jeong, J. W. et al. Materials and optimized designs for human-machine interfaces via epidermal electronics. Adv. Mater. 25, 2013; 6839–6846.

[33]Inal Sahika et al. Conjugated Polymers in Bioelectronics Accounts of Chemical Research 2018; 51 (6), 1368-1376

[34] Rivnay, J., Inal, S., Salleo, A. et al. Organic electrochemical transistors. Nat Rev Mater 3, 2018; 17086.

[35] Strakosas X. et al. The organic electrochemical transistor for biological applications. Journal of Applied Polymer Science 2015; Vol. 132 , Issue 15.

[36] Galliani M. et al. Flexible Printed Organic Electrochemical Transistors for the Detection of Uric Acid in Artificial Wound Exudate. Adv.Materials Interface 2020; Vol. 7, Issue 23, 2001218.

[37]Tarabella G. et al. New opportunities for organic electronics and bioelectronics: ions in action. Chem. Sci., 2013; 4, 1395-1409.

[38] Campana, A. Cramer, T. Simon, D. T. Berggren, M. Biscarini, F. Electrocardiographic recording with conformable organic electrochemical transistor fabricated on resorbable bioscaffold Adv. Mater. (Deerfield Beach, Fla.) 2014;26, 3874.

[39]Khodagholy D.,Doublet T.,Quilichini P.,Gurfinkel, M., Leleux, P., Ghestem, A., Ismailova, E., Herve, T.,Sanaur, S., Bernard, C., Malliaras G. G. In vivo recordings of brain activity using organic transistors Nat. Commun. 2013; 4, 1575.

[40]Torricelli F., Adrahtas D.Z., Bao Z. et al. Electrolyte-gated transistors for enhanced performance bioelectronics. Nat Rev Methods Primers 2021; 1, 66.

[41]Obite F, Ijeomah G, Bassi JS. Carbon nanotube field effect transistors: toward future nanoscale electronics. International Journal of Computers and Applications Taylor & Francis 2019; 41(2):149–64.

[42] Panzer M.J., Frisbie D.C., Exploiting Ionic Coupling in Electronic Devices: Electrolyte-Gated Organic Field-Effect Transistors. Adv. Materials Vol.20,16, 2008; 3177-3180.

[43]Parkula V. Organic Electronic Transistors for Biosensing. [Ph.D dissertation] Università degli Studi di Modena e Reggio Emilia: Modena 2019.

[44] Wang D., Noël V., Piro B. Electrolytic Gated Organic Field-Effect Transistors for Application in Biosensors—A Review. Electronics. 2016; 5(1): 9.

[45]Stewart Z. Organic Thin-Film Transistors and TIPS-Pentacene. Lewis Honors College Capstone Collection 2013; 11.

[46] Kergoat L., Piro B., Berggren M., Horowitz G., Pham M.-C., Advances in organic transistor-based biosensors: From organic electrochemical transistors to electrolyte-gated organic field-effect transistors. Anal. Bioanal. Chem. 2012; 402, 1813–1826.

[47]Kim SH., Hong K., Xie W., et al. Electrolyte-Gated Transistors for Organic and Printed Electronics. Advanced Materials 2013; 25(13):1822–46.

[48] Selvaraj M. Organic Electronic Transistors and Microfluidics for Cancer Biomarker Sensing [Ph.D dissertation] University of Catania, 2021.

[49] Melzer K, Brändlein M, Popescu B, et al. Characterization and simulation of electrolyte gated organic field-effect transistors. Faraday Discuss The Royal Society of Chemistry 2014; 174(0):399–411.

[50] Di Lauro M, Casalini S, Berto M, et al. The Substrate is a pH-Controlled Second Gate of Electrolyte-Gated Organic Field-Effect Transistor. ACS Appl Mater Interfaces American Chemical Society 2016; 8(46):31783–90.

[51] Cramer T, Kyndiah A, Murgia M, et al. Double layer capacitance measured by organic field effect transistor operated in water. Appl Phys Lett American Institute of Physics 2012; 100(14):143302.

[52] Borges-González J, Kousseff CJ, Nielsen CB. Organic semiconductors for biological sensing. J Mater Chem C The Royal Society of Chemistry 2019; 7(5):1111–30.

[53] Casalini S, Leonardi F, Cramer T, et al. Organic field-effect transistor for label-free dopamine sensing. Organic Electronics 2013; 14(1):156–63.

[54] Macchia E, Manoli K, Holzer B, et al. Single-molecule detection with a millimetre-sized transistor. Nature Communications Nature Publishing Group 2018; 9(1):3223.

[55] Berto M, Vecchi E, Baiamonte L, et al. Label free detection of plant viruses with organic transistor biosensors. Sensors and Actuators B: Chemical 2019; 281:150–56.

[56] Kergoat L, Herlogsson L, Braga D, et al. A Water-Gate Organic Field-Effect Transistor. Advanced Materials 2010; 22(23):2565–69.

[57] Cardoso AR, Moreira FTC, Fernandes R, et al. Novel and simple electrochemical biosensor monitoring attomolar levels of miRNA-155 in breast cancer. Biosensors and Bioelectronics 2016; 80:621–30.

[58] Stern E., Wagner R., Sigworth F.J., Breaker R., Fahmy T.M., Reed, M.A. Importance of the debye screening length on nanowire field effect transistor sensors. Nano Lett. 2007; 7, 3405–3409.
[59] Kergoat L, Piro B, Berggren M, et al. Advances in organic transistor-based biosensors: from organic electrochemical transistors to electrolyte-gated organic field-effect transistors. Anal Bioanal Chem 2012; 402(5):1813–26.
[60] Kergoat L., Piro B., Berggren M., Pham M.-C., Yassar A., Horowitz G., DNA detection with a water-gated organic field-effect transistor. Org. Electron. 2012; 13, 1–6.
[61] Suspène C., Piro,B., Reisberg S., Pham M.-C., Toss, H., Berggren M., Yassar, A., Horowitz G. Copolythiophene-based water-gated organic field-effect transistors for biosensing. J. Mater. Chem. B 2013; 1, 2090–2097.
[62] Palazzo G., Tullio DD., Magliulo M., et al. Detection Beyond Debye's Length with an Electrolyte-Gated Organic Field-Effect Transistor. Advanced Materials 2015; 27(5):911–16.
[63] Magliulo M., Mallardi A., Mulla MY., et al. Electrolyte-Gated Organic Field-Effect Transistor Sensors Based on Supported Biotinylated Phospholipid Bilayer. Advanced Materials 2013; 25(14):2090–94.
[64] Diacci C, Berto M, Di Lauro M, et al. Label-free detection of interleukin-6 using electrolyte gated organic field effect transistors. Biointerphases American Vacuum Society 2017; 12(5):05F401.
[65] Berto M, Casalini S, Di Lauro M, et al. Biorecognition in Organic Field Effect Transistors Biosensors: The Role of the Density of States of the Organic Semiconductor. Anal Chem American Chemical Society 2016; 88(24):12330–38.

[66] Whitesides G. M., The origins and the future of microfluidics, Nature 2006; 442 368–373.
[67] Terry S. C., Jerman J. H., Angell J. B., A gas chromatographic air analyser fabricated on a silicon wafer, IEEE Trans. Electron Devices, ed. 26, 1979 ; 1880–1886.
[68] Sackmann E.K., Fulton A.L., Beebe D.J., The present and future role of microfluidics in biomedical research, Nature 2014; 507,181-189.
[69] Capretto L., Carugo D., Mazzitelli S., Nastruzzi C., Xunli Z., Microfluidic and lab-on-a-chip preparation routes for organic nanoparticles and vesicular systems for nanomedicine applications, Adv. Drug Deliv. Rev. 2013; 65, 1496-1543.
[70] Chin C.D., Linder V., Sia S.K., Lab-on-a-chip devices for global health: Past studies and future opportunities, Lab Chip 2007; 7, 41-57.

[71] Harrison D. J., Fluri K., Seiler K., Fan Z., Effenhauser C. S.,Manz A., Micromachining a miniaturized capillary electrophoresis-based chemical analysis system on a chip, Science, 261, 1993; 895–897.

[72] Kopp M. U., Mello A. J. De, Manz A., Chemical amplification: continuous-flow PCR on a chip, Science, 280, 1998; 1046–1048.

[73] Manz A., Becker H., Parallel capillaries for high throughput in electrophoretic separations and electroosmotic drug discovery systems, Transducers 97, Int. Conf. Solid-State Sens. Actuators, 2, 1997; 915–918.

[74] Chiem N., Harrison D. J., Microchip-based capillary electrophoresis for immunoassays: analysis of monoclonal antibodies and theophylline, Anal. Chem., 69, 1997; 373–378.

[75]Ng J. M. K., Gitlin I., Stroock A. D., Whitesides G. M., Components for integrated Poly (dimethyl siloxane) microfluidic systems, Electrophoresis, 23, 2002; 3461–3473.

[76] Dietzel A., Microsystems for Pharmatechnology Manipulation of Fluids, Particles, Droplets, and Cells, Springer, 2015.

[77] Stone H. A., Kim S., Microfluidics: basic issues, applications, and challenges, AIChE J., 47, 2001; 1250–1254.

[78] McDonald J. C., Whitesides G. M., Poly (dimethylsiloxane) as a material for fabricating microfluidic devices, Acc. Chem. Res., 35, 2002; 491–499.

[79]https://www.elveflow.com/microfluidic-reviews/general-microfluidics/history-of-microfluidics/

[80] Xia Y., Whitesides G. M., Soft lithography, Angew. Chemie Int. Ed., vol. 37, 1998; no. 5, pp. 550–575.

[81]Annese VF, Hu C. Integrating Microfluidics and Electronics in Point-of-Care Diagnostics: Current and Future Challenges. Micromachines. 2022; 13(11):1923.

[82] Squires T. M., Quake S. R., Microfluidics: fluid physics at the nanoliter scale, Rev. Mod. Phys., 77, 2005; 977–1026.

[83] Landau L.D., Lifshitz E.M., Fluid Mechanics, 2nd English ed.,Vol. 6, Elsevier, 1987.

[84] Nyugen Nam-Trung, Fundamentals and Application of Microfluidics, Second Edition, 2006.

[85]Torino Stefania, Engineering of Microfluidic Devices for cell hydrodynamic manipulation [Ph.D dissertation] University of Naples "Federico II", 2015.

[86] Chen Y-T., Lee Y-C., Lai Y-H,. Lim J-C., Huang N-T., Lin C-T., Huang J-J., Review of Integrated Optical Biosensors for Point-of-Care Applications. Biosensors. 2020; 10(12):209.

[87]Pires N.M., Dong T., Hanke U., Hoivik N., Recent developments in optical detection technologies in lab-on-a-chip devices for biosensing applications. Sensors (Basel). 2014; 14(8):15458-79.

[88] Lin Peng et al. Organic Electrochemical Transistors Integrated in Flexible Microfluidic Systems and Used for Label-Free DNA Sensing, Adv.Materials Vol 23, Issue 35, 2011; 4035-4040.

[89]Pappa, Anna-Maria et al. Organic Transistor Arrays Integrated with Finger-Powered Microfluidics for Multianalyte Saliva Testing. Advanced healthcare materials vol. 5, 17 (2016): 2295-302.

[90]Fernandes A. C. et al., Multi-function microfluidic platform for sensor integration, New Biotechnology vol.47, 2018;8-17.

[91]Frasconi, M.; Mazzarino, M.; Botrè, F.; Mazzel, F. Surface plasmon resonance immunosensor for cortisol and cortisone determination. Anal. Bioanal. Chem. 2009, 394, 2151–2159.

CHAPTER 2

MATERIALS AND FABRICATION

2.1 Introduction

In this chapter, I will discuss on the fabrication methods and materials both for microfluidic EGOFET devices. The state of art for the microfabrication techniques will be presented. Low cost fabrication method of planar electrodes (Source and Drain) on the flexible polymeric film will be explained and presented as the part of the EGOFET. The organic semiconductor selected for generating a conducting channel in the transistor and its properties will be discussed.

The additive manufacturing techniques like 3D printers and screen printing are discussed. Various type of 3D printers for fabricating the different parts of the microfluidic systems are shown. The adhesive and elastomeric materials employed for generating microfluidic devices with techniques such as replica molding and laser technique will be discussed.

Moreover, the chemical functionalization protocols of the gates for sensing oligonucleotides and proteins are shown. To test the microfluidic device performance, proteins like protein bovine serum albumin (BSA) and molecules like self-assemble monolayers (SAM) are used. These molecules and their usage inside of the microfluidics are explained.

2.2 Fabrication Techniques

2.2.1 Laser Lithography

Laser lithography is a known method in the microfabrication processes for the ablation of the thin metallic films. It achieves a predefined and controlled micrometric size ablation on either rigid or flexible substrates. The desired pattern is designed with Computer-aided design (CAD) and then converted into a binary image for the laser. In this work, the purpose of the laser ablation of the thin metallic films like gold, aluminum etc. is the fabrication of the interdigitated electrodes and the gates for the Electrolyte Gated Organic field effect transistors (EGOFETs). Additionally the laser lithography is used for manufacturing the adhesive microfluidic devices.

For fabricating the Source (S) and Drain (D) interdigitated electrodes for EGOFETs, the laser marker has been used to ablate 70 nm gold deposited on flexible Kapton substrate [1]. The laser marker ScribaR® (Figure 2.1) was manufactured by Scriba Nanotecnologie S.r.l, Bologna (IT). It has a Nd: YAG infrared (IR) laser source (centre wavelength k ¼ 1064 nm) which produces short pulses of 100 ns duration. The laser source is fixed, where the focus and the movement of the stage in X and

Y directions are controlled by micrometrical motors. Important parameters such as the pulse width, the power, the speed of the beam and the repetition frequency have to be optimized for the chosen substrate material. The achieved resolution of the ablation could be 10 µm - 20 µm in X, Y and Z-axis with this infrared laser marker [1].

A secondlaser marker Marko® (Laser point S.r.l., Milan,Italy) was used to fabricate similar electrode design. In Marko®, the laser beam passes through the moving lens and it is deflected by galvanometric mirrors according to the X and Y coordinates in the desired test pattern [3]. The working principle can be seen in Figure 2.1. In the upcoming sub-chapters, the examples of the fabricated electrodes, gates and microfluidic devices, which are fabricated with this technique will be shown.

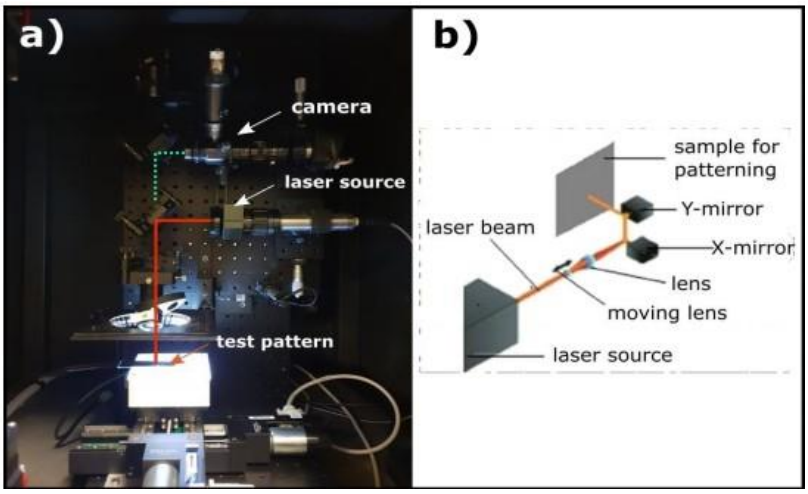

Figure 2.1: a) Optical setup of the laser marker ScribaR, b) the schematics of scanning head component of Marco [2, 3].

2.2.2 Fabrication of EGOFET Device using Laser Lithography

In the literature, the EGOFET has an architecture with the top gate and the bottom Source and Drain contacts configuration [4]. Depending on which disease is targeted for biosensing, the gate electrode will be functionalized with target bio receptors.

Firstly, the interdigitated Source and Drain electrode pattern have been designed with the 2D software (Draftsight, Dessault Systems) and then optimized according to the laser ablation process (Figure 2.2). The design geometry was made with objective Width/ Length (W/L) ratio of 3000 in order to achieve high Source Drain current [2].

The chosen substrate for fabricating Source and Drain interdigitated electrodes was a thin flexible foil of Kapton with a 50µm thickness. 99.99% pure gold sputtering was accomplished by Creavac Gmbh (Dresden, Germany) to metallize the surface of the polymeric foil [2]. The Kapton substrate has one side coated and obtained in Ultra High Vacuum Evaporation. It contains 10 nm Nickel Chromium (NiCr) as adhesion promoter and 70 nm Au± 15%. For the ablation on Kapton substrate for the interdigitated electrodes and the planar gates, the following parameters are optimized. The power is chosen as 0.3 Watt, scanning speed is 180 mm/s and the pulse repetition frequency is 20 kHz.

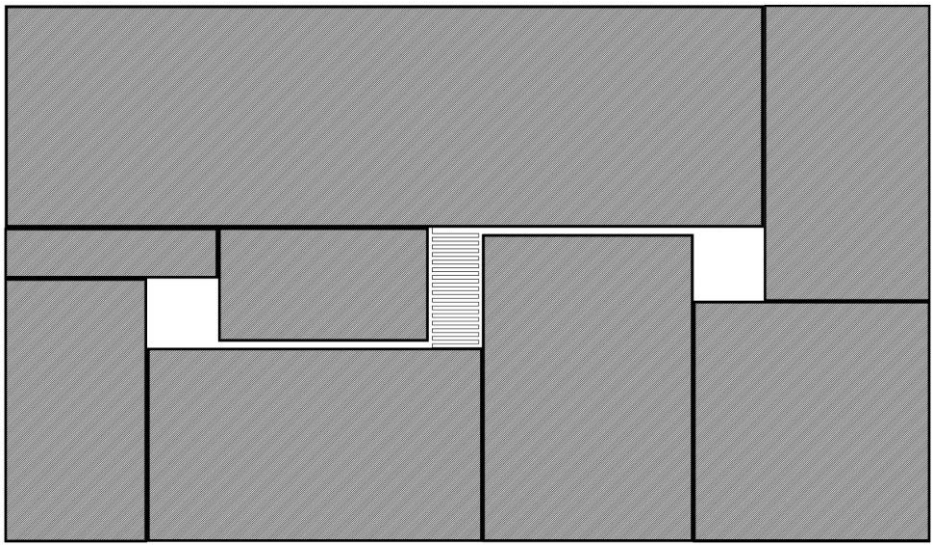

Figure 2.2: 2D Geometry of the interdigitated electrode pattern for the laser ablation. The test pattern is designed with DraftSight [2].

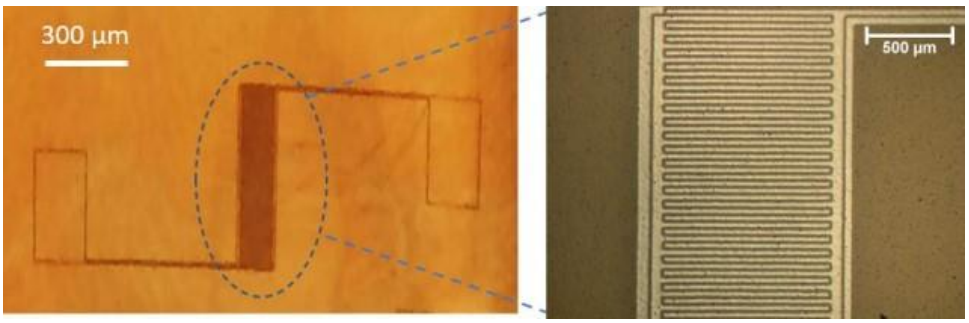

Figure 2.3: Images obtained with optical microscope (magnification 5X and 20X) of the Au – Kapton after ablation with laser marker [2].

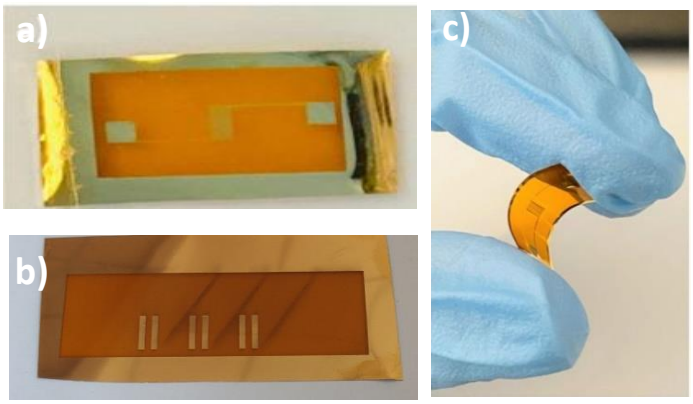

Figure 2.4: a) Picture of the Source and Drain interdigitated electrodes of the EGOFET device b) Picture of the ablated multi gates on flexible substrate Kapton c) The flexibility of the interdigitated electrodes.

After the ablation, the interdigitated electrodes were sonicated with Ethanol, then DMF (Dimethylformamide) was dropcasted on top of them for 5 minutes for increasing surface tension. Afterwards, the electrodes were rinsed with distilled water, in order to remove any ablation and DMF residues. At last, it was dried with the Nitrogen gas. The ablated interdigitated electrodes were checked and controlled under the optical microscope for the continuity in the pattern before the drop casting of Tips- Pentacene (Figure 2.3) [5].

The gate electrodes considered for integration with microfluidic device are flat and flexible. They are constituted by metalized polymeric foil with thickness ranging between 50 and 100 µm. The metalized gold foil was structured with laser ablation in order to obtain an array of rectangular electrodes with dimensions 4 x 1 mm, separated by 1 mm empty space. The ablated multi-gates were sonicated first with Ethanol, and then cleaned with Piranha solution, (a mixture of sulfuric acid (H2SO4) and hydrogen peroxide (H2O2) in ratio 1:1. After washing in distilled water, the gates were dried with the Nitrogen gas.

2.2.3 Fabrication of Flexible Adhesive Microfluidics using Laser Lithography

In my PhD work, I design and fabricate the microfluidic devices, which are then integrated with EGOFET for biosensing applications. One of them is H-shaped microfluidic mixer. This mixer will be explained in details in the upcoming Chapter 4 and 5, meanwhile here I report the details of the fabrication methods for producing these devices. They could be fabricated with either laser lithography or soft lithography depending on the material choice.

For fabrication of the adhesive microfluidics, a double sided adhesive tape (TESA 4970) with a thickness of 245 µm from Beiersdorf AG, Hamburg, Germany.is best performing. The material choice for microfluidics plays an important role on the performance of the device, so the adhesive material is selected from the substrates which have been used for manufacturing devices in healthcare sector [3]. The thickness of adhesive tape determines the thickness of microfluidic channel. The adhesive thickness and its strength are important parameters for the device performance and the sealing of the complete system.

The fabrication process goes similar to the fabrication of the interdigitated electrodes pattern. Firstly, the adhesive tape was attached to a planar support and placed on top of the stage of the laser marker Marko®. The finalized CAD drawing was imported to the software of the laser beam

(Figure 2.5 a). The important parameters like power and the scanning speed are optimized for the microfluidic cutting process. For adhesive material, the power is chosen as 7W with the pulse repetition frequency 30 Hz. After the process is completed, the excess of adhesive tape is removed manually to expose the fluidic microchannel. The result is presented in Figure 2.5 b. A top layer of PMMA was equally processed with laser lithography to prepare the top boundary of the fluidic cell.

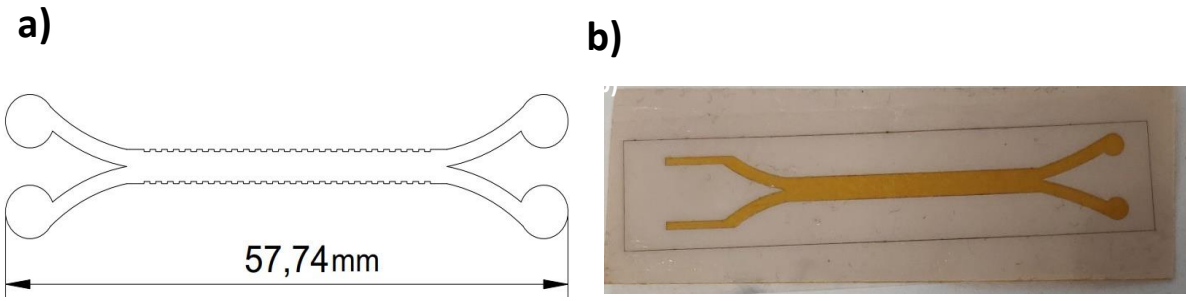

Figure 2.5: a) 2D Geometry of the H microfluidic mixer for the laser ablation. The pattern is designed with DraftSight. b) Picture of the adhesive microfluidic mixer after the integration with inlet tubings.

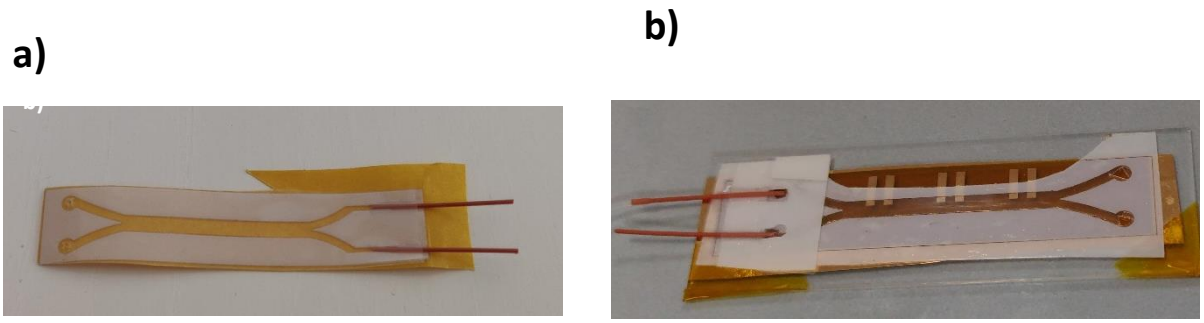

Figure 2.6: a) Picture of the adhesive microfluidic mixer after the integration with inlet tubings b) Picture of the adhesive microfluidic mixer after the integration with multi gates.

Another example for adhesive microfluidics could be seen in the Figure 2.7. The fabrication process with laser lithography is same as described before. The only difference is that this microfluidic has multi-levels. The assembly process is described in the Figure 2.7 b. After assembly of the adhesive microfluidics, they are integrated with the sensing unit for biosensing.

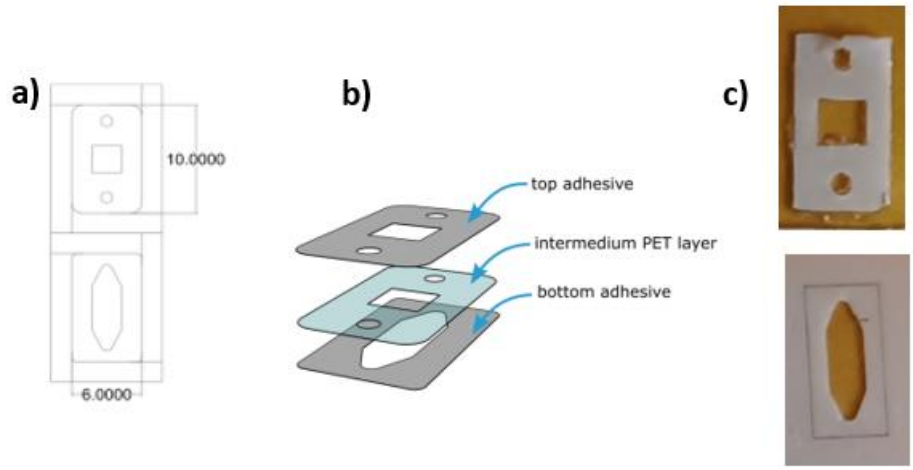

Figure 2.7: a) CAD design in micrometer b) Adhesive microfluidics assembly process [3] c) Final products after removal of unnecessary adhesive.

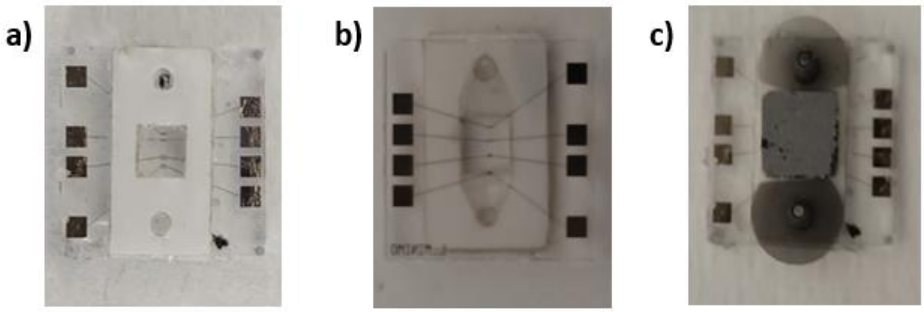

Figure 2.8: a) Top view of the integration of adhesive microfluidics with the microelectrodes test pattern b) Bottom view of the system c) Fully assembled device with gate and connectors.

2.2.4 Drop casting of organic semiconductor

Organic semiconductors have been tested extensively also in transistors working as biosensors such as Electrolyte Gated Organic Field Effect Transistors (EGOFETs). In particular, for the present thesis work, I employed a derivative of pentacene, TIPS-pentacene, developed specifically for solution-based deposition processes. Drop casting technique is a direct technique for creating semiconducting thin-films on top of the interdigitated electrodes in short amount of time without needing any high temperature or vacuum conditions Pentacene instead requires thermal evaporation in high vacuum conditions for creating a thin film deposition [2].

With the drop casting method, acrystalline thin film layer is created in less than 5 minutes. The formation of the crystals and the crystal morphology affect the transistor performance. Due to this reason, it is important to control the rate of deposition of the semiconductor. Compared to the spin coating technique, the volume of semiconducting material is much less with drop casting technique. Only 0.5 µl of TIPS-pentacene solution has been used to create the conductive channel (Figure 2.10). Apart from the usage of low volume of the material and control of the deposition rate, there are other advantages like highly cost efficient and no necessary pre or post steps.

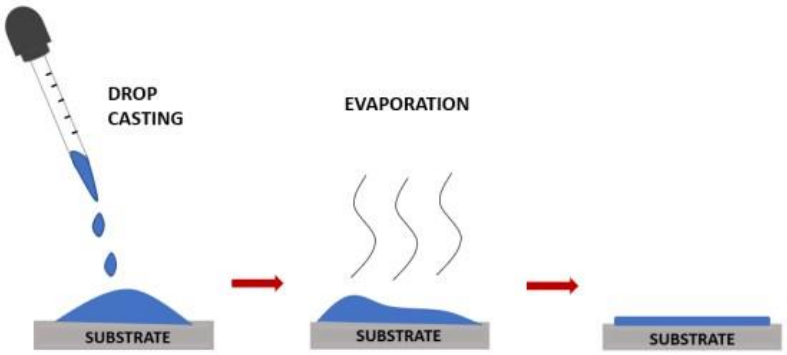

Figure 2.9: Simple block diagram of the drop casting process [2].

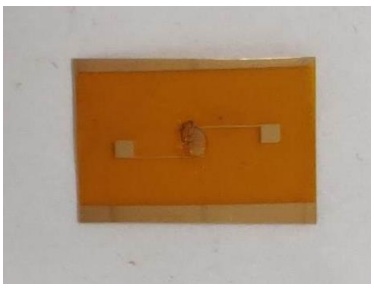

Figure 2.10: Picture of the interdigitated S and D electrodes after the drop casting process.

2.2.5 Tips-Pentacene organic semiconductor

The conventional transistors are a crucial part of today consumer electronics since they have the ability to amplify and turn on or off the signals. They are made of semiconductor materials such as an amorphous or a crystalline silicon, germanium. However, fabricating transistors could be costly, since they need multiple manufacturing processes in cleanroom. The recent studies show that certain organic semiconductors could be an alternative for the traditional silicon, for certain applications [28, 29]. They are cheaper to manufacture and to process also on larger substrates. Moreover, they are more flexible than rigid silicon substrates [5].

When it comes to the performance of the transistor, there are two important parameters. First one is the carrier mobility. The second important parameter is the on/off ratio. This is calculated with the current across the Source and Drain when a voltage is applied divided by the current when no voltage is applied [5, 28].The carrier mobility simplifies to resonance across a conjugated molecule, which allows a charge to move from one terminal to the next [5].This ideal situation is only possible for the small organic semiconductors though, so the charge could hop from one to the next molecule. This charge transfer requires highest occupied molecular orbital (HOMO) overlap of molecular orbitals. However, this is not easy, since there is an electron-electron repulsion between the orbitals [5, 29].

One of the first organic molecules that is investigated is pentacene, shown Figure 2.11 a. The crystal structure and molecular orbitals of the molecule show very poor overlap between HOMO orbitals, since it forms a herringbone crystal structure in which each acene backbone is positioned nearly perpendicular to its neighbor, meaning weak overlap between HOMO orbitals [5]. The potential carrier mobility of the pentacene is largely wasted due to this reason. The other disadvantage is that the molecule is not soluble in many common organic solvents. This complicates the deposition process and increases the cost. Additionally, pentacene can react with oxygen, causing the lost of conjugation to the newly formed bond [32].

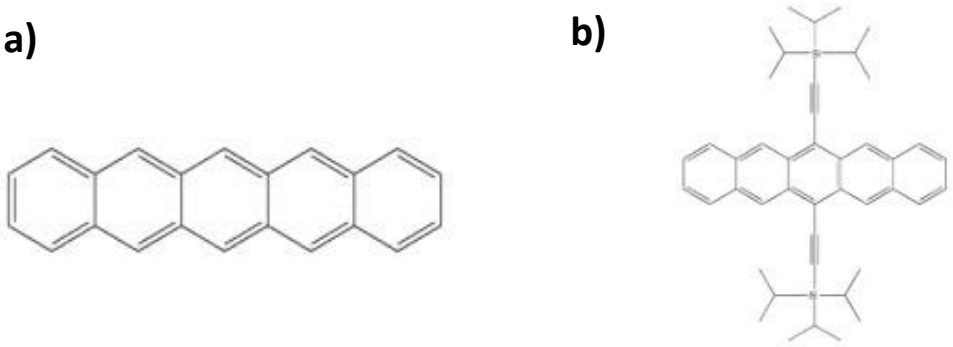

Figure 2.11: a) The molecule structure of pentacene b) The molecule structure of TIPS-Pentacene or 6,13-Bis(triisopropylsilylethynyl)pentacene [5].

To overcome the disadvantage regarding processability, 2 triisopropylsilylethynyl acetylene is added to pentacene. The resulting molecule is known as TIPS-Pentacene, shown in Figure 2.8b [5]. This new molecule has higher solubility in organic solutions due to the substitution onto pentacene with isopropyl groups [2, 5]. It is a p-type semiconductor, which has five benzene rings with two side groups (Figure 2.11b).Compared to Pentacene, the carrier mobility of TIPS-Pentacene greatly increases [31]. The reason for this is that, when the TIPS groups are added onto pentacene, the crystal structure flattens out and acene backbones begin to stack on top of one another. However, this does not mean that HOMO orbital overlaps are maximized, as the orbitals repel. Yet, one can tweak the crystal structure of the molecule and, therefore, change the overlap of the acene backbone until overlap is obtained [30]. After achieving the overlap, the carrier mobility is improved compared to the pentacene. Depending on the semiconductor type, the charge transfer occurs between different orbitals. If the charges are electrons, there is the interaction between the lowest unoccupied molecular orbitals (LUMOs) while if the semiconductor transport holes (p-type) the highest occupied molecular orbitals (HOMOs) are engaged.

In this PhD work, TIPS-Pentacene was used to create the conducting channel between Source and Drain electrodes in the Electrolyte Gated Organic field effect transistors (EGOFET). Total of 0.5 µl volume of TIPS –Pentacene was used for the deposition on top of the interdigitated S and D electrodes. This volume is sufficient to form a good microcrystalline structure. The solvents

evaporates in few seconds and molecules form homogeneous crystalline domains. These domains help the charge carriers to hop from one molecule to the other and increase the charge mobility [33].

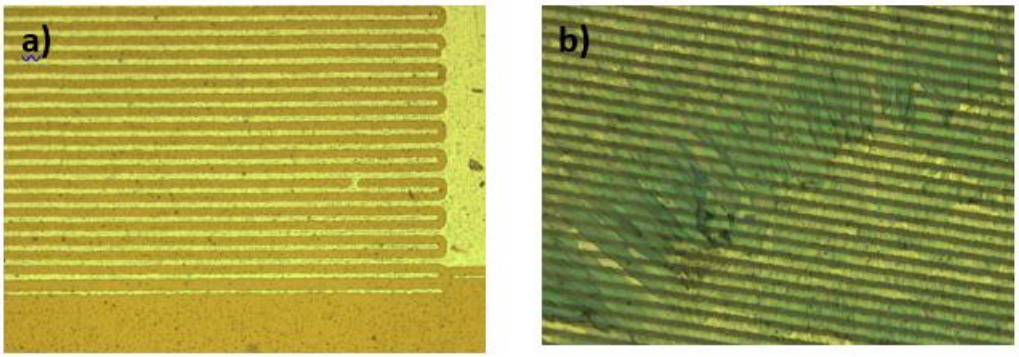

Figure 2.12:a) Optical image of the interdigitated electrodes before drop casting of TIPS-pentacene, b) after dropcasting 0.5 µl of TIPS-pentacene, the formation of the micro crystals could be seen.

2.2.6 3D Printing

3D printer technique is an additive manufacturing (AM) technique that creates pieces from three dimension computer-aided design (CAD) by adding material layer by layer until the designed pieces are formed. The majority of the 3D printers use light source for curing the light reactive material called photopolymeric resin into hardened plastic.3D printer technologies have been around since the 1980s [9]. With the recent advances in technology and materials, they become more accessible and cost efficient for different application areas like engineering, dentistry and healthcare [10-13].
The printing process starts initially with the design. The design programs such as CAD, Sketch Up or PreForm generate three-dimensional models, later exported as a STL files. This file is readable by the software of the printer. The certain printing parameters such as slice thickness, material choice or support structures could be adjusted depending on the design. The software also gives a preview for the slicing process of the model into layers, which are represented as horizontal cross-sections of the piece. Depending on the 3D printer type, it might fabricate the piece layer by layer through solidifying resin or sintering powder. Afterwards, the created parts are removed from the printer and post-curing process starts. It begins with the sonication with ethanol alcohol for the removal of any uncured resin. Later, the sonicated parts are post cured with UV light for the solidification of the created parts surfaces.
The main advantages of 3D printers are the fast prototyping, the speed and the cost efficiency. 3D printers could produce parts or prototypes for running tests under few hours. This allows designers to identify any error or malfunction in the design and optimize the design for better functionality.

Moreover, same equipment and same material can be used for multiple production. This helps with the cost efficiency. Traditional methods for fabricating microchannel could be costly, so 3D printers are good alternative choice for this. In the upcoming section, I will explain three different types of 3D printer that I used during my PhD work. These are Digital Light Processing (DLP), Stereolithography (SLA) and Fused Deposition Modelling (FDM).

2.2.6.1 Digital Light Processing (DLP)

Digital Light Processing (DLP) and Stereolithography (SLA) are the most common used 3D printers. They both create the pieces by polymerizing a liquid photopolymeric resin with a light source, which has certain wavelengths. When the resin is exposed to these wavelengths, the monomers and oligomers are polymerized, turning into solidified rigid material. The main difference between DLP AND SLA is the light source. DLP uses an UV light from a projector and cures a complete layer/entire slice at a time, whereas SLA uses an UV laser beam to trace the shape of each layer. In DLP, the light source remains stationary, while the laser in SLA moves to trace each layer.

The desktop B9 Creator 3D printer is used for fabricating the moulds of the microfluidic devices. The model of the 3D printer is "B9Creator V1.2HD" with resin “B9R-2-Black”. It has a resin tank with a transparent window sliding back and forth to refill the liquid photopolymeric resin near the exposure area. The build table moves vertically into the photopolymer resin, in order to build up the model layer by layer [2, 3, 14] since the light source doesn’t move. With the B9 Creator, the achieved resolution is 50 µm in X, Y-axis, and up to 25 µm along Z-axis. The printed pieces have high accuracy, isotropicity, and smooth surface finish [2].

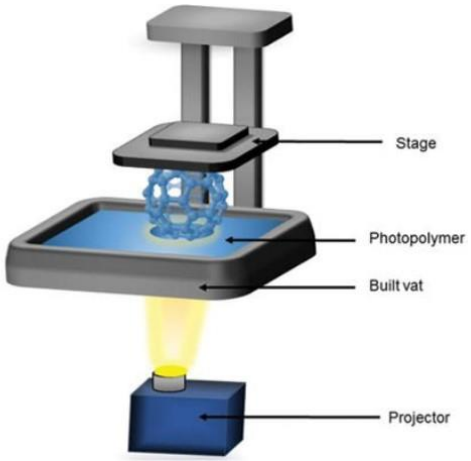

Figure 2.13: Schematics of DLP 3D printer [15].

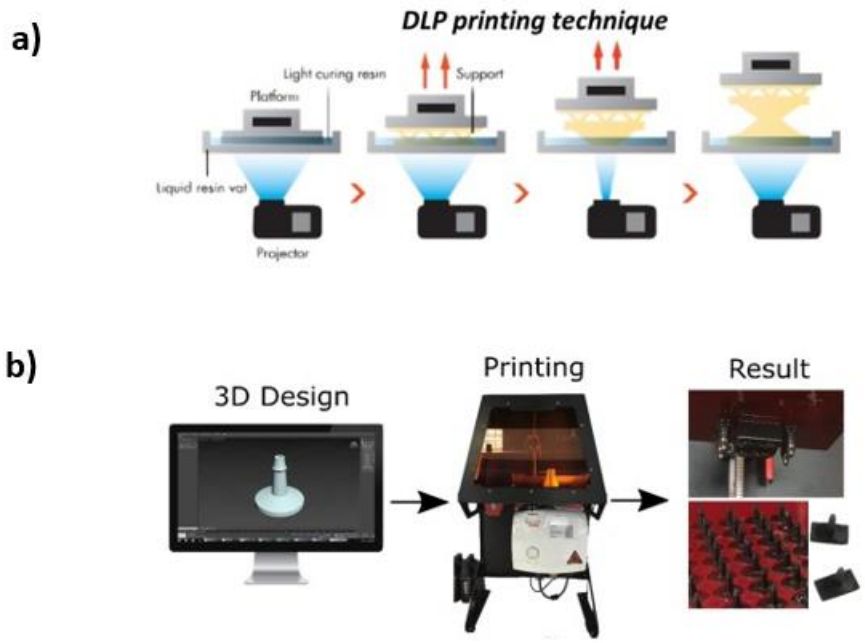

Figure 2.14: a) DLP printing technique b)Printing process from design to product [3].

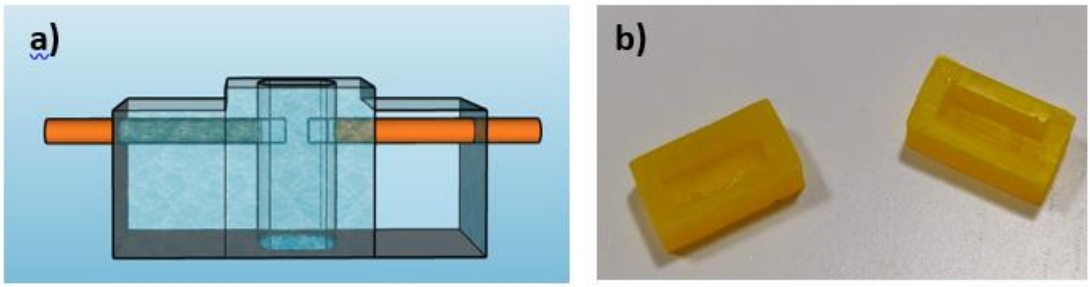

Figure 2.15: a) The design of the microfluidic pools with Sketch Up b) The 3D printed moulds with DLP for the microfluidic pools.

2.2.6.2 Stereolithography (SLA)

Dr. Hideo Kodama was the first scientist to invent modern approach to stereolithography. The system works by curing photosensitive polymers with UV light. In the description reported in his paper, a vat of photopolymer material is exposed to a UV light that hardens the part and builds up the model in layers [17]. After him, Charles Chuck was the one who patented the stereolithography technology in 1986 [18]. Afterwards, he founded a company called 3D Systems to commercialize this technology. He described his method of the printing with layer by layer by curing a light sensitive photopolymer by ultraviolet light. Since this printing process use light instead of heat, all process takes place at the room temperature, which makes the printing process easier. Additionally, the printed objects are less affected by from either thermal expansion or contraction artifacts [16]. The achieved resolution with SLA is circa. 85 µm depending on the laser spot size.

The SLA 3D printing process is similar to DLP. Both processes use liquid photo polymeric resins during printing. The resin is exposed to the light, where the UV laser draws a cross-section layer by layer until the design is created [16]. In the process of the formation of each layer, the monomers in resin form covalent bonds. However, this polymerization reaction is not completed; instead, the layer is kept in a semi-reacted state called the green state. This state differs from the completely cured state, since there are still polymerizable groups on the surface. When the next layer is formed, the polymerization reaction will also include the groups on the previous layer, thus forming covalent bonds not just laterally, but also with the previous layers. Due to this reason, there is little to no difference between the Z-axis and the XY plane in terms of chemical bonds on a molecular level [16, 34]. This provides high degrees of lateral strength, resulting in isotropic parts, where the strength of the parts does not change with orientation. This property is not seen in the objects that are printed by FDM. The used 3D SLA printer is from Formlabs, the model is "Form 3+".

Figure 2.16: A graphic presentation of the components of Stereolithography (SLA) 3D printer of Formlabs [16].

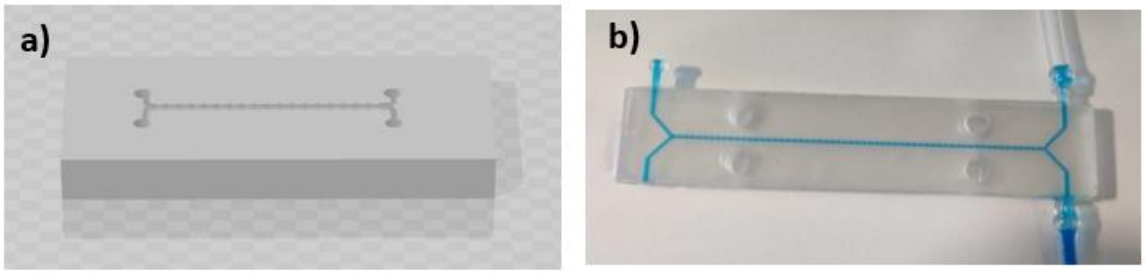

Figure 2.17: a) The design program PreForm is used for FormLabs for the design of the microfluidic device b) 3D-printed prototype microfluidic mixer with connectors and tubes.

2.2.6.3 Fused Depositon Modeling (FDM)

Fused Deposition Modeling printers use melted plastics to build objects layer by layer. The working principle is that they extrude thermoplastic filaments like ABS (Acrylonitrile Butadiene Styrene), PLA (Polylactic Acid) through a heated nozzle. It melts the material and build the plastic layer one by one until the object is created. Each deposited line of PLA or ABS is consisted of highly entangled polymer chains, which hold together tightly and strongly [16]. However, unlike SLA, FDM layer surfaces are not fully adhered to each other but partially adhered to their surrondings. This means, that there are voids in between the lines. Additionally, this adhesion is a mechanical

adhesion, not a chemical. As a result, FDM-printed objects have different mechanical properties based on the direction and not equally strong in all directions [36].

This anisotropy property limits the application areas for FDM-printed objects and requires careful consideration when it comes to the design and load bearing parts [16]. Apart from anisotropy, FDM has a lower resolution around 250–800 micron depending on the nozzles compared to the other 3D printers. In my PhD work, I worked with FDM for printing the mechanical clamps for sealing of the microfluidics.

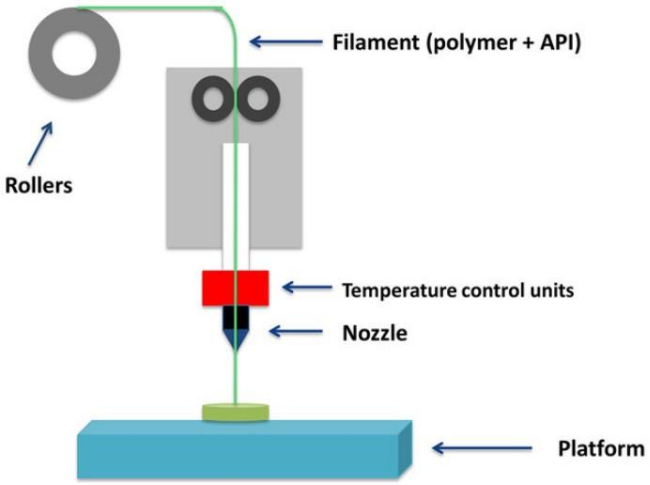

Figure 2.18: A graphic presentation of the components of FDM [35].

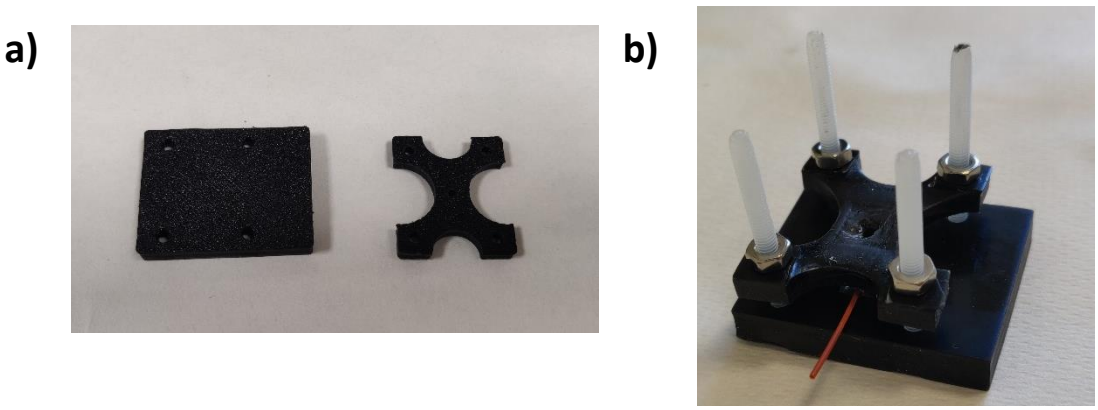

Figure 2.19: a) 3D printed mechanical clamps for the sealing b) Complete sealed system with the mechanical clamps for Micrux electrochemical sensor and microfluidic pool with tubing for inlet and outlet.

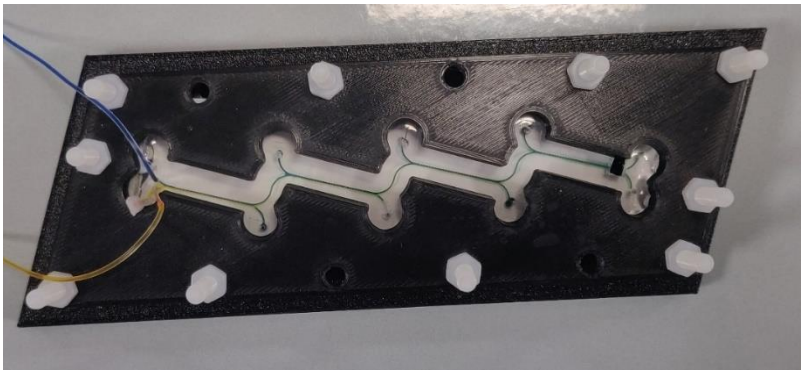

Figure 2.20: Complete sealed system with the mechanical clamps for microfluidic device with four mixers.

2.2.7 Replica Moulding (Soft Lithography)

In this PhD work, polydimethylsiloxane (PDMS) is used to create a microfluidic device apart from laser lithography (Chapter 2.2.1) to be integrated with an Electrolyte-Gated Field Effect Transistor (EGOFET) and an electrochemical sensor like Micrux. In order to create PDMS based microfluidics, soft lithography technique is used. In Figure 2.19, this process could be seen step by step. PDMS (liquid) mixed with a cross-linking agent is poured into a microstructured mold and heated to obtain an elastomeric replica of the mold after PDMS is cross-linked [37, 38].

PDMS is an elastomeric polymer, which is used for fabricating and fast prototyping of the microfluidic devices. Its structure contains carbon and silicon. The PDMS empirical formula is (C2H6OSi)n and its fragmented formula could be seen in Figure 2.18, n being the number of monomers repetitions. The non-cross-linked PDMS may be almost liquid. The siloxane bonds result in a flexible polymer chain with a high level of viscoelasticity. After cross-linking, PDMS becomes a solid hydrophobic elastomer [37]. PDMS has many advantages such as transparency in the range of 230-700 nm wavelength, conformal bonding to sensor substrate and permeability to gases for specific biological applications with cell cultures [2, 21].

For preparing PDMS, curing agent and PDMS pre polymer (SYLGARD 184 Silicone Elastomer Kit) are mixed in the weight ration of 1:10. Afterwards, the PDMS mixture is put inside a vacuum chamber for 1 hour for removing any air bubbles into the fluid. After degassing, PDMS is poured upon the molds, which are fabricated through 3D printer. Afterwards, PDMS mixture could be thermally cured at room temperature for 48 hours or at the oven at 70ºC for 12-15 hours. Then the

PDMS replica is peeled off gently and sealed on top of glass by using O2 plasma or on top of the sensor with the mechanical clamps.

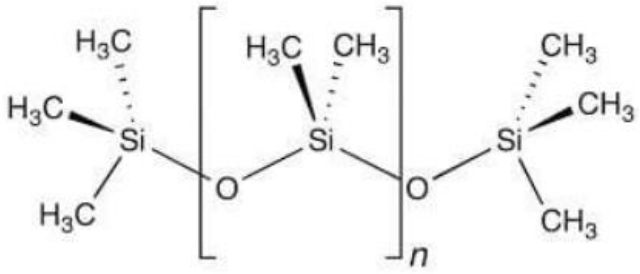

Figure 2.21: Fragmented formula of PDMS [37].

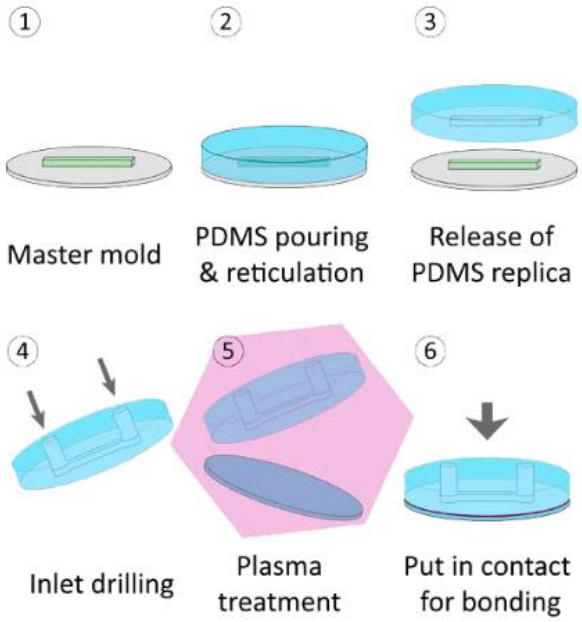

Figure 2.22: Schematic representation of the soft lithography process step-by-step [37].

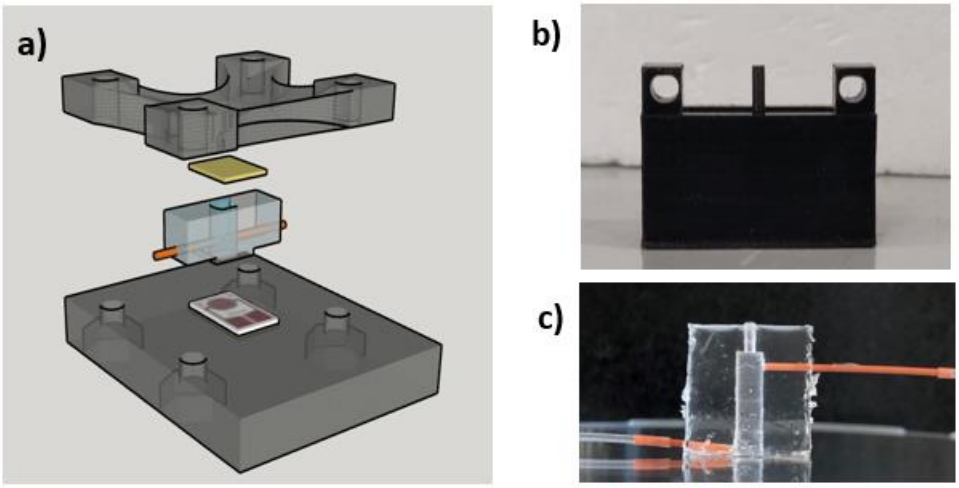

Figure 2.23: a) 3D design for microfluidic pool; placed with the electrochemical sensor and mechanical clamps b) 3D printed master for the microfluidic pool c) PDMS microfluidic pool with the tubings for inlet and outlet for on top of the sensing unit.

The microfluidic chamber positioned on the transistor channel is made with a small eye-shaped chamber with overall dimensions 5 x 1 x 3 mm. Two vias for inlet and outlet of liquid were obtained on the PDMS fluid cell and were connected to external pump systems by means of peek tubing with internal diameter equal to 500 µm.

2.2.8 Screen Printing

Printing techniques like screen, inkjet and aerosol jet printing have been used for manufacturing of cost and material efficient electronic devices on different flexible substrates such as paper, plastic and textile [39,40,41]. The comparison of these printing techniques in details could be found in Table 1. In this sub-chapter, the screen-printing will be elucidated.

The basic principle of screen printing could be seen in Figure 2.21a. This process requires a screen mesh with the design on it. The screen printing is one of the most efficient and fast printing techniques once the screen mesh has been created. The printing occurs when the ink is pushed through screen mesh to create the design on the below surface. The most commonly used surfaces are polyfoils such as PET, paper and fabrics. In the present PhD thesis, DEK Horizon 03iX under ambient conditions (≈22 °C and 50 RH%) was used. During printing, one of the most important

and challenging parameters is the alignment of the substrate and mesh screen. Other important parameters to be considered for good printing are: the viscosity of the inks and their adhesion on different substrate types. For this, optimization of the operative pressure depending on the substrates, such as tattoo paper and PET, is a matter or preliminary studies and experiments.

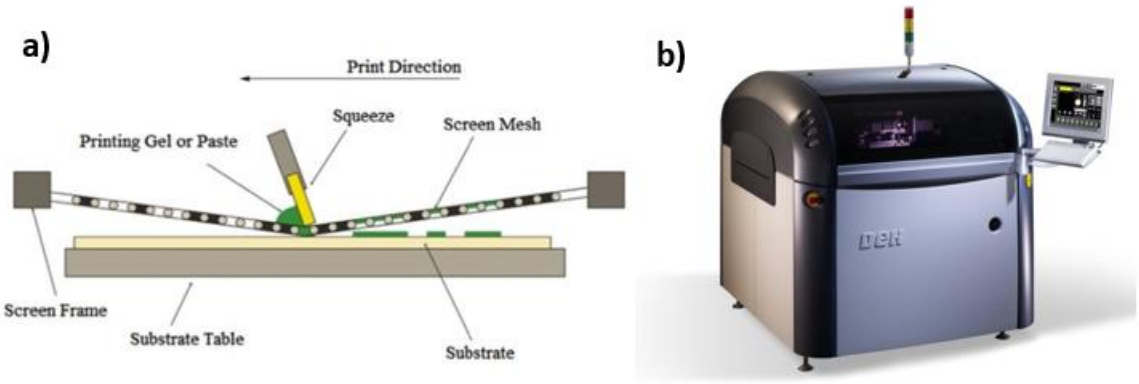

Figure 2.24: a) Schematic representation of screen printing [27] b) The used screen printer is DEK Horizon 03iX.

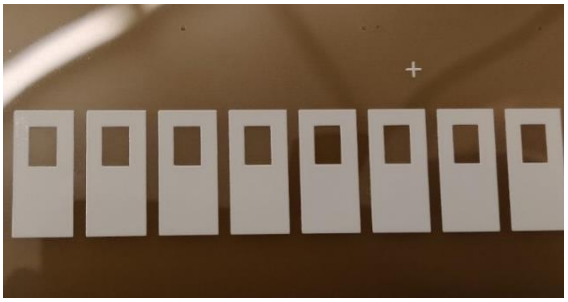

Figure 2.25: Screen-printed microfluidic pools on top of PET substrate.

The plastic films (125 µm thick PET, purchased from Policrom) were used as flexible substrates for printing sessions. Prior to use the foils , the plastic substrates were thermally stabilized by preheating in the oven for 30 min at 150 °C for a better adhesion. For the screen meshes, polyester-based screens with different mesh sizes (depending on the deposited layer) were acquired from Marabu Scandinavia AB and used for printing different designs. After printing sessions, depending on the ink choice, the post treatment occurs either with UV curing or thermal curing in the oven.

	Screen Printing	Inkjet (Dimatrix)	Aerosol Jet
Resolution	~ 80 µm [39]	~ 50 µm	~ 20 µm [39]
Substrate	Paper, PET, Textile	Paper, PET, Kapton	Paper, PET (polyfoil)
Advantages	Fast printing Mass Production	Fast printing Without Mask	High Resolution Without Mask
Disadvantages	• Alignment • Cost of multiple Screens • Cost of inks and cleaning chemicals • Pre and post treatments • Screen gets clogged	• Cost of inks • Inks smudge • Nozzle could be clogged	• Very complex • Not fast printing • Expensive equipment

Table 1: Comparison of three different printing techniques

Compared to the other printing techniques like Inkjet and Aerosol Jet, Screen-printing has lower resolution around 80 µm. With all the three printing techniques, different substrate like paper, textile or polyfoil (PET) could be used. Screen-printing has different advantages like mass production and fast production. However, it requires the screens for the designs. For the Inkjet and Aerosol Jet, there is no need for the masks. They do the printing directly on the substrate. For the screen-printing, the other disadvantages are the alignment, the cost of multiple screens and pre and post treatments. When it comes to Inkjet printing, the disadvantages are the clogging of nozzles and the cost of inks. For the aerosol printing, the main disadvantages are very complex and expensive equipment and slow printing process.

2.3 Materials for functionalization

2.3.1 Protein standard for validation of dilution rate in microfluidic mixer

To test microfluidic mixer performance, a protein solution is used and quantified by UV-Vis spectroscopy. The selected protein is bovine serum albumin (BSA). This protein is widely available in the plasma; it exhibits the function of providing pH buffering and maintaining the osmotic blood pressure and has been widely used as a carrier to deliver drugs and small active molecules [47]. In the biosensing applications, BSA is used, since it is an inexpensive choice for blocking active sites of the sensing interfaces and to resist nonspecific adsorption in biological environments [48,49]. Additionally, BSA can be easily detected with UV Spectroscopy. BSA has a weight 66 kDa and the molar extinction coefficient $\varepsilon 280 = 43824\ M^{-1}\ cm^{-1}$. More detail can be found in Chapter 3.6 of the characterization methods. Lastly, BSA was purchased from Sigma Aldrich. Different concentrations of the BSA were diluted in 10 ml of PBS (pH 7.2, 0.1 M concentration) in different vials.

2.3.2 Materials for self-assembly monolayers (SAM) detection

Self-assembled monolayers (SAM) are molecular assemblies, which are formed spontaneously on surfaces by adsorption [52]. They consist of a head group (linking group), backbone (main chain) and functional end active group (Figure 2.26). The head group molecules could be thiols or phosphonates that have a strong affinity to the substrate and anchors the molecule to it [51]. The substrate could be gold, silver, copper, nickel, platinum etc. The terminal group determines certain properties to the surface like hydrophilicity or hydrophobicity and they can be also used to anchor other molecules such as biomolecules by weak interaction or covalent bonds [50, 53]. One of the type of SAM is alkanethiols, which are molecules with a back bone, $(C\text{-}C)^n$ alkyl chain ,a tail group, and a S-H head group. The adsorption of alkanethiols on gold substrate is most studied for SAM formation [54-57] since the gold as a substrate is easy to pattern and deposit. Additionally, gold is an inert metal and biocompatible. It does not oxidize at temperatures below its melting point or not react with atmospheric O2.

The bare surfaces of metals tend to adsorb adventitious organic materials readily because these adsorbates lower the free energy of the interface between the metal or metal oxide and the ambient environment. In case of alkanethiols, the formation of a thiolate requires the chemical activation of the S-H bond of the thiol [51]. In the literature, it is stated that the sulfur gold interaction is semi-covalent and has a strength of approximately 40 kcal/mol and a net energy for adsorption of alkanethiolates on gold of 5 kcal/mol (exothermic) [50,58].

SAMs formation by adsorption occurs by immersing a substrate into a dilute solution of alkane thiol. Depending on the type of alkanethiolates, SAM could form within minutes to hours at room temperature. The formation of SAM on top of the gold could be affected by certain parameters such as the solvent choice, the temperature, and the concentration of adsorbate, immersion time, purity of the adsorbate and chain length.

The structures of SAMs are characterized by different techniques like XPS [59-61], Fourier transform infrared spectroscopy (FTIR) [62], electrochemistry [63], Raman spectroscopy [64]. Additionally, the atomic force microscopy (AFM) and scanning tunneling microscopy (STM) are commonly used for the mechanisms of SAM formation and determine the important structural features. STM can image the shape, spatial distribution, terminal groups and their packing structure [65, 66]. AFM has been used to determine chemical functionality, conductance, magnetic properties, surface charge, and frictional forces of SAMs [67, 68].

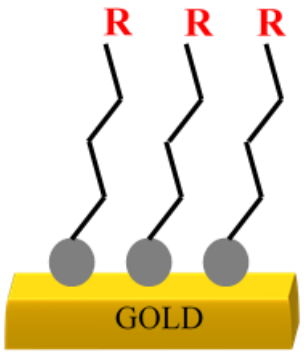

Figure 2.26: Schematic diagram of a SAM of alkanethiolates on a gold surface with the head group (grey circle), alkane chain (black) and terminal functional group (represented by R).

In the beginning, the adsorbate molecules either form a disordered mass of molecules or form an ordered two-dimensional lying down phase [69]. Thiol molecules chemisorb on the gold substrate through the S- head group forming a strong covalent bond, in a process that takes at least some minutes to hours. During the process, the thiol molecule loses the mercaptan H atom, transforming itself in a thiolate [50]. The adsorption process is described as follows. Reaction 1a and 1b correspond to the physisorption and the chemisorption. Due to the strong chemisorption of the head groups, more stable monolayers are created compared to the physisorbed ones [50].

$$CH_3(CH_2)_nSH + Au \rightarrow (CH_3(CH_2)_nSH)physAu \quad (2.1)$$

$$(CH_3(CH_2)_nSH)physAu \rightarrow CH_3(CH_2)_nS–Au + 1/2H2 \quad (2.2)$$

For higher molecular coverage, a longer time requires depending on the type of thiols and it begins to form three-dimensional crystalline or semi-crystalline structures on the gold surface [70]. The head molecules come together on the substrate, while the tail groups assemble far from the substrate. The monolayer packs tightly due to van der Waals interactions thereby reducing its own free energy To minimize the free energy, the molecules adopt conformations, which allow high degree of Van der Waals forces and in some cases hydrogen bonding with the surrounding molecules [71] . Van der Waals forces arise from the dipoles of molecules and are thus much weaker than the surrounding surface forces at larger scales [50,51].

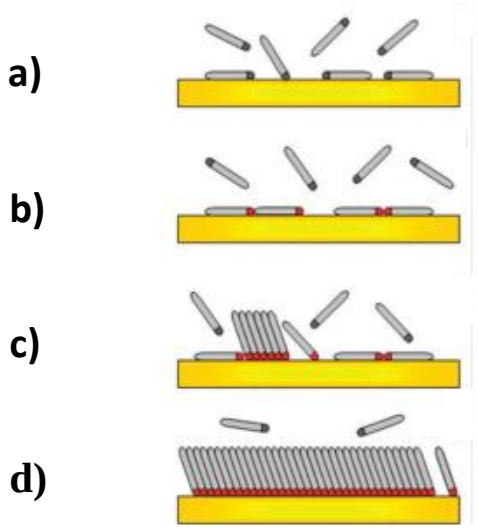

Figure 2.27: Schematic representation of the different steps taking place during SAM formation on gold a) physisorption, b)lying down phase formation, c) nucleation of standing up phase, d) standing up phase [50].

In this PhD work, different commercially available SAMs were used for the detection of them. They are reported in Table 2. All were purchased from Sigma Aldrich. Before any use, all SAM types were diluted in 10 ml of PBS up to 0.1 mM concentration (pH 7.2)

	Linear Formula	**Molecular Weight in g/mol**
3-Mercapto-1-propanol (95%)	$HS(CH_2CH_2CH_2)OH$	92.16
6-Mercapto-1-hexanol (97%)	$HS(CH_2)_6OH$	134.24
8-Mercapto-1-octanol (98%)	$HSCH_2(CH_2)_6CH_2OH$	162.29
9-Mercapto-1-nonanol (96%)	$C_9H_{20}OS$	176.32

Table 2: Description of the all used thiols

2.3.3 Materials for oligonucleotide detection

For detection the oligonucleotides, different RNA sequences (P) w and 4 different target RNA sequences (T) were purchased from Metabion international, with which the gold gates were functionalized. The probes have with a thiol group (HS-), a sequence of 5 adenines and a spacer of 5 carbon atoms (5C) at the 5'-terminus to improve the adhesion with the gold gate. The probes are stocked in a SSPE buffer (Sigma Aldrich) solution, which consist of 0.02M EDTA ,2.98M NaCl, 0.2M phosphate buffer (PBS). The targets are kept in a a Tris-HCl solution with 0.02M Tris, 0.14M NaCl, 0.001M MgCl2. All the probes and targets are diluted with the Tris-EDTA solution with 0.01M EDTA , 0.05M NaCl, 0.01M Tris.

2.3.4 Gate electrodes for miRNA-21 biosensor

Gold wires were purchased from Nanovision S. r.l, Brugherio (IT) with purity of 99.99%, a length of 2.5 cm and a diameter of 1.5 mm. The gold wire has proven to be a good alternative to the classical planar/flat surface, due to the possibility to regenerate the surface with sulfuric acid cleaning procedure, and easy operation for functionalization and contact making. In order to assemble the gate electrode on top of the electrolyte and to obtain a final model, a 3D printed gate holder was designed and fabricated. Polydimethylsiloxane was used to generate a pool, which could contain 70 μL–80 μL of the buffer solution and preserve contact pads from leaking buffer solution.

2.3.5 miRNA-21 functionalization protocol

Synthetic oligonucleotides were purchased from Metabion Internation AG, according to the following sequences:

- •miRNA-21-3p derived sequence (5'- CAACACCAGUCGAUGGGCUGU- 3'), as the target analyte

- •Thiol-C6-AAA AAAA-5'- UAGCUUAUCAGACUGAUGUUGA – 3', synthetized with thiol group, C6 and 7 adenine spacers, as the probe

- •miRNA-141 derived sequence (5'-CAUCUUCCAGUACAGUGUUGGA- 3'), as the control unrelated sequence (CTR)

The stock solutions for probe and target containing segments of miRNA sequences were prepared in (sodium chloride-sodium phosphate-ethylenediaminetetraacetic acid) (SSP-EDTA) and tris (hydroxymethyl) aminomethane hydrochloride (Tris-HCl) like previously reported in literature [42]. 2-mercaptoethanol (2-ME) blocking agent was selected to reduce the direct interaction between the target analyte and the gold surface. All the reagents were purchased from Merck-Sigma Aldrich.

The following gate functionalization steps were carried out:

1) Gate-1 was functionalized with 2-mercaptoethanol for the whole night at the room temperature, then rinsed with the ultrapure water before assembling.

2) Gate-2 was functionalized with probe (2 μM), for the whole night at room temperature. Later, G2 was rinsed with ultrapure water and then placed in the vial containing 1 mM concentration of the blocking agent (2-ME), in order to block the non-specifc bindings.

Hybridization with the different concentrations of the target analyte was performed by incubating the Gate-2 at 37ºC for 30 min in the oven [43]. The vials have different miRNA-21 concentrations, which were prepared by using hybridization (Tris-EDTA-NaCl) buffer [2]. The hybridization process started from the vials with lower concentrations to higher concentrations. Each vial incubation lasted at 37°C for 30 minutes with the same Gate -2 electrode [42, 43]. After hybridization process, reference gate Gate-1 and sensing gate Gate-2 were electrically characterized by the Source Measurement Unit (SMU).

2.3.6 Gate electrodes for α-synuclein biosensor

The metal electrodes were cleaned by sonication in acetone and isopropanol. The devices were then exposed to UV Ozone cleaner for 25 minutes. Subsequently, the chip was immersed in a solution of 2,3,4,5,6-pentafluorothiophenol (PFBT, 2 μL/mL in isopropanol) for 15 minutes to functionalize the gold Source-Drain contacts, rinsed with isopropanol and dried over N2. In the devices with the coplanar gate electrode, before the Source-Drain PFBT functionalization, the planar gate electrode was passivated by a thick coating of dextran (i.e. drop-casting of a dextran solution 10 mg/mL) [44]. Such a sacrificial layer was removed by immersing the device in water after the deposition of the organic semiconductor in order to leave the gate electrode uncovered.

2.3.7 Materials for α-synuclein biosensor

Human α-synuclein, glutaraldehyde (25% wt), potassium chloride, sodium phosphate dibasic, iron(III) ferrocyanide, polystyrene (MW 10000 g/mol), chlorobenzene, 2,3,4,5,6-pentafluorothiophenol, dextran (from Leuconostoc Mesenteroides, MW= 64.000-76.000 g/mol), and gold wire (Ø 0.5 mm) were purchased from Sigma Aldrich. Sodium chloride and glycerol were purchased from Panreac Quimica. Recombinant His-tagged Protein G was obtained from BioVision,

Inc. HS–$(CH_2)11$–$(OCH_2CH_2)_6$–NH_2·HCl (abbreviated as $HSC_{11}EG_6NH_2$) was purchased from ProChimia Surfaces. The anti-(α-synuclein) antibody, α-synuclein(211) that binds to monomeric α-synuclein, was purchased from Santa Cruz Biotechnology, Inc. The organic semiconductor, 2,8-Difluoro-5,11-bis(triethylsilylethynyl)anthradithiophene (diF-TES-ADT), was obtained from Lumtec.

2.3.8 Functionalization of gold wire gates for α-synuclein biosensor

The polycrystalline Au wire was cleaned according to the following protocol: (i) immersion in NaOH 1 M, heating at above 100 ˚C for 15 minutes, (ii) immersion in concentrated H2SO4 heating at above 100 ˚C for 15 minutes, (iii) Au electropolish by sweeping the potential from -0.1 V to 1.6 V (15 cycles in H2SO4 1 M, as solvent). The functionalization protocol for approach I consisted of the following steps:

(i)Incubation in the solution of HSC11EG6NH2 (1 mM EtOH) at 4 °C overnight. The Au wire was successively rinsed with EtOH and bidistilled water and dried by N2 flow.

(ii)Activation of the amino-group by dipping the HSC11EG6NH2-coated wire in a solution of glutaraldehyde (2.5% wt in water) at 4°C for 1 h, and successively rinsed with bidistilled water.

(iii)Incubation into the anti-(α-synuclein) antibody solution (40 µg/mL in PBS 1x pH 7.2) at RT for 15 minutes.

Approach II consisted of these steps:

(i)Incubation in Recombinant His-tag protein G solution (140 µg/mL in PBS 1x pH 5.5) at RT for 15 minutes.

(ii)Incubation into the anti-(α-synuclein) antibody solution (40 µg/mL in PBS 1x pH 5.5) at RT for 15 minutes.

The α-synuclein solutions were prepared by subsequent dilution starting from 1 mg/mL concentration in PBS 1x pH 7.2. The Ab-coated Au surfaces were incubated for 15 min at R.T with α-synuclein solutions of increasing concentrations in the range from 0.25 pM to 250 nM and finally abundantly rinsed with PBS 1x pH 7.2 before measurements.

2.3.9 Functionalization of the coplanar Au-gate by using the microfluidics

The self-assembled monolayer formation on the coplanar gate electrode was carried out ex-situ by PDMS-assisted printing technique [44]. Afterwards, the microfluidics setup was assembled and the chambers were filled with the electrolyte solution from Inlet, employing a peristaltic pump from Watson-Marlow (400 series pump). At this point, activation of the SAM amino-groups by glutaraldehyde (100 µL, 2.5% v/v) and subsequent Ab (50 µL, 40 µg/ml) immobilization was performed in-situ, by injecting the corresponding solutions from Inlet2 at a flow rate equal to 10 µl/min, connecting simultaneously a peristaltic pump at the Outlet to pump out the same fluid.

Then, buffer solution (PBS 1mM) was injected at 10 µl/min through Inlet 2 in order to wash away physisorbed biomolecules, approximatively for 5 minutes. The subsequent α-synuclein sensing was performed in-situ, by injecting the solution containing the receptors (50 µl) at a flow rate of 10 µl/min from Inlet2, for about five minutes. After each functionalization step, a fresh PBS 1x solution was streamed through Inlet 2 for at least 3 minutes in order to remove the physisorbed molecules. Finally, the flow was stopped and three transfers were recorded in the linear regime, measuring the device with the sensing gate. The concentrations of α-synuclein solution sensed were the following: 2.5 pM, 25 pM, 250 pM, 2.5 nM, 25 nM,250 nM. Each sensing experiment started and finished with an electrical characterization by exploiting the reference gate electrode in order to cross-check the overall operation status of the organic semiconductor.

2.4 References:

[1] Campana A, Cramer T, Greco P, et al. Facile maskless fabrication of organic field effect transistors on biodegradable substrates. Appl. Phys Lett American Institute of Physics 2013; 103(7):073302.

[2] Selvaraj M. Organic Electronic Transistors and Microfluidics for Cancer Biomarker Sensing [Ph.D dissertation] University of Catania, 2021.

[3]Parkula V. Organic Electronic Transistors for Biosensing [Ph.D dissertation] Università degli Studi di Modena e Reggio Emilia: Modena 2019.

[4] Magliulo M, Mulla MY, Manoli K, et al. Ultrasensitive printable biosensors for point-of-care applications. 2015 Available at: https://spie.org/news/5961-ultrasensitive-printable-biosensors-for-point-of-care-applications.

[5]Stewart Z. Organic Thin-Film Transistors and TIPS-Pentacene. Lewis Honors College Capstone Collection 2013; 11.

[6] Farag AAM, Yahia IS. Structural, absorption and optical dispersion characteristics of rhodamine B thin films prepared by drop casting technique. Optics Communications 2010;283(21):4310–17.

[7] Park J, Lee S, Lee HH. High-mobility polymer thin-film transistors fabricated by solventassisted drop-casting. Organic Electronics 2006; 7(5):256–60.

[8] Kajal P, Ghosh K, Powar S. Manufacturing Techniques of Perovskite Solar Cells 2018; pp.341–64.

[9] https://www.sculpteo.com/en/3d-learning-hub/basics-of-3d-printing/the-history-of-3d-printing/

[10] Wu C, Yi R, Liu Y-J, et al. Delta DLP 3D printing with large size. 2016 IEEE/RSJ International Conference on Intelligent Robots and Systems (IROS), 2016.

[11] Whitley D 3rd, Eidson RS, Rudek I, Bencharit S. In-office fabrication of dental implant surgical guides using desktop stereolithographic printing and implant treatment planning software: A clinical report. J Prosthet Dent. 2017 Sep;118(3):256-263.

[12] Murphy, S. V & Atala, A. 3D bioprinting of tissues and organs. Nat. Biotechnol.32, 2014;773.

[13]Fadoul, H. E., Siddig, M. A. El, Juntawong, N. & Hussein, A. A. El. Smart hydrogels for 3D bioprinting. Int. J. Bioprinting, 2016;7, 1–8 .

[14] Ko D-H, Gyak K-W, Kim D.,Emerging Microreaction Systems Based on 3D Printing Techniques and Separation Technologies, Journal of Flow Chemistry 2017; 7(3):1–10.

[15] https://www.3dsourced.com/3d-printing-technologies/digital-light-processing-dlp/

[16] https://formlabs.com/3d-printers/

[17] Hideo Kodama, Automatic method for fabricating a three-dimensional plastic model with photo-hardening polymer, Review of Scientific Instruments 52, 1981; 1770-1773.

[18]Charles W. Hull, (1986), Apparatus for production of three-dimensional objects by stereolithography, (U.S. Patent No. 4,575,330).

[19] Xia, Y. & Whitesides, G. M. Soft Lithography. Angew. Chem. Int. Ed. 37, 1998;550–575.

[20] Duffy, D. C., McDonald, J. C., Schueller, O. J. A. & Whitesides, G. M. Rapid Prototyping of Microfluidic Systems in Poly(dimethylsiloxane). Anal. Chem. 70; 1998; 4974–4984.

[21] Mata, A., Fleischman, A. J. & Roy, S. Characterization of polydimethylsiloxane (PDMS) properties for biomedical micro/nanosystems. Biomed. Microdevices 7, 2005; 281–293.

[22] Fujii T. PDMS-based microfluidic devices for biomedical applications. Microelectronic Engineering 2002; 61–62:907–14.

[23] Jo B-H, Van Lerberghe LM, Motsegood KM, et al. Three-dimensional micro-channel fabrication in polydimethylsiloxane (PDMS) elastomer. Journal of Microelectromechanical Systems 2000; 9(1):76–81.

[24] Zabihipour, M., Lassnig, R., Strandberg, J. et al. High yield manufacturing of fully screen-printed organic electrochemical transistors. npj Flex Electron 4, 2020;15.

[25] Peter Andersson Ersman et al. Flex. Print. Electron, 2017; 2045008.

[26] Wang X, Nilsson D, Norberg P. Printable microfluidic systems using pressure sensitive adhesive material for biosensing devices. Biochim Biophys Acta. 2013;1830(9):4398-401.

[27] Kumari, R., Kumar, V. Impact of zinc doping on structural, optical, and electrical properties of CdO films prepared by sol–gel screen printing mechanism. J Sol-Gel Sci Technol,2020; 94648–657.

[28] Katz, H. E; Bao, Z. The Physical Chemistry of Organic FieldEffect Transistors. J. Phys. Chem. B. 1999 ; 104, (4), 671— 678.

[29] Oliver, Y. Charge Transport in Organic Conjugated Materials: From the Molecular Picture to the Macroscopic Properties. Ph.D. Thesis, Academie Universitaire Wallonie Bruxelles, France. 2008.

[30]Park, S. K.; Mourey, D. A.; Han, J. I.; Anthony, J. E.; Jackson, T. N. Environmental and operational stability of solutionprocessed 6,13-bis(triisopropyl-silylethynyl) pentacene thin film transistors. Org. Electron. 2009; 10, (3), 486–490.

[31] Anthony, J. E. The Larger Acenes: Versatile Organic Semiconductors. Angew. Chem. Int. Ed. 2008; 47, (3), 452— 483.

[32] Fudickar, W.; Linker, T. Why Triple Bonds Protect Acenes from Oxidation and Decomposition. J. Am. Chem. Soc. 2012; 134, (36), 15071—15082.

[33] Giri G, Verploegen E, Mannsfeld SCB, et al. Tuning charge transport in solution-sheared organic semiconductors using lattice strain. Nature 2011; 480(7378):504–08.
[34] Lyu, Yang et al., Architecture of covalent bonds between filament layers to enhance performance of 3D printing biodegradable polymer blends., Polymer Testing, 2022; Vol. 106, 107456.
[35] https://www.3dbeginners.com/what-is-fdm-3d-printing/.
[36] Zou, Rui Xun et al., Isotropic and anisotropic elasticity and yielding of 3D printed material, Composites Part B-engineering 99, 2016; 506-513.
[37]https://www.elveflow.com/microfluidic-reviews/general-microfluidics/the-poly-di-methyl-siloxane-pdms-and-microfluidics/.
[38] Xia, Y. Whitesides, G. M. Soft Lithography. Angew. Chem. Int. Ed. 37, 1998; 550–575.
[39] Makhinia, Anatolii et al. "High Performance Organic Electrochemical Transistors and Logic Circuits Manufactured via a Combination of Screen and Aerosol Jet PrintingTechniques." Advanced Materials Technologies 7, 2022; 2200153.
[40]V. Beni, D. Nilsson, P. Arven, P. Norberg, G. Gustafsson, A. P. F. Turner, ECS J. Solid State Sci. Technol. 2015; 4, S3001.
[41]M. Berggren, D. T. Simon, D. Nilsson, P. Dyreklev, P. Norberg, S. Nordlinder, P. Andersson Ersman, G. Gustafsson, J. J. Wikner, J. Hederén, H. Hentzell, Adv. Mater. 2016; 28, 1911.
[42] Cardoso AR, Moreira FTC, Fernandes R, et al. Novel and simple electrochemical biosensor monitoring attomolar levels of miRNA-155 in breast cancer. Biosensors and Bioelectronics 2016; 80:621–30.
[43] Bhagavan NV, Ha C-E. Chapter 21 - Structure and Properties of DNA. In: Bhagavan NV, Ha C-E, Eds. Essentials of Medical Biochemistry (Second Edition) Academic Press: San Diego2015;pp. 381–400.
[44] Leonardi F, Tamayo A, Casalini S, et al. Modification of the gate electrode by self-assembled monolayers in flexible electrolyte-gated organic field effect transistors: Work function: Vs. capacitance effects. RSC Advances 2018; 8(48):27509–15.
[45] Temiño I, Pozo FG Del, Ajayakumar MR, et al. A Rapid, Low-Cost, and Scalable Technique for Printing State-of-the-Art Organic Field-Effect Transistors. Advanced Materials Technologies 2016; 1(5):1–7.
[46] Zhang Q, Leonardi F, Casalini S, et al. High performing solution-coated electrolyte-gated organic field-effect transistors for aqueous media operation. Scientific Reports Nature Publishing Group 2016; 6:1–10.

[47] Li Yang et al., Electrochemical Biosensor with Enhanced Antifouling Capability Based on Amyloid-like Bovine Serum Albumin and a Conducting Polymer for Ultrasensitive Detection of Proteins in Human Serum, Analytical Chemistry 2021; 93 (42), 14351-14357.

[48] Sweryda-Krawiec, B.; Devaraj, H.; Jacob, G.; Hickman, J. J. A New Interpretation of Serum Albumin Surface Passivation. Langmuir 2004; 20, 2054– 2056.

[49] Park, J. H.; Jackman, J. A.; Ferhan, A. R.; Ma, G. J.; Yoon, B. K.; Cho, N.-J. Temperature-Induced Denaturation of BSA Protein Molecules for Improved Surface Passivation Coatings. ACS Appl. Mater. Interfaces 2018; 10, 32047– 32057.

[50] Leonardi F., Self-Assambled Monolayers (SAMs) in Organic Field-Effect Transistors [Ph.D dissertation] University of Bologna, 2014.

[51]Love et al., Self-Assembled Monolayers of Thiolates on Metals as a Form of Nanotechnology Chem. Rev. 2005; 105 (4):1103–1170.

[52] Barlow, S.M.; Raval R., Complex organic molecules at metal surfaces: bonding, organisation and chirality, Surface Science Reports. 2003; 50 (6–8): 201–341.

[53] Wang, Yantian et al., A potentiometric protein sensor built with surface molecular imprinting method, Biosensors & bioelectronics vol. 24,1, 2008; 162-6.

[54] Bain Colin D. et al, Formation of monolayer films by the spontaneous assembly of organic thiols from solution onto gold, Journal of the American Chemical Society 1989; 111 (1), 321-335.

[55] Nuzzo Ralph G. et al, Spontaneously organized molecular assemblies. 3. Preparation and properties of solution adsorbed monolayers of organic disulfides on gold surfaces, Journal of the American Chemical Society 1987; 109 (8), 2358-2368.

[56] Bain Colin D., Evall Joe, and Whitesides George M., Formation of monolayers by the coadsorption of thiols on gold: variation in the head group, tail group, and solvent, Journal of the American Chemical Society 1989; 111 (18), 7155-7164.

[57] Bain Colin D., Whitesides George M., Formation of monolayers by the coadsorption of thiols on gold: variation in the length of the alkyl chain, Journal of the American Chemical Society 1989; 111 (18), 7164-7175.

[58] Dubois Lawrence H., Zegarski Bernhard R., Molecular ordering of organosulfur compounds on Au (111) and Au(100): Adsorption from solution and in ultrahigh vacuum, J. Chem. Phys. 1993; 98, 678.

[59] Walczak Mary M. et al., Structure and interfacial properties of spontaneously adsorbed n-alkanethiolate monolayers on evaporated silver surfaces, J. Am. Chem. Soc. 1991 ;113, 7, 2370–2378.

[60]Porter Marc D. et al, Spontaneously organized molecular assemblies. 4. Structural characterization of n-alkyl thiol monolayers on gold by optical ellipsometry, infrared spectroscopy, and electrochemistry, J. Am. Chem. Soc. 1987; 109, 12, 3559–3568.

[61] Bain Colin D. et al., Comparison of self-assembled monolayers on gold: coadsorption of thiols and disulfides, Langmuir 1989; 5, 3, 723–727.

[62] Nuzzo Ralph G. et al, Fundamental studies of the chemisorption of organosulfur compounds on gold (111). Implications for molecular self-assembly on gold surfaces, J. Am. Chem. Soc. 1987, 109, 3, 733–740.

[63] Widrig Cindra A., Chung Chinkap, Porter Marc D., The electrochemical desorption of n-alkanethiol monolayers from polycrystalline Au and Ag electrodes, Journal of Electroanalytical Chemistry and Interfacial Electrochemistry 1991; Vol. 310, Issues 1-2, 335-359.

[64] Bryant Mark A., Pemberton Jeanne E., Surface Raman scattering of self-assembled monolayers formed from 1-alkanethiols: behavior of films at gold and comparison to films at silver, J. Am. Chem. Soc. 1991, 113, 22, 8284–8293.

[65] Häussling, L., Michel, B., Ringsdorf, H. and Rohrer, H. Direct Observation of Streptavidin Specifically Adsorbed on Biotin-Functionalized Self-Assembled Monolayers with the Scanning Tunneling Microscope. Angew. Chem. Int. Ed. Engl. 1991; 30: 569-572.

[66] Widrig Cindra A., Alves Carla A. and Porter Marc D., Scanning tunneling microscopy of ethanethiolate and n-octadecanethiolate monolayers spontaneously absorbed at gold surfaces, J. Am. Chem. Soc. 1991; 113, 8, 2805–2810.

[67] Tamada Kaoru et al., Surface Phase Behavior of n-Alkanethiol Self-Assembled Monolayers Adsorbed on Au(111): An Atomic Force Microscope Study, Langmuir 1997, 13, 6, 1558–1566.

[68] Liu Gang-yu, Salmeron Miquel B., Reversible Displacement of Chemisorbed n-Alkanethiol Molecules on Au(111) Surface: An Atomic Force Microscopy Study, Langmuir 1994, 10, 2, 367–370.

[69] Schwartz, D.K., Mechanisms and kinetics of self-assembled monolayer formation, Annu. Rev. Phys. Chem. 2001; 52: 107–37.

[70] Vos, Johannes G., Robert J. Forster, Tia E. Keyes, Interfacial Supramolecular Assemblies 2003; Wiley. pp. 88–94.

[71] Ferguson Melinda K. et al., Well-Ordered Self-Assembled Monolayers Created via Vapor-Phase Reactions on a Monolayer Template, Langmuir 2004 ; 20, 8, 3319–3323.

CHAPTER 3

CHARACTERIZATION METHODS

3.1 Introduction

In this chapter, I will explain the characterization techniques for the sensor responses and to assess the performance of microfluidic devices. In subchapter 3.2, the electrical characterization instrumentation and protocols are described for organic electronics for biosensing application.

In subchapters 3.3 and 3.4, I will give a brief overview of the electrochemistry methods such as cyclic voltammetry and impedance spectroscopy. These methods were used to characterize the gold electrodes and for the evaluation of the relationship between the functionalization time with thiolated molecules and coverage of the electrodes.

In subchapter 3.5, I will describe the surface plasmon resonance, as a analytical tool to determine the binding constant between antibody and target analyte, or also other affinity-based interactions. Lastly, in subchapter 3.6, I will explain UV spectroscopy for assessing the microfluidic mixer.

3.2 Electrical Characterization

For the electrical characterization of EGOFETs, a Source -Measurement Unit (SMU) was used. The chosen SMU Agilent (California, U.S.A) model B2912 SMU features high-resolution recording, up to 10 fA /100 nV, and low-noise electronics [1]. The SMU was used for applying fixed and sweepingpotentials to the device and to record the corresponding output current of the device. The instrument has two independent source and measurement channels. Channel 1 was used for applying the potentials between Gate and Source whereas Channel 2 to apply the potentials between Source and Drain. The instrument communicates with its customized software, where each measured channel's current could be plot after each potential scanning.

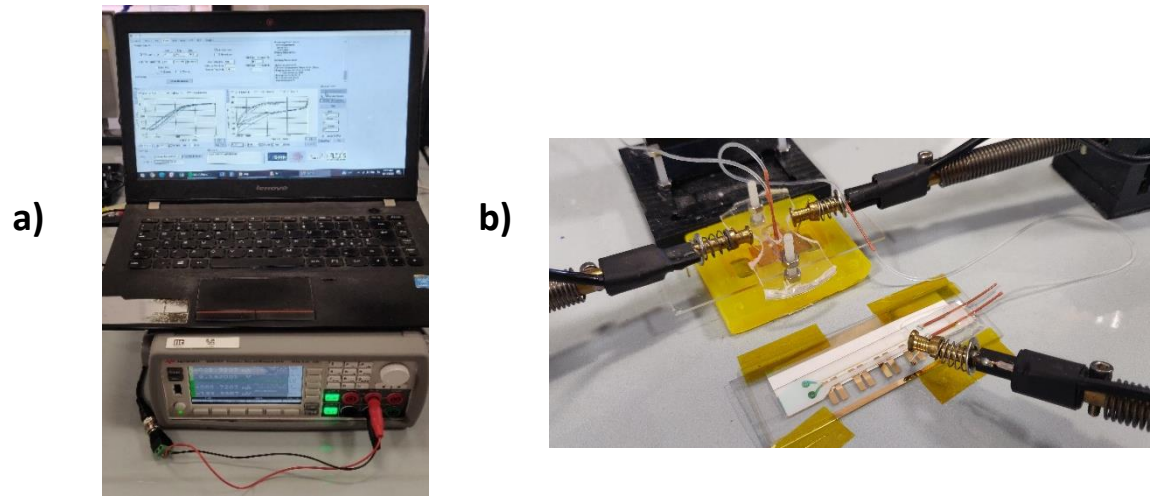

Figure 3.1: a) Electrical characterization set-up with the SMU and the software program b) the EGOFET device during measurement with probes.

The EGOFET is operated in low voltage range less than 1V. The applied potentials between Gate and Source are usually between 0.0 V to -0.7 V, meanwhile Drain-Source voltages are kept at constant value at -0.2 V, and hence the EGOFET devices are operated in the linear regime. After fixing the potential, the other parameters like the delay per steps (1ms) in Gate-Source potential or continuous measurements were chosen accordingly.

For multi gates EGOFET measurements, the transfer curves were recorded in order, starting from gate electrode 1 to gate electrode 8, consecutively for 5 times. The gate electrodes were measured before and after microfluidic flow experiment with thiol moieties. Transfer curves were obtained by measuring channel current (IDS) upon sweeping Gate-Source voltages in the range from 0V to -0.6V with steps of -1 mV at a fixed Drain-Source voltage Vds=-0.2 V. The recorded data during the experiment was analysed by Originlab Origin Pro 2018 Software.

3.3 Electrochemical Characterization

3.3.1 Cyclic Voltammetry

Cyclic Voltammetry is an electrochemical method for measuring redox events occurring at the electrode surface [2]. CV setup includes a potentiostat, an electrochemical cell and the three electrodes, which are immersed in the solution K3[Fe(CN)6]. This solution is prepared with 5 mM of potassium ferrocyanide in 0.1M of KCl. The working electrode (WE) is the electrode of interest on which the measurements are performed. The WE must be composed of a redox-inert material in the potential range of interest and the surface of the electrode must be extremely clean [2]. The reference electrode (RE) is used for establishing a reference potential and made of silver/silver chloride (Ag/AgCl). The counter electrode (CE) is made of platinum and used for the electroneutrality of the solution. The CE electrode assures that the kinetics of the reaction occurring at the surface of the CE do not interfere with any reactions on the WE. It is important to know that the surface area of the CE electrode is greater than the surface area of the WE [2].

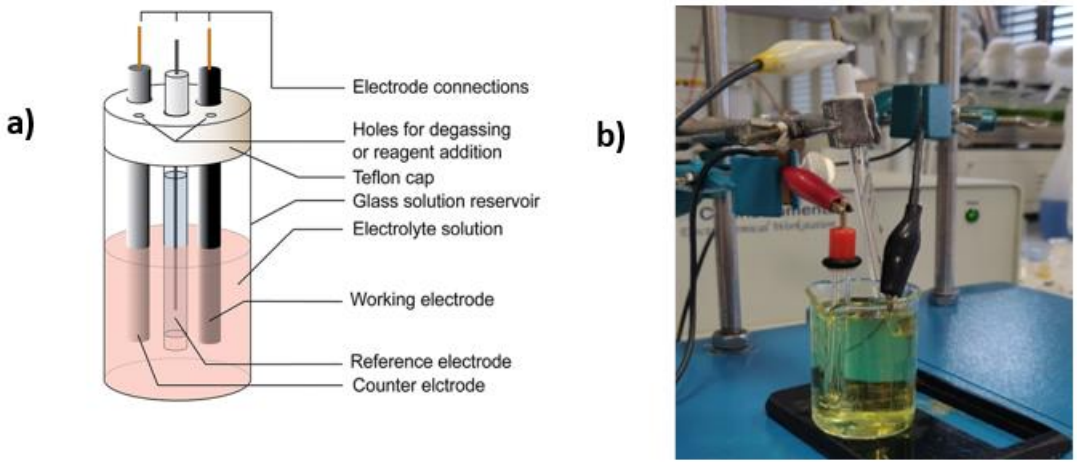

Figure 3.2: a) Schematic representation of an electrochemical cell for CV experiments [5] b) Experimental set-up with the three electrodes.

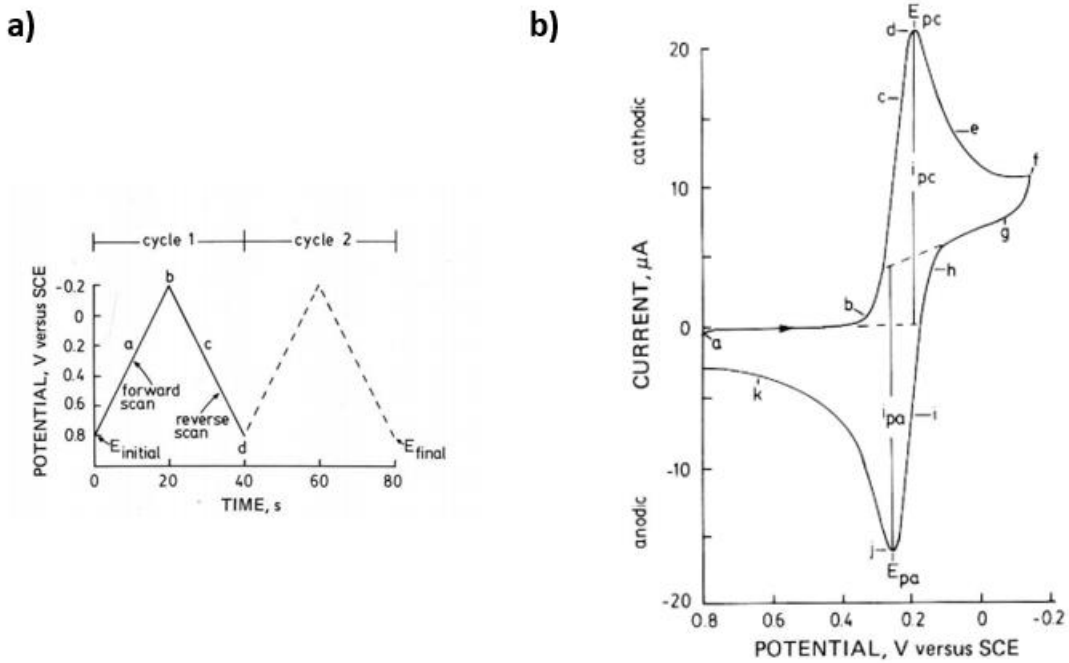

Figure 3.3: a)Excitation signal for cyclic voltammetry [3] b) Cyclic voltammogram of K3Fe(CN)6 with the scanrate 50 mV/s [3].

CV measurements are obtained by measuring the current at the working electrode vs the reference during the potential scan. The current can be considered the response signal to the potential excitation signal, which is a triangular potential that is applied between the working electrode (WE) and reference electrode (RE) (Figure 3.3) [3]. This triangular potential excitation signal sweeps the potential between two set values. Firstly, it scans negatively and then the scan direction is reserved, with a positive scan [3].

When the potential is negative enough to reduce $Fe^{III}(CN)_6^{3-}$, the cathodic current increases rapidly from b to d point in Figure 3.3b until the concentration of $Fe^{III}(CN)_6^{3-}$ at the electrode surface decreases. The redox reactions could be seen in the equation 1 and 2. Afterwards, the current starts to decrease since the solution surrounding the electrode is depleted of $Fe^{III}(CN)_6^{3-}$ due to its electrolytic conversion to $Fe^{II}(CN)_6^{4-}$ [3]. Afterwards, the scan direction is reversed to the opposite direction. However, The potential is still negative enough for reducing $Fe^{III}(CN)_6^{3-}$ so the cathodic current still continues, even though the potential is reversed and scanning in the positive direction. When the potential becomes positive enough to cause oxidation, $F^{eII}(CN)_6^{4-}$ is oxidized and the anodic current increases (i ⟶ j in Figure 3.3b) until the solution surrounding the electrode is depleted of $Fe^{II}(CN)_6^{4-}$ [3,5]. As a result, the current decreases (j ⟶ k). The redox potential ($E_{\frac{1}{2}}$) is found in the middle of the anodic and cathodic peaks in the CV plot and could be seen in the equation 3.3.

$$Fe^{III}(CN)_6^{3-} + e \longrightarrow Fe^{II}(CN)_6^{4-} \qquad (3.1)$$

$$Fe^{II}(CN)_6^{4-} \longrightarrow Fe^{III}(CN)_6^{3-} + e \qquad (3.2)$$

$$E_{\frac{1}{2}} = \frac{(E_{pa} + E_{pc})}{2} \qquad (3.3)$$

$$E = E^0 + \frac{RT}{nF} \ln \frac{(Ox)}{(Red)} = E^0 + 2.3026 \frac{RT}{nF} \log_{10} \frac{(Ox)}{(Red)} \qquad (3.4)$$

The concentrations of $Fe^{III}(CN)_6^{3-}$ / $Fe^{II}(CN)_6^{4-}$ change in solution at the electrode surface when the potential excitation signal is applied. This change at the electrode surface is described by the Nernst equation for a reversible system (Equation 3.4). The Nernst equation describes the potential of an electrochemical cell (E) with the standard potential of a species (E^0) and the ratio of the oxidized (Ox) and reduced (Red) analyte in the system at equilibrium. In the equation, F is Faraday's constant, R is the universal gas constant, n is the number of electrons, and T is the temperature [5].

As the potential is scanned negatively or positively, the concentration of $Fe^{III}(CN)_6^{3-}$ at the electrode surface changes accordingly in order to assure the Fe ratio in the Nernst equation for the applied potential. The concentration-distance profiles during the CV could be seen in Figure 3.4. The illustrations show that the solution concentration (C) varies as a function of distance (x) from the electrode surface during CV [3].

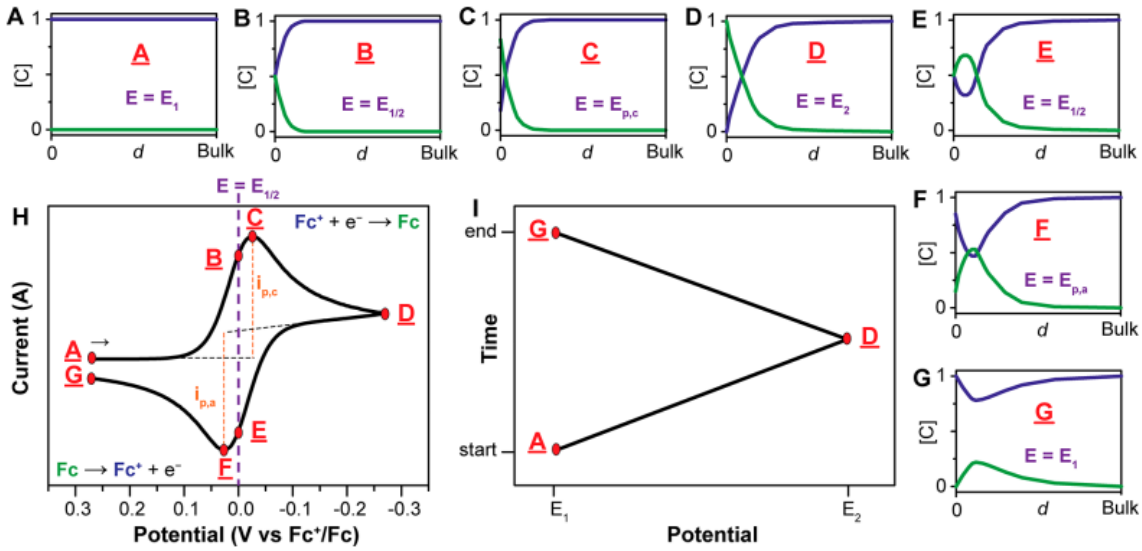

Figure 3.4: (A–G): Concentration profiles (mM) for Fc+ (blue) and Fc (green) as a function of the distance d from the electrode in bulk solution (H): Voltammogram measurements of the reversible reduction of a 1 mM Fc+ solution to Fc, with a scan rate of 100 mV s–1, whereas ip,c is the peak cathodic current and ip,a is the peak anodic current. (I): Applied potential as a function of time for a generic cyclic voltammetry experiment, with the initial, switching, and end potentials represented (A, D and G, respectively)[1,5].

3.3.2 Impedance Spectroscopy

Impedance (Z) describes the resistance for the current. For DC current, impedance and resistance are the same. For alternative current, impedance has a real and an imaginary part.

$$Z=E/I= Z_0 \exp(i\Phi) = Z_0(\cos\Phi + i\sin\Phi) \qquad (3.5)$$

$$1/Z= (1/R) + (1/i\omega C) \qquad (3.6)$$

Impedance spectroscopy (IS) is widely used to measure the capacitance of optimally polarizable electrodes, resulting in the development of models for the different functionalised electrodes [9]. The measurements are carried out in the frequency domain. The Nyquist plot is created by plotting the real part of the impedance on the X-axis and the imaginary component on the Y-axis [1].

With the Nyquist plot is possible to describe the equivalent electrical circuit (Randles Circuit, Figure 3.6a). This equivalent circuit is used to describe the electronic transfer from electrode to the solution and the capacity of the electrical double layer. In the circuit, R_s is the resistance of the solution, R_{CT} is the resistance of charge transfer, C_{dl} is the double-layer capacitance of the electrolyte interface. Z_w represents Warburg impedance. The Warburg impedance is the dominating effect at low test frequencies. In the Figure 3.6b, this could be seen a straight line with a slope of 45˚. This figure is defined by a semi-circle with a diameter equal to the charge transfer resistance R_{ct} at high frequencies, when the diffusion time constant is substantially longer than the signal period [1,27].

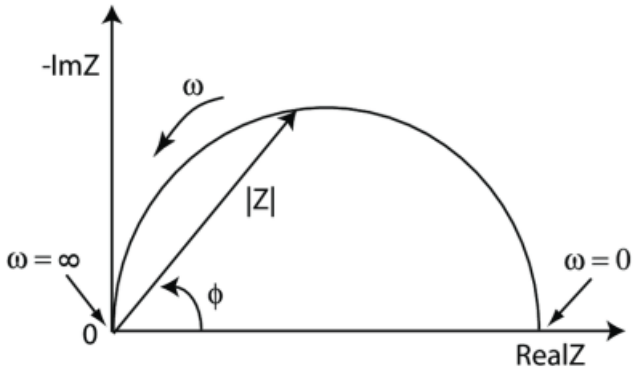

Figure 3.5: Nyquist plot with Impedance vector [10].

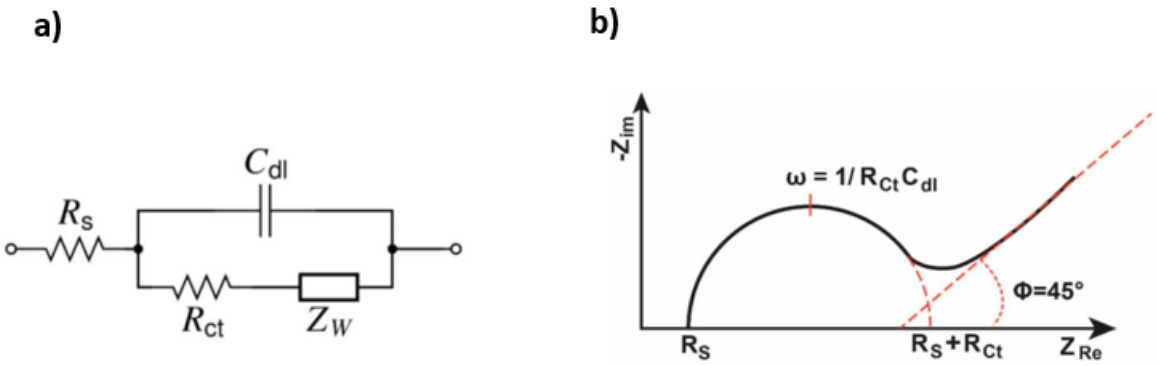

Figure 3.6:a)Equivalent Randles circuit, in which Rs is the resistance of the solution, RCT is the resistance to charge transfer, Cdl is the double-layer capacitance of the electrolyte interface [11] b) Nyquist plot of the equivalent circuit.

3.3.3. Electrochemical characterization for SAMs

In this PhD thesis, CV measurements are performed in a 5 mM solution of $[Fe(CN)_6]^{3-/4-}$ with a CH Instrument potentiostat model 760c. A three-electrode cell was assembled with the working electrode (WE), a Pt wire as a counter electrode (CE) and an Ag/AgCl electrode (Elbatech, Livorno Italy) as a reference electrode (RE). The CV measurements are performed in the voltage range between -0.20V and 0.45V with the scan rate 0.05 V/s for detecting different concentrations of SAMs on gold. For calculating the electroactive surface area of the gold with different SAM types, CV was measured at different scan rates (0.01 V/s, 0.05 V/s, 0.1 V/s, 0.15 V/s, 0.2 V/s) with sweeping the potential from -0.2 V to 0.45 V. The voltage values for the cathodic and anodic peaks are used for calculating the average mean potential value, which is used as the initial voltage for the EIS measurements.

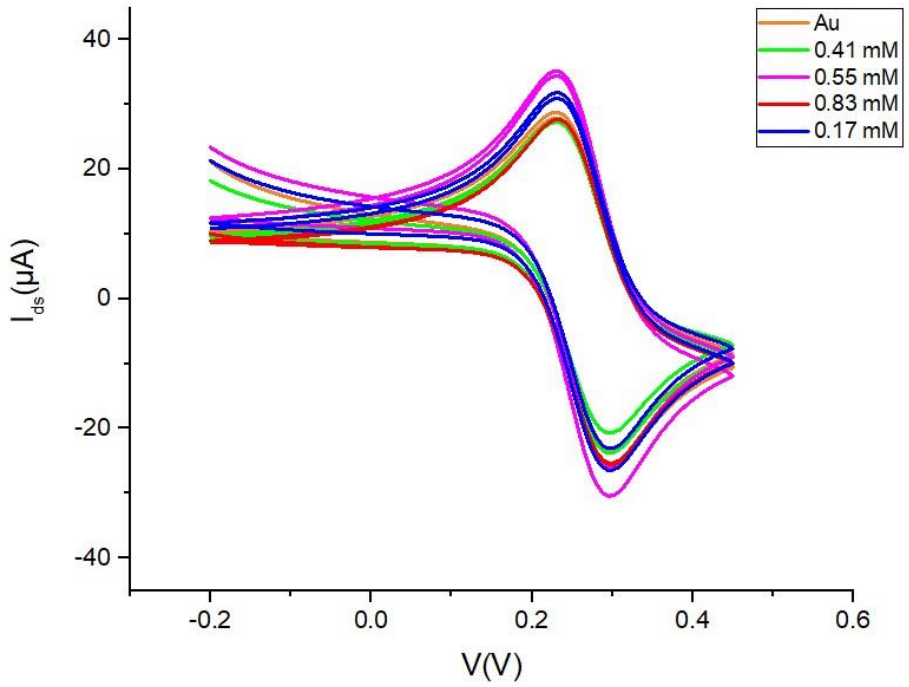

Figure 3.7: CV measurements for 3-Mercapto-1-propanol with the different concentrations. Before any measurements, the reference measurement is done with gold. MS stands for the mother solution with the concentration 1.66μM. The mother solution is then diluted manually with PBS to reach the solutions with different concentrations. Each gold gate is incubated in the separated vials for 10 minutes.

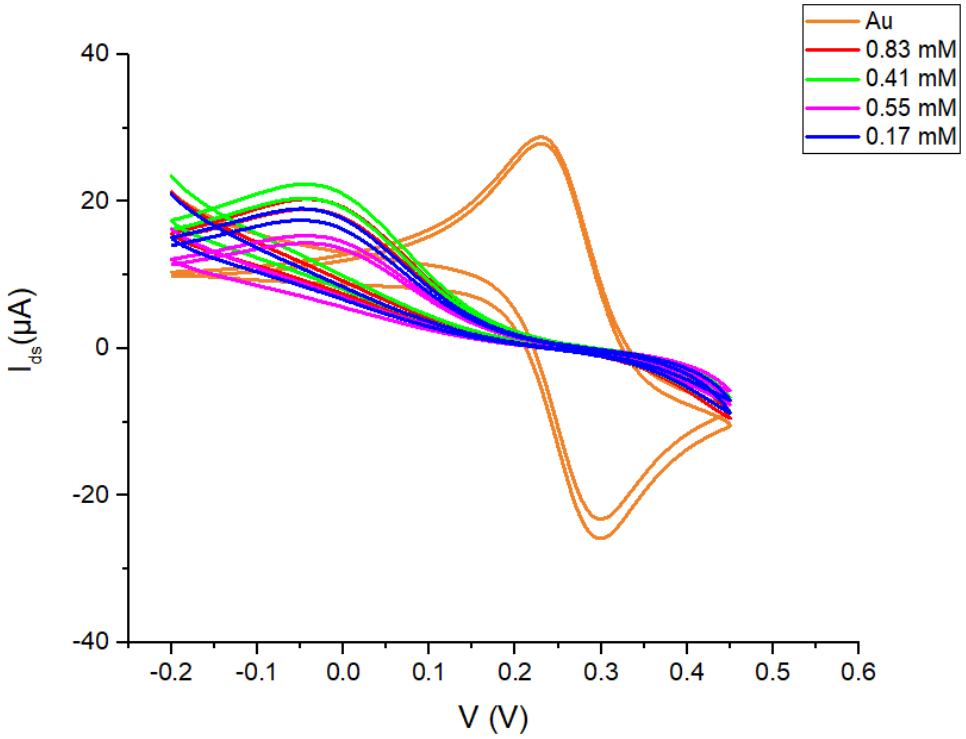

Figure 3.8: CV measurements for 8-Mercapto-1-octanol with the different concentration. Before any measurements, the reference measurement is done with gold. MS stands for the mother solution with the concentration 1.66μM. The mother solution is then diluted manually with PBS to reach the solutions with different concentrations). Each gold gate is incubated in the separated vial for 10 minutes.

3.3.4. Electrochemical characterization for [miRNA-21-3p]

The impedance spectroscopy data were acquired by using a CH Instrument potentiostat 760c model with a three-electrodes set-up, where the gate electrode was connected as working electrode,alongside an Ag/AgCl reference electrode (Elbatech, Livorno Italy) and a Pt wire as counter electrode, all in an electrochemical cell, filled with an aqueous solution of 5 mM K3(FeCN6), 0.1 M KCl. The impedance spectra were recorded between 0.1 Hz and 100 MHz, at a fixed potential of 0.2 V. The Nyquist plots fits were obtained with the EIS Spectrum Analyzer software.

3.3.5. Electrochemical characterization for α-synuclein

Electrochemical characterisation of the sensing platform was realized with a potentiostat/galvanostat Autolab (PGSTAT128N). The measurements were carried out in a standard three-electrode configuration cell by using Pt, Ag/AgCl, and Au as the counter, reference, and working electrode, respectively.

Electrochemical Impedance Spectroscopy (EIS) was recorded between 0.1 MHz to 0.1 Hz with an AC amplitude equal to 10 mV. The set point voltage was the redox potential of the ferricyanide probe. The impedance response was fitted by means of Randles circuit, whose components are the solution resistance (R_s) in series with the charge transfer resistance (R_{CT}) and the Warburg element (W), whereas in parallel the double-layer capacitance (C_{dl}) [6].
Cyclic voltammetry (CV) was measured at different scan rates (10 mV/s, 30 mV/s, 60 mV/s, 90 mV/s, 100 mV/s, 200 mV/s, 300 mV/s, 400 mV/s, 500 mV/s), sweeping the potential from -0.1 V to 0.45 V. Differential Pulse Voltammetry (DPV) was recorded sweeping the potential from -0.1 V to 0.5 V, at a sweep rate equal to 10 mV/s and its modulation amplitude equal to 25 mV. For the reductive desorption of thiols from Au surface, DPV was recorded sweeping the potential from -0.1 V to -1.4 V in NaOH 1 M. The whole batch of electrochemical measurements was performed in an aqueous solution containing $K_3[Fe(CN)_6]$ 5 mM, KCl 100 mM, and 50 mM of sodium phosphate buffer. The different pHs were adjusted by using small aliquots of NaOH or HCl 1 M. The non-faradaic measurements were carried out in a solution of KCl (100 mM) and sodium phosphate (50 mM) at pH 7.2

3.4 Surface Plasmon Resonance

Surface Plasmon Resonance is a real-time, optical label free method to detect the interaction of the analyte and receptor molecules. It is the gold-standard technique to study ligand binding protein interactions, which are important for many applications in medical science [15–17]. From the early 1960s, the excitation of surface plasmons was studied and analysed [20]. In 1990s, the first commercially SPR named Biocare was available in the market and it became the most reliable, accurate, real time instrument effectively measuring the interaction of bio molecules [21].
There are two main types of SPR sensors: Propagating SPR sensors and localized SPR sensors. In PSPR sensors the surface plasmon excited on the gold film will propagate into the interface. On the other hand, the localized SPR sensors do not exhibit propagation, when the sensor is based on plasmon excitation on nano structured gold film [22].
SPR measures the refractive index near to the chip surface; this exploits total internal reflection of light at a surface-solution interface to produce an electromagnetic field or evanescent wave that extends a short distance (up to 300 nm) into the solution [18].

In order to detect the binding of an analyte molecule to a receptor molecule, the receptor molecule is usually immobilised on the sensor surface by adsorption or by covalent binding and the analyte molecule is injected in the aqueous solution through the flow cell. During binding between receptor and analyte molecules, the refractive index changes, thereby increasing the intensity of the signal. Polarised light from a laser source is directed through a prism, which is the under surface of the gold film where surface plasmons are generated at a critical angle of the incident light. This absorption of light is seen as a decrease in intensity of the reflected light [1, 18].

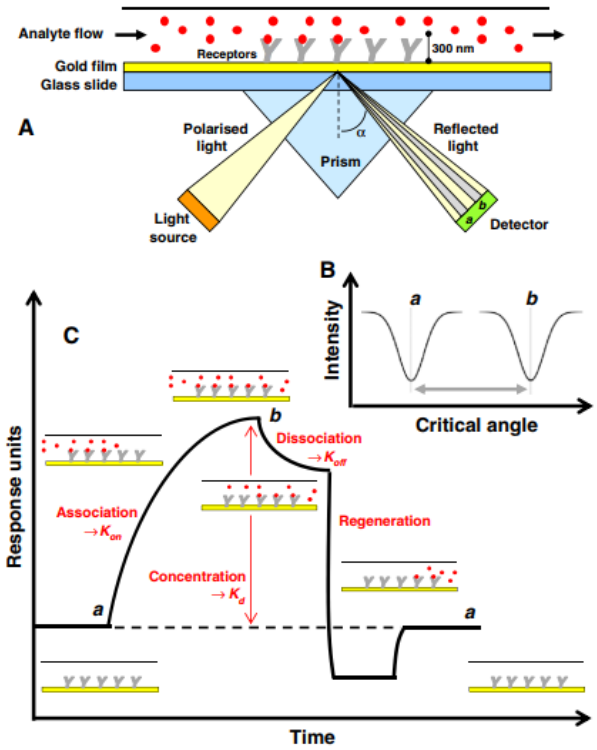

Figure 3.9: Schematic illustration of the basic SPR experiment for measuring the binding of an analyte molecule to a receptor molecule. A) Instrument set up for an SPR experiment based on BIAcore™ technology B) Change in the critical angle of incident light from angle a to angle b on binding of an analyte molecule to a receptor molecule. C. Response of the SPR experiment in the form of a sensorgram. If interaction between the immobilised receptor molecule and the analyte molecule occurs, the refractive index at the surface of the gold film changes and this is seen as an increase in signal intensity [18].

In the initial phase, all immobilised receptor molecules have not been exposed to analyte molecules and the response corresponds to the starting critical angle. Analyte molecules are injected into the flow cell; if they bind to the immobilised receptor molecules, there is an association phase during which binding sites become occupied and the shape of this curve can be used to measure the rate of association (K_{on}). When a steady-state is achieved (all binding sites occupied in this example) the RU corresponds to the changed final critical angle b. This maximum RU relates to the concentrations of immobilised receptor and analyte molecules and so it can be used to measure the binding affinity (K_d). When analyte molecules are removed from the continuous flow there is a dissociation phase during which binding sites become unoccupied and the shape of this curve can be used to measure the rate of dissociation (K_{off}). The surface can then be regenerated and returned to the critical angle to start the experiment again [18,23-26].

3.4.1 Surface Plasmon Resonance Imaging (SPRI) experiments for [miRNA-21-3p]

Gold chips for SPRI were purchased from Xantec Bioanalytics (Germany). The biochips were washed with ethanol and dried under a nitrogen stream. An SPR Imaging apparatus (GWC Technologies, USA) equipped with a white light source and an SF-10 prism coupled with a polydimethylsiloxane microfluidic device was used for the experiments as elsewhere described [7]. SPR image data were converted into percentage of reflectivity (%R) using the equation %R = 85 (Ip/Is) where Ip and Is refer to the intensity of the reflected p- and s-polarized light, respectively. Kinetic data was obtained by plotting the difference in %R (Δ%R) from selected regions of interest of SPR images as a function of time. PDMS microfluidic device with six parallel microchannels (80 μm depth, 1.4 cm length, 400 μm width) was used to achieve independent control of parallel interactions occurring on the gold chip surface.

The probe was immobilized on the gold surface by introducing solution (0.2 μM in PBS, flow rate 10 μL min^{-1} for 30 minutes) in the microfluidic device in contact with the SPRI gold surface. After the probe immobilization and equilibration with PBS, the modified surface was passivated with 2-mercaptoethanol (1 mM in PBS) for 15 minutes. miRNA-21 target and miRNA-141 (CTR, control scrambled sequence) solutions (100 pM in PBS + $MgCl_2$ 10 mM) were injected (10 μL min-1) into parallel channels of the microfluidic device for 30 minutes. The discrimination between target and control sequences was assessed by comparing SPRI signals produced by PBS running buffer before and after target and CTR adsorption.

3.4.2 Surface Plasmon Resonance (SPR) experiments for α-synuclein

For the characterisation of the bio-functionalised Au surface for α-synuclein, it was used a SPR platform (*Sensia ß-SPR*), that employs the Kretschmann configuration and incorporates two flow cells (300 nL each) for an independent analysis. The sample is a 1 cm^2 gold chip (2 nm Cr, 50 nm Au), whereas the whole setup works in a semi-automated way. The flow rate was set at 25 μL/min. The sensor surface was excited with a 670 nm light source. Gold chips were cleaned according to the following protocol: sonication in acetone, EtOH, and bidistilled water for 1 min respectively. The final step consisted of exposing the surface to the UV Ozone cleaner for 30 min.

3.5 UV Spectroscopy

The most common and easy method for analysing the protein characteristics and concentration in solution is UV spectroscopy. Proteins absorb UV-light due to their aromatic amino acid content and the absorption is related to total concentration. This makes the analysis easy for measuring the protein concentration using a pre-defined extinction coefficient. For the UV absorbance, two amino acids are primarily responsible: tryptophan and tyrosine. They exhibit a molar absorption coefficient at a wavelength of 280nm, but the peak absorbance of the protein itself is largely determined by the concentration [12].

The UV spectroscopy is a sensitive and non-destructive technique, and it requires only small amounts of sample for the analysis. This technique measures the interaction of molecules with electromagnetic radiation. The energy of the light is used to promote electrons from the ground state to an excited state. A spectrum is obtained when the absorption of light is measured as a function of the wavelength [12].

The concentrations of proteins in solution can be easily calculated by absorbance measurements with the Lambert- Beer Law. The absorbance (A) is related to the intensity of the light before (I_0) and after (I) passage through the protein solution. The absorbance depends linearly on concentration, which can be seen in the Equation 3.8.

$$A = -\log_{10}(I/I_0) \qquad (3.7)$$

$$A_{280} = c\, l\, \varepsilon \qquad (3.8)$$

c is the molar concentration, *l* is the path length of cuvette in cm, and ε in M^{-1} cm^{-1} is the molar absorption coefficient. The concentration of the protein in the solution can be calculated directly from its absorbance.

The chosen UV spectroscopy was Agilent Varian Cary 50 Scan UV Visible Spectrophotometer. The instrument has dual beam, Czerny-Turner monochromator, 190–1100 nm wavelength range, approximately 1.5 nm fixed spectral bandwidth, full spectrum Xe pulse lamp single source with exceptionally long life, dual Si diode detectors, quartz over coated optics, scan rates up to 24000 nm/min and 80 data points per s maximum measurement rate [13].

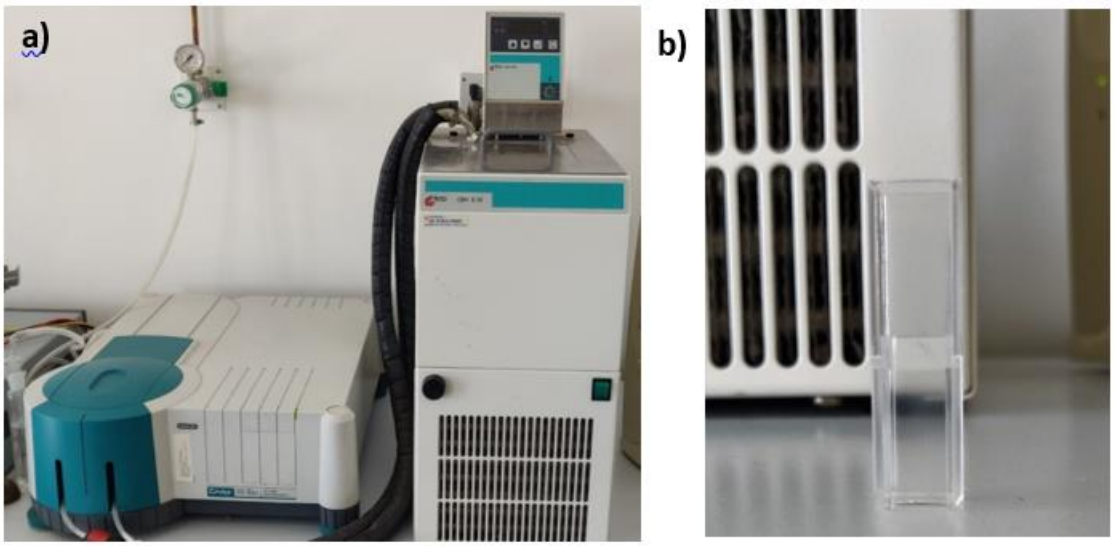

Figure 3.10: a) UV Spectroscopy set up b) The used cuvette with the optical length of 1 cm.

3.5.1 UV Spectroscopy for the evaluation of the microfluidic mixer performance

To assess the designed microfluidic mixer performance, the protein Bolvine Serum Albumin (BSA) was used. Different concentrations of BSA were prepared for the measurements with the microfluidic mixers. BSA solution was used in place of the biological sample and PBS as the buffer. The design and simulations of the mixers could be found in Chapters 4. During the experiments, the solutions were collected from the outlets after the mixing occurred. The collected samples were then analysed with the UV spectroscopy. The spectra for the analysis were chosen between 250 nm- 400 nm, since BSA has an absorption peak at 280 nm. BSA has a weight 66 kDa and the molar extinction coefficient ε_{280} =43824 M^{-1} cm^{-1} [12] since it has two tryptophans, Trp-134 at surface and Trp-213 in hydrophobic fold [14]. Before any analysis of the collected samples, reference measurements were done with the PBS solution (pH 7.2, 0.1 M concentration) and with the water to have a correct baseline for the spectra.

3.6 References

[1] Selvaraj M. Organic Electronic Transistors and Microfluidics for Cancer Biomarker Sensing [Ph.D dissertation] University of Catania, 2021.

[2] Parkula V. Organic Electronic Transistors for Biosensing [Ph.D dissertation] Università degli Studi di Modena e Reggio Emilia: Modena 2019.

[3] Kissinger PT, Heineman WR. Cyclic voltammetry. J Chem Educ American Chemical Society 1983; 60(9):702.

[4] Gomaa EA, Negm A, Abu-Qarn RM. Cyclic voltammetry study of the electrochemical behavior of vanadyl sulfate in absence and presence of antibiotic. Measurement 2018; 125:645–50.

[5] Elgrishi, N. et al. A Practical Beginner's Guide to Cyclic Voltammetry. J. Chem. Educ. 95, 2018; 197–206.

[6] Bard AJ, Faulkner. LR. Electrochemical Methods: Fundamentals and Applications, America 2002.

[7] Grasso G, D'Agata R, Zanoli L, et al. Microfluidic networks for surface plasmon resonance imaging real-time kinetics experiments. Microchemical Journal 2009; 93(1):82–86.

[8] Rusling, J. F. & Suib, S. L. Characterizing Materials with Cyclic Voltammetry. Adv. Mater. 6**,** 1994; 922–930.

[9] Macdonald DD. Reflections on the history of electrochemical impedance spectroscopy. Electrochimica Acta 2006; 51(8):1376–88.

[10]Addy SA. Electrochemical arsenic remediation for rural Bangladesh. Lawrence Berkeley National Lab. (LBNL), Berkeley, CA (United States) 2008.

[11] Grossi M, Riccò B. Electrical impedance spectroscopy (EIS) for biological analysis and food characterization: a review. Journal of Sensors and Sensor Systems Copernicus GmbH 2017; 6(2):303–25

[12] Schmid Franz-Xaver, Biological Macromolecules: UV-visible Spectrophotometry, 2001; Encyclopedia of Life Sciences, eLS. - London, UK.

[13] www.agilent.com/cs/library/specifications/Public/si-0821.pdf

[14]Wang Pei-Yun et al.,Differentiating the protein dynamics using fluorescence evolution of tryptophan residue(s): A comparative study of bovine and human serum albumins upon temperature jump, Chemical Physics Letter 2021; Vol. 781, 138998.

[15] Silin V, Plant A. Biotechnological applications of surface plasmon resonance. Trends in Biotechnology 1997; 15(9):353–59.

[16]Gopinath SCB. Biosensing applications of surface plasmon resonance-based Biacore technology. Sensors and Actuators B: Chemical 2010; 150(2):722–33.

[17] Altintas Z, Uludag Y, Gurbuz Y, et al. Development of surface chemistry for surface plasmon resonance based sensors for the detection of proteins and DNA molecules Elsevier Science B.V., Amsterdam. 2012.

[18] Patching SG. Surface plasmon resonance spectroscopy for characterisation of membrane protein–ligand interactions and its potential for drug discovery. Biochimica et BiophysicanActa (BBA) - Biomembranes 2014; 1838(1, Part A):43–55.

[19] Vinogradov AP, Dorofeenko AV, Pukhov AA, et al. Exciting surface plasmon polaritons in the Kretschmann configuration by a light beam. Phys Rev B American Physical Society 2018; 97(23):235407.

[20] Homola J, Yee SS, Gauglitz G. Surface plasmon resonance sensors: review. Sensors and Actuators B: Chemical 1999; 54(1):3–15.

[21] Schasfoort RBM. Chapter 2: History and Physics of Surface Plasmon Resonance. In: Handbook of Surface Plasmon Resonance 2017; pp. 27–59.

[22] Zeng S, Baillargeat D, Ho H-P, et al. Nanomaterials enhanced surface plasmon resonance for biological and chemical sensing applications. Chem Soc Rev The Royal Society of Chemistry 2014; 43(10):3426–52.

[23]M.A. Cooper, Advances in membrane receptor screening and analysis, J. Mol. Recognit. 17, 2004 ; 286–315.

[24]M. Besenicar, P. Macek, J.H. Lakey, G. Anderluh, Surface plasmon resonance in protein–membrane interactions, Chem. Phys. Lipids 141,2006 ; 169–178.

[25] H.N. Daghestani, Theory and applications of surface plasmon resonance, resonant mirror, resonant waveguide grating, and dual polarization interferometry biosensors, Sensors (Basel) 10, 2010; 9630–9646.

[26]H. Mozsolits, W.G. Thomas, M.I. Aguilar, Surface plasmon resonance spectroscopy in the study of membrane-mediated cell signalling, J. Pept. Sci. 9, 2003; 77–89.

[27] Itagaki M. Principle and Analytical Method of Impedance Spectroscopy. Hyomen Kagaku 2012; 33(2):64–68

CHAPTER 4

MIXING IN MICROFLUIDIC DEVICES: NUMERICAL SIMULATIONS AND VALIDATION WITH UV-VIS SPECTROSCOPY

4.1 Introduction

In this chapter, I will report the numerical simulations that were conducted with the software COMSOL Multiphysics for the fluid dynamics. To visualize the fluid behaviour inside of the microfluidic devices or to optimize the designs, the simulations were required. First, I will introduce the numerical simulations and finite element method (FEM). Then, to study the concentration gradient obtained by diffusion inside of microfluidic mixer, the simulations with different flowrates were done. The result of manipulation of the diffusion gradient could be seen in Chapter 5. Additionally, the simulations were completed for the time evolution of the concentration of α-synuclein inside the sensing chamber of the microfluidic device for label-free immunodetection of α-synuclein with electrolyte-gated organic field-effect transistor (EGOFET). Lastly, for the study of H-mixer and the optimization of its design, the simulations were conducted for achieving serial dilution of the biological samples.

4.2 Finite Element Method

The mathematical equations are derived for a continuous domain. Then the equations are discretized and solved for a finite number of points of the domain. The discretization of the domain in finite elements produce a mesh [1]. For a given geometry, a mesh is created for solving the equations. There are different methods for the discretization. I will focus on the Finite Element Method (FEM). This method is based on a general discretization procedure of continuum problems [2]. It contains many small and interconnected elements and a close representation of the boundaries of complicated domains. The method gives a piece-wise approximation to the equations, which are complex partial differential equations, reducing to either linear or nonlinear simultaneous equations [1, 3].

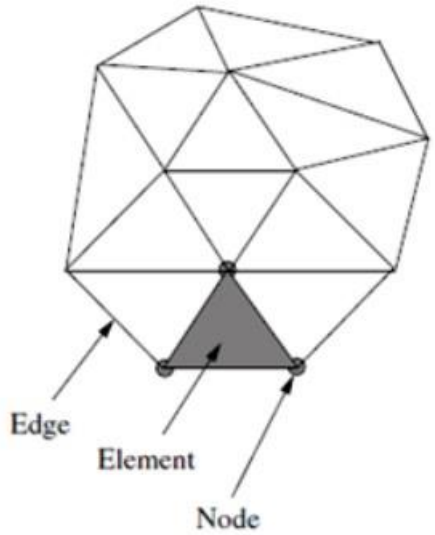

Figure 4.1: Finite element mesh with the schematic presentation of the edge, element and node [3].

Finite Element Method is solved in a continuum geometry problem, by dividing the solution region into non-overlapping elements or sub-regions. With this discretization, a variety of element shapes like triangles, quadrilaterals are created. Each element is formed by the connection of a certain number of nodes, which can be seen in Figure 4.1. Afterwards, the type of interpolation function is selected for the variation of the field variable over an element. Following, element equations are formed and numerically solved [1, 2, 3].

4.3 COMSOL Multiphysics

COMSOL Multiphysics is a computation software, which is finite element (FEM) and partial differential equation (PDE) solver for different physics and engineering applications. Multiphysics simulation, also shortens as multiphysics is referred to the simulations that involve multiple physical models or multiple simultaneous physical phenomena and the interactions among them [1]. In this PhD work, to understand and predict the fluids behaviour, Microfluidics Module from COMSOL is used. This module has a variety of physics interfaces for modeling and predicting the fluid behaviour inside of a microfluidic channel.

4.3.1 The COMSOL Laminar Flow Interface

The fluid flow in microfluidic devices is defined as laminar flow, so the Laminar Flow interface is used, which is found under the Single-Phase Flow branch. It used for computing the velocity and pressure fields for the flow of a single-phase fluid in the laminar flow regime [6]. The laminar flow occurs when the viscous forces are dominant over inertial and it is defined by the low Reynolds number, a ratio between inertial forces and viscous forces. In higher Reynolds numbers, inertial forces dominate and lead to the turbulence. In the Laminar Flow interface, the Navier-Stokes equations for the conservation of momentum and conservation of mass (Eq. 4.1) [6] are solved for the given geometry of the microfluidic device.

4.3.2 The COMSOL Transport of Diluted Species Interface

Another interface, which is mentioned a lot in this thesis, is the Transport of Diluted Species interface. It is used to compute the concentration field of a dilute solute in a solvent [6]. The transport of species depends on the diffusion and convection and implements the mass balance (Eq. 4.4) [1]. Diffusion is mathematically described with Fick`s Law (Eq. 4.2). The diffusion depends on the Diffusion coefficient, which determines how fast a molecule diffuses a certain distance. Large biomolecules such as proteins have Diffusion coefficients in the range 1x $10^{-9}\ \mathrm{m}^2/\mathrm{s}$ and 1 x$10^{-11}\ \mathrm{m}^2/\mathrm{s}$ [35].

4.4 Microfluidics simulation for manipulating the diffusion gradient inside of H-cell mixer

To study laminar flow and diffusion gradient within microfluidics, an H- shaped mixer is used. The design has the two inlets and two outlets and the total length of 58 mm. One inlet is for the buffer, which has low concentration 0 µmol /m^3. The other one is for the initial concentration (c_0) with concentration equal to 1 µmol /m^3. These streams flow into the upper and lower inlets with identical pressure potential, which leads to same velocity along channel. At the end of the simulation, these two species will mix completely and achieve the average of two species 0.5 µmol/m^3 at each outlet. This mixing is achieved with the flow rate 15 pl/s. With this low flow rate, the two fluids have more time to diffuse the one to other. However, in the lab environment this low flow rate like 15 pl/s is hard to implant and cause problem due to the pumps. The mixing mechanism of H-mixer depends only on diffusion, since it is laminar flow (Re <1) and there are no active elements to cause any turbulence. The fluid dynamics and the laws of convection and diffusion acting at the micrometric scale are described with the Navier –Stokes equation where Laplace pressure and time dependent surface wettability of polymer plays a predominant role with respect to the gravity dependant forces. For predicting the fluid dynamics inside of the mixer, COMSOL Multiphysics Software program are used for the simulations. The computational fluid dynamics (CFD) module is chosen for this purpose. The flows inside of the microfluidics are defined as laminar, miscible, viscous and incompressible fluids. As a result, laminar flow (spf) from single-phase flow interface and transport of diluted species (chds) from chemical species transport interface are selected as the multi-physics in the simulation. The chosen geometry is meshed with meshing systems, calibrated for fluid dynamics. For the best simulation results, the fine mesh is chosen, which consists of 129536 domain elements and 18282 boundary elements and can be seen in Figure 4.2.

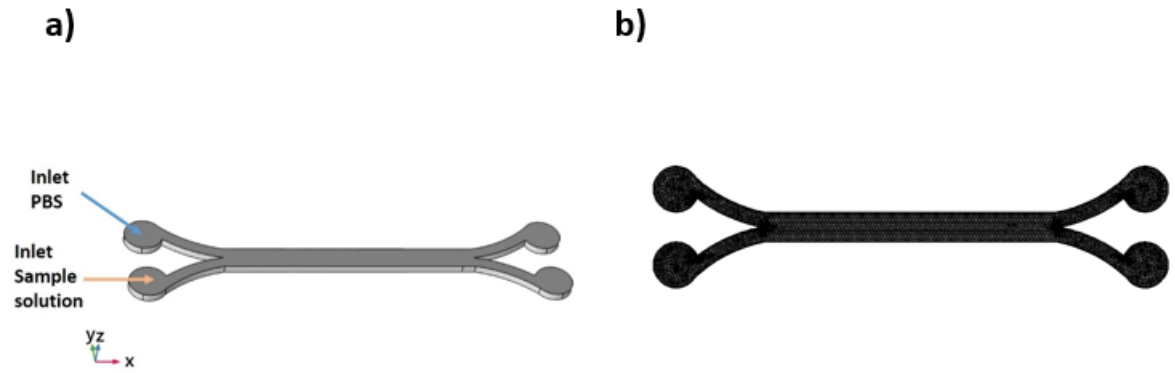

Figure 4.2: a) H-mixer geometry and solutions b) The fine mesh for the H-mixer design.

The simulation solves Navier–Stokes equation and convection-diffusion equation for the given geometry. In the Navier –Stokes equation (Eq. 4.1), the parameters are V, which is the fluid velocity, ρ is fluid density, p is the pressure, μ is the viscosity of the fluid and F is the body forces per unit volume. The environmental parameters such as temperature and the pressure are kept constant (Table 1). The fluid viscosity for water at 293.15 [K] is used for the simulation, since it is convenient for real life sample. The diffusion coefficient is chosen in the range of 1x 10^{-9} m^2/s and 1 x10^{-11} m^2/s, since the most of the biological molecules have the diffusion coefficient in this range [35]. Another important consideration is that there is no slip along the walls, meaning no velocity relative to boundaries such as walls.

Name	Description	Expression
Flow rate	Q	2 μl/min to 20 μl/min
Fluid viscosity	μ	1 mPa.s
Temperature	T	293.15 [K] (20˚C)
Initial concentration	c_0	1 μmol/m^3
Diffusion coefficient	D	1E-9 to 1 E-11 m^2/s
Pressure	p	1 [atm] Pa

Table 1: The parameters in COMSOL simulations

$$\rho\frac{\partial V}{\partial t} + \rho(V.\nabla)V = -\nabla p + \mu\nabla^2 V + F \qquad (4.1)$$

As previously mentioned, the flow is laminar in the microfluidics. In laminar flow, when the two flow streams come together, they flow parallel and do not mix due to the lack of turbulence [8]. The only mixing occurs by cause of diffusion of molecules across the interface between the fluids. Diffusion is a random process of the mass transfer of molecules, which is the evolution of their concentrations in space and time [9]. Diffusion drives a net flux of particles from high to low concentration and it stops as equilibrium is reached, which leads to the homogenous solution. This process is described in mathematical way also known as the Fick's first law (Eq. 4.2).

$$j_{diff} = -D \cdot \nabla c \qquad (4.2)$$

The flux due to diffusion depends on the gradient of concentration ∇c and the diffusion constant D in $[m^2 s^{-1}]$. During diffusion, the sum of diffuse particles should be equal to change in particle concentration, due to the conservation of the mass. As a result, the Fick's second law is derived from the first law.

$$\frac{\partial c}{\partial t} = -D\nabla^2 c \qquad (4.3)$$

In the microfluidics, addition to diffusion, the convection also contribute to the flux due to bulk fluid motion [9]. In the presence of diffusion and convection together, the change of concentration in control volume is described in the equation 4.4:

$$\frac{\partial c}{\partial t} + \boldsymbol{u} \cdot \nabla c = \nabla \cdot (D \nabla c) \qquad (4.4)$$

The convection diffusion equation is applied for the finite element simulation of the mixer, where the value of the diffusion coefficient $D = 6 \times 10^{-10}\ \mathrm{m^2/s}$ is set, as the diffusion coefficient of alkanethiols solutions in water [7]. According to the simulations, the concentration at the outlets should be approximately equal to half of the concentration at the inlet with the right flow rate. With higher flow rate, it is seen that the laminarity feature of the streamflow increase and reduce the diffusion gradient, in the end reducing the mixing ratio at the outlet of the microfluidic cell. With the lower flow rate, a concentration gradient forms along the diffusion interface of the channel, since the contact time of the flows is increased [8]. The comparison of the of the concentration profiles with the two flow rates 2 µl/min and 20 µl/min could be seen in the Figure 4.3. Since forming the diffusion gradient depends on the flow rate, one can manipulate this and change the

concentration profile along the microfluidic path. The application of this feature could be seen in Chapter 5.

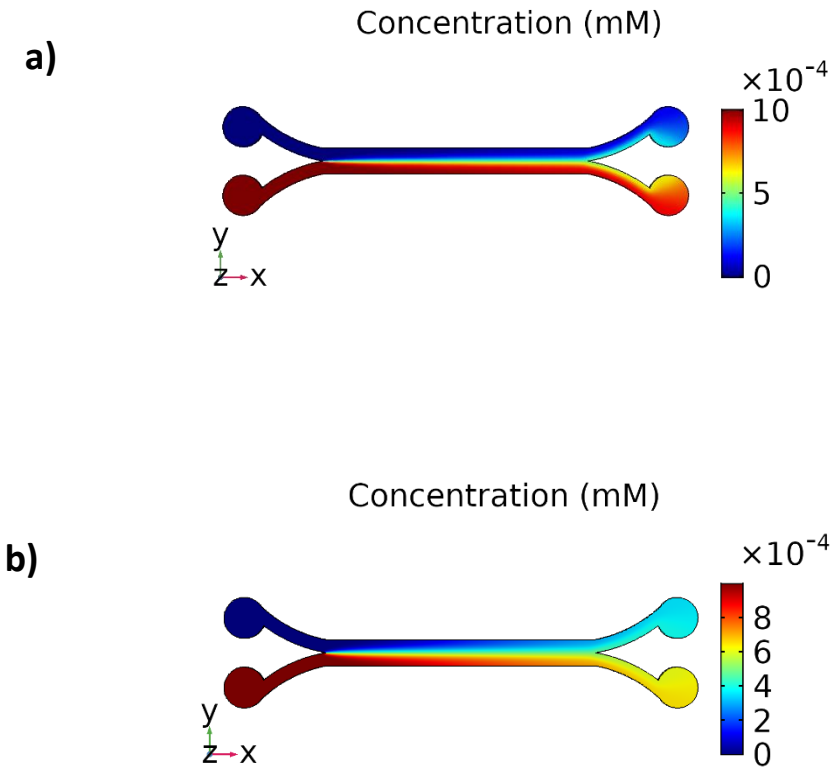

Figure 4.3: Comparison of the concentration profiles from the COMSOL simulations a) with the flowrate 20 µl/min b) 2 µl/min.

4.5 Study and the optimization of the geometry of H-mixer for serial dilution

Microfluidic mixers have been gaining lots of interest, since which they are used for creating necessary concentration gradients for the biological and chemical processes [12, 13, 14]. The usual methods for diluting the samples are the manual serial dilutions. However, these methods are time consuming and require skilled researchers and large equipment like Autosampler. Therefore, they are not suitable for Point of Care (POC) devices.

In the microfluidics, as previously mentioned, the flow is laminar and the mixing mechanism depends on the diffusion due to lack of turbulence. With this, there are two important fluid dynamics components occurring inside of a microfluidic mixer at the same time. The diffusion tends to generate concentration gradients, whereas the convection moves fluid volumes in a flow direction. This means, that the convection cannot lead to mass transfer between fluid streams, since it is tangent to a flow direction [8, 9]. On the counter part, the mixing based on the diffusion is very slow process. Special geometrical designs have been developed or external energy supplies have been used for increasing mixing efficiency. They are labelled as the passive and active mixers.

Active mixers use external energy sources to obtain mixing, whereas passive mixers do not have any external forces, but using only fluid dynamics in specific geometry of the channels [15]. The active mixers use external energy sources such as electric field [16], acoustic [17, 18], magnetic field [19] and mechanical actuators [20]. They achieve high mixing efficiency, yet they are harder to fabricate and difficult to integrate with other components [21]. Most importantly, they require external power sources [22].

Passive mixers are easier to fabricate and integrate with other components compared to the active mixers. Additionally, they do not harm any biological samples, since they do not induce any electrical, mechanical or thermal damage agitation [23]. The contact area between the different flows are increased by either changing geometry of channels or adding geometrical features such as groove systems [24,25], obstacles [26], barriers [27] to induce transversal advection [23] or using low flow rates.

The use of serpentine channels can be given as an example for changing the geometry of channels [21, 28]. Through curved channels, the fluids experience additional centrifugal force. Due to this additional force, a radial pressure gradient is formed and generated a transverse flow, which leads to an increased the contact area [23]. As a result, the mixing efficiency increases. As for adding geometrical features, the herringbone design is one of the best-known design to speed up the diffusion process [25].

In this design, the asymmetric grooves on the floor of the microchannel are used for generating a transverse component to the flow. Due to this transverse component, the different flows are stretched and folded into one, which leads to extend contact surface [23]. There are examples of the passive mixers from the literature for different application areas [29-31].

My goal in microfluidic design was to fabricate of microfluidic device, which achieves serial dilution of the biological samples. Additionally, this device should be easy to integrate with biosensor based on organic electronics, so there should be second outlet in the design for simultaneously measuring.

4.5.1 The design of the H-shaped mixer

As seen in the previous chapter, the H-mixer is achieving complete mixing at flow rate difficult to control. µm. Therefore, the flow rate has to be increased. With higher flow rate like 150 nl/s, the previous mixing rate, which is fifty percent at each outlet, is not achieved. In order to compensate the low flow rate, the longer channel or the geometry optimization is needed to increase interface area between fluids.

Adding geometrical features to the microfluidic channels are very well known method. The half-rectangular shape has been chosen for the obstacle shape, since it leads to the best mixing performance due to the two sharp corners [32, 33]. These obstacles mimic the chaotic behaviour inside of the channel and increase the interface area between fluids. During the optimization of the design, the comparison of the mixing performance between straight channels and channels with obstacles is investigated. The optimization of the design is ended up with the length of 25 mm with multiple obstacles on the sides of the wall for higher flow rates such 150 nl/s or higher for the biological molecules with the diffusion coefficient in the range of 1x 10^{-9} m^2/s o 1 x10^{-11} m^2/s. The channel width is around 600 µm and it decreases to 300 µm with the rectangular obstacles. The obstacles are located all along the microfluidic path and the details could be seen in Figure 4.4.

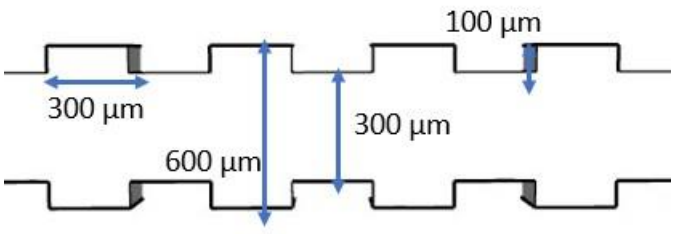

Figure 4.4: Details of the obstacles on the walls of the microfluidic mixer.

4.5.2 The COMSOL simulations and results

For COMSOL simulations, the computational fluid dynamics (CFD) module is used. The laminar flow (spf) from single-phase flow interface and transport of diluted species (chds) from chemical species transport interface are once again selected. The optimized geometry is meshed with meshing systems for fine mesh, which is calibrated for fluid dynamics.The Navier- Stokes and convection-diffusion are solved, whereas the environment parameters are kept constant. Table 1 shows all the parameters for the simulation. With the new optimized design, the mixing is achieved with the high flow rate. The initial concentration mixes the buffer and the both outlets, the final concentration is the half of the initial concentration. The result of the concentration profile from the simulation could be seen Figure 4.6. When the velocity field is studied from Figure 4.7, it is seen higher velocity between obstacles in microfluidic path. Due to the obstacles, the cross section area is decreased, which amplifies the velocity of the species. These obstacles cause chaotic behaviour in which, fluids stretches and folds into one another. This makes the interface area larger, which enhances the diffusion process and hence the mixing.

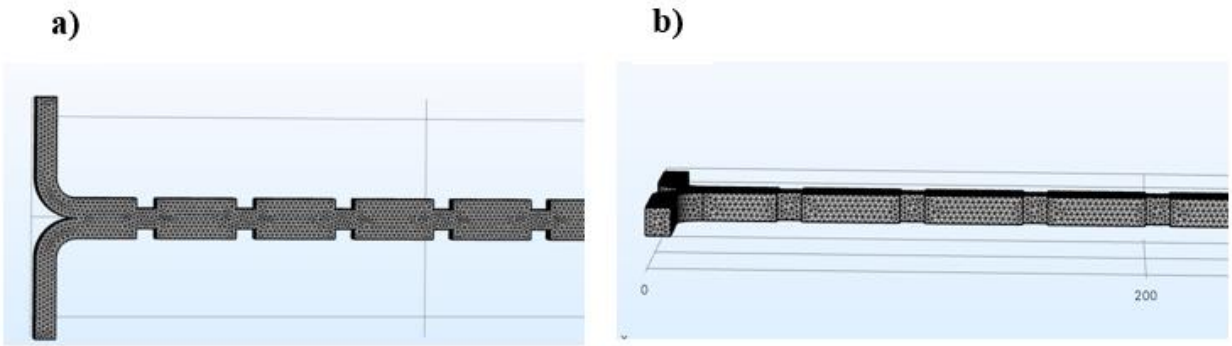

Figure 4.5: Close up illustrations of the fine mesh geometry of the design: a) from top and b) from side.

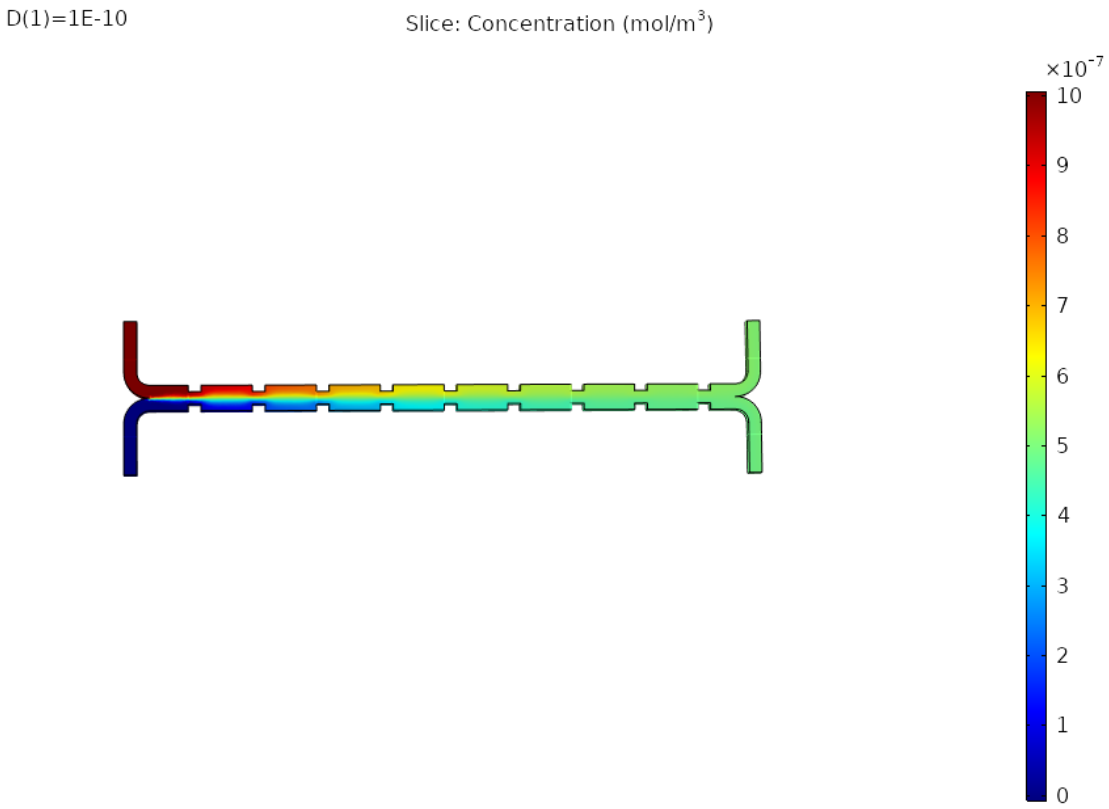

Figure 4.6: The concentration result at the two outlets, achieving the half of the initial concentration of the mother solution for the diffusion coefficient D =1 x10^{-10} m^2/s.

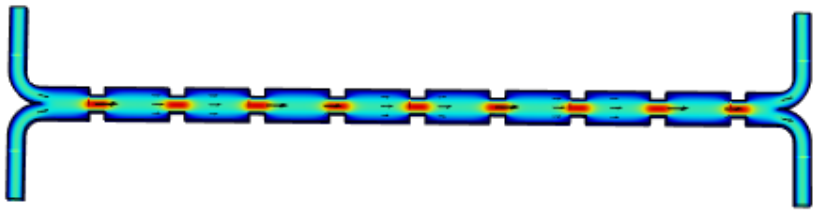

Figure 4.7: The velocity field of the fluids flow inside of the microfluidic mixer. Velocity magnitude is in mm/s.

4.6 Validation of the simulation results

To validate the simulation results, I conducted the experiments with the microfluidic mixer. The protein Bolvine Serum Albumin (BSA) was chosen, since it is the most abundant protein in blood plasma [34]. Moreover, the diffusion coefficient in aqueous solution at the room temperature is in the range of the simulations. The different concentrations of BSA were prepared for the measurements, whereas PBS was used as the buffer. During the experiments, the flow rate is fixed at 2 µl/min and the solutions were collected from the both outlets after the mixing occurred. The collected samples were then analysed with the UV spectroscopy. More information could be found in Chapter 3.

From the analysis with the UV spectroscopy, it is confirmed that the mixing ratio at the outlets of the microfluidic mixer is the half of the initial concentration, as the simulation implied. Additionally, the mixing ratio is the same for both outlets. Figure 4.8a shows that the absorption peaks of the collected samples are matching. With the Lambert Beer law and the absorption peak values, the corresponding protein concentration of the samples were calculated (Figure 4.8b). For the reproducibility of the mixer performance, the experiments were repeated with the different initial concentrations, using different prototypes of the microfluidic mixer. UV Spectroscopy confirms that the microfluidic mixer achieves the same mixing ratio as the previous example, about half of the initial concentration.

Additionally, the volume dependency was investigated to see if it affects the mixing performance. From the absorbance spectra in Figure 4.10 a, it was clear the mixing performance is independent of the volume of the initial inlet solutions. The corresponding protein concentrations were calculated according to the absorption peaks in the UV spectroscopy. The relative error percentage for the mixing ratio were also calculated with the concentrations from the simulation results and real life measurements. It is seen from Table 1 that the simulation results were matched with the experimental results with error of 8.16 %.

To validate that the geometry optimization improve the diffusion, I did the same experiments with the mixer with the same channel length but without the obstacles. The measurements are done with the BSA and PBS with the same flow rate 2 µl/min as previous experiments. From the measurements, it is seen that without the obstacles, the mixer cannot achieve the half of the initial concentration at the outlets, since there are no more obstacles, causing chaotic behaviour for speeding up the diffusion. The straight channel length was not long enough to achieve complete mixing, which could be seen in Figure 4.11.

a)

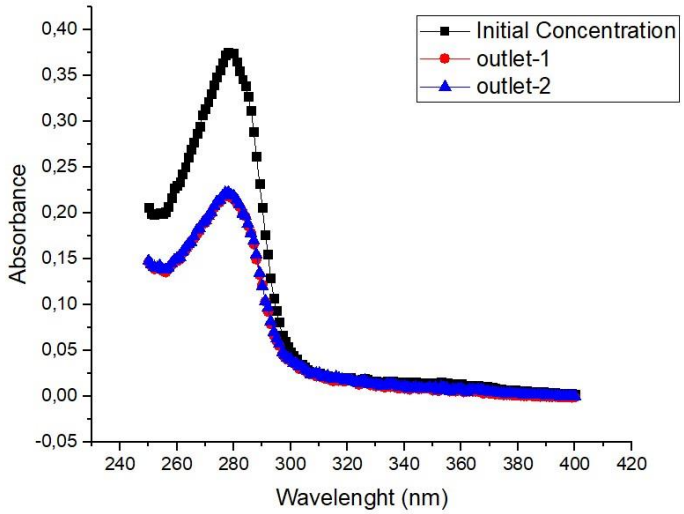

b)

Initial Concentration	Concentration at Outlets
8.5 µM	4.6 µM

Figure 4.8: a) The absorbance spectra for the BSA solutions that were collected from the outlets of the microfluidic mixer. The absorption peak of the BSA could be seen around 280 nm. b) Comparison of the initial concentration and the concentration at the outlets of the microfluidic mixer that calculated from the absorbance peaks in the absorption spectroscopy.

a)

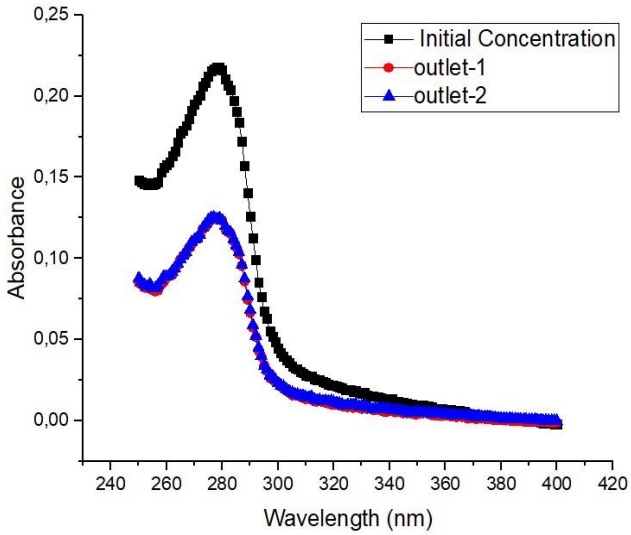

b)

Initial Concentration	Concentration at Outlets
5 µM	2.65 µM

Figure 4.9: a) For the reproducibility of the mixer performance, the BSA solutions were collected from the outlets and analysed with UV-Spectroscopy. b) Comparison of the initial concentration and the concentration at the outlets of the microfluidic mixer.

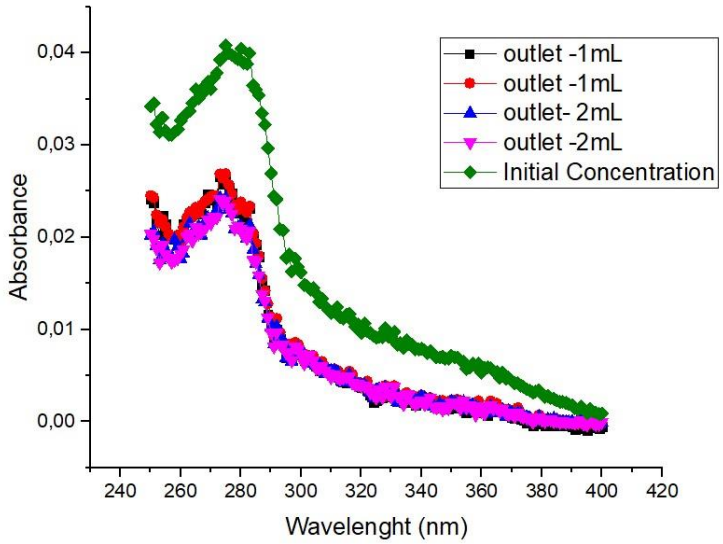

Figure 4.10: To assess the microfluidic mixer performance, the volume dependency of the mixing was investigated. From the absorbance spectra, it was clear the mixing performance is independent of the volume of the initial inlet solutions. The corresponded protein concentrations were calculated according to the absorption peaks.

Initial Concentration	Concentration at Outlets	Volume	Error (%)
0.9 µM	~0.49 µM	1mL	8.16 %
0.9 µM	~0.46 µM	2mL	2.17 %

Table 2: The comparison of the initial concentration and final concentration of the BSA solutions versus the volume of the solutions with the relative error percentage.

a) **b)**

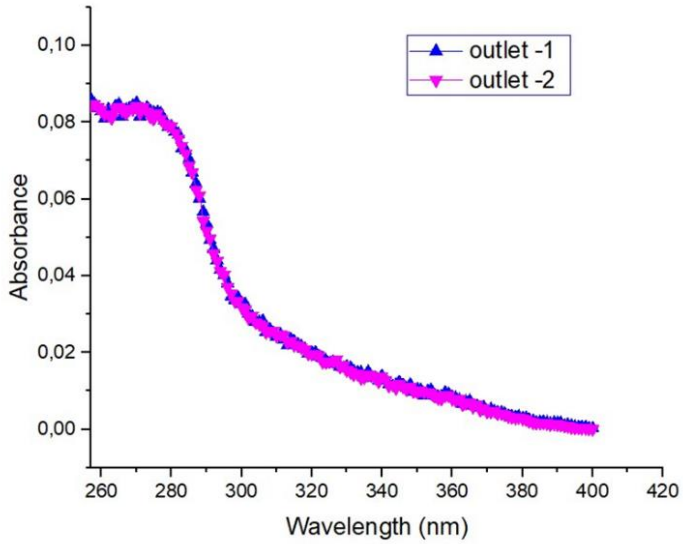

Initial Concentration	Concentration at Outlets
3 µM	~ 2 µM

Figure 4.11: a) The absorbance spectra for the BSA solutions that were collected from the outlets of the straight channel microfluidic mixer. b) Comparison of the initial concentration and the concentration at the outlets r that calculated from the absorbance peaks in the absorption spectroscopy.

4.6.1 Serial dilution

After achieving the intended the mixing ratio with the mixer with the obstacles, I designed the device for the serial dilution. For this purpose, the mixer`s second outlet is used, since both of the outlets have the same mixing ratio. The principle of the serial dilution could be seen in Figure 4.13. After completing the first round of the mixing, the sample from outlet 2 is put back again into the inlet 2, whereas inlet 1 is still used for the buffer. This cycling can go on as long as it is needed. At every round, the mother solution is replaced from the solution from outlet 2. I did multiple cycles with the same microfluidic mixer. In the Figure 4.14 a, the absorption spectra could be seen for the first, fourth and eighth cycle of the mixing. Since the mixer achieves the half of the initial concentration at the every round, the fourth cycle would be already one order of magnitude of dilution. From the spectra, the protein concentrations are calculated and could be seen in Table 2. The one order of magnitude is achieved after the fourth cycle as predicted. To be certain of the mixer performance, the areas under the absorption peaks are integrated. From the Figure 4.14 b, it can be seen that the integrated areas under the absorption peaks and the calculated concentrations are matching.

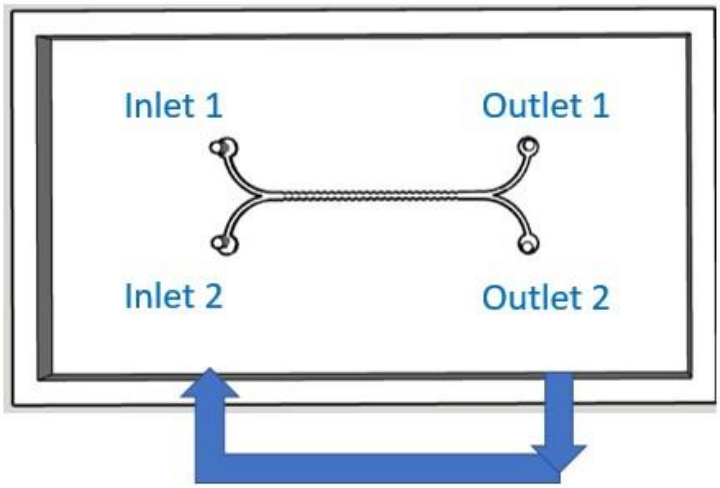

Figure 4.12: Serial dilution with one mixer. The outlet 2 is connected to the inlet 2 to create a loop. The samples could be diluted as long as it requires.

a)

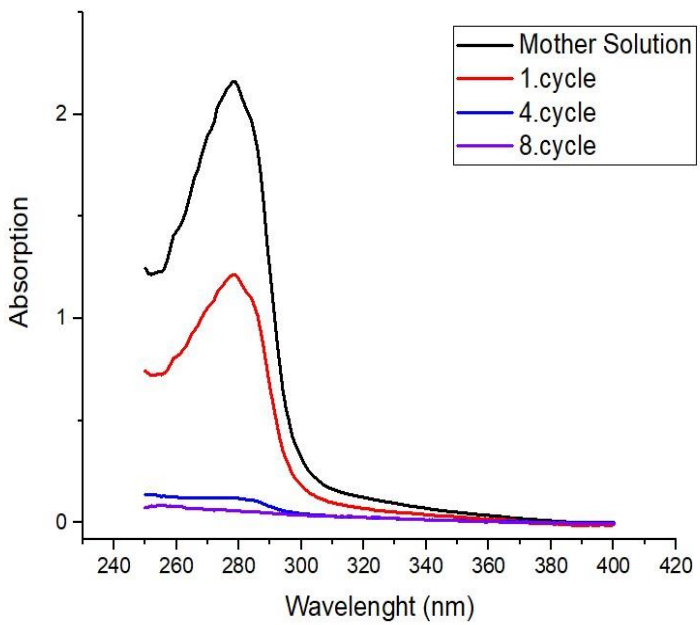

b)

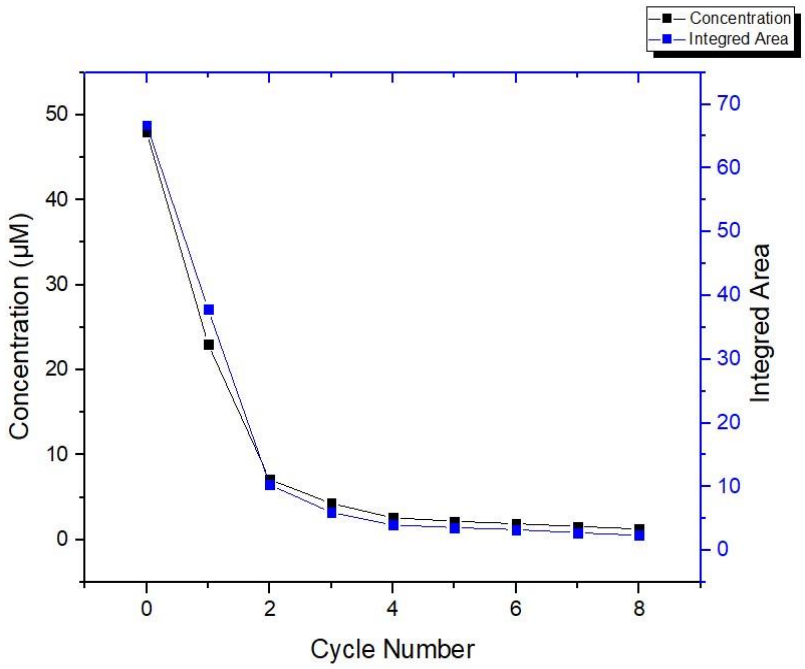

Figure 4.13: a) The absorbance spectra of the BSA solutions after the serial of dilution cycles. b) From the absorption peaks, the corresponded protein concentrations were calculated and compared with the integrated area under the absorption peaks.

Initial Concentration	Concentration after 1.Cycle	Concentration after 4.Cycle	Concentration after 8.Cycle
48 µM	24.4 µM	2,7 µM	1,2 µM

Table 3: The comparison of the final concentration at the outlets after the serial dilution with multiple cycles

Appendix to Chapter 4

Microfluidics simulation for label-free immunodetection of α-synuclein by using a microfluidics coplanar electrolyte-gated organic field-effect transistor

Time evolution of the concentration of *α*-synuclein inside the sensing chamber of the microfluidic device is calculated using commercial finite element solver Comsol Multiphysics ®. The simulation involved coupled time-dependent solution of Navier-Stokes (NS) and convection-diffusion equations for the interior geometry of the full microfluidic device, including both chambers and inlets and outlet sections [10]. The fluid velocity field and pressure were calculated according to the following form of Navier-Stokes, neglecting the inertial term.

$$\rho \partial \mathbf{u}/\partial t = +\rho \mathbf{u}\cdot\nabla\mathbf{u}+\nabla\cdot[-p2\mathbf{I}+ \mu(\nabla\mathbf{u}+\nabla\mathbf{u}^{T})] \qquad (4.5)$$

u is the velocity field of the fluid, ρ the fluid density (for PBS buffer assumed equal to 1), *p* the pressure, **I** the identity tensor and μ the fluid viscosity. We assumed a quadratic dependence of viscosity with respect to the analyte concentration, according to:

$$\mu = 0.001+0.0005c^2 \qquad (4.6)$$

We did not consider the disjoining pressure in Navier-Stokes equation, although it may a dominant effect in short distances close to the PDMS walls [11].

The α-synuclein concentration was determined according to convection diffusion equation (4.4).

The mesh for the computation was generated with tetrahedral assembly, with approximately $190\cdot10^3$ domain elements. The iterative and coupled solution of Equation 4.4, 4.5 and 4.6 returned the values for the velocity and pressure field inside the microfluidic chambers and time evolution for α-synuclein concentration, as depicted in Figure 4.14 a,b.c.

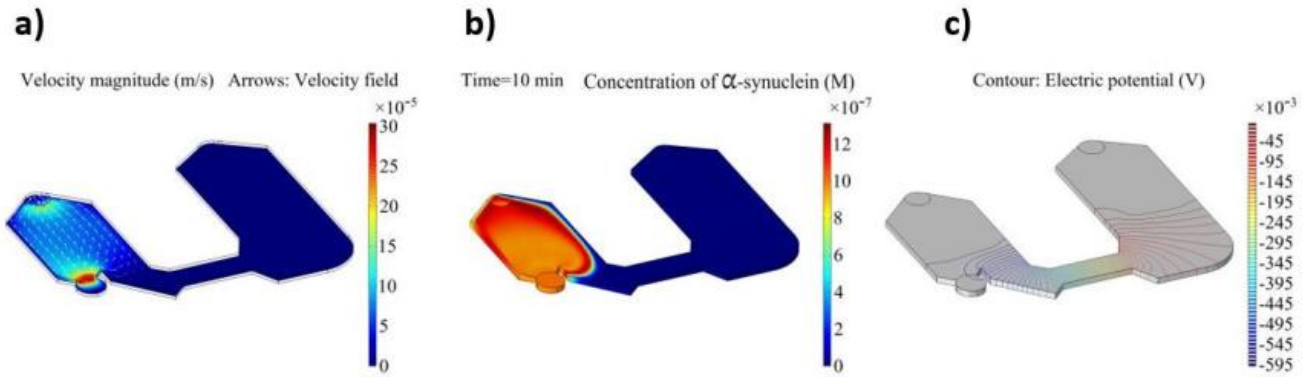

Figure 4.14: a) Velocity field inside the microfluidics during sample injection resulting from finite element simulation. b) Concentration of α-synuclein within "Chamber 2" after 10 min from the injection. c) Potential contour plot in electrolyte between sensing gate and interdigitated electrodes.

The volume defined for Navier-Stokes and convection-diffusion simulation was also employed to calculate the potential across the electrolyte solution, by finite element calculation of the combined system of equations:

$$\nabla \cdot (\varepsilon_0 \varepsilon_r \mathbf{E}) = \vartheta_V \qquad (4.8)$$

$$\mathbf{E} = -\nabla V \qquad (4.9)$$

where **E** is the electric field, V is the potential, ε_r is the relative permittivity of PBS buffer ($\varepsilon_r = 80$) and ϑ_V is the charge volume density where we imposed that no charge is moved across the boundary ($\mathbf{n} \cdot \mathbf{D} = 0$), except for the electrodes of gate and source where the potential was set to -0.6 and 0 V, respectively. The potential contour resulting from the simulation is reported in Figure 4.14 c.

4. 7 References

[1] Torino Stefania, Engineering of Microfluidic Devices for cell hydrodynamic manipulation [Ph.D dissertation] University of Naples "Federico II", 2015.

[2]Zienkiewicz O.C., Taylor R.L. The Finite Element Method, 5th Edition, Volume 2: Solid Mechanic, Butterworth-Heinemann 2000.

[3] Lewis R.W., Nithiarasu P., Seetharamu K.N. Fundamentals of the Finite Element Method, John Wiley &Sons 2004.

[4] Kleinstreuer C., Modern Fluid Dynamics: Basic Theory and Selected Applications in Macro- and Micro-Fluidics, Springer 2009.

[5] Zimmerman W. B. J., COMSOL Process modeling and simulation with finite element methods World Scientific Publishing Co. Pte. Ltd., 2004.

[6] COMSOL Multiphysics Documentation: The Microfluidics Module.

[7]Asiaei S., Nieva P.M., Studying the Kinetics of Thiols Self-Assembled Monolayer Formation in Microfluidic Channels. Particulate Science and Technology 2016; 34(4): 397–406.

[8] Squires T. M., Quake S. R. Microfluidics: fluid physics at the nanoliter scale. Rev. Mod. Phys., 77, 2005; 977–1026.

[9] Landau L.D., Lifshitz E.M., *Fluid Mechanics,vol.6, 2nd English ed.* Elsevier, 1987.

[10] Greco P., Facchini M., Cavallini M., Ruani G., Dionigi C., Biscarini F. Fabrication of Ordered Carbon Nanotube Structures by Unconventional Lithography. Phys. Status Solidi B 2010; 247 (4), 877–883.

[11]Transport Phenomena, Revised 2nd Edition | Wiley https://www.wiley.com/en-it/Transport+Phenomena%2C+Revised+2nd+Edition-p-9780470508633 (accessed Jun 5, 2020).

[12] Walker G. M., Monteiro-Riviere N., Rouse J., O'Neill A. T. A linear dilution microfluidic device for cytotoxicity assays, Lab Chip 2007; 7, 226–232.

[13] Zheng G., Lu L. Development of Microfluidic Dilution Network-Based System for Lab-on-a-Chip Microalgal Bioassays, Anal. Chem. 2018; 90, 13280−13289.

[14]Chen C. et al A microfluidic concentration generator for dose-response assays on ion channel pharmacology, Lab Chip 2012; 12, 794-801.

[15] Nguyen N.T., Wereley S. Fundamentals and Application of Microfluidics. Artech House 2002; ISBN 1-58053-343-4.

[16] Krishnaveni T., Renganathan T., Picardo J.R., Pushpavanam S., Numerical study of enhanced mixing in pressure-driven flows in microchannels using a spatially periodic electric field Phys. Rev.2017; 96, 033117.

[17] Ñama N., Huang P.-H., Huang T.J., Constanzo F. Investigation of micromixing by acoustically oscillated sharp-edges. Biomicrofluidics 2016; 10, 024124.

[18] Destgeer G., Im S., Ha B.H., Jung J.H., Ansari M.A., Sung H.J. Adjustable, rapidly switching microfluidic gradient generation using focused travelling surface acoustic wave, Appl. Phys. Lett. 2014; 104, 023506.

[19] Ryu K.S. et al. Micro magnetic stir-bar mixer integrated with parylene microfluidic channels Lab Chip 2004; 6, 608-613.

[20]Abbas Y., Miwa J., Zengerle R., von Stetten F. Active continuous-flow micromixer using an external braille pin actuator array Micromachines 2013; 4, 80-89.

[21] Joshua Clark Mixing Enhancement in Serpentine Micromixers with a Non-Rectangular Cross-Section Micromachines 2018; 9, 107.

[22] Cai G., Xue L.,Zhang H., Lin J. A review of micromixers Micromachines 2018; 8, 274.

[23]Fainman Y., Lee L., Psaltis D., Yang C., Optofluidics: Fundamentals, Devices, and Applications, McGraw Hill Professional, 2010.

[24] Stroock A.D., Whitesides G.M., Chaotic mixer for microchannels, Science 2002; 295, 647-651.

[25] Fodor P.S., Kaufman M. The evolution of mixing in the staggered herring bone micromixer Mod. Phys. Lett. B 2011; 25, 1111-1125.

[26] Alam A.,Afzal A., Kim K.-Y. Mixing performance of a planar micromixer with circular obstructions in a curved microchannel Chem. Eng. Res. Des, 2014; 92,423-434.

[27] Kim D.S., Lee S.W. A barrier embedded chaotic micromixer. J. Micromech. Microeng. 2004; 15, 798-805.

[28] Rhoades T., Kothapalli C.R., Fodor P.S. Mixing Optimization in Grooved Serpentine Microchannels. Micromachines. 2020; 11(1):61

[29] Jeon N. L., Whitesides G. M., Generation of solution and surface gradients using microfluidic systems. Langmuir, 16, 2000; 8311–8316.

[30]Chang J. K., Bang H., Fabrication of the PDMS microchip for serially diluting sample with buffer Microsystem Technologies 9, 2003; 555–558.

[31] Kim C., Lee K., Kim J. H., Shin K. S., Lee K.-J., Kim T. S., Kang J. Y. A serial dilution microfluidic device using a ladder network generating logarithmic or linear concentrations Lab Chip, 8, 2008; 473–479.

[32] Sarma P., Patowari P. K., Design and Analysis of Passive Y-Type Micromixers for Enhanced Mixing Performance for Biomedical and Microreactor Application Journal of Advanced Manufacturing Systems, Vol.15, 2016; 161-172.

[33] Rasouli M. R., Mehrizi A. Abouei, Lashkaripour A. Numerical Study on Low Reynolds Mixing of T-Shaped Micro-Mixers with Obstacles Trans. Phenom. Nano Micro Scales 3(2), 2015; 68-76.

[34] Monkos K. Temperature and concentration dependence of translational diffusion coefficient for human serum Albumin in aqueous solutions at different Ph Ann.Acad. Med.Siles. 2013; 67, 3,184-193.

[35] Bruus H., Theoretical Microfluidics, Oxford Master Series in Condensed Matter Physics, 2007.

CHAPTER 5

INTEGRATION OF MICROFLUIDIC DEVICES WITH ORGANIC ELECTRONIC DEVICES

5.1 Introduction

In this chapter, I will present different example of the integration of the microfluidics with EGOFET. First example is the integration of the microfluidic mixer with the multi-gate EGOFET. The microfluidic mixer allows to control the diffusion spread based on the flow rate of the incoming streams. The performance of the diffusion mixer has been tested by evaluating the concentration of albumin protein in the outlets. The capability of the multi gate EGOFET to detect the concentration profile along the microfluidic channel induced by diffusion has been demonstrated with thiol moieties forming organic layers or self-assembly monolayers on top of the sensing gate. Diffusivity dependent modulation of the gate work function is reflected on EGOFET transfer characteristics, threshold voltage and transconductance. Another example of the integration is a microfluidic device with EGOFET biosensor for the detection of α-synuclein, a model biomarker for Parkinson disease, neurodegenerative disease. The biosensor is coupled with a fluidic compartment for electrolyte and for sample solution, where diffusion is controlled with steps of the perfusion protocol. A further example is the integration of EGOFET with the four mixers for achieving one order of magnitude of dilution of the biological samples. Last examples for the integration are the EGOFET biosensor for the detection of 1L-1b and of IL-6 with the Extended Gate - OECT Biosensors.

5.2 Detection of diffusion gradients with multiple gates electrolyte gated organic transistors

I described in previous chapter microfluidics as the field of science and technology of systems that allow to effectively control small amounts of fluid (micro or nanolitres) by using channels and other micro electromechanical systems with dimensions of tens to hundreds of micrometres [1]. They have been used in various application areas like chemical and biological analysis, point of care devices, and drug development, even for the generation of biofunctional interfaces in molecular diagnostic devices [2, 3, 4, 5].

Integration of microfluidics with biosensors has been gathering lots of interest since they simplify the sample transport, reagent mixing or the immobilization of biorecognition molecules or the subsequent delivery of the targeted biomarkers to the transducer interface [6-10]. Electrolyte gated organic field-effect transistors (EGOFET) are one of the most suitable for biosensing, since they use the electrolyte media as dielectric and are able to detect ultra-low concentrations of biomarkers [11-14].

The sensing mechanism relies on the capacitive coupling between the gate and the transistor channel made with organic semiconductor. The potential of the gate electrode is sensitive to antigen binding at surface bound recognition sites, which is capacitively coupled to the channel. If the biorecognition happens in Electrochemical Double Layers (EDL) near the gate electrode surface, the devices are very sensitive even to low amount of adsorbed biomolecules. Integration of EGOFET with microfluidic devices makes multiple biomarkers detection possible by miniaturization and multiplexing gate electrodes [10, 15, 16].

For the biosensing with EGOFET, one must functionalize the gate electrode [17,18] or the organic semiconductor channel [19] with the biorecognition groups for the target. Several functionalization strategies on the gate electrode have been successfully demonstrated like grafting of antibodies or aptamers either by the Protein G or by self-assembled monolayers (SAMs) [14,19,20]. SAMs are organic materials that form a thin, packed, and robust interface on the surface of noble metals such as gold, and are extensively studied in organic electronics [21,22]. SAMs are usually formed from the immersion of the transducer surfaces in the thiolic solutions for long periods.

SAMs in organic electronics are studied not only for the gate functionalization, but also for the functionalization on Source and Drain electrode since the S/D electrode and organic semiconductor interaction improves device contact resistance. A better alignment of SAMs and the organic semiconductor energy levels causes more efficient charge injection [21,23]. Investigating the formation of SAMs has been quite important to improve the functionalization protocols and device performance.

The formation of SAMs on the gold gate depends not only on the chemical structure of the molecules but also on how they come contact in with the transducer surface. Microfluidics help to deliver the thiol molecules to the transducer surfaces, so the kinetics of the formation and the overall duration of incubation improve [5].

Here, I present the integration of EGOFET with a microfluidic mixer for an electroanalytical application for monitoring self-assembly monolayers (SAM) formation on top of gold gates. The possibility to control the self-assembled monolayer formation is achieved by means of the diffusion interface within the streams of buffer and thiol-containing buffer. For this purpose, we linked the microfluidic mixer with EGOFET by means of an electrolyte bridge. The SAMs form on the gates subject to concentration gradient determined by diffusion inside the microfluidic channel. Considering the geometry of the experimental microfluidic device and the solute diffusivities, the concentration gradient is more spread across the microfluidic channel with flowrates below 2 µl/min. For this reason, the SAM formation is repeated also at flow rates in a slightly extended range. The capability of the multi-gate EGOFET to detect the diffusion profile along the microfluidic channel is caused by changes of the work function of the metallic gate and is therefore reflected in modulation of the transfer characteristics of the EGOFET. As a result, the output current is decreasing in correlation with the axial position of the gate along the microfluidic channel.

5.2.1 Integration of gate electrodes within the microfluidic H-mixer

The alignment of the substrate with array of gate electrode and the adhesive microfluidics was controlled visually and performed by the operator manually. The main channel of the microfluidic h-mixer contained the extremity of the gate electrodes on the side of the buffer line (see Figure 4a). Therefore, the electrodes in contact with the electrolyte solution are just located in the initial buffer stream. This assembly allowto record the formation of Au-alkanethiol layers on the surface of the gate electrodes by means of EGOFET devices, so the gate electrodes are exposed just to a diffusion based concentration gradient generated by h-mixer. The top boundary of the microfluidics, made with PET foil (200 µm thickness), was aligned and bonded with the rest of the microfluidic with integrated electrodes. The closed system included two inlets and two outlets, according to the design of the h-mixer.

5.2.2 UV spectroscopy validating performance of H-mixer

COMSOL Multiphysics Software program is used for the simulations of the microfluidic mixer. The computational fluid dynamics (CFD) module is chosen and more details can be found in Chapter 4. To validate the simulation results of the manipulating the diffusion gradient with the different flowrates, an experiment was performed with the dye colours to visualize the flows (see Fig.5 2).

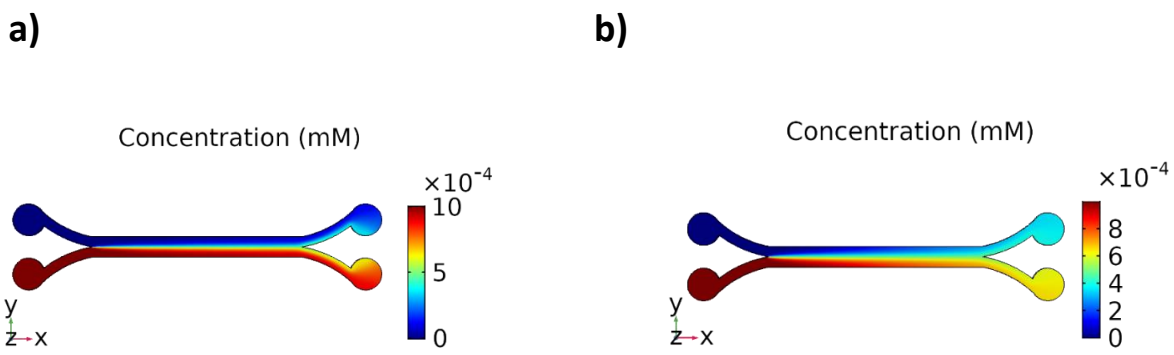

Figure 5.1: Simulation results and comparison of the concentration profiles from the COMSOL simulations a) with the flowrate 20 µl/min b) 2 µl/min.

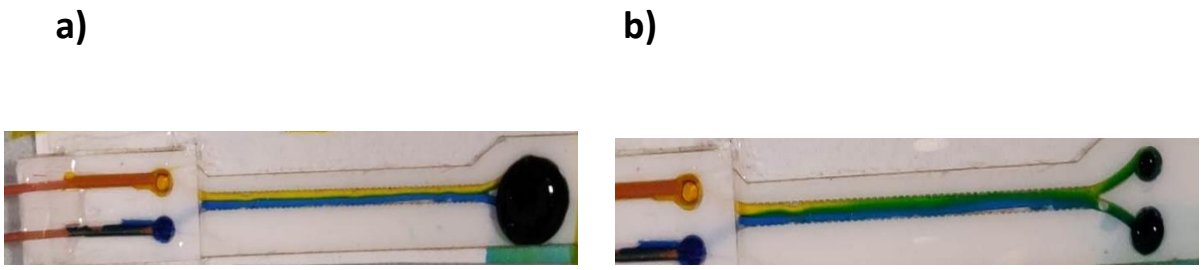

Figure 5.2: Testing the simulation results of the microfluidic mixer with colour dyes (yellow and blue) a) with the flowrate 20 µl/min b) 2 µl/min to visualize the laminar flow and the diffusion gradient.

The performance of the microfluidic mixer has been validated with UV -visible spectroscopy, quantifying the diffusion of protein (albumin), inside a stream of PBS buffer. The concentration at the two outlets is determined by the diffusion ratio and the geometry of the H-cell. The optical spectra measured for each outlet of the mixer can be seen in Chapter 4, where it is repeated for 4 consecutive cycles, in order to provide higher degree of dilution.

According to the simulation performed with Comsol Multiphysics, the outlet concentration at the end of each cycles should be approximately equal to half of the concentration at the inlet (see Chapter 4, Figure 4.14 a,b).

The absorption spectra confirm that the concentration at consecutive outlet sections are reduced by half. Higher flow rate will increase the laminarity feature of the streamflow and reduce the diffusion gradient, in the end reducing the mixing ratio at the outlet of the microfluidic cell. Besides optical methods used to describe the concentration profile in diffusion processes, we devised the possibility to use EGOFET since the gate electrode is very sensible to the change in work function happening due to adsorption of molecules.

5.2.3 Architecture of the EGOFET integrated with microfluidic H-mixer

In the common known architecture of EGOFET, the gate is immersed in the electrolyte on top of the channel for biosensing [13]. In the present architecture, the electrolyte acts as a dielectric and is contained by a PDMS based pool. The sensing electrode is provided by the gate inside the electrolyte. Since the device works as long as there is a liquid connection between the gate and the channel, the gate is put nearby the channel in the other microfluidic device. The connection between the channel and the outside placed gate is made through the electrolyte bridge by flexible silicon tubing (See Fig.4b). This tube has a diameter of 0.51 mm and provides a liquid connection between two microfluidics. These two microfluidics are the microfluidic pool and the microfluidic h-mixer. To test the dependency of the length of the tubing, the different lengths are tested. The current (I_{ds}) signal decreases, especially after 30 cm and shows the saturated behaviour afterwards.

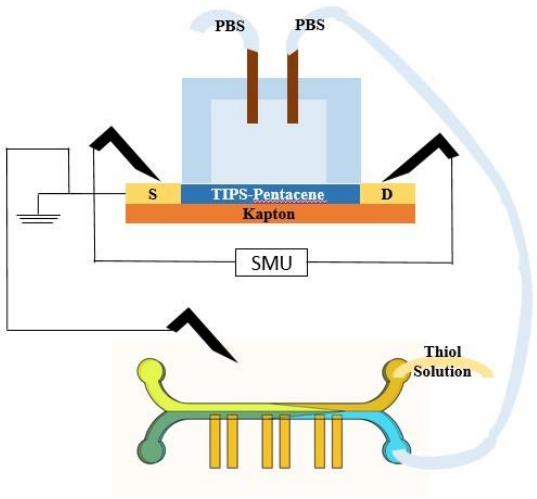

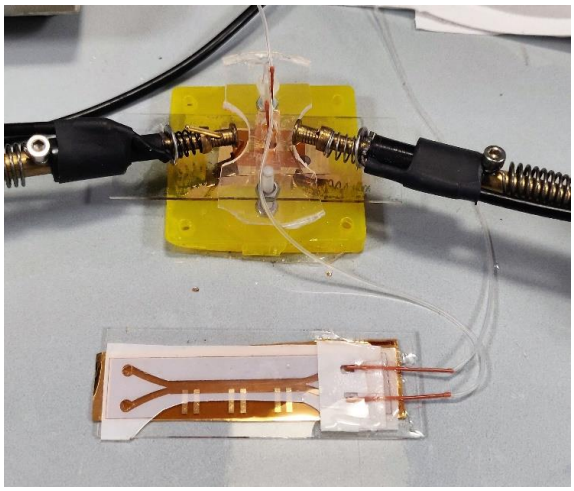

Figure 5.3: a) Schematic presentation of the architecture of EGOFET with two microfluidic devices through electrolyte bridge b) Picture of the EGOFET integrated with the microfluidic mixer.

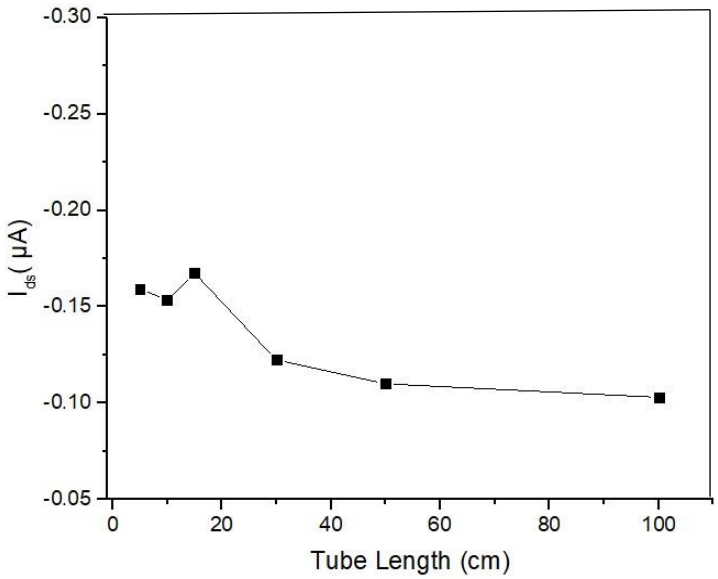

Figure 5.4: Dependency of the length of the tubing vs the current. The different lengths of tubing are tested. The current (Ids) signal decreases, especially after 30 cm and shows the saturated behaviour afterwards.

5.2.4 EGOFET Characterization

In the microfluidic h-mixer, the first two gates (G1 and G2) are near the inlet and last two gates (G5 and G6) are positioned near the outlet. Gate 3 and Gate 4 are in the middle. All six gates inside of the mixer were first measured with PBS for reference. Then thiol solutions were perfused with two different flow rates in consecutive experiments, (20 µl/min and 2 µl/min) through inlet 2 at initial concentration of 1 mg/ml, whereas PBS is injected as buffer for the inlet 1. Afterwards the device characteristics were recorded again. Transfer curves were obtained by measuring channel current I_{ds} upon sweeping Gate-Source voltages in the range from 0 V to -0.7 V with steps of -1 mV at a fixed Drain-Source voltage V_{DS}=-0.2 V. The device mostly is operated in the linear regime. The different transfer curves for the gates are shown in Figure 5.5 for 3-Mercapto-1-propanol depending the gate positions inside of microfluidics. The transfer curves were also recorded for 6-Mercapto-1-hexanol and 9-Mercapto-1-nonanol,which could be seen in Figure 5.6 and Figure 5.7. In particular, in Fig.5.5. the I_{ds} recorded when gate electrode 1 was the bias does not show a substantial change between the two experiments at different flow rates. This proves that the adsorption of diffusing molecules at that coordinate is not influenced by the flow rate, hinting to a reaction-limited kinetics.

By looking at Fig. 5.5, it is possible to appreciate that gate 3 is in different position with respect to the developing gradient of concentration inside the h-mixer. When operated at 20 µL/min, the streams present limited diffusion at the interface, therefore not changing the gate electrode work function and current (6 nA) by thiol adsorption. When operated at 2 µL/min, I_{ds} was significantly reduced by almost one order of magnitude (2 nA), valorising the hypothesis that the concentration gradient induced diffusion of 3-mercapto-1-propanol through the interface leading to organic layer formation. Gate 5 electrode transfer curve depicted in Fig. 5.5. is showing a similar effect. With the flow rate 20 µl/min, the laminar flow induces a thin diffusion zone all along the microfluidic channel, while with the flow rate 2 µl/min, diffusion gradient occurs largely inside of the microfluidic channel, at an axial position after Gate 1 coordinate.

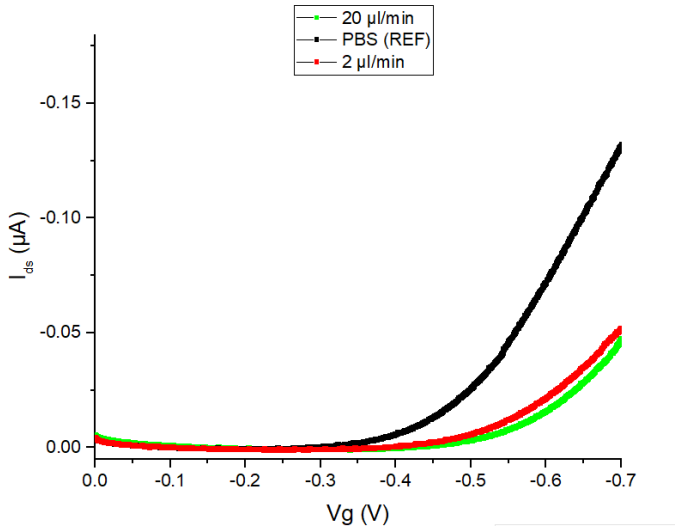

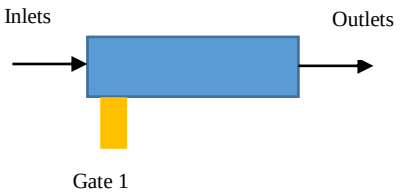

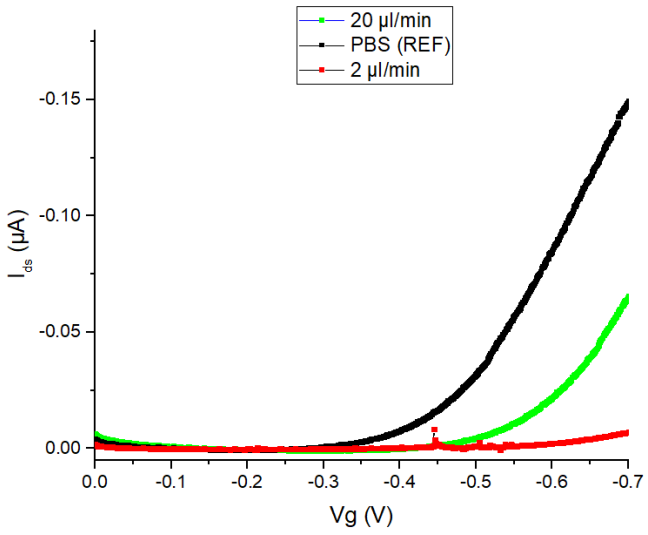

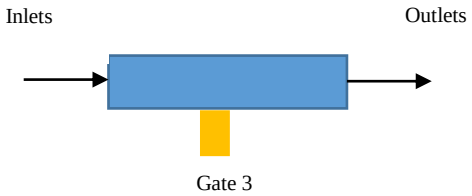

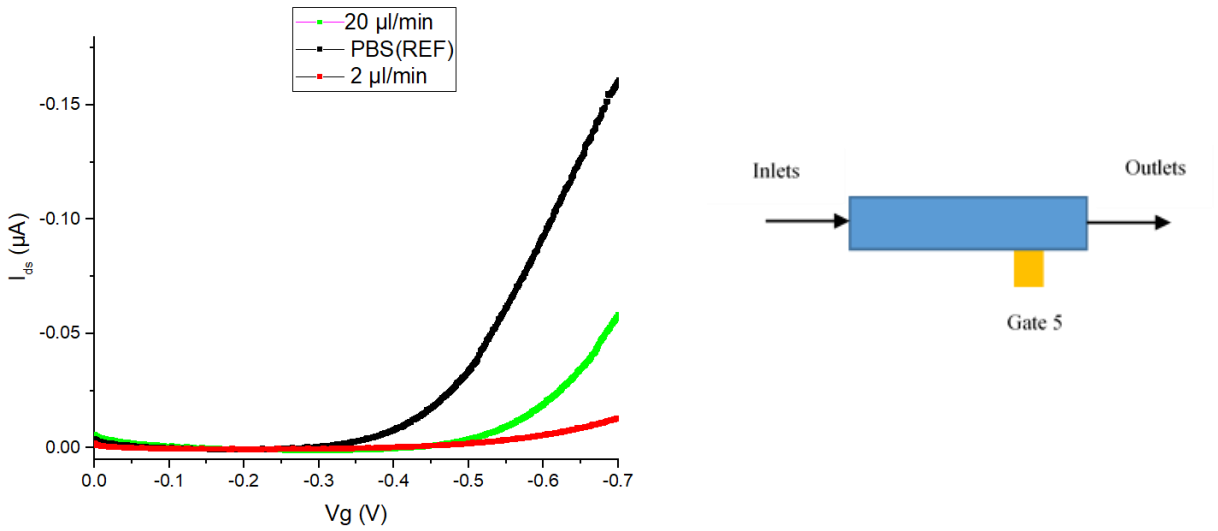

Figure 5.5: Transfer curves of EGOFET device for 3-mercaptopropanol depending on the position of the gates inside of the microfluidic channel. The currents show difference depending the positions of the gates and depending on the flowrates.

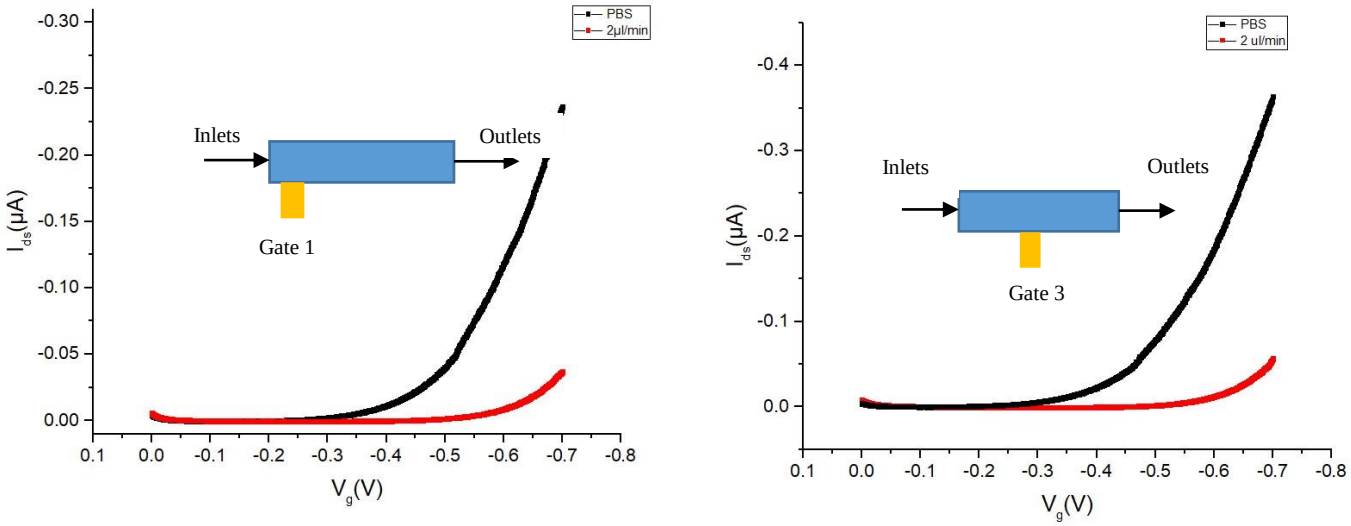

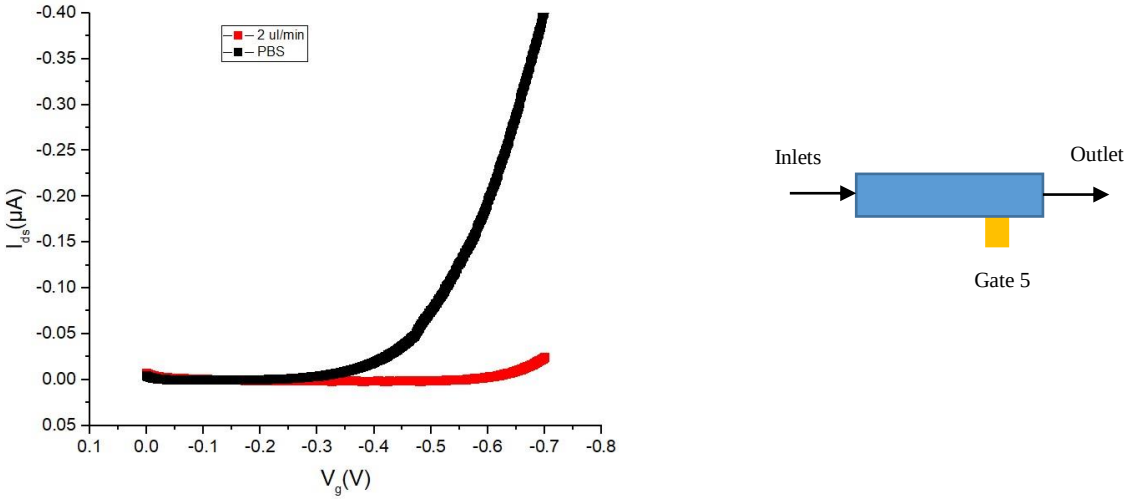

Figure 5.6: Transfer curves of EGOFET device for 6-mercapto-hexanol depending on the position of the gates inside of the microfluidic channel.

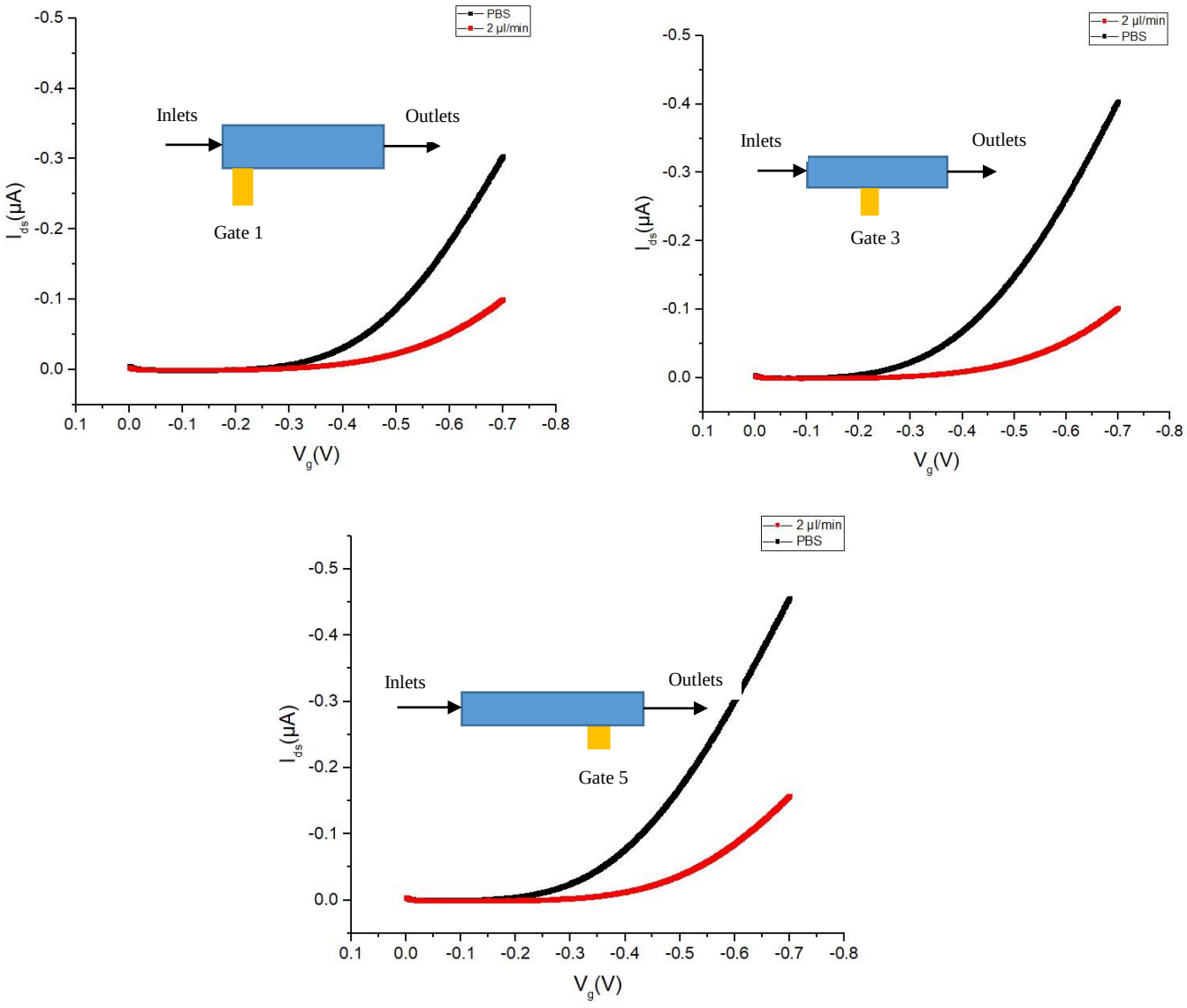

Figure 5.7: Transfer curves of EGOFET device for 9-mercapto-nonanol depending on the position of the gates inside of the microfluidic channel.

In order to confirm the experimental results, showing a concentration gradient dependent response for 3-mercaptopropanolI performed a control experiment with a simple microfluidic channel, with same length, injecting the thiol solution in both inlets, with flow rate of 2µl/min. The Figure 5.10 confirms that all the gates induced almost equal bias to the EGOFET channel and induced almost equal Drain-Source current, independently from the gate position. Therefore, signal and threshold voltage remains the same without any gradient.

5.2.5 CV measurements for the concentration profiles inside of the microfluidic mixer

To test the concentration profiles inside of the microfluidic channel from the simulations, we performed CV measurements of sample solutions prepared with thiol concentration equal to values extracted from the Comsol FEM simulation of h-mixer at specific 4 axial positions along the main channel. The thiol aqueous solutions had concentration of 0.17 µM, 0.41 µM, 0.55 µM and 0.83 µM. Since the concentrations are very close to each other, it was investigated if the signals could be differantited looking at resistance to electron transfer in redox reactions happening during cyclic voltammetry. For CV measurements, the bare gold (Au) measurement was used as a reference.

In Figure 5.8, Cyclic voltammograms are reported for the samples at different concentration of 3 mercaptopropanol. As expected the position of the reduction and oxidation peaks are not changed, and also the peak intensities are not clearly related with the concentration of thiol in the incubation vial. Apparently the CV current is almost entirely dependant on the electron transfer and is not sensitive to change in capacitance due to partial adsorption of thiol layer on gold substrates.

In order to give a quantification of the SAM coverage on gold gate, we performed CV measurements with different scan rates for the different thiol moieties. Self-assembly process has two stages, first an initial fast stage in which in the first few minutes of the self-assembly mostly of monolayer is formed, depending on the thiols type and the concentration. This stage is followed by the second rearrangement stage [5]. So the incubation time is rightfully chosen.

For electrochemically reversible electron transfer processes, the Randles-Sevcik Equation describes how the peak current i_p (A) increases linearly with the square root of the scan rate v (V s^{-1}), where n is the number of electrons transferred in the redox event, A (cm^2) is the electrode surface area

(geometric surface area), D (cm^2 s^{-1}) is the diffusion coefficient of the oxidized analyte, and C (mol cm^{-3}) is the bulk concentration of the analyte [20].

$$i_p = 0.4663 \cdot n\,F\,A\,C \cdot \left(\frac{n\,F\,v\,D}{RT}\right)^{1/2} \qquad \text{(Eq. 5.1)}$$

The Randles-Sevcik equation becomes simplified, when the solution is at the room temperature:

$$i_p = 2.69105 \cdot n^{\frac{3}{2}}\,A\,D^{\frac{1}{2}}\,C\,v^{\frac{1}{2}} \qquad \text{(Eq. 5.2)}$$

From the equation 5.2, the coverage rate for the electrode after 10 minutes incubation is calculated and is plot in Fig. 5.8.

Randles-Sevcik Equation accounts for linearity in plots of i_p versus $v^{\frac{1}{2}}$ as can be seen in Fig. 5.8.c) [20]. All the trends recorded for the thiols moieties are linear with respect of $v^{\frac{1}{2}}$, but the rate is higher for the molecule with shorted alkyl chain (3 units) and reduced for the molecules with chain length 6 and 9. This proves that the performed CV measurements are electrochemically reversible and the electron transfer only occurs via surface, but not surface-adsorbed species. 3-mercaptopropanol shows 10% coverage rate, compared to the other SAMs like 6-Mercaptohexanol 40 % and 9-Mercaptononanol 60%.

a)

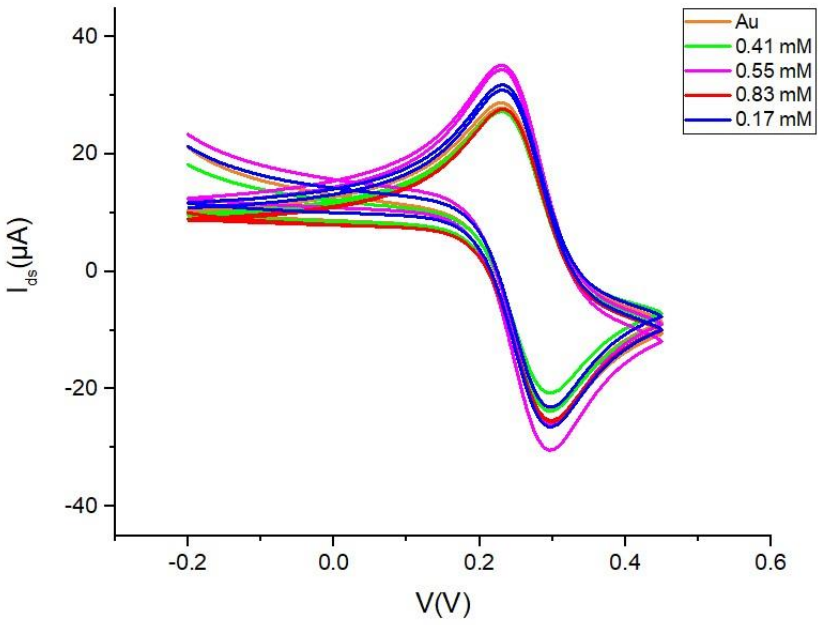

b)

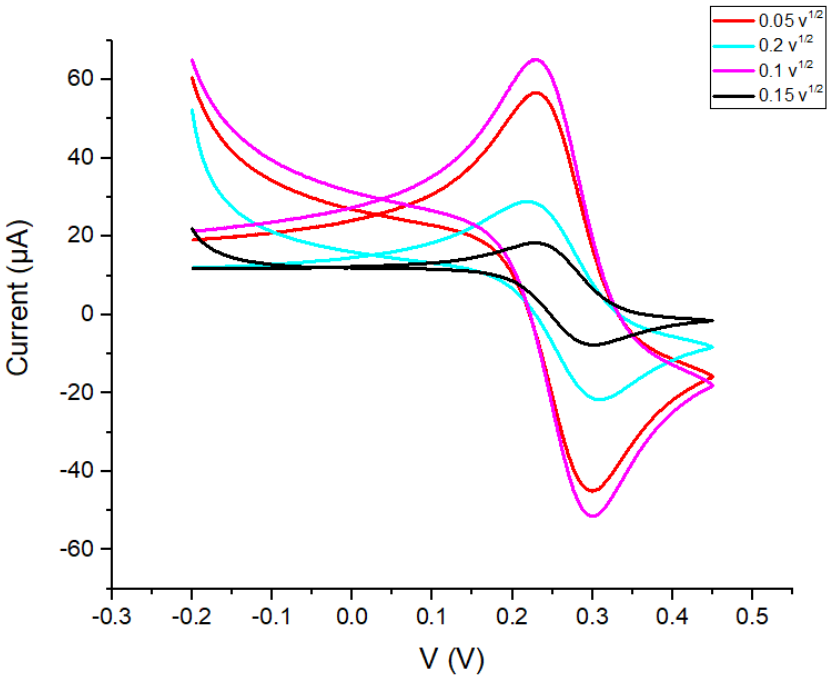
0.05 v^1/2
0.2 v^1/2
0.1 v^1/2
0.15 v^1/2
Current (µA)
V (V)

c)

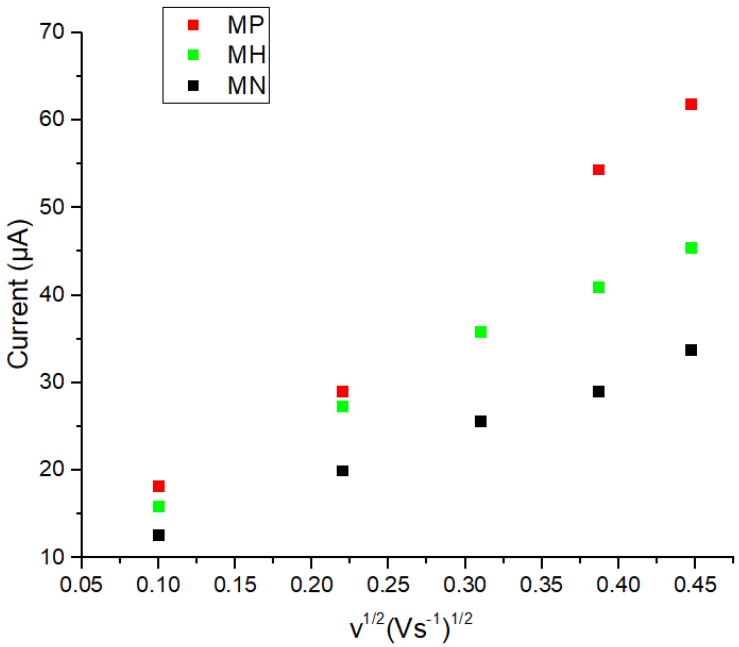
MP
MH
MN
Current (µA)
v^1/2(Vs^-1)^1/2

d)

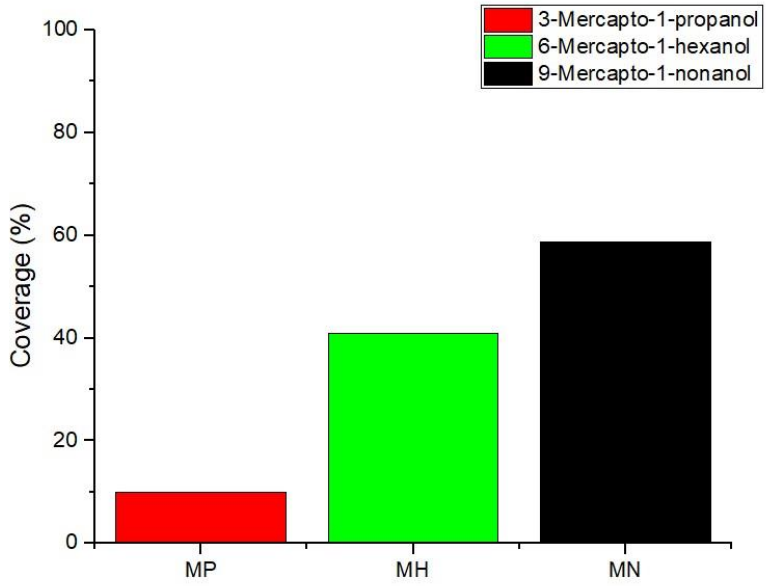

Figure 5.8: a) CV measurements with 3-mercaptopropanol depending on the concentration profiles inside the microfluidic channel. b) CV measurements for 3-mercaptopropanol with different scan rates c) All the trends recorded for the thiols moieties are linear with respect of $v^{1/2}$. *d) SAM coverage rate for 10 minutes incubation with different SAMs. The coverage rates are calculated with the Randles-Sevcik equation.*

5.2.6 Discussion

The response of the EGOFET device is changing with gates exposed to increasing concentration of 3-mercapto-1-propanol due to thiol concentration gradient build up in the h-mixer. . The effect of the flow rate on the thiol adsorption on the gate electrodes and corresponding EGOFET transfer characteristics can be addressed by looking at variations of transistor property versus gate number. From the transfer curves, it is seen that the output current is decreasing in correlation with the axial position of the gate along the microfluidic channel. The voltage threshold also shows similar correlation. It is possible to normalize the output current of the gate exposed to thiol diffusing front with respect to the current of the same gate recorded during the priming of the microfluidic device with streaming PBS flows.

The signal *S* was calculated according to the following equation :

$$Signal = \frac{I_{ds,ref} - I_{ds,SAM}}{I_{ds,ref}} \quad \text{(Eq. 5.4)}$$

Where $I_{ds,ref}$ stands for the average of Drain-Source currents recorded for each gate electrode, and $I_{ds,SAM}$ for the corresponding measurement after streaming of thiol solution.

The threshold voltage shift was calculated changes after SAM functionalization. This shift is calculated according to:

$$\Delta V_{th} = V_{th,SAM} - V_{th,REF} \quad \text{(Eq.5.5)}$$

Where $V_{th,REF}$ is the threshold voltage of each gate wet by buffer solution, and $V_{th,SAM}$ refers to threshold voltage extracted for the gate after interacting with thiol solution.

The values of *S* and ΔVth extracted from EGOFET transfer characteristics are reported for each gate position in Figure 5.9. The concentration gradient appears to modulate the signal for MP, rising from a value of 0.6 to approximately 1, after gate 3, but only for the 2 µl/min flow rate.

a)

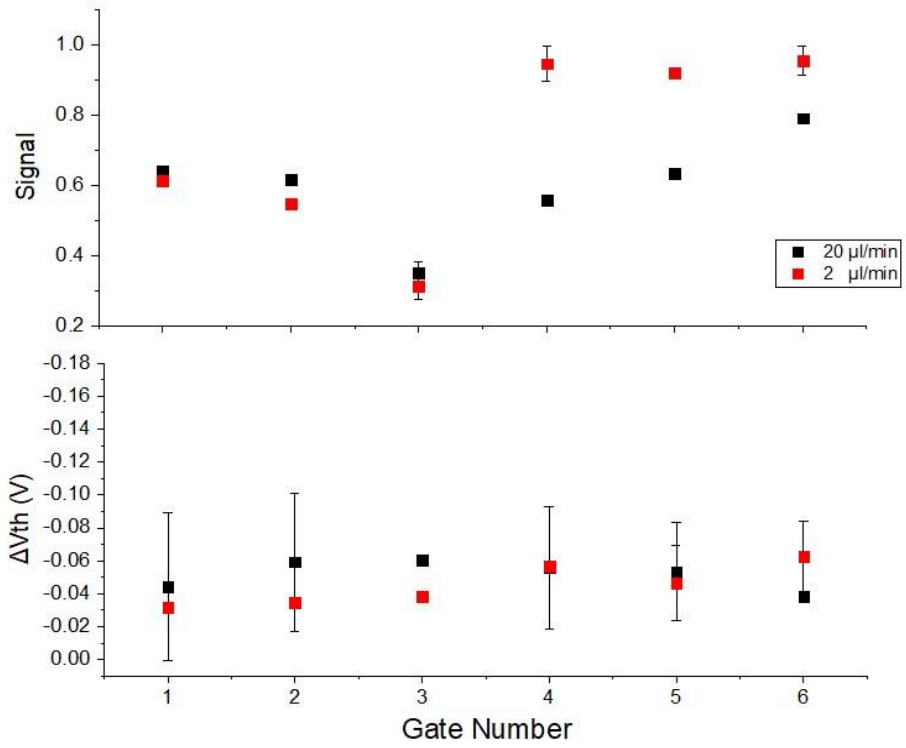

b)

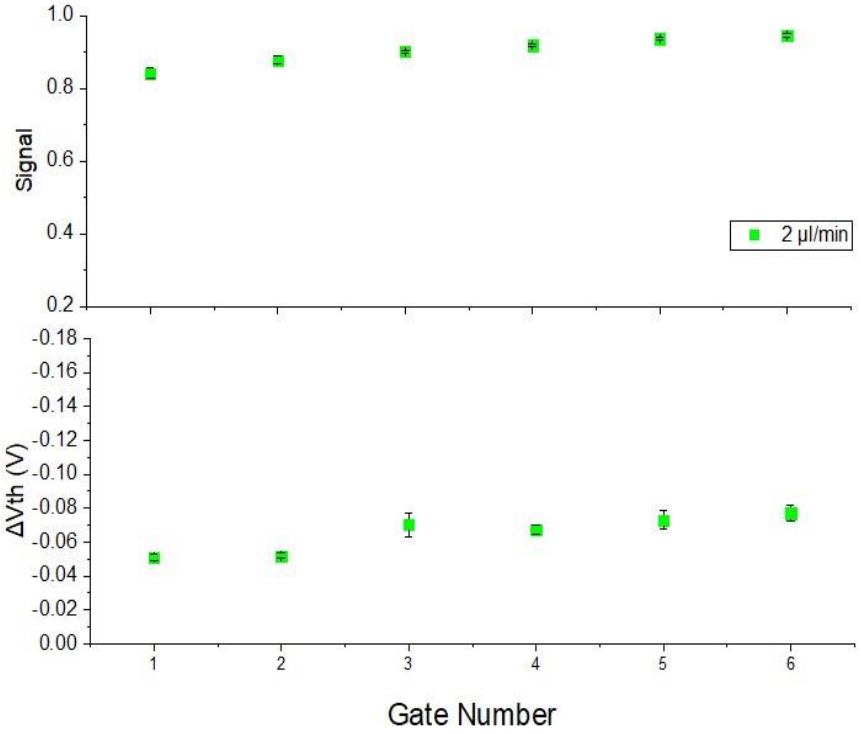

c)

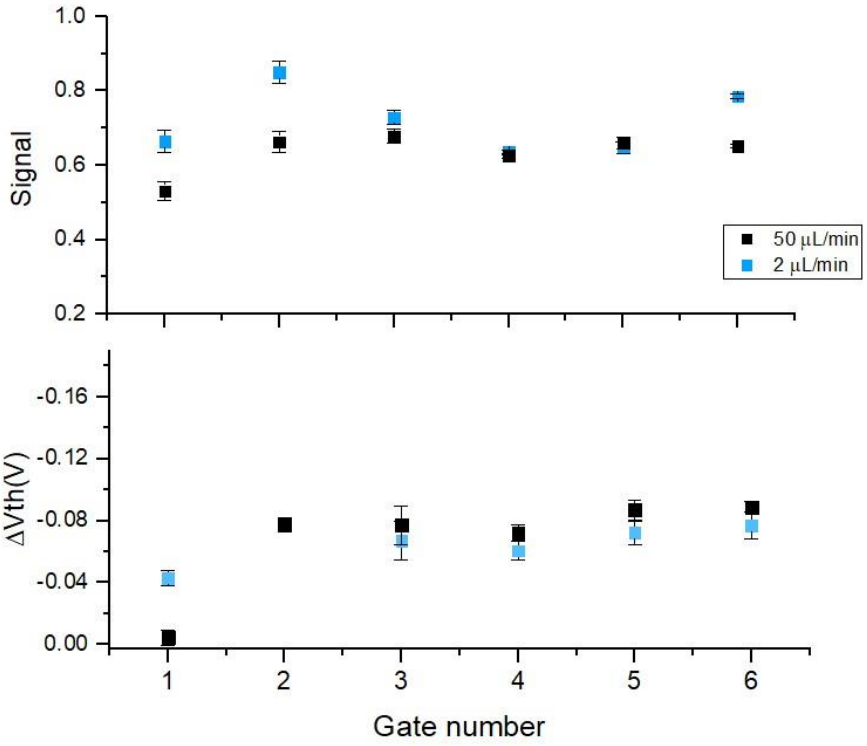

Figure 5.9: a-b-c) The results for the signal calculations and the shift of the threshold voltages for 3-mercaptopropanol, 6-mercaptohexanoland, 9-mercaptononanol vs. the gate position inside of the mixer.

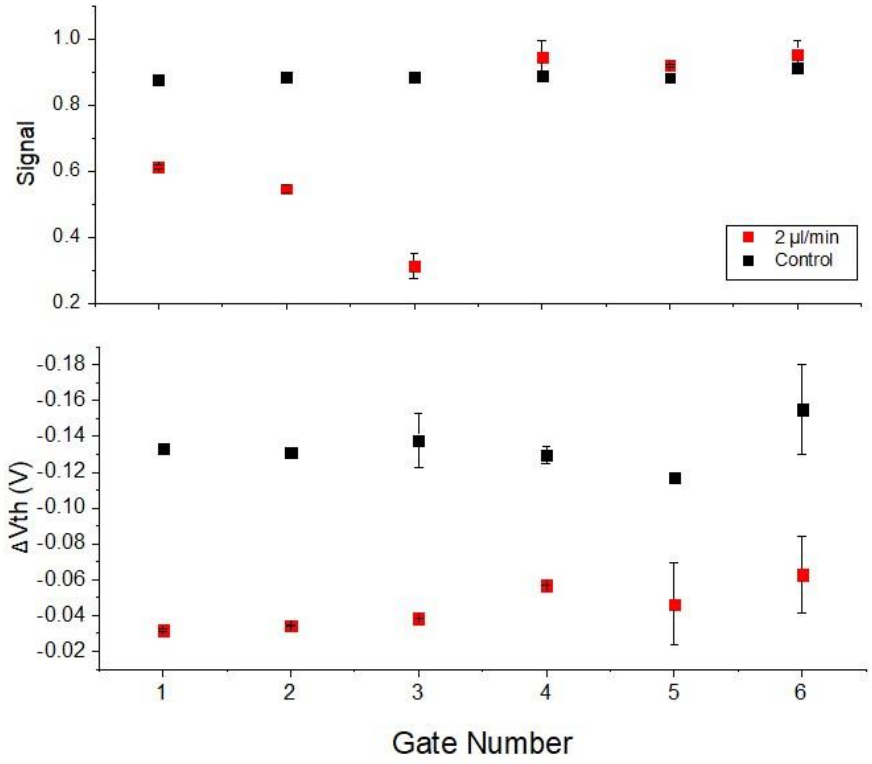

Figure 5.10: From control experiment, the signal and the shift of the threshold voltage for 3-mercaptopropanol are calculated.

From FEM simulation, we can extract a value of concentration of approximately 10^{-6} M near the position of Gate 1 and 2. Since for this concentration, the time for completion of the self-assembled monolayer is larger than 12 hours [5] Asaei according to a simplistic model of adsorption, it is reasonable to accept that the amount of 3-mercapto-1-propanol molecules chemisorbed on the surface do not form a layer with high coverage. This conclusion is also supported by other work in literature using micropipette based scanning electrochemical microscopy [27]. 6-Mercapto-1-hexanol and 9-Mercpato-1-nonanol are showing a signal almost non-dependant on the Gate position. This experimental result can be explained by the fact that they start to form a self-assembled monolayer that is more energetically favourable and therefore the bulk concentration to accomplish high surface coverage is of the order of 10^{-8} M. The solution concentration in the microfluidic h-mixer, albeit in gradient generated by diffusion from the mixing interface, is not affecting the functionalization of the gate electrodes.

SAM formation causes an increase or decrease of the metal work function of the gate electrode depending on the length of the backbone chain and to the nature of the terminal group [23]. Since the used SAMs differ only in their backbone length, but not the terminal group, the change of the work function directly relates to the length of backbone chain. It affects the formation of the electrical double layers, causing a change in the overall capacitance [24]. The dipole moment of the alkanethiols forming the SAMs on the gold gate electrode is affecting the slope of transfer curves of EGOGET, resulting more negative threshold voltage Vth.

In the next paragraph we propose a simplistic autocatalytic model for describing the EGOFET response with respect to the concentration of solution in proximity of each gate and the coverage expected from the CV measurements. In this evaluation, we did not distinguish between the adsorption from the liquid phase and rearrangement of randomly adsorbed molecules, both phenomena accounted for in the autocatalytic reaction.

The species involved in the approximated scheme are named as T, corresponding to the thiol molecules in solution and T_{ads}, the thiolated organic layer formed on the gold surface. Alkanethiols adsorption on the gold surface occurs potentially along the boundaries of already formed islands, for this reason we consider as dominant the kinetic contribution related with the self-assembled monolayer formation, with respect to random adsorption. The reaction model can be expressed as

$$T + T_{ads} \rightleftharpoons 2\,T_{ads}$$

With k_{ads} being the kinetic constant for adsorption along the thiol patches borders and k_{des} the desorption constant, the model equation for T_{ads} specie is

$$\frac{dT_{ads}}{dt} = \frac{T^0 + T^0_{ads}}{1 + \left(\frac{T^0}{T^0_{ads}}\right) e^{-K\left(T^0 + T^0_{ads}\right)t}} \qquad \text{(Eq. 5.6)}$$

Where the parameter $K = \frac{k_{ass}}{k_{dis}}$ is the ratio between the said kinetic constants and input as single parameter in the fitting.

Experimental values for $k_{ass} = 11.5 \times 10^{-3}\, m^3\, (mol\, s)^{-1}$ and $k_{dis} = 6 \times 10^{-3}\, s^{-1}$ have been reported in previous works [26] and in the present analysis enter as simplistic K constant, fixed equal to $2 \times 10^3 M^{-1}$ .The characteristic sigmoidal curve of the autocatalytic process is superimposed on signal/coverage data for 3-mercapto-1-propanol, whereas for 6-mercapto-1-hexanol and 9-mercapto-1-nonanol the slope of the catalysed phase is not evident, suggesting that the concentration required for observing the signal growth was overpassed.

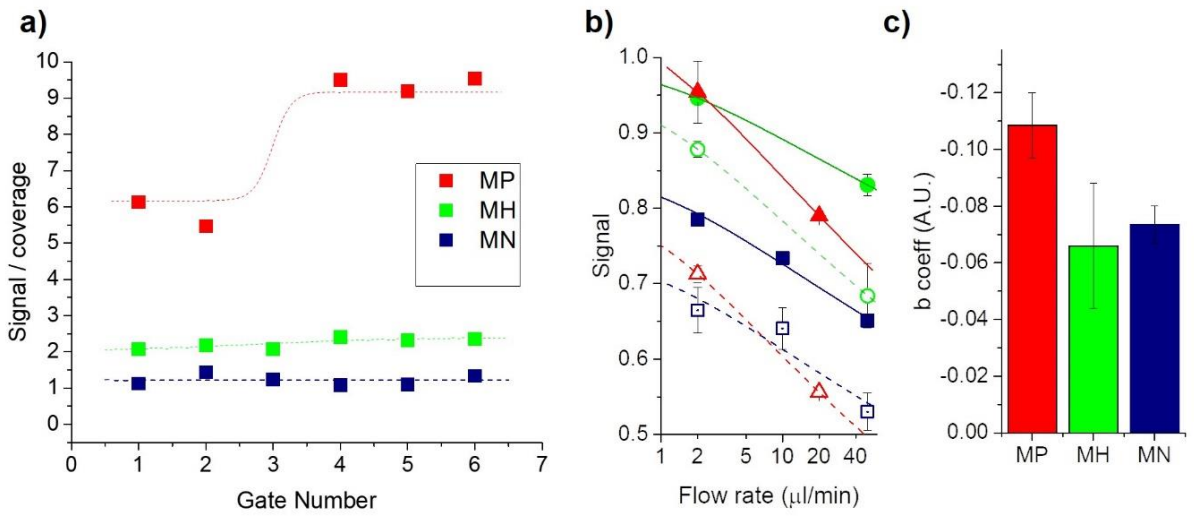

Figure 5.11: a) The ratio between EGOFET signal and coverage obtained by CV measurement is reported versus gate number. Dot lines are the result of fitting with the kinetic model described in the text. b) EGOFET signal versus flow rate plot for selected gates covered with MP (red triangles), MH (green circles) and MN (blue squares) (Filled symbols = gate 6, empty symbols = gate 1). Continuous and dashed lines are the result of fitting the data with power law model. c) The b exponent of the transport-limited model is reported for the different thiols, error bars are for uncertainty in parameter estimation.

In order to verify a potential limitation of the kinetics induced by transport phenomena, and compare the results between the thiol species, EGOFET signal is plot against flow rate, for selected gates. A power law decay ($S \propto (1 - fr)^b$), dependent on the flow rate *fr*, is superimposed to data points to extract a semi quantitative parameter for comparison, which is the exponent *b*. The rationale is to verify whether the signal is changing considerably with flow rate (transport-limited operative interval) or stays approximately constant with flow rate (reaction-limited operative interval). In 5.11.c, the exponent extracted from power law fitting is approximately equal to -0.11 for MP, while for MH and MN is approximately -0.07.

The higher rate of decay for MP is suggesting that only for this short chain compound we are in the transport-limited regime, whereas for MH and MN the diffusion experiments were already in the reaction-limited region.

The EGOFET shows high sensitivity to change in work function of the gate electrode surface. The possibility to control the self-assembled monolayer formation is achieved by means of the diffusion interface within the streams. The diffusion across the interface of the H-mixer is not changing the migration of ions, but the presence of thiol in solution is affecting the capacitance modulating the current between source and drain in the transistor. The potential of the electrolyte solution remains unaffected by the diffusion process but a change in ionic concentration is also changing the extent of the electric double layer on both gate and semiconductor. It is important to note here that the adsorption kinetics of SAM on the gate is balanced by the effective exposure of the gold to the electrolyte solution, so that the change in signal is not just proportional on the gate coverage achieved during streamflow.

5.2.6 Summary

Here, I present EGOFET as an electroanalytical tool for monitoring self-assembly monolayers on top of gold gates. The possibility to control the self-assembled monolayer formation is achieved by means of the diffusion interface of within the streams. For this purpose, we integrate the microfluidic mixer with EGOFET with the electrolyte bridge. The mixer helps with formation of SAMs on the gates with diffusion gradient inside of microfluidic channel. The developed diffusion gradient in the microfluidic channel is controlling the thiol based monolayer formation on gold gates. Since the diffusion gradient is more spread inside of microfluidic channel with the low flowrates such as 2 µl/min, the effect of flow rate on the SAM formation is studied by looking at signal from EGOFET. The capability of the multi gate EGOFET to detect the diffusion profile along the microfluidic channel is demonstrated by correlating the results of finite element simulation with the output current decreasing in correlation with the axial position of the gate along the microfluidic channel for 3-mercapto-1-propanol, whose chemisorption reaction appears to be transport limited For the other two alkanethiols species, the concentration gradient developed in the h-mixer is not reflected in a sigmoidal shape signal, as for the smaller thiol. This result may be explained by the tendency to form ordered self-assembled monolayers starting from low bulk concentration, making dissociation less favourable.

Finally the integration of multigate EGOFET with microfluidic device presented in this paper may be regarded as a usefull prototype for the automated generation of dose curves, once the gate electrodes are functionalized initially with biorecognition compound of interest, thanks to the concentration profile generated by diffusion.

5.3 Label-free immunodetection of α-synuclein by using a microfluidics coplanar electrolyte-gated organic field-effect transistor

Label-free immunosensors that exploit an organic semiconductor channel as the transducer of the biorecognition events are emerging as ultrasensitive and highly specific devices for bioanalytical assays, with figures of merit often comparable, sometimes even superior (with levels of detection down to a few target molecules), to those characterizing the workhorse of bioanalytical techniques viz. the enzyme-linked immunosorbent assays (ELISA) [28]. With comparison to label-free electronic sensors based on inorganic semiconductors, as CHEM-FETs (i.e., chemical field-effect transistors [29]) or MOSFETs (i.e., metal-oxide field-effect transistors [30]), organic biosensors offer other important advantages, such as the closer proximity with the aqueous environment (the organic semiconductor channel is immersed in the biologically relevant fluid), the stability of operations in aqueous electrolytes (the typical hysteresis and bias stress observed in ambient operations of organic electronics devices disappear in immersion conditions), the possibility to be interfaced or integrated as arrays with living systems, thanks to the large-area manufacturing on flexible substrates and a suitable bio/functional interface.

Two main device architectures are used in biosensing in aqueous liquids: i) EGOFETs[31] and ii) organic electrochemical transistors (OECTs) [32]. EGOFETs rely on the capacitive coupling between the gate electrode and the active material, whereas OECTs exploit the ion diffusion along with the electrochemical doping of the active material [33]. Relevant bio-applications include electroceuticals [34], bioelectric signal recording [35, 36], neuromorphic devices [37, 38], and biosensors [24,39,40].

In the case of EGOFET biosensors, the functionalization with a biorecognition group can be done either at the gate electrode [39], or at the organic semiconductor channel [41, 42]. Magliulo et al. [43] successfully demonstrated both physisorption and chemical grafting of sensing receptors onto the semiconducting channel achieving excellent results towards the quantification of streptavidin and C-reactive protein in a wide range of concentrations, namely from 1μM to 10nM and from 2μM to 2pM, respectively. However, the approach exerted by using a functionalised gate is generally

more convenient, because it avoids the surface engineering of the organic semiconductor, which can affect its electrical properties and stability during the aqueous operation. As a result, several metal functionalisation strategies have been successfully demonstrated such as the grafting of antibodies/aptamers mediated either by the Protein G or by self-assembled monolayers (SAMs) [21,22,40-45].

The ultimate achievement was the effective detection down to single-molecule of immunoglobulins G/M by co-functionalising the gate electrode with a SAM endowed with hydrogen-bonding interactions that amplify the individual biorecognition event by a cooperative reorientation of the SAM [23]. As the limits of detections are pushed down to such low concentrations, and since many relevant biomarkers, even when overexpressed, are present at extremely low concentration during their pathophysiological condition (*e.g.* inflammatory cytokines), it is crucial to guarantee the electrical stability in these label-free devices. This is particularly important aiming at a new generation of biosensing point-of-care (POC) systems or early diagnostic tools for the detection of relevant biomarkers. Thus, the effort on engineering the optimal interface immunochemistry must be paralleled by the effort in endowing the sensor with compact microfluidics able to guarantee the required stability of parameters during the measurement. The success of such microfluidics has been extensively explored in other types of label-free devices such as the electrochemical [47-50]. These excellent examples share the same goal, namely a compact chip to be used as a POC test [51].

Here it is reported on an α-synuclein label-free sensor based on an EGOFET as electronic transduction, whose gate electrode is functionalised by a monoclonal anti-(α-synuclein) antibody. Two different surface functionalization strategies to graft the anti-(α-synuclein) antibody (*i.e.* SAM and Protein G) are explored. The EGOFET sensor is integrated into a novel microfluidics layout designed *ad-hoc* to standardize the measurements. This microfluidics consists of separately accommodating the gate and the organic semiconductor, thereby avoiding cross contamination during the sample dispensing, even though their electrical connection is always preserved for its proper operation. Additionally, the microfluidics is crucial to avoid the fast evaporation of solvent/water, which would produce a temporal drift of the target concentration and hence of the relevant electrochemical potentials in the device. The microfluidics embedded EGOFET featuring a coplanar gate reaches a sensitivity up to 37(±5) mV/dec and a limit-of-detection (LOD) as low as 0.25 pM in phosphate buffer saline (PBS) solution at pH = 7.2 performing analytical tests that take only a few minutes.

5.3.1 Characterization of the sensing platforms

Anti-(*α*-synuclein) antibodies (Abs) have been tethered onto the polycrystalline Au by means of two different approaches, the so-termed “approach I” and “approach II” (Figure 5.12). The former relies on an amino-terminated pegylated thiol (HSC11EG6NH2), whose amino groups have been successively activated with glutaraldehyde (Gl) [60, 61].

This leads to a functionalized Au extremely reactive towards primary amines, which are usually abundant in the Abs backbone (see Figure 5.12a). The second approach does not covalently graft the antibody to the surface but instead tethers it to the His-tagged recombinant Protein G (PG),that is anchored to the Au electrode. PG is able to target efficiently the crystallizable Ab region [37–39]. Furthermore, PG is robustly anchored to the polycrystalline Au thanks to its His tag that exhibits an affinity towards different metals such as Ni and Au (Figure 5.12 b) [65, 66].

Since there is not an established protocol for tethering a bio-molecule onto a metal surface without affecting partially its bio-functionality, it is pursued both approaches that have pros and cons and compared the outcomes of the sensing devices in order to establish the most suitable approach. For instance, approach I yields covalent albeit random Ab grafting, whereas approach II guarantees more oriented Ab immobilization onto the Au surface although non-covalent interactions are involved.

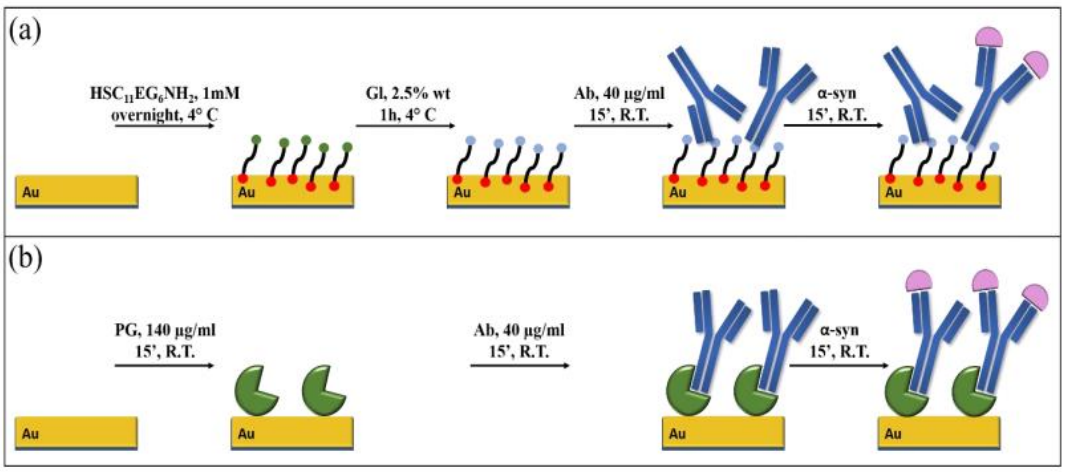

Figure 5.12: Scheme of the Au surface functionalization protocol with Approach (a) I and (b) II.

5.3.2 Impedance spectroscopy and differential pulse voltammetry

The first goal was to verify the presence of the surface binders (*viz.* $HSC_{11}EG_6NH_2$-based SAM and PG), their reactivity towards Abs and consequently, their sensitivity towards α-synuclein. By electrochemistry (i.e., electrochemical impedance spectroscopy and differential pulse voltammetry), the PG grafting yielded a pronounced area normalised *RCT* increase (Δ*RCT*) up to 20 kΩ/cm2 and a consequent decrease of the current density (Δ*J*) down to 440 μA/cm2 (Figure 5.13 a,b).As expected, the $HSC_{11}EG_6NH_2$-based SAM features higher Δ*RCT* (~120 kΩ/cm2) than PG due to its more ordered and compact packing onto the Au surface (see Figure 5.13 c). Both functionalization approaches were successfully tested towards a 0.25 μM solution of *α*-synuclein proving their sensing ability towards this analyte. In particular, the two approaches exhibit opposite trends of the response with respect to Abs adsorption and detection of *α*-synuclein.

The $HSC_{11}EG_6NH_2$-based SAM (i.e. higher coverage and molecular packing) showed an increase of Δ*RCT* and a consequent Δ*J* decrease (Figure 5.13 d) after being incubated with *α*-synuclein. Conversely, PG showed a decrease of Δ*RCT* and a consequent Δ*J* increase (i.e. lower coverage and molecular packing). Albeit it is beyond the scope of this paper, these experimental proofs hint at a relevant redistribution of the surface charge on the metal due to the pairs Ab-PG as well as AbPG-synuclein. In addition, the different response could also be influenced by the Au SAM bond formation that leads to permanent electric dipoles.

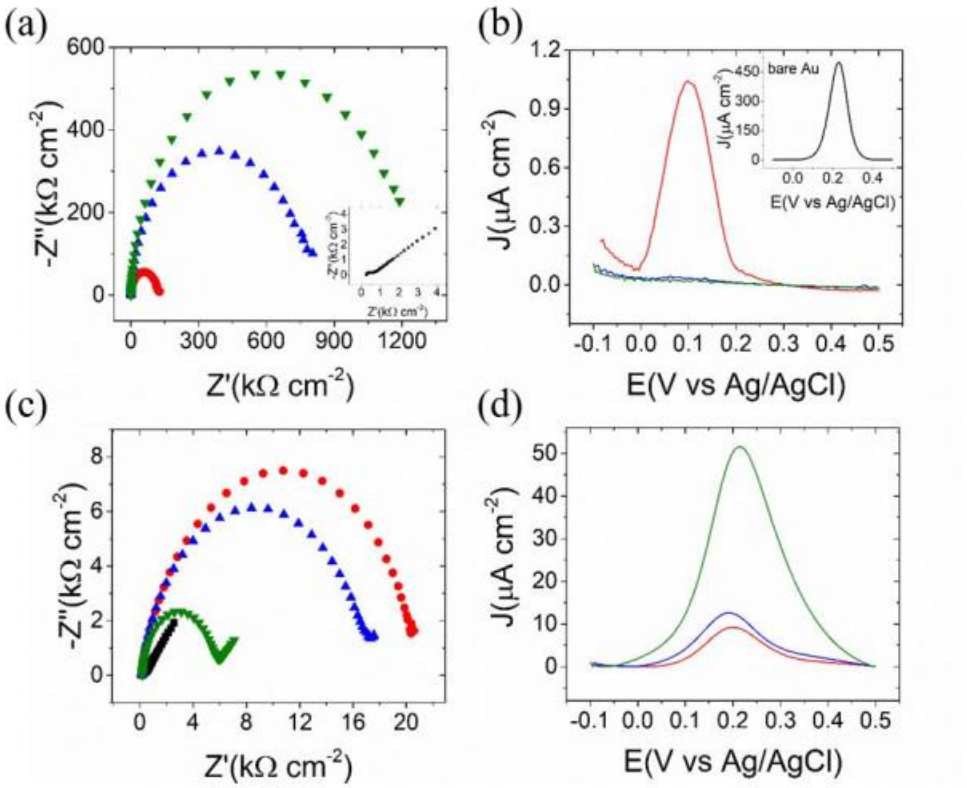

*Figure 5.13: EIS and DPV characterization of the Ab functionalized surface. Approach I. (a) EIS: SAM coated Au (red curve), Ab-SAM-coated Au (blue curve), after incubation in a solution of α-synuclein 0.25 μM (green curve). In the inset, the curve relative to pristine Au is represented, (b) DPV: SAM-coated Au (red line), Ab-SAM-coated Au (blue line), after incubation in a solution of α-synuclein 0.25 μM (green line). In the inset, the DPV of pristine Au is reported. Approach II. (c) EIS: bare Au (black curve), PG-coated Au (red curve), Ab-PG-coated Au (blue curve), after incubation in a solution of α-synuclein 0.25 μM(green curve). (d) DPV: PG-coated Au (red line), Ab-PG-coated Au (blue line), after incubation in a solution of α-synuclein 0.25 μM (green line)***.***

5.3.3 Surface Plasmon Resonance (SPR) characterization

In order to further characterize the functionalized substrates, surface plasmon resonance (SPR) has been used to assess the two approaches on a planar Au film (Figure 5.14 a,b). As explained in the Chapter 3, the SPR is equipped with microfluidic channels that allow real-time monitoring of the absorption process. The excellent sensitivity of this technique allowed us to track the reflected light variation (*%ΔR*), which is directly related to the Au surface grafting. In particular, *ΔR* as a function of time allows one to monitor the kinetics of this phenomenon.

Apart from demonstrating the successful glutaraldehyde activation of $HSC_{11}EG_6NH_2$-based SAM in approach I, as well as the PG adsorption on gold in approach II, the transient *ΔR* change related to the surface functionalization with anti-(*α*-synuclein) Ab was monitored and exponentially fitted for both approaches (Ab concentration was fixed at 40μg/ml).

It turned out that approach I was faster than approach II yielding f = 112 (±1) s and f = 212 (±1) s, respectively. Although a calibration curve and more advanced measurements would be required for achieving a quantitative analysis, it can be stated that approach II leads to the adsorption of more anti-(*α*-synuclein) Ab (*ΔR* = 12) with respect to approach I (*ΔR* = 6). Concerning the *α*- synuclein recognition (concentration selected equal to 250 nM), a larger *ΔR* is recorded for approach II with respect to approach I. Thus, these data do not only hint a larger amount of anti(*α*-synuclein) Ab in approach II, but also an improved control of Ab orientation onto the Au surface. In agreement with the electrochemistry results, SPR measurements confirm the successful Ab functionalization of the surfaces employing both approaches, as well as their capability to sense *α*-synuclein.

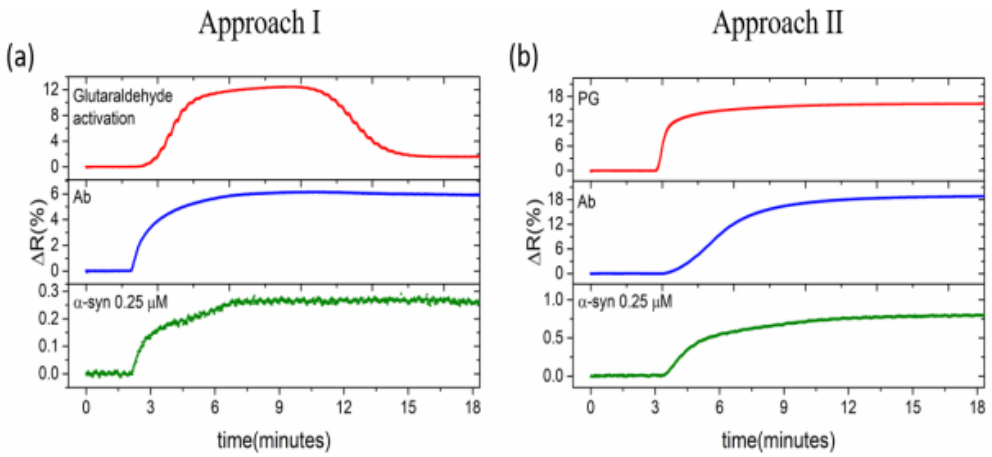

Figure 5.14: SPR characterization of the functionalized substrates: (a) approach I and (b) approach I.

5.3.4 Top-gated EGOFETs: α-synuclein detection

Since both approaches turned out to be extremely responsive towards α-synuclein, It has been then employed as gate terminals into a standard EGOFET architecture (see Figure 5.15 a). This allows one to monitor the detection of α-synuclein by using a transistor. Concerning the general architecture of the device, *Kapton*® as a flexible supporting substrate for the interdigitated electrodes has been choosen.

The channel area was coated by a thin-film blend composed of the organic semiconductor 2,8-Difluoro-5,11-bis(triethylsilylethynyl)anthradithiophene (diF-TESADT) and polystyrene (PS) deposited by bar-assisted meniscus shearing (BAMS), as reported earlier [67–69]. As previously published, the role of PS improves the general stability of the electrical performances, especially when operated in liquid [69–75]. This is achieved due to the vertical phase separation of the two components that takes place during the deposition; in other terms, the organic semiconductor crystallizes sandwiched between a bottom PS layer and a top thin skin PS layer.

Finally, the device was exposed to phosphate-buffered saline (PBS) solution at pH 7.2, where a top gate electrode was immersed, namely an Au wire (Figure 5.15 a). The *I-V* transfer characteristics were acquired after the *ex-situ* functionalization of the gate with anti-(*α*-synuclein) Ab. Subsequently, the electrode was immersed in benchmark solutions of *α*-synuclein and, afterwards, implemented as top gate electrode in the standard EGOFET layout (Figure 5.15 a). This guaranteed no chemical and/or biological contamination onto the organic semiconductor surface.

Prior to any sensing experiment, electrical conditioning was always performed (*i.e.*, *VDS* and *VGS* equal to -0.1 V for 20 minutes) and the *ex-situ* functionalization was verified step by step by recording at least three transfers for each step (Figure 5.15 b,c). Aiming at avoiding misleading interpretation, additional *I-V* transfer characteristics were acquired at the end of each sensing experiments by using a freshly cleaned Au wire (*viz*. gate electrode). This allowed us to verify if any extrinsic phenomena (such as bias stress or damaging of the semiconducting film) related to the device were contributing to the recorded trends. These final cross-checks clearly elucidated the direct interplay between the functionalization steps and the electrical changes occurring at the transistor .Two well-defined trends were observed corresponding to the two approaches. In particular, approach I shows a positive shift of the *I-V* transfer after exposure of the gate to an increasing concentration of α-synuclein, whereas approach II exhibits a negative one (Figure 5.15 d,e).

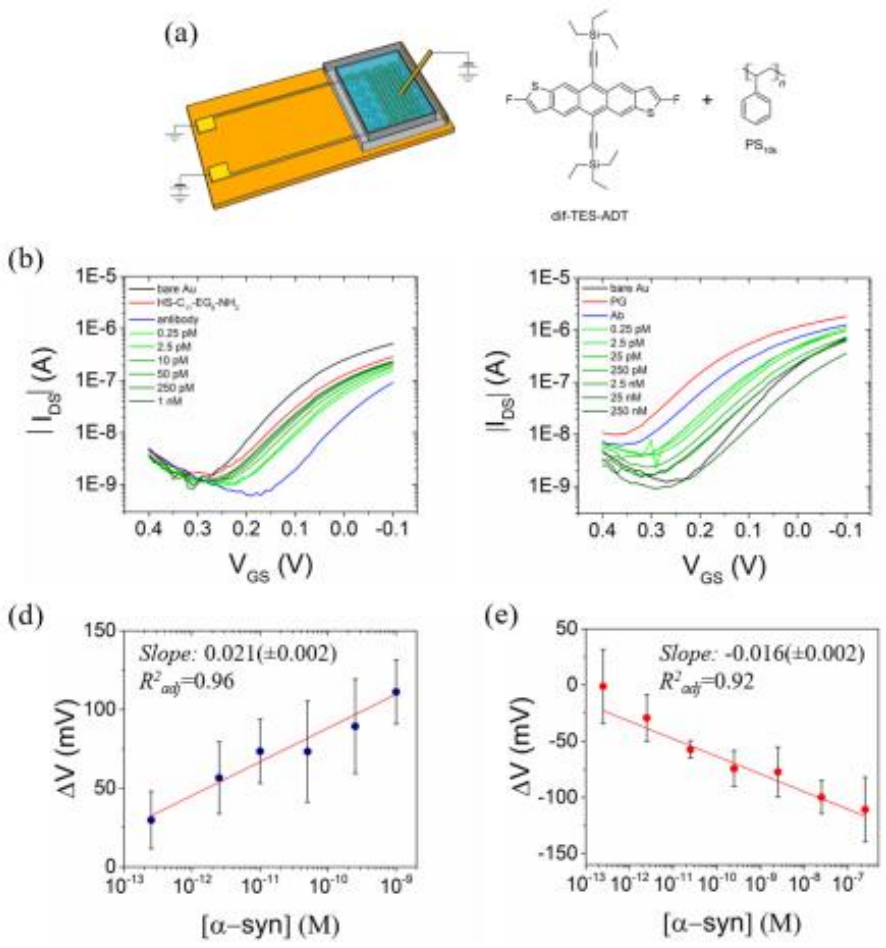

Figure 5.15: (a) Schematic image of the top-gated EGOFET and molecular structure of diF-TES-ADT and PS. I-V transfer characteristics of the EGOFET (VDS = -0.1 V) with (b) Ab-SAM-coated Au gate (approach I) and (c) Ab-PG-coated Au gate (approach II), upon interaction with α-synuclein. The sensing response for both approaches in terms of ΔV is depicted, respectively, in (d) and (e) plots. The bar error is relative to three measurements.

As widely reported in the literature, an organic or biological coating assembled onto the gate surface or the semiconducting material can drastically affect the electrical performance of the transistor operated in aqueous media [13,39,41,44,77,78]. The introduction of surface dipoles can either build-up an additional potential into the device or lead to a relevant change of the electrical double-layer capacitance. Aiming at a more quantitative description, an extraction of ΔV solely related to the bio-molecular recognition event regardless of the device-to-device variability, which affects usually the threshold voltage was performed. For this reason, the data have been extracted by adopting the mathematical elaboration suggested by *Ishikawa et al*. [79–81], as follows:

$$\Delta V = \frac{\Delta I}{g_m} \qquad \text{(Eq. 5.7)}$$

where $\Delta I=(I_{DS,ini}-I_{DS,fin})$ is the difference between the $I_{DS,\mathrm{ini}}$ related to the device functionalized by the anti-(α-synuclein) Ab and the $I_{DS,fin}$ corresponding to a specific concentration of antigen, and gm is the maximum transconductance (namely the first derivative of I_{DS} versus V_{GS}). In particular, it has been decided to verify the device sensitivity at the gate bias, where the g_m is the highest, namely -0.07 V. At the end of the sensing experiments, approach I yields a shift of +111(±20) mV, while an opposite shift of -111(±29) mV is found in approach II. In accordance with the electrochemical data, our EGOFETs sensed two opposite trends corresponding to the two functionalization approaches (Figure 5.15 d,e).

Concerning approach I, the sensing trend can be explained by considering the outer charges arising from the *α*-synuclein [59]. As reported in the literature, α-synuclein has an isoelectric point (pI) equal to 4.67, thus it is negatively charged at physiological pH (*viz.* pH > pI) [83]. As a result, a *p*-doping effect takes place due to an increase of negative charges onto the gate electrode. This leads to an extra accumulation of positive charge carriers into the conductive channel of diF-TESADT. Furthermore, the response ranges from 0.25 pM to 1 nM featuring a sensitivity equal to 21(±2) mV/dec.

On the contrary, a rationalization based on simply the PI of α-synuclein does not hold for approach II due to the presence of different bio-molecules on the surface. In this case, the sensing range appears wider than in approach I, namely from 0.25 pM to 0.25 µM, with a sensitivity of -16(±2) mV/dec. In other terms, both approaches reveal similar sensitivities, but approach II reached two orders of magnitude higher the upper limit of the sensitivity range (i.e., up to 0.25 µM). This outcome is consistent with the SPR assays, which qualitatively pointed to a more efficient Au electrode for the detection of α-synuclein in approach II. Furthermore, both approaches show comparable LOD values, namely at pM concentration. This high sensitivity makes these devices well-suited to study pathological versus physiological levels of this biomarker [84].

5.3.5 Coplanar gating: in-situ (bio)-functionalization

Although top-gated architecture allowed us to verify the sensibility of the functionalized EGOFET, this technology can be solely used at the laboratory scale for proof-of-concept. Aiming at more sound technology, a coplanar gate architecture is demanded along with a well-suited microfluidic cell for the sample handling. The coplanar architecture improves intrinsically the electrical characterization of such device, because it exerts an ideal control of the gate area immersed in aqueous solution.

Furthermore, it allows a straightforward implementation to more sophisticated circuitry, because no mobile electrodes are used like the Au wire in the top gate architecture. In this case, two planar gates termed “reference” and “sensing” (Figure 5.16 a) has been designed. According to this layout, a microfluidic cell composed of two well-defined chambers, so-termed “chamber 1” and “chamber 2” was manufactured.

The former contains the reference gate along with the source/drain electrodes covered by the organic semiconductor, whereas the latter hosts the sensing gate. These chambers are joined together by a “connecting channel”, whose role is fundamental for the overall functioning of this self-standing chip (Figure 5.16 b). This connecting channel guarantees the electrical connection between the sensing gate and the organic semiconductor through the electrolyte media. Furthermore, it enables to inject the sample containing α-synuclein or antibodies in “chamber 1” avoiding the cross-contamination of the organic semiconductor.

In other terms, chamber 1 together with the connecting channel are always filled by phosphate buffer, and chamber 2 is filled with different solutions. The use of peristaltic pumps together with the narrow section of the connecting channel guarantee the proper functioning of the chip. This has been experimentally verified by using the reference electrode, which allowed us to verify the electrical performance of the organic semiconductor at the beginning as well as at the end of the sensing experiments.

This has been experimentally verified by using the reference electrode, which allowed us to verify the electrical performance of the organic semiconductor at the beginning as well as at the end of the sensing experiments.

Such coplanar architecture was tested by using approach I. The sensing gate was *in-situ* functionalized (See Chapter 2.3). Subsequently, the sensing experiments were also performed *in-situ* by injecting the α-synuclein solutions for 5 minutes and then rinsing 3 minutes with the electrolyte media. The *I-V* transfer characteristics were acquired by spanning the gate-source voltage from 100 mV to -400 mV and with a V_{DS} = -0.1 V. (Figure 5.16 c). The data turned out to be coherent with the previous experiments related to the top-gated EGOFETs. As a result, a positive doping was observed by increasing the α-synuclein concentrations, reaching a LOD of 2 pM, ΔV value as high as +166(±52) mV and a slight increase in sensitivity (37(±5) mV/dec) with respect to the top gated devices (Figure 5.16 d).

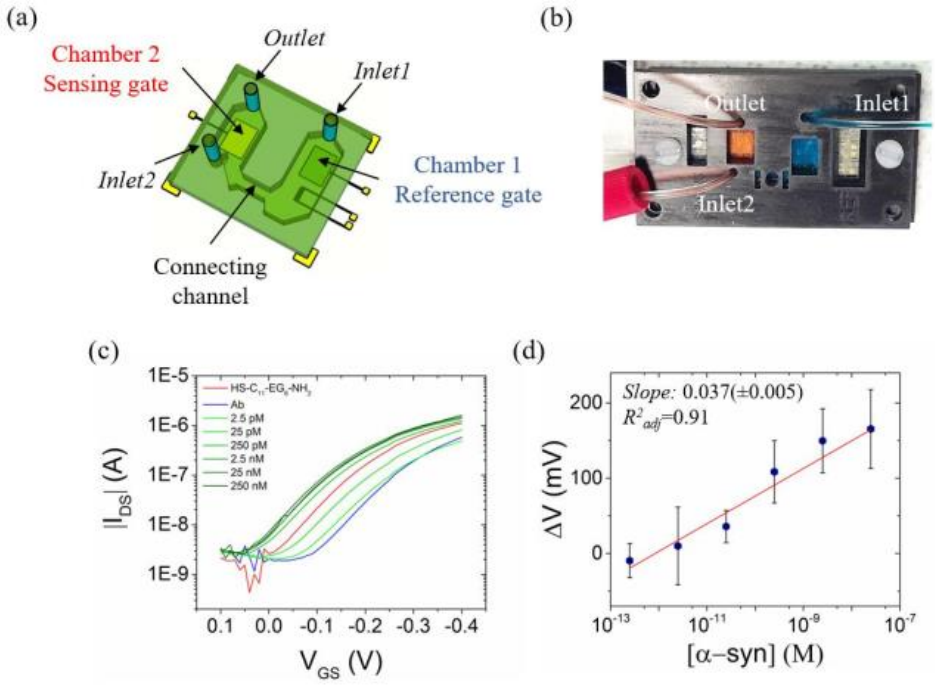

Figure 5.16: a) 3D scheme of the microfluidic setup. b) Real image of the microfluidic setup filled with red and blue dyes, the sensing chamber and the device chamber, respectively. c) Transfer characteristics (VDS=-0.1 V) of the sensing experiment employing the EGOFET with Ab-SAM-coated coplanar-gate Au gate (approach I) and d) relative calibration curve.

5.3.6 Summary of microfluidic based α-synuclein detection

A sensing platform based on a dual coplanar electrolyte-gated organic field-effect transistor in a microfluidic chamber has been demonstrated to detect *α*-synuclein, a hallmark of neurodegeneration in important pathologies like Parkinson's and Alzheimer's down to LOD equal to 0.25 pM. The optimum immuno-detection strategy based on anti-(*α*-synuclein) monoclonal antibody was inferred by a comparative study of two surface functionalisation routes of the gate electrode. Both showed similar sensitivities and LOD values, but they showed different response ranges, namely approach II had a wider range than approach I (*viz*. 0.25 pM - 250 nM versus 0.25 pM - 1 nM, respectively). The microfluidics layout has been designed to avoid crosscontamination between the sensing gate and the organic semiconductor. Such an approach allowed the *in-situ* functionalisation of the sensing gate and the electrical tests with reference solutions of *α*-synuclein. The herein reported devices combine the high sensitivity and short measurement tests, with the electrical readout and the simplicity and upscaling compatibility of the fabrication methods employed. Thus, these devices showed excellent potential for the prognostics and diagnosis of synucleinopathies such as PD, and also can provide a promising label-free tool for gaining insights into the role of *α*-synuclein and its aggregation mechanism, which is pivotal for a comprehensive understanding of such neurodegenerative diseases. Future work will be devoted to fabricating technologically more advanced devices to validate them in a larger set of samples and test the label-free sensors reported using real samples from patient's fluids.

5.4. Integration of the four mixers with EGOFET

In the previous Chapter 4, the simulations and validation of the controlled diffusion mixer are shown. It is possible to have a serial dilution with only one mixer, which is explained in details. In order to achieve also the integration with the biosensor I prototyped this device with 4 mixers in series, therefore the mixer achieves the half of the initial concentration after the geometry optimization and one dilution of one order of magnitude is achieved with 4 mixers in a row.

Each mixer has two outlets, which are used one for buffer line and other for measuring and each of them are connected to the previous mixer. In total, there are 4 buffer inlets and one inlet for mother solution. Each mixer has the channel width and height of 400 μm. Overall dimension of the device with all 4 mixers is 11,5cm x 6, 5 cm and the sketch and the picture of the device could be seen in Figure 5.17. The master of the microfluidics is fabricated with 3D printer, and then replica moulding is used with PDMS for the prototype. The device is sealed with the mechanical clamps. To test any leakages from the microfluidics, the blue and yellow dye colours are used. In Figure 5.18 a,b it could be seen.

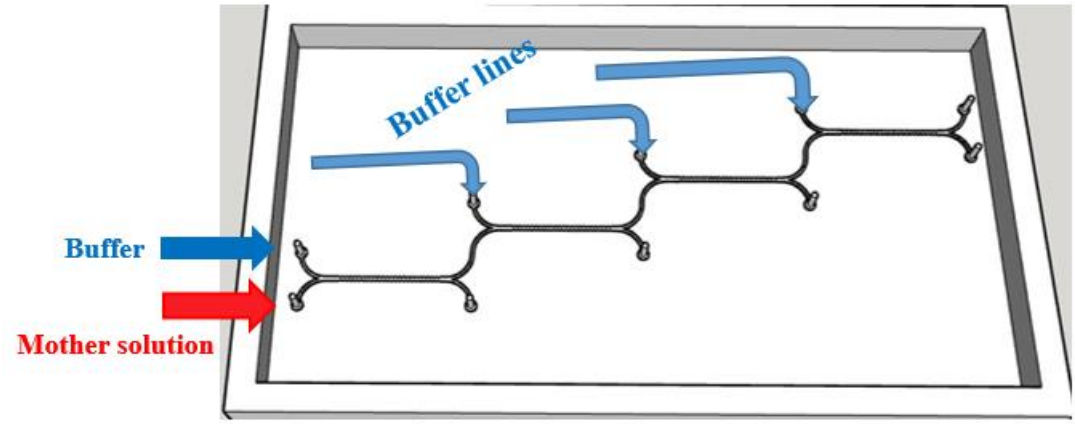

Figure 5.17: a) Sketch Up design for 4 mixers in series with the buffer lines and mother solution line.

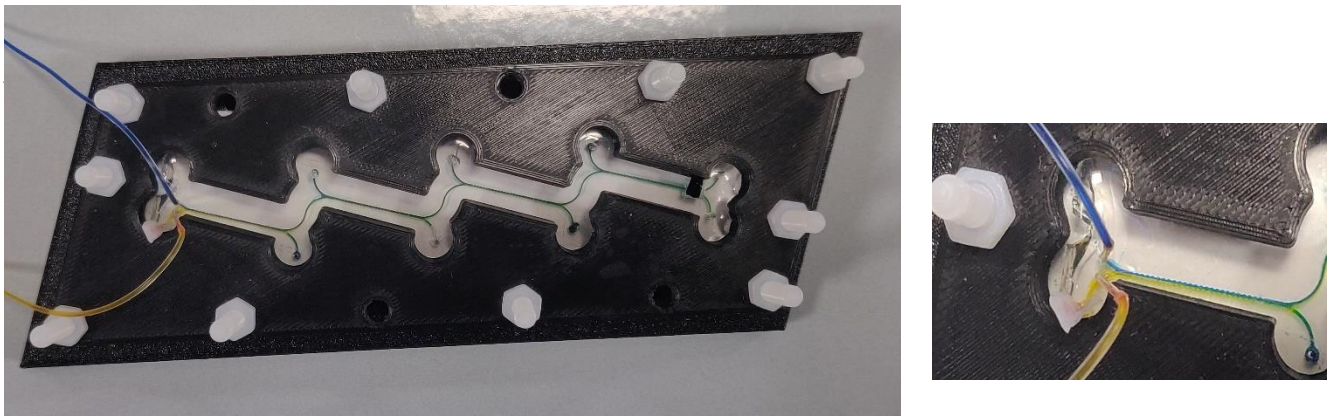

Figure 5.18: a) The four mixers in series, mechanically clamped and tested with the dye colours. b) Zoom picture of the first mixer with the blue and yellow dye colour.

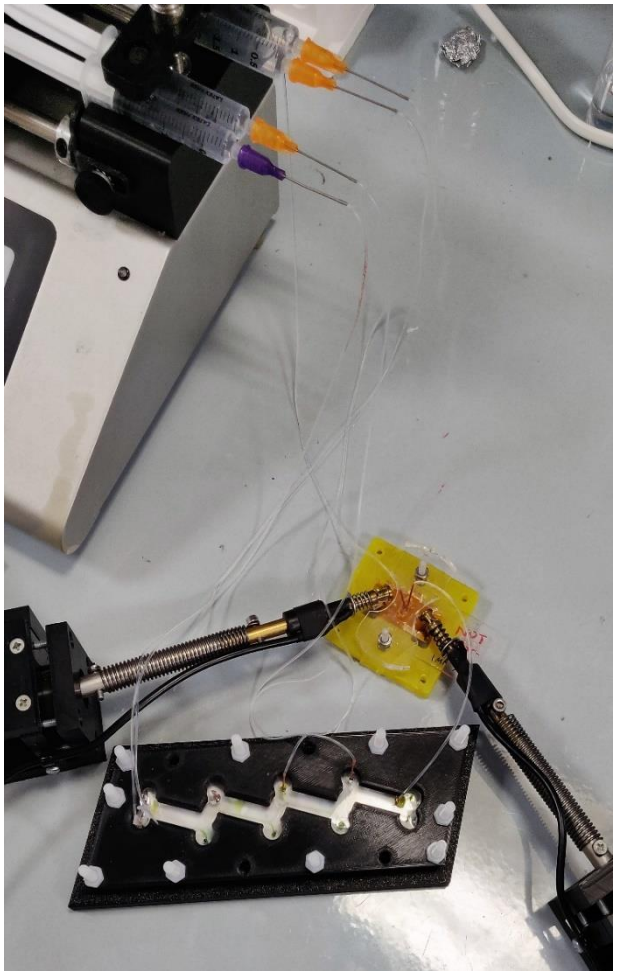

Figure 5.19: The measurement set-up with the syringe pump and SMU. EGOFET is connected through Electrolyte Bridge to the microfluidic device with 4 mixers.

After checking the microfluidics, it is integrated with TIPS-pentacene based EGOFET through Electrolyte Bridge, with gold wire gate (1mm diameter) put alternatively at the outlet of each H-mixer. For buffer, PBS (0.1 mM concentration, pH 7.2) is used, whereas 3-3-mercaptopropanol (1 mg/ml) is chosen for the mother solution. The reference level is measured with PBS, without any other solution. 3-3-mercaptopropanol is a type of alkanethiol moiety, which forms organic monolayer (SAM) on top of the gold gate. This can be detected very easily with EGOFET, since the gate work function changes and it is reflected on EGOFET transfer characteristics. After each mixer, the measurements are performed to see the different concentration of the SAMs. As expected, after each dilution, the solution was more diluted, causing the increase of the current. Since the concentration of SAM after first dilution is higher compared to the others, it has the lowest current.

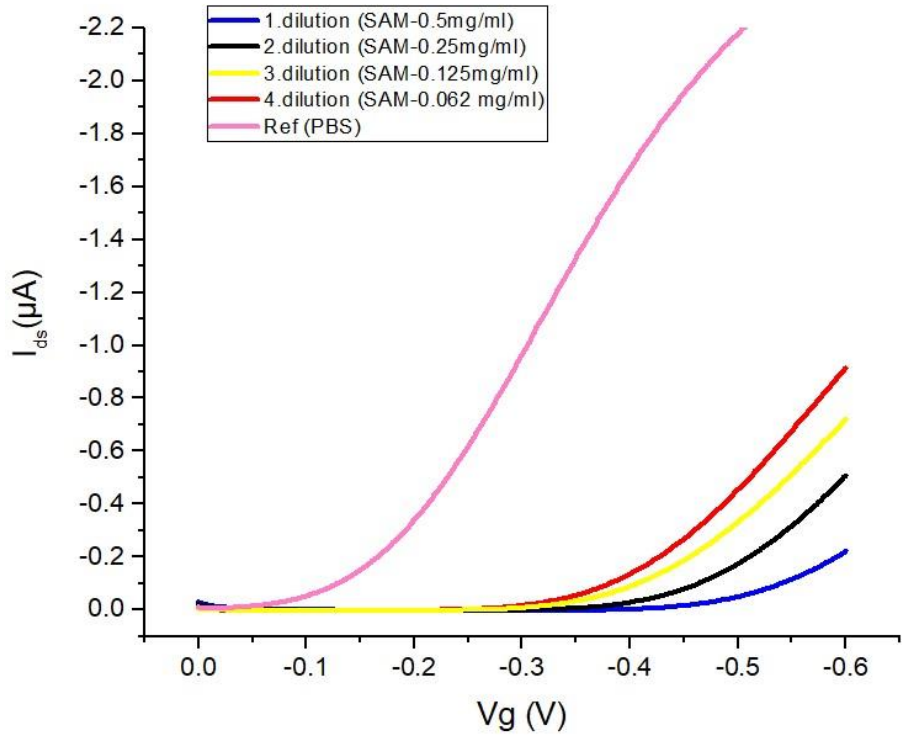

Figure 5.20: The transfer curves for 3-3-mercaptopropanol after being diluted with the buffer PBS. Reference level is measured just with PBS. After each mixer, the measurements are performed to see the different concentration of the SAMs.

5.5 Integration of microfluidic devices with OECTs for biosensing

In the framework of the MSCA Action BORGES in which I was involved, I made design and fabrication of several prototypes for the integration of different kind of biosensors, such as organic electrochemical transistors, based on polymer electrolytes PEDOT:PSS, or dual biosensors SPR-FET, based on coated optical fibre and graphene FET. The following examples are achieved with the collaboration of Pamela Allison Manco Urbina, fellow early stage research from BORGES (MSCA –ITN- ETN grant agreement no. 813863). In these examples, the sensing unit is based on PEDOT:PSS and the different biomarkers such as IL-1b and IL-6 are chosen for the detection.

5.5.1 Biosensor for detection of IL-1b

Interleukin-1 β is a pro inflammatory cytokine that modulates neurotoxic neurotransmission [85]. biosensor for its detection consists in a PEDOT:PSS based organic electrochemical transistor and a PDSM microfluidic for fluid confinement and perfusion. Firstly, the transistor response is tested for the changes in ionic strength with distilled water versus 50mM Phosphate Buffer solution. A peristaltic pump with the flowrate of 15 rpm is used for the fluid flow.

From Figure 5.22, it can be seen that the sensor was quite sensitive to the changes in ionic strength of the solutions. For the detection of IL-1b with the sensor, the current over time is recorded. First 50 mM Phosphate Buffer (PB) solution, then Assay Buffer (AB) is flushed. Assay Buffer is consisted of 0.1% BSA and 0.05% Tween20 in 50mM PB solution. Then, different concentrations (1pM, 10 pM, 50 pM) of IL-1β in AB solution are tested. The device response could be seen in Figure 5.23 with the current peaks. The current increases with the increasing concentration of analyte of IL-1b. Each current peak corresponded to the specific concentration.

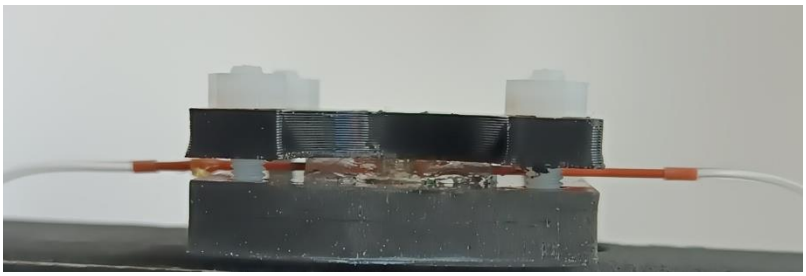

Figure 5.21: Biosensor for detection of IL-1b, which is integrated with PDMS microfluidics.

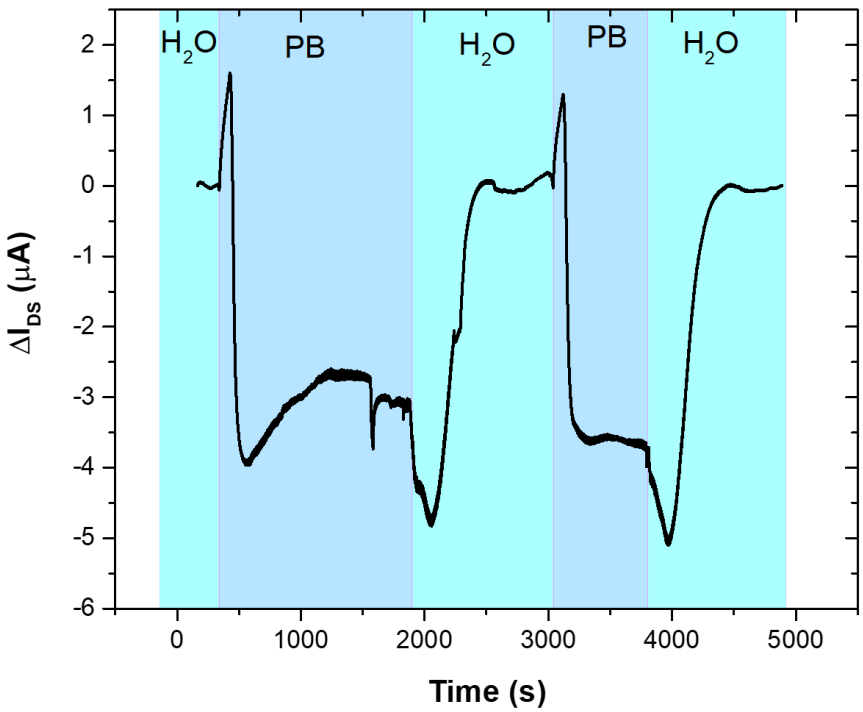

Figure 5.22: Testing transistor response to changes in ionic strength with distilled water vs 50mM Phosphate Buffer solution.

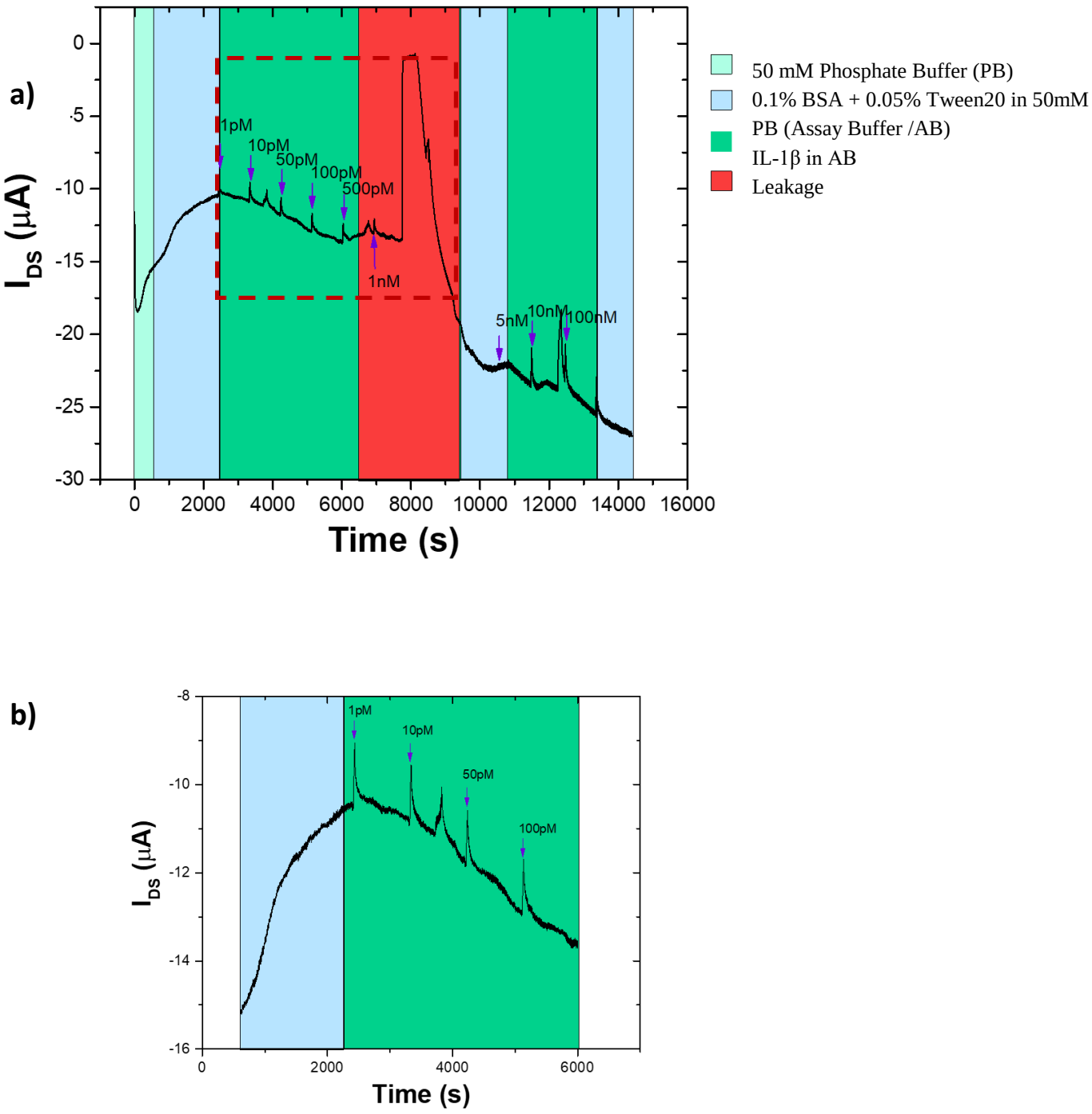

Figure 5.23: a) The current of the device is recorded over time. Different concentrations of IL-1β in AB solution are tested. The current peaks are corresponded to the specific concentrations. b) Close up of the region in the graph with the current peaks for different concentrations like 1 pM, 10pM, 50 pM, 100pM].

5.5.2 Detection of IL-6 with Extended Gate - OECT Biosensor

For detection of IL-6, the Extended-Gate OECT architecture is chosen, which can be seen in Figure 5.24 and 5.25. The main principle of the extended gate is that the changes in the electrochemical potential at the extended gate produce changes in the other gate electrochemical potential, since both of the gates are physically connected. Those changes modulate the drain current upon binding of the target molecule. Assay Buffer (AB) and different concentrations of IL-6 in Assay Buffer are run through the OECT. An increase in the current with increasing concentrations of the analyte (interleukin 6) could be seen in the Figure 5.26. However, it could be seen between 8000 and 10000s, the device was not functioning normally and there is a random increase of the current. This occurs due to the evaporation of the Electrolyte on the gate-channel chamber.

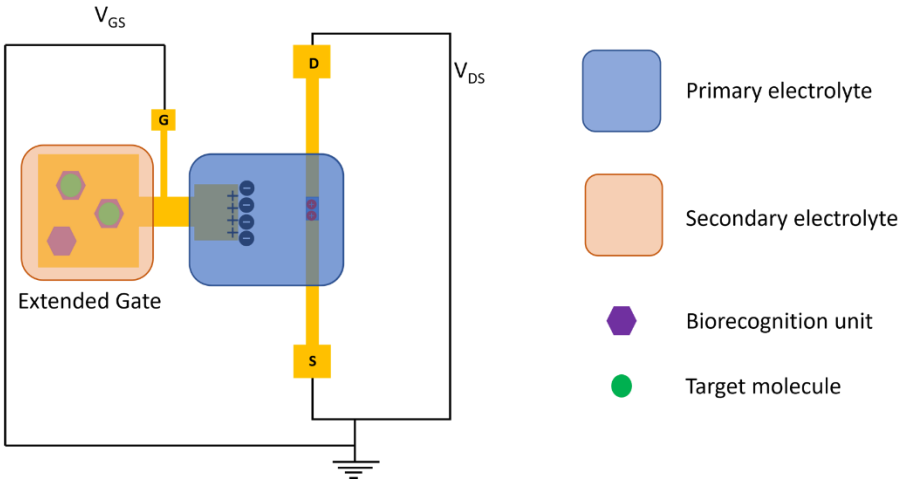

Figure 5.24: Schematic presentation of the extended gate organic electrochemical transistor (OECT) with the primary and secondary electrolyte.

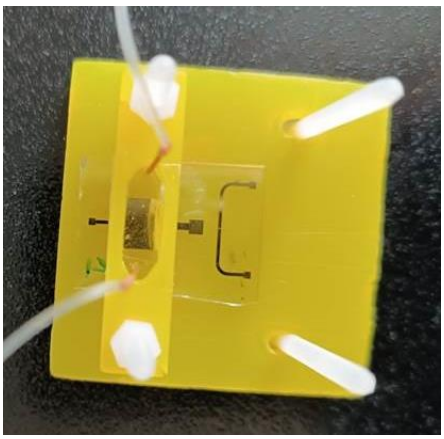

Figure 5.25: Picture of the extended gate-OECT integrated with the microfluidics and tubings, sealed with the mechanical clamp.

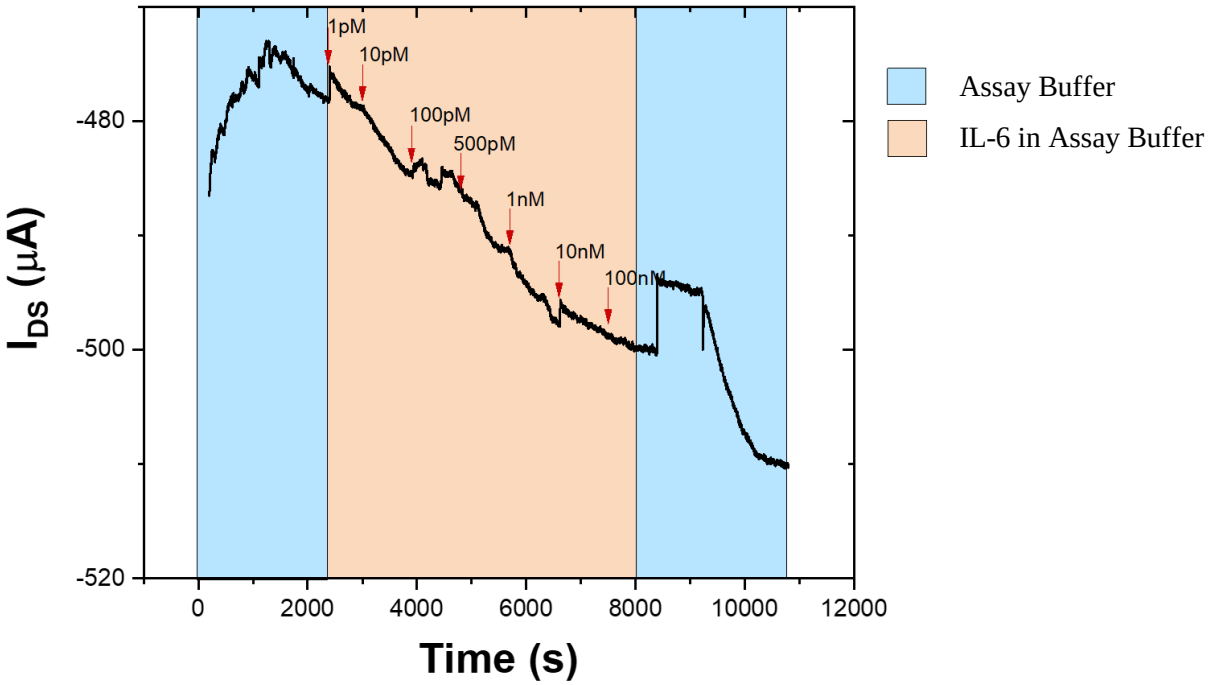

Figure 5.26: The current of the device is recorded over time. An increase in the current could be seen with increasing concentrations of the analyte (IL-6). The concentration of Il-6 in Assay Buffer is in the range 1pM and 100 nM.

5.6 References

[1] Whitesides G. M., The origins and the future of microfluidics, *Nature*, 442, 2006: 368–373.

[2] Tomeh Mhd Anas and Xiubo Zhao, Recent Advances in Microfluidics for the Preparation of Drug and Gene Delivery Systems, *Molecular pharmaceutics* vol. 17,12,2020: 4421-4434.

[3] Berlanda Simon F. et al, Recent Advances in Microfluidic Technology for Bioanalysis and Diagnostics, *Anal. Chem.* 2021: 93, 1, 311–331

[4] Barbosa, Ana I, and Nuno M Reis. , A critical insight into the development pipeline of microfluidic immunoassay devices for the sensitive quantitation of protein biomarkers at the point of care, *The Analyst* vol. 142, 6, 2017: 858-882.

[5] Asiaei Sasan, Nieva Patricia M., Studying the kinetics of thiols' self-assembled monolayer formation in microfluidic channels, Particulate Science and Technology, 2016: 397-406.

[6] Loo Jacky F.C. et al, Integrated Printed Microfluidic Biosensors, Trends in Biotechnology Volume 37, Issue 10, 2019: 1104-1120.

[7] Islam S., Shukla S., Bajpai V.K. *et al.*, Microfluidic-based graphene field effect transistor for femtomolar detection of chlorpyrifos, Sci Rep 9, 2019: 276.

[8] Annese V.F., Hu C., Integrating Microfluidics and Electronics in Point-of-Care Diagnostics: Current and Future Challenges, Micromachines 2022:13, 1923.

[9] Dorfman Kevin D., Adrahtas Demetra Z., Thomas Mathew S., Frisbie C. Daniel,Microfluidic opportunities in printed electrolyte-gated transistor biosensors, Biomicrofluidics 14, 2020: 011301.

[10] Parkula, Vitaliy et al., Harnessing Selectivity and Sensitivity in Electronic Biosensing: A Novel Lab-on-Chip Multigate Organic Transistor.,*Analytical chemistry* vol. 92,13, 2020: 9330-9337.

[11] Sensi Matteo et al., Anti-drug antibody detection with label-free electrolyte-gated organic field-effect transistors, Chem. Commun., 57, 2021: 367-370.

[12] Macchia, Eleonora et al. "Organic Field-Effect Transistor Platform for Label-Free, Single-Molecule Detection of Genomic Biomarkers." *ACS sensors* vol. 5, (6), 2020: 1822-1830.

[13] Berto M. et al., EGOFET Peptide Aptasensor for Label-Free Detection of Inflammatory Cytokines in Complex Fluids, Advanced Biosystems vol.2 ,2, 2018: 1-8.

[14] Di Lauro M. et al Liquid-Gated Organic Electronic Devices Based on High-Performance Solution-Processed Molecular Semiconductor. Advanced Electronic Materials 2017; 3(9): 1–6.

[15] Ricci Simona et al., Label-free immunodetection of α-synuclein by using a microfluidics coplanar electrolyte-gated organic field-effect transistor, Biosensors and Bioelectronics, 2020: 167, 112433.

[16] Selvaraj Meenu et al., Label Free Detection of MiRNA-21 with Electrolyte Gated Organic Field Effect Transistors (EGOFETs)." Biosensors and Bioelectronics 182, 2020: 113144.

[17]Solodka K. et al., Detection of Neurofilament Light Chain with Label-Free Electrolyte-Gated Organic Field-Effect Transistors, *Advanced Materials Interfacies,* Volume 9, Issue 11, 2022.

[18] Urbina Pamela A. M., Physical insights from the Frumkin isotherm applied to electrolyte gated organic transistors as protein biosensors, J. *Mater. Chem. C*, 2021:9, 10965-10974.

[19] Stoliar et al., Charge Injection Across Self-Assembly Monolayers in Organic Field-Effect Transistors: Odd-Even Effects, *J. Am. Chem. Soc.* 2007: 129, 20, 6477–6484.

[20] Elgrishi, N. et al. A Practical Beginner's Guide to Cyclic Voltammetry. J. Chem. Educ. 95, 2018; 197–206.

[21] Casalini Stefano et al., Multiscale Sensing of Antibody–Antigen Interactions by OrganicTransistors and Single-Molecule Force Spectroscopy, *ACS Nano* 2015: 9, 5, 5051–5062

[22] Berto M. et al., Label free detection of plant viruses with organic transistor biosensors, Sensors and Actuators B: Chemical Vol. 281, 2019: 150-156.

[23] Leonardi F. et al, Modification of the gate electrode by self-assembled monolayers in flexible electrolyte-gated organic field effect transistors: Work function: Vs. capacitance effects, RSC Advances Vol. 8, 2018: 48, 27509-27515.

[24] Casalini Stefano et al, Self-assembled monolayers in organic electronics, Chemical Society Reviews, Vol.46, 2017: 40-71.

[25]Liu C. et al., Contact engineering in organic field-effect transistors, Mater. Today, 2015: 18, 79–96.

[26] Damos Flavio S. et al. Determination of Thickness, Dielectric Constant of Thiol Films, and Kinetics of Adsorption Using Surface Plasmon Resonance. Langmuir 2005; 21(2): 602–9.

[27]Kumakli Hope et al. Observing Real-Time Formation of Self-Assembled Monolayers on Polycrystalline Gold Surfaces with Scanning Electrochemical Cell Microscopy *Langmuir* 2022;,38, 30, 9148–9156.

[28] Engvall E, Perlmann P. Enzyme-linked immunosorbent assay (ELISA) quantitative assay of immunoglobulin G. Immunochemistry 1971; 8(9):871–74.

[29] Kaisti M. Detection principles of biological and chemical FET sensors. Biosensors and Bioelectronics Elsevier B.V. 2017; 98:437–48.

[30] Guo J, Ai Y, Cheng Y, et al. Volumetric measurement of human red blood cells by MOSFET based microfluidic gate. Electrophoresis 2015; 36:1862–65.

[31] Kergoat L, Herlogsson L, Braga D, et al. A water-gate organic field-effect transistor. Advanced Materials 2010; 22(23):2565–69.

[32] Kergoat L, Piro B, Berggren M, et al. Advances in organic transistor-based biosensors: From organic electrochemical transistors to electrolyte-gated organic field-effect transistors. Analytical and Bioanalytical Chemistry 2012; 402(5):1813–26.

[33] Rivnay J, Inal S, Salleo A, et al. Organic electrochemical transistors. Nature Reviews Materials 2018; 3:17086.

[34] Jonsson A, Inal S, Uguz L, et al. Bioelectronic neural pixel: Chemical stimulation and electrical sensing at the same site. Proceedings of the National Academy of Sciences 2016; 113(34):9440–45.

[35] Cramer T, Chelli B, Murgia M, et al. Organic ultra-thin film transistors with a liquid gate for extracellular stimulation and recording of electric activity of stem cell-derived neuronal networks. Physical Chemistry Chemical Physics 2013; 15(11):3897–905.

[36] Campana A, Cramer T, Simon DT, et al. Electrocardiographic recording with conformable organic electrochemical transistor fabricated on resorbable bioscaffold. Advanced Materials 2014; 26(23):3874–78.

[37] Desbief S, Casalini S, Guerin D, et al. Electrolyte-gated organic synapse transistor interfaced with neurons. Organic Electronics Elsevier B.V 2016; 38:21–28.

[38] Burgt Y Van De, Lubberman E, Fuller EJ, et al. A non-volatile organic electrochemical device as a low-voltage artificial synapse for neuromorphic computing. Nature Materials 2017; 16(4):414–18.

[39] Casalini S, Leonardi F, Cramer T, et al. Organic field-effect transistor for label-free dopamine sensing. Organic Electronics Elsevier B.V. 2013; 14(1):156–63.

[40] Wang N, Yang A, Fu Y, et al. Functionalized Organic Thin Film Transistors for Biosensing. Accounts of Chemical Research American Chemical Society 2019; 52:277–87

[41]Torsi L, Magliulo M, Manoli K, et al. Organic field-effect transistor sensors: A tutorial review. Chemical Society Reviews 2013; 42(22):8612–28.

[42]Torsi L, Farinola GM, Marinelli F, et al. A sensitivity-enhanced field-effect chiralsensor. Nature Materials 2008; 7(5):412–17.

[43]Magliulo M, Tullio D De, Vikholm-Lundin I, et al. Label-free C-reactive protein electronic detection with an electrolyte-gated organic field-effect transistor-based immunosensor. Analytical and Bioanalytical Chemistry Analytical and Bioanalytical Chemistry 2016; 408(15):3943–52.

[44] Berto M, Casalini S, Lauro M Di, et al. Biorecognition in organic field effect transistors biosensors: The role of the density of states of the organic semiconductor. Analytical Chemistry 2016; 88(24):12330–38.

[45] Magliulo M, Mallardi A, Mulla MY, et al. Electrolyte-gated organic field-effect transistor sensors based on supported biotinylated phospholipid bilayer. Advanced Materials 2013;25(14):2090–94.

[46] Macchia E, Manoli K, Holzer B, et al. Single-molecule detection with a millimetre-sized transistor. Nature Communications Springer US 2018; 9(1).

[47] Guo J. Uric Acid Monitoring with a Smartphone as the Electrochemical Analyzer. Analytical Chemistry 2016; 88:11986–89.

[48] Huang X, Xu D, Chen J, et al. Smartphone-based analytical biosensors. Anales de la Quimica Royal Society of Chemistry 2019; 143:5339–51.

[49] Zeng F, Duan W, Zhu B, et al. Paper-Based Versatile Surface-Enhanced Raman Spectroscopy Chip with Smartphone-Based Raman Analyzer for Point-of-Care Application. Analytical Chemistry 2019; 91:1064–70.

[50] Xu K, Zhou R, Takei K, et al. Toward Flexible Surface-Enhanced Raman Scattering (SERS) Sensors for Point-of-Care Diagnostics. Advanced Science 2019; 6(16):1900925.

[51] Xu D, Huang X, Guo J, et al. Biosensors and Bioelectronics Automatic smartphone-based microfluidic biosensor system at the point of care. Biosensors and Bioelectronic Elsevier B.V. 2018; 110(February):78–88.

[52]Goedert M, Jakes R, Spillantini MG. The Synucleinopathies: Twenty Years on. Journal of Parkinson's Disease 2017; 7:S53–71.

[53]Gould N, Mor DE, Lightfoot R, et al. Evidence of native α-synuclein conformers in the human brain. Journal of Biological Chemistry 2014; 289(11):7929–34.

[54]Spillantini MG, Goedert M. The Alpha-Synucleinopathies : Parkinson's Disease, Dementia with Lewy Bodies, and Multiple. Annals New York Academy of Sciences 2000; 920:16–27

[55]Chang CW, Yang SY, Yang CC, et al. Plasma and Serum Alpha-Synuclein as a Biomarker of Diagnosis in Patients With Parkinson's Disease. Frontiers in Neurology 2020;10(January):1–7.

[56]Twohig D, Nielsen HM. α -synuclein in the pathophysiology of Alzheimer's disease. Molecular Neurodegeneration Molecular Neurodegeneration 2019; 14:1–19.

[57]Wennström M, Surova Y, Hall S, et al. Low CSF Levels of Both α-Synuclein and the α-Synuclein Cleaving Enzyme Neurosin in Patients with Synucleinopathy. PLoS ONE 2013;8(1).

[58]Shi M, Zabetian CP, Hancock AM, et al. Significance and confounders of peripheral DJ-1 and alpha-synuclein in Parkinson's disease. Neuroscience Letters Elsevier Ireland Ltd 2010; 480(1):78–82.

[59]Bougea A, Stefanis L, Paraskevas GP, et al. Plasma alpha-synuclein levels in patients with Parkinson's disease: a systematic review and meta-analysis. Neurological Sciences Neurological Sciences 2019; 40(5):929–38.

[60]Betancor L, López-Gallego F, Hidalgo A, et al. Different mechanisms of protein immobilization on glutaraldehyde activated supports: Effect of support activation and immobilization conditions. Enzyme and Microbial Technology 2006; 39(4):877–82.

[61]Walt DR, Agayn VI. The chemistry of enzyme and protein immobilization with glutaraldehyde. TrAC - Trends in Analytical Chemistry 1994; 13(10):425–30.

[62]Choe W, Durgannavar TA, Chung SJ. Fc-binding ligands of immunoglobulin G: An overview of high affinity proteins and peptides. Materials 2016; 9(12):994.

[63]Song HY, Zhou X, Hobley J, et al. Comparative study of random and oriented antibody immobilization as measured by dual polarization interferometry and surface plasmon resonance spectroscopy. Langmuir 2012; 28(1):997–1004.

[64]Young MB, Oh BK, Lee W, et al. Study on orientation of immunoglobulin G on protein G layer. Biosensors and Bioelectronics 2005; 21(1):103–10.

[65]Iori F, Corni S, Felice RD. Unraveling the interaction between histidine side chain and the Au(111) surface: A DFT study. Journal of Physical Chemistry C 2008; 112(35):13540–45.

[66] Yang Z, Zhao YP. Adsorption of His-tagged peptide to Ni, Cu and Au (1 0 0) surfaces: Molecular dynamics simulation. Engineering Analysis with Boundary Elements 2007;31(5):402–09

[67] Pozo FG Del, Fabiano S, Pfattner R, et al. Single crystal-like performance in solution-coated thin-film organic field-effect transistors. Advanced Functional Materials 2016; 26:2379–86.

[68]Temiño I, Pozo FG Del, Ajayakumar MR, et al. A Rapid, Low-Cost, and Scalable Technique for Printing State-of-the-Art Organic Field-Effect Transistors. Advanced Materials Technologies 2016; 1(5):1–7.

[69]Zhang Q, Leonardi F, Casalini S, et al. High performing solution-coated electrolyte-gated organic field-effect transistors for aqueous media operation. Scientific Reports Nature Publishing Group 2016; 6:1–10.

[70]Campos A, Riera-Galindo S, Puigdollers J, et al. Reduction of Charge Traps and Stability Enhancement in Solution-Processed Organic Field-Effect Transistors Based on a Blended nType Semiconductor. ACS Applied Materials and Interfaces 2018; 10(18):15952–61.

[71] Leonardi F, Casalini S, Zhang Q, et al. Electrolyte-Gated Organic Field-Effect Transistor Based on a Solution Sheared Organic Semiconductor Blend. Advanced Materials 2016; 28:10311–16.

[72] Paterson AF, Treat ND, Zhang W, et al. Small Molecule/Polymer Blend Organic Transistors with Hole Mobility Exceeding 13 cm2V-1s-1. Advanced Materials 2016; 28(35):7791–98.

[73]Pérez-Rodríguez A, Temiño I, Ocal C, et al. Decoding the vertical phase separation and its impact on C8-BTBT/PS Transistors properties. ACS Applied Materials & Interfaces 2018; 10:7296–303.

[74] Temiño I, Pozo FG Del, Ajayakumar MR, et al. A Rapid, Low-Cost, and Scalable Technique for Printing State-of-the-Art Organic Field-Effect Transistors. Advanced Materials Technologies 2016; 1:1600090.

[75] Zhang Q, Leonardi F, Casalini S, et al. High performing solution-coated electrolyte-gated organic field-effect transistors for aqueous media operation. Scientific Reports Nature Publishing Group 2016; 6(November):1–10.

[76] Zhao K, Wodo O, Ren D, et al. Vertical Phase Separation in Small Molecule:Polymer Blend Organic Thin Film Transistors Can Be Dynamically Controlled. Advanced Functional Materials 2016; 26:1737–46.

[77] Kergoat L, Piro B, Berggren M, et al. DNA detection with a water-gated organic field-effect transistor. Organic Electronics: physics, materials, applications Elsevier B.V. 2012; 13(1):1–6.

[78]Roberts ME, Mannsfeld SCB, Queralto N, et al. Water-stable organic transistors and their application in chemical and biological sensors. Proceedings of the National Academy of Sciences 2008; 105(34):12134–39.

[79] Ishikawa FN, Curreli M, Chang H, et al. A Calibration Method for Nanowire Biosensors to Suppress Device-to-Device Variation. ACS Nano 2009; 3(12):3969–76.

[80]Duan X, Li Y, Rajan NK, et al. Quantification of the affinities and kinetics of protein interactions using silicon nanowire biosensors. Nature Nanotechnology Nature Publishing Group 2012; 7(6):401–07.

[81] Lee BY, Sung MG, Lee J, et al. Universal parameters for carbon nanotube network-based sensors: Can nanotube sensors be reproducible? ACS Nano 2011; 5(6):4373–79.

[82]Hammock ML, Knopfmacher O., Naab BD, et al. Investigation of protein detection parameters using nanofunctionalized organic field-effect transistors. ACS Nano 2013;7(5).

[83]Gould N, Mor DE, Lightfoot R, et al. Evidence of native α-synuclein conformers in the human brain. Journal of Biological Chemistry 2014; 289(11):7929–34.

[84] Lee PH, Lee G, Park HJ, et al. The plasma alpha-synuclein levels in patients with Parkinson's disease and multiple system atrophy. Journal of Neural Transmission 2006; 113(10):1435–39.

[85] Jackson G.D., Magnetic Resonance in Epilepsy (Second Edition) Neuroimaging Techniques CHAPTER 4 - Temporal Lobe Epilepsy 2005; Pages 99-176.

CHAPTER 6
ORGANIC TRANSISTORS FOR THE DETECTION OF OLIGONUCLEOTIDE BIOMARKERS

6.1 Introduction

In this chapter, label-free detection for miRNA with the dual gate EGOFET architecture is explained. MicroRNAs (miRNA) are a class of biomarkers whose relevance in oncology is increasing enormously, especially for neuroblastoma and lung cancer [3]. Detection of miRNA in lower concentrations in blood comes is important for cancer early diagnosis and patient monitoring. Due to these reasons, developing label-free biosensors for miRNA detection and quantification has become important.

In this chapter, the dual gate configuration of EGOFET for sensing miRNA is described. The device has the two gates, one sensing and one reference. Both gates are immersed in the electrolyte above the transistor channel. The thermodynamic model of the reaction equilibria in the experiments are described. The binding free energy characteristic of the hybridization on the device surface was found to be approximately 20% lower with respect to the reaction in solution, hinting to partially inhibiting effect of the surface and presence of competing reactions [32].

6.2 Label free detection of miRNA-21 with Electrolyte Gated Organic Field Effect Transistors

MicroRNAs (miRNA) are a class of biomarkers whose relevance in oncology is enormously increasing, especially for neuroblastoma and lung cancer [3]. Detection of miRNA circulating in blood show promise for cancer early diagnosis and patient monitoring [2] besides providing insights into the cellular path of disease. Since miRNAs with different sequences may act either as tumor promoter or as tumor suppressor in the presence of interacting drugs [1], it turns out that accurate methods for quantification of miRNA are of potential impact for both diagnostics and study of therapeutic efficacy. For these reasons, PCR-assisted low volume analytic protocols, as well as PCR-free isothermal amplification methods, are emerging as new techniques to tackle the difficult task of counting small number of oligonucleotides in complex matrices [4].

Among the numerous miRNAs involved in disease diagnostics and therapy, miRNA-21 is one of the most studied because has been conserved through evolution of vertebrates up to humans and its main biological functions are linked with anti-apoptosis and pro-survival factors [5]. In the immune system, miRNA-21 has been shown to regulate the gene coding for inflammation biomarker IL-12 [6]. Temporary silencing of miRNA-21 was correlated with cell differentiation and development in thyroid cells [7], whereas in the large majority of cancer diseases, miRNA-21 is upregulated. High levels of miRNA-21 were correlated, as promoting progression, with breast cancer [8], pancreatic cancer [9], lung cancer [10], glioblastoma [11].

The concentration of oligonucleotides is measured in clinical studies with quantitative PCR. More recently, analytical tools based on PCR-free hybridization in microfluidics appeared, where surface plasmon resonance and droplet-based microfluidics are exploited [12].

Electrochemical methods for miRNA detection were extensively investigated. An example consists of gold nanoparticles functionalized with DNA-bioreceptor and using iridium complexes for redox reactions. This approach yields femtomolar limit of detection (LOD) in controlled hybridization [13]. Another example features sensing probes, synthetized as complementary strands to the mature miRNA, anchored to a gold electrode surface by means of thiol chemistry [14], and capable to detect attomolar levels of miRNA-155 (marker of breast cancer). Optical detection, based on either absorption or fluorescence, requires labelling of the probe with either gold nanoparticles [15] or fluorescent molecules whose signal changes upon the formation of the duplex [16]. Molecular beacons, consisting of paired fluorophore and quencher [17], yield a fluorescent label upon the separation of the two parts induced by hybridization.

Label-free biosensors, based on electronic or ionic transport, transduce a specific reaction of the target analyte with a modulation of the charge transport in an inorganic [18] or organic semiconductor [19] channel, thus changing the current flowing in the channel. Electrolyte gated organic field-effect transistors (EGOFET) are able to quantify ultra-low concentrations of diverse biomarkers [20–23]. Moreover, this architecture offers the opportunity to integrate complementary techniques sensitive to biorecognition, such as fluorescence microscopy or surface plasmon resonance [24].

EGOFET enables ultrasensitive detection of antigens because the electrostatic potential of the gate electrode, which is sensitive to antigen binding at surface bound recognition sites, is capacitively coupled to the channel. An amplified shift of the Fermi level of the organic semiconductor is achieved even for low amount of biomolecules adsorbed or grafted on the gate electrode [19]. Multiple biomarkers detection is possible within the same integrated EGOFET microfluidic device, by miniaturization and multiplexing gate electrodes immersed in the electrolyte solution. Demonstration of multigate architecture was reported by our group for the detection of inflammatory biomarker TNFα using aptamer functionalization with standard manufacturing processes employed for printed circuit board production [25].

Here, we report the fabrication and assessment of an EGOFET device with dual gate architecture designed for sensing spiked solutions containing a single-stranded segment of miRNA-21 (miRNA-21-3p, also termed target analyte (T)) at concentrations down to picomolar range. Our device enables differential monitoring of the electronic response of the transistor, thanks to one of the gate electrodes, termed G2, grafted with the complementary sequence bioreceptor (miRNA-21-5p, also termed probe (P)), and the other gate electrode, termed G1, functionalized with a tightly packed organic monolayer aimed to reduce the unspecific adsorption. The G1 electrode serves as an internal reference electrode, whereas the G2 electrode as the sensing electrode. Characterization of EGOFET devices allows evaluating the difference in current across the organic semiconductor, modulated by the number of target nucleotides hybridized on the sensing gate surface. Complementary information was then obtained by Surface Plasmon Resonance Imaging (SPRI) performed on the same oligonucleotide pair, providing an assessment of the surface coverage and hybridization efficiency on Au biochip. Physical parameters correlated to the signal for functionalization and hybridization reactions are the change in refractive index (SPRI) and the electronic current transduced by the organic transistor (EGOFET).

6.2.1 EGOFET in dual gate configuration

We describe first the architecture of the dual gate EGOFET designed for miRNA sensing (Figure 6.1). The electrode G1 is a gold wire functionalized with 2-Mercaptoethanol (ME) monolayer, while the electrode G2 is a gold wire, symmetric to G1 with respect to the channel, functionalized with the thiolated probe P. The sequence of P was synthesized according to a sequence reported for human miRNA-21-5p [26]. According to my protocol, before the EGOFET operations, G2 is incubated in buffer solutions spiked with different target concentrations [T].

In Figure 6.1a, we schematically depict the hybridization of the probes P grafted to G2 with the target analyte T. The electrode G2 is then immersed together with G1 in the buffer electrolyte of the device that comprises an organic semiconductor channel patterned on polyimide substrate (Kapton™, 50 μm) (Figure 6.1b). The aqueous electrolyte is contained in a polydimethylsiloxane (PDMS) reservoir. Figure 6.1c shows optical images at two different magnifications of the semiconductor channel. In particular, the optical micrograph in polarized light reveals the presence of large crystalline domains across the channel. The functionalization steps of the gate electrodes are assessed by both SPR and the electrical characterization of each EGOFET before and after each step. Details on the fabrication procedure and functionalization steps are provided in Chapter 2.6.1 and Chapter 2.6.2.

The stage holder with gate electrodes (Figure 6.1c) was removed from the electrolyte reservoir and electrode G2 was incubated in vials each containing different concentrations of T, starting from 10 pM to 300 pM.

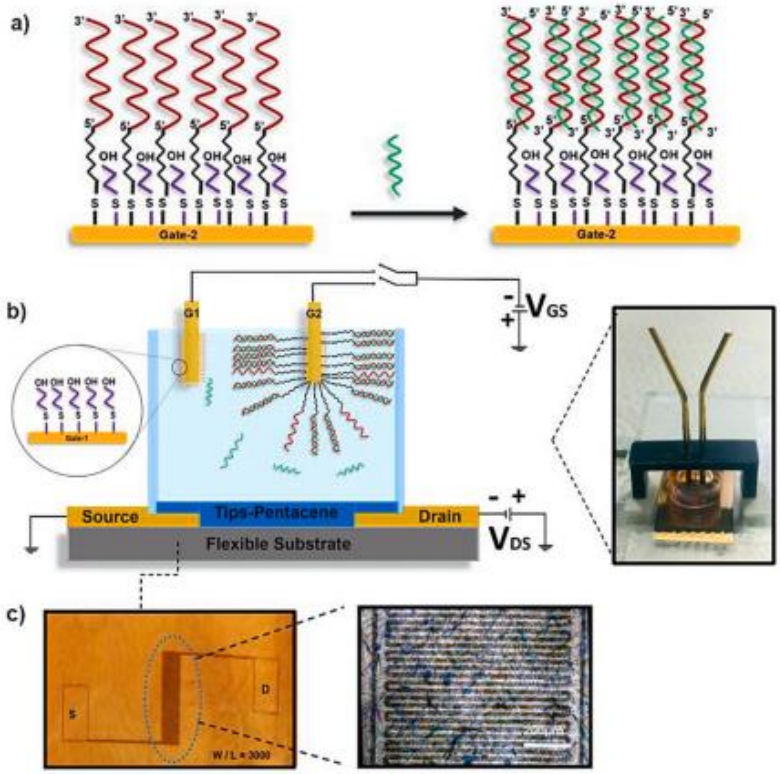

Figure 6.1: Functionalization of a) G2 with probe and 2-ME (left) and the hybridization process of the target analytes with G2 after incubation (right). b) Schematic drawing illustrating the architecture of the dual-gate EGOFET device featuring the PDMS microfluidics pool sealed on top of the Source and Drain interdigitated electrodes covered with TIPS-pentacene. c) Morphology of EGOFET showing a detail of the test pattern with interdigitated electrodes and contact pads, a polarized light microscopy image (10x objective) evidencing the crystals in the channel formed by TIPS-pentacene thin film.

6.2.2 EGOFET after hybridization

Transfer curves of the device were obtained by measuring channel current (*IDS*) upon sweeping Gate-Source voltages in the range from -0.2V to -0.9V with steps of -1 mV at a fixed Drain-Source voltage *VDS* =-0.2 V. The transfer curves of the EGOFET are acquired first by sweeping the voltage bias of reference G1, while leaving sensing G2 floating. Then, within two minutes, they were acquired by sweeping the voltage bias of sensing G2, while leaving G1 floating.

The values of both Drain-Source and Gate-Source currents were acquired to ensure that no short-circuit or faradaic process occurred. In order to evaluate the precision and reproducibility of the measurement performed with EGOFET, the laser ablation of the interdigitated electrodes and the deposition of the organic semiconductor upon the transistor channel were repeated for each experiment.

Figure 6.2 shows an example of transfer curves recorded with G1 and G2 at different concentration [T]. The extent of residual leakage current was less than 30 nA, compared to the on-current measured in the range of 0.1 to 1 μA. I recall that only G2 was previously incubated in a buffer solution spiked with the target analyte at concentration [T]. The transfer curves for the G2 gate sweeps $I_{DS}([T], V_{GS})_{G2}$ show a decrease of current with increasing concentration [T]. Conversely, the transfer curves (dashed lines) $I_{DS}([T], V_{GS})_{G1}$ are narrowly distributed around a central value of the buffer transfer curve $I_{DS}(0, V_{GS})_{G1}$. The first evidence suggests a sizable change in the charge distribution in the proximity of the gold surface of G2 is induced by the formed hybridized complex, with respect to the single-stranded oligonucleotide. This is not observed in the case of G1. Indeed the transfer characteristics acquired by sweeping G1 after the incubation of G2 in the target analyte solution exhibit modest fluctuations with respect to the curve recorded with the pure buffer solution, [T]=0. We ascribe these fluctuations to unspecific adsorption of target molecules on G1 during measurement, that may detach from G2 and diffuse through the solution. This process is depicted in the zoom of Figure 6.1b. The scarce sensitivity of the electrode G1 to [T] enables us to assume that, in the range of [T] explored, the transfer curves driven by G1 are independent on [T], viz. $\langle I_{DS}([T], V_{GS})\rangle_{G1} \approx \langle I_{DS}(V_{GS})\rangle_{G1}$.

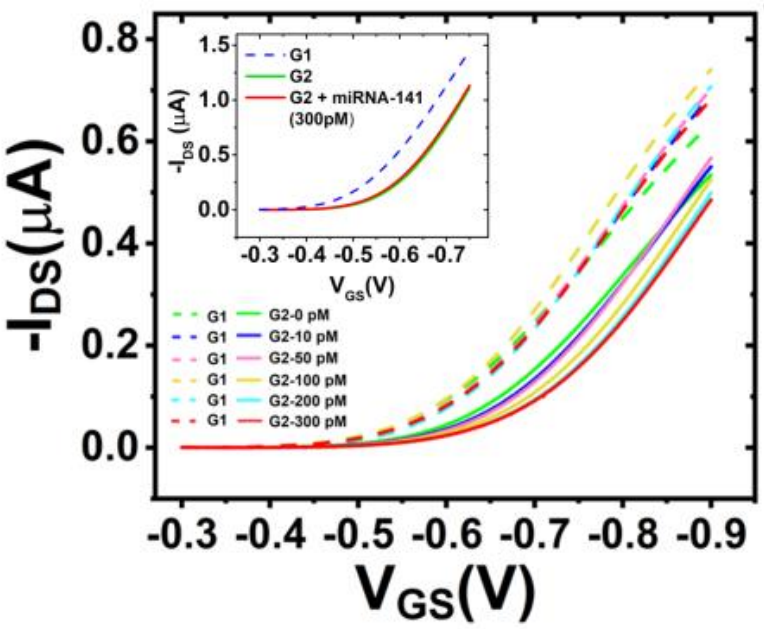

Figure 6.2: Transfer curves of EGOFET device with two-gate electrodes, characterized after incubation of both gates with solutions containing different concentrations of the target analyte; the solid lines obtained with G2 are markedly separated from the dashed curves obtained with G1 Transfer characteristics with G1 are plotted with the same color of G2 to indicate the measurement taken few minutes after G2. The response of the device to 300 pM concentrated miRNA-141 solution is plotted in the inset, confirming the selectivity of the probe.

Mean transfer curves are estimated as the logarithmic mean of N=10 measurements for each concentration by sweeping G2, and N=15 measurements for each concentration by sweeping G1:

$$\langle I_{DS}([T], V_{GS})\rangle_{G2} = 1A \cdot \langle e^{\ln[I_{DS}([T],V_{GS})/1A]}\rangle_{G2} \approx 1A \cdot e^{\langle \ln[I_{DS}([T],V_{GS})/1A]\rangle_{G2}} \quad (6.1a)$$

$$\langle I_{DS}([T], V_{GS})\rangle_{G1} = 1A \cdot \langle e^{\ln[I_{DS}([T],V_{GS})/1A]}\rangle_{G1} \approx 1A \cdot e^{\langle \ln[I_{DS}(V_{GS})/1A]\rangle_{G1}} \approx \langle I_{DS}(V_{GS})\rangle_{G1} \quad (6.1b)$$

Here the pre-factor imparts the physical dimension, and the exponent of the right equation is the logarithmic mean:

$$\langle \ln[I_{DS}([T], V_{GS})/1A]\rangle = \frac{1}{N}\sum_{i=1}^{N} \ln\left[I_{DS,i}([\mathrm{T}], V_{GS})/1A\right] \quad (6.2)$$

The experimental error is estimated as:

$$\frac{\delta I_{DS}}{\langle I_{DS}\rangle} \approx \sqrt{\frac{1}{N-1}\sum_{i=1}^{N}(\ln(I_{DS}/1A) - \langle \ln(I_{DS}/1A)\rangle^2} \quad (6.3)$$

This procedure to calculate the mean is motivated by the transfer curve spanning by orders of magnitude in the small V_{GS} range of operations: since the arithmetic mean will wash out small features because the largest transfer curve overwhelms the others, even if it were an outlier, it is preferred to adopt the logarithmic mean as detailed previously [25].

The logarithmic mean transfer curves, estimated from three devices each, are shown in Figure 2b with G1 (orange) and G2 (colours, each representing one concentration). The error is depicted by the corresponding colour shades, and as also clear from eq. 6.3 increases with the current, hence with applied V_{GS}.

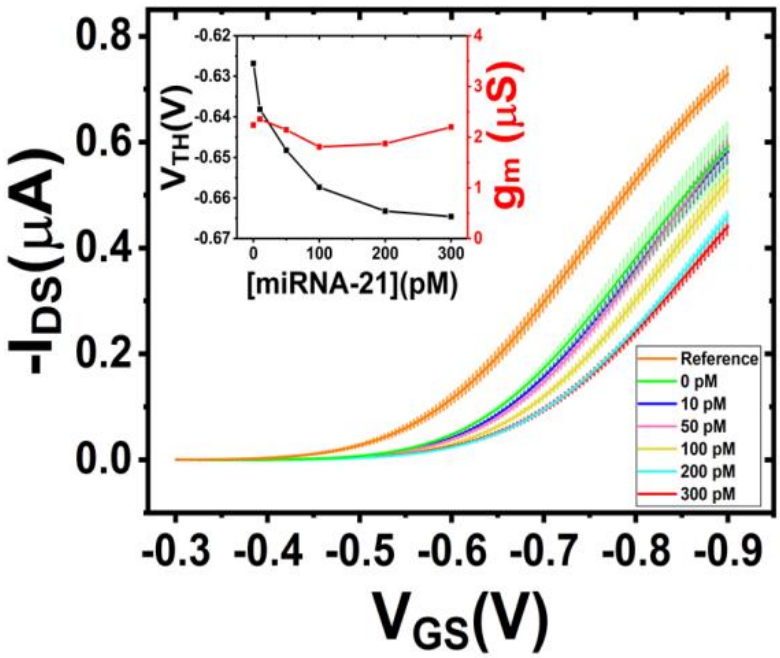

Figure 6.3: Plot of the logarithmic average of the transfer curves of G1 and G2 showing clear, distinct trends with statistical error. In the inset the decay of G2 threshold voltage is depicted with transconductance values reported to be almost constant at varying target concentration.

The logarithmic mean transfer curves, estimated from three devices each, are shown in Figure 6.3 with G1 (orange) and G2 (colors, each representing one concentration). The error is depicted by the corresponding color shades, and as clear from equation 6.3 increases with the current, hence with applied V_{GS}.

The transfer curves in Figure 6.2 and Figure 6.3 are recorded for hybridization with the target miRNA-21 solution. The measurement protocol is set to acquire the transfer curves mostly in the linear regime regime $|V_{DS}| << |V_{GS} - V_{Th}|$ that can be described according to the equation:

$$I_{DS}([T], V_{GS}) = g_m([T], V_{DS}) \cdot [V_{GS} - V_{Th}([T])] \quad (6.4)$$

Here, g_m is the transconductance that depends linearly on both V_{DS} and W/L, where W and L are the channel width and length, respectively. V_{DS} and W/L are kept fixed. The threshold voltage V_{Th} represents the internal field to overcome for turning the device on. Both transconductance and threshold voltage are, in principle, sensitive to the interaction between P and T, and hence to [T]. In particular hybridization, that affects the surface potential of the gate G2, is reflected in the threshold voltage shift, and may also appear in g_m as the density of states may be changed.

In the inset of Figure 6.3, we show the threshold voltage and the transconductance extracted from the mean transfer curves $\langle I_{DS}([T], V_{GS})\rangle_{G2}$ by applying the linear fit eq. 4. We observe a logarithmic decay of $V_{Th,G2}$ vs [T]. On the other hand, we notice that the slope of the linear region of the transfer curves in Fig. 2b does not change substantially even when the curves are progressively offset towards more negative voltage values with increasing concentration. This is evidenced by the transconductance values in Fig. 2b right axis that exhibits a substantial invariance vs [T]. The presence of the negatively charged hybridized probe/target pair on the sensing gate explains both the absence of change in transconductance and the shift of the V_{TH} to more negative voltages. The more negative hybridized sensing layer induces a positive image charge on the electrode surface, thus making the gate electrode potential less negative.

In order to experimentally minimize the device-to-device variations, it is convenient referring the changes in the transfer curves to the mean curve of the reference electrode G1, the latter being largely insensitive to [T]. Therefore, we combine the transfer curves $\langle I_{DS}([T], V_{GS}\rangle_{G2}$ (obtained by sweeping the voltage at the sensing electrode G2), with $\langle I_{DS}(V_{GS})\rangle_{G1}$ (obtained by sweeping the voltage the reference electrode G1) to yield the signal S_{ref}:

$$S_{ref}([\mathrm{T}], V_{GS}) = 1 - \frac{\langle I_{DS}([\mathrm{T}], V_{GS})\rangle_{G2}}{\langle I_{DS}(V_{GS})\rangle_{G1}} \qquad (6.5a)$$

Similarly, in order to model the dose curve later, we define the signal *S* referred to G2 as:

$$S([\mathrm{T}], V_{GS}) = 1 - \frac{\langle I_{DS}([\mathrm{T}], V_{GS})\rangle_{G2}}{\langle I_{DS}(0, V_{GS})\rangle_{G2}} \qquad (6.5b)$$

The brackets indicate the averaging process of the transfer curves that is described in the previous section. The definition imposes a relation between *S* and S_{ref} in terms of $A(V_{GS}) = \frac{\langle I_{DS}(V_{GS})\rangle_{G1}}{\langle I_{DS}(0,V_{GS})\rangle_{G2}}$

$$S([\mathrm{T}], V_{GS}) = [1 - A(V_{GS})] + S_{ref}([\mathrm{T}], V_{GS}) \cdot A(V_{GS}) \tag{6.6}$$

Thus, the signal S_{ref} measured with respect to the reference electrode must be both rescaled and offset to be reconducted to the signal recorded with the gate G2 alone. The error on the signal is estimated by error propagation starting from the error eq. 6.3:

$$\delta S([\mathrm{T}], V_{GS}) = \delta A(V_{GS})\left[1 + S_{ref}([\mathrm{T}], V_{GS})\right] + A(V_{GS}) \cdot \delta S_{ref}([\mathrm{T}], V_{GS}) \tag{6.7a}$$

$$\delta S([\mathrm{T}], V_{GS}) = \left\{\frac{\delta\langle I_{DS}\rangle_{G1}}{\langle I_{DS}\rangle_{G1}} + \frac{\delta\langle I_{DS}\rangle_{G2}}{\langle I_{DS}\rangle_{G2}}\right\} \cdot A(V_{GS})\left[1 + S_{ref}([\mathrm{T}], V_{GS})\right] + A(V_{GS}) \cdot \left[1 - S_{ref}([\mathrm{T}], V_{GS})\right] \cdot \left\{\frac{\delta\langle I_{DS}([\mathrm{T}],V_{GS})\rangle_{G2}}{\langle I_{DS}([\mathrm{T}],V_{GS})\rangle_{G2}} + \frac{\delta\langle I_{DS}\rangle_{G1}}{\langle I_{DS}\rangle_{G1}}\right\} \approx 2 \cdot A(V_{GS}) \cdot \left\{\frac{\delta\langle I_{DS}([\mathrm{T}],V_{GS})\rangle_{G2}}{\langle I_{DS}([\mathrm{T}],V_{GS})\rangle_{G2}} + \frac{\delta\langle I_{DS}\rangle_{G1}}{\langle I_{DS}\rangle_{G1}}\right\} \tag{6.7b}$$

The assumption in eq. 6.7b is that the relative errors of the transfer curves acquired upon G2 sweeping are comparable. In eq. 6.7b we omitted the dependence of V_{GS} for sake of brevity.

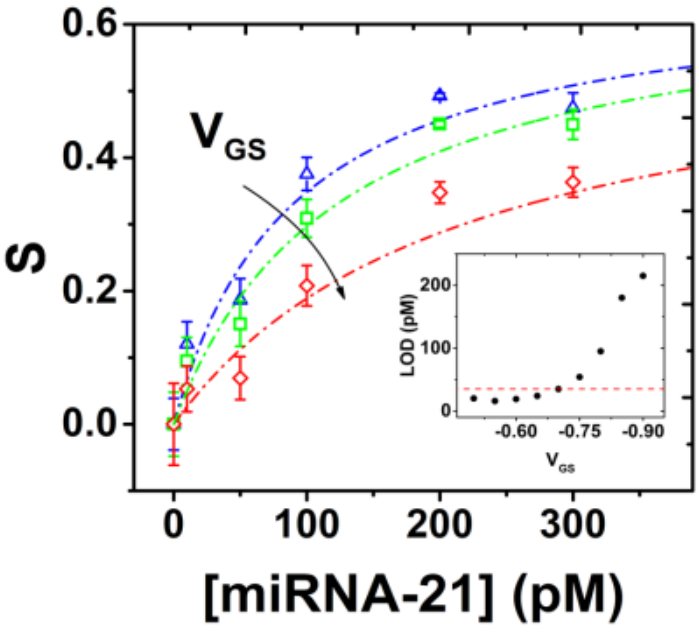

Figure 6.4: Fitting of the dose curves calculated at three different VGS (-0.6 blue, -0.7 green, -0.8 red) V using eq. 18; inset, plot of LOD vs VGS, extracted from the fitting curve value corresponding to three times the error reported for measurements without the target analyte (dashed line indicating the value of 35 pM as maximum for VGS ≥ -0.7 V.

The dose curves shown in Figure 6.4 compare *Sref* and the signal *S* from eq. 6.6 vs [T] both acquired at VGS=-0.6, -0.7, -0.8 V. The signal *S* slows down at concentrations approaching 300 pM. we estimate, based on the transfer curves and the error width obtained from 20experiments, that the sensitivity of the biosensor is below 50 pM, with a LOD taken to be the value of concentration corresponding to $S = 3 \cdot \delta S([0], V_{Gs})$ in the fit reported in Figure 6.4. The LOD is approximately equal to 35 pM for gate voltages below -0.75 C (inset Figure 6.4), while the LOD increases and the sensitivity (slope) decreases as V_{GS} becomes more negative (see the curves in Figure 6.4).

6.2.3 Thermodynamics of the biorecognition events

We derive now an analytical function that describes the dose curves as in Figure 6.4 for the dual gate device. The aim is not only to devise an invertible function for the dose curve, but to derive it from a chemical model that enables us to understand how biorecognition is translated into the device response. In doing this, we assume that the device (system) is in quasi-equilibrium conditions, thus we neglect this time kinetic effects. Thus, we draw the different equilibria that characterize our system, and we envision four relevant equilibria.

We start from G2 that is functionalized with the probe P, whose activity (that we take equal to concentration) is termed p_0. G2 is first incubated in the solution containing the target T at initial concentration t_0, then a first equilibrium (hybridization on the G2 electrode surface) is attained:

$$P + T \rightleftharpoons PT \tag{6.8}$$

Here *PT* is the probe-target pair concentration whose equilibrium constant K_{PT} is the binding association constant on the electrode:

$$K_{PT} = \frac{[PT]}{[P][T]} = \frac{[PT]}{(p_0 - [PT])[T]} = \frac{(p_0 - [P])}{[P][T]} \tag{6.9a}$$

$$K_{PT} = \frac{x_{eq}}{(1 - x_{eq})(t_0 - x_{eq} \cdot p_0)} = \frac{x_{eq}}{(1 - x_{eq})(1 - x_{eq} \cdot p_0 / t_0) \cdot t_0} \tag{6.9b}$$

Here, $[T]$ is the concentration of target in solution, $[P]$ concentration of the free probe on the electrode, and $x_{eq} = [PT]/p_0$ is the equilibrium fraction of the hybridized probe. Langmuir modelling described the behaviour of DNA and RNA sensors based on fluorescence or electrochemistry, although the hybridization process may involve multiple reactions in competition with detection and characteristic reaction kinetics may also be regulated by hindrance effects between target and probe oligonucleotides or by the presence of the surface itself [27]. The signal$S([T])$, dependence on x_{eq} can be described as in the Langmuir isotherm:

$$S = S_{max} x_{eq} = S_{max} \frac{K_{PT} \cdot [T]}{1 + K_{PT} \cdot [T]} \quad (6.10)$$

We record the signal after the electrode G2 has equilibrated in the buffer solution of the device. Hence we write the other equilibria involving G2 and the buffer solution:

$$P \rightleftharpoons C \quad (6.11a)$$

$$T + C \rightleftharpoons TC \quad (6.11b)$$

$$PT \rightleftharpoons TC \quad (6.11c)$$

that represent, respectively, the desorption of probe from the electrode surface (eq. 11a), the recognition between probe and target in the bulk solution (eq. 6.11b) where *C* is the probe that in limited amount has desorbed from the gate surface and diffuses nearby the surface free in solution, and *TC* accounts for the desorption of probe/target from the electrode surface (6.11c). The respective equilibrium constants are:

$$K_{des} = \frac{[C]}{[P]} \quad (6.12a)$$

$$K_a = \frac{[TC]}{[C][T]} \quad (6.12b)$$

$$K_{det} = \frac{[TC]}{[PT]} \quad (6.12c)$$

That represent respectively the desorption constant (6.12a), the binding association constant in solution (6.12b), and the detachment constant that leads to a partition of the associated pair between electrode and solution. Mass conservation imposes that:

$$[C] + [TC] + [P] = p_0 \quad (6.13a)$$

$$[T] + [TC] + [PT] = t_0 \quad (6.13b)$$

By multiplying eq. 6.12a and eq. 6.12b, dividing them by eq. 12c and comparing to eq. 6.9, we establish the relationship among the four constants:

$$\frac{K_a K_{des}}{K_{PT}} = K_{det} \quad (6.14)$$

We express $[C]$ from eq. 6.12a, $[TC]$ from eq. 6.12b, then we obtain:

$$[P] = \frac{p_0}{1+K_{des}+K_a K_{des}[T]} \quad (6.15a)$$

$$[T] = \left\{1 + \frac{K_{PT}+K_a K_{des}}{1+K_{des}+K_a K_{des}[T]} p_0\right\}^{-1} t_0 \quad (6.15b)$$

Upon simplification, eq. 6.15b yields the second order equation:

$$K_a K_{des}[T]^2 + [T]\{1 + K_{des} + (K_{PT} + K_a K_{des})p_0 - K_a K_{des} t_0\} - \{K_{des} + 1\}t_0 = 0 \quad (6.16)$$

Expressed also in terms of K_{det}

$$K_a K_{des}[T]^2 + [T]\left\{1 + K_{des} + K_a K_{des}\left(1 + \frac{1}{K_{det}}\right) p_0 - K_a K_{des} t_0\right\} - \{K_{des} + 1\}t_0 = 0 \quad (6.17)$$

Finally, if we solve for [T] and we plug it into eq. 6.10, we obtain the analytical function describing the signal $S([T])$:

$$S = S_{max}\frac{K_{PT}\cdot[(K_{PT}+K_aK_{des})p_0+1]\cdot(\sqrt{Wt_0+1}-1)}{K_{PT}\cdot[(K_{PT}+K_aK_{des})p_0+1](\sqrt{Wt_0+1}-1)+2K_aK_{des}} \quad (6.18)$$

Being $W = \frac{4K_aK_{des}}{[(K_{PT}+K_aK_{des})p_0+1]^2}$ to simplify notation.

We notice from eq. 6.18 that *S* scales as $\sqrt{t_0}$ when $W \cdot t_0 \gg 1$, thus matching the Hill-type power law dependence shown by [27]:

$$S \approx S_{max}\frac{\left\{\frac{2K_{PT}\sqrt{K_aK_{des}}}{[(K_{PT}+K_aK_{des})p_0+1]}\right\}\cdot\sqrt{t_0}}{1+\left\{\frac{2K_{PT}\sqrt{K_aK_{des}}}{[(K_{PT}+K_aK_{des})p_0+1]}\right\}\cdot\sqrt{t_0}} = S_{max}\frac{K_{1/2}\cdot\sqrt{t_0}}{1+K_{1/2}\cdot\sqrt{t_0}} \quad (6.19)$$

Instead, it scales as t_0, hence Langmuir type, when $W \cdot t_0 \ll 1$:

$$S \approx S_{max}\frac{\left\{\frac{2K_{PT}K_aK_{des}}{[(K_{PT}+K_aK_{des})p_0+1]}\right\}\cdot t_0}{1+\left\{\frac{2K_{PT}K_aK_{des}}{[(K_{PT}+K_aK_{des})p_0+1]}\right\}\cdot t_0} \approx S_{max}\frac{\left\{\frac{2K_{PT}K_aK_{des}}{[K_{PT}p_0+1]}\right\}\cdot t_0}{1+\left\{\frac{2K_{PT}K_aK_{des}}{[K_{PT}p_0+1]}\right\}\cdot t_0} \approx S_{max}\frac{K_1\cdot t_0}{1+K_1\cdot t_0} \quad (6.20)$$

Thus, the simple model predicts these two important cases as limit behaviors. Hence, I used the generalized Langmuir isotherm function (18) to fit the dose curve of the EGOFET biosensor. The only free fitting parameter is the equilibrium constant constant K_{PT}, whereas the other parameters S_{max}, K_a, K_{des}, and p_0 were fixed. In particular, K_a=1.15 10^{17} is calculated from the interaction between miRNA sequences same of P and T in solution from software DINAMELT [28]. K_{des} was arbitrarily fixed at 10^{-15} to indicate that it is strongly unlikely, S_{max} =0.65 and p_0=30 pM.

From the analysis of experimental signal data retrieved from EGOFET current output, we obtain the value for the binding constants, for instance at V_{GS}= -0.75 V as in the plot of Figure 6.4 is equal to K_{PT} = $8.8\times10^9 \pm 1.8\times10^9$. Similarly, fitting of data was applied to all the dose plots starting from V_{GS}=-0.5V to V_{GS}=-0.9V.

This allows us to analyze the dependence of the binding constant with respect to the values of gate voltage. From the values of K_{PT} obtained by best fit with eq. 6.18, we plot the data in Figure 6.5, keeping the temperature equal to 37°C (as in the incubation phase). There is a non-linear monotonic trend with respect to V_{GS}, which can be interpreted in terms of free energy of hybridization, as reported in the following.

6.2.4 Calculation of free energy from Electrolyte-gated field-effect transistor (EGOFET) characteristics

The equilibrium constant K_{PT} is related to the molar free energy of hybridization at the G2 electrode (ΔG_0) and the electrostatic free energy (ΔG_e), according to the following factor expression:

$$K_{PT}(V_{GS}) = e^{-\frac{\Delta G_0}{RT}} \cdot \Delta e^{-\frac{\Delta G_e}{RT}} \quad (6.21)$$

Where R is the gas constant and T is the absolute temperature. When we expand the enthalpic part of ΔG_e at the second order, we obtain

$$\Delta G_e = \delta Q_{\text{eff}} \cdot (V_{\text{GS}} - V_0) + \delta C_{\text{eff}} \cdot (V_{\text{GS}} - V_0)^2 \quad (6.22)$$

δQ_{eff} represents the variation in effective charge, δC_{eff} the variation in effective capacitance and V_0 the voltage that annihilates the expansion of the electrostatic free energy eq. 6.22. In the present work V_0 has been selected equal to the minimum V_{GS} resulting from the fitting, as explained further. By expanding equations (21) and (22) we get:

$$-RT \cdot \ln K_{PT} = \Delta G_0 + \delta Q_{\text{eff}} \cdot (V_{\text{GS}} - V_0) + \delta C_{\text{eff}} \cdot (V_{\text{GS}} - V_0)^2 \quad (6.23a)$$

and by grouping, we obtain the fitting function:

$$-RT \cdot \ln K_{PT} = \left(\Delta G_0 - \delta Q_{\text{eff}} V_0 + \delta C_{\text{eff}} {V_0}^2\right) + (\delta Q_{\text{eff}} - 2\delta C_{\text{eff}})\, V_{\text{GS}} + \delta C_{\text{eff}} \cdot {V_{\text{GS}}}^2 \quad (6.23b)$$

$$-RT \cdot \ln K_{PT} = A + B\, V_{\text{GS}} + C\, {V_{\text{GS}}}^2 \quad (6.23c)$$

Upon the binding of probe-target, the contribution due to the changes of the surface charge and of the surface dipole moment are represented by the linear terms in equation (6.23). The change of capacitance δC_{eff} includes both the change of interfacial capacitance between electrolyte and the gate electrode, and the change of polarizability upon hybridization. We fit the data in Figure 6.5 with the parabolic equation (6.23c), then we extract the values of the physical properties from the best fit values *A*, *B*, and *C*. These are reported in Table 1.

A (kJ/mol)	B (kJ/molV^{-1})	C(kJ/molV^{-2})	ΔG_0(kJ · mol^{-1})	δQ_{eff}(kC · mol^{-1})
-55.48±3.8	25.77±11.57	29.42±8.51	-83.3	54.77

Table 1: Best fitting parameters obtained from eq. 6.23c and the corresponding thermodynamics properties ΔG_0 *and* δQ_{eff} *derived from eq. 6.23b.*

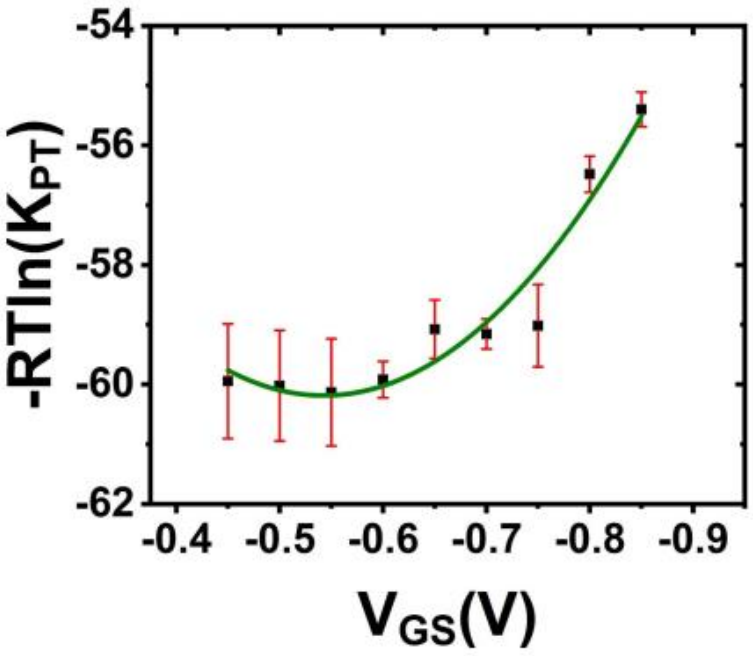

Figure 6.5: Gate–voltage dependent affinity constant KPT extracted from all dose curves; green continuous line is the best fit from equation (6.23c).

Binding free energy was thus obtained based on the function of voltage. We find V_0=-0.45 V as the value of V_{GS} that zeroes the derivative of eq. 23c. We then extract ΔG_0 =-83.3kJ/mol. ΔG_0 was then compared with the binding energy generated by the simulation software DINAMELT [28] for the sequences of probe and target. The value of ΔG_0 calculated for the bulk reaction, according to [29], is -101.2kJ/mol. We infer that our ΔG_0 value in Table 1 for the G2 electrode is comparable with respect to the binding constant in solution. The value extracted from our EGOFET measurement is approximately 20% lower and this reduced value appears compatible with reduced efficiency of hybridization due to spatial confinement, as it is also investigated with the SPR experiments described below.

We obtained the electrostatic free energy at V_{GS} = -0.75V equal to -13.52kJ/mol by multiplying δQ_{eff} = 24.6 kC/mol with (V_{GS}-V_0) and for the contributions arose from the changes in capacitance and polarizability is obtained by multiplying δC_{eff} with (V_{GS}-V_0) ^{2}. The capacitive contribution to ΔGe is 0.05kJ+/mol at V_{GS} = -0.5V and increases as a power law with the drain-source voltage until 5.8kJ/mol at V_{GS} = -0.9V. The charge contribution is predominant in the electrostatic free energy and shows a linear dependency with the applied gate-source voltage (from -2.4kJ/mol to -24.26kJ/mol at V_{GS}=-0.9V). The primary role of charge could be related to the presence of the negatively charged phosphategroups on the target RNA filaments, as observed also from the V_{TH} trend.

6.2.5 SPRI Characterization

We used surface plasmon resonance to obtain independent evidence of the interaction between probe and miRNA-21 target analyte. With this aim, we immobilized probe on the gold surface of the SPR sensor through direct interaction between the thiol moiety available in the structure of probe and the gold surface. Figure 6.6 shows a representative SPR sensorgram for the probe immobilization. The linear time-dependence of the signal detected during the adsorption of the probe is a consequence of mass-transport limited kinetics for the adsorption process.

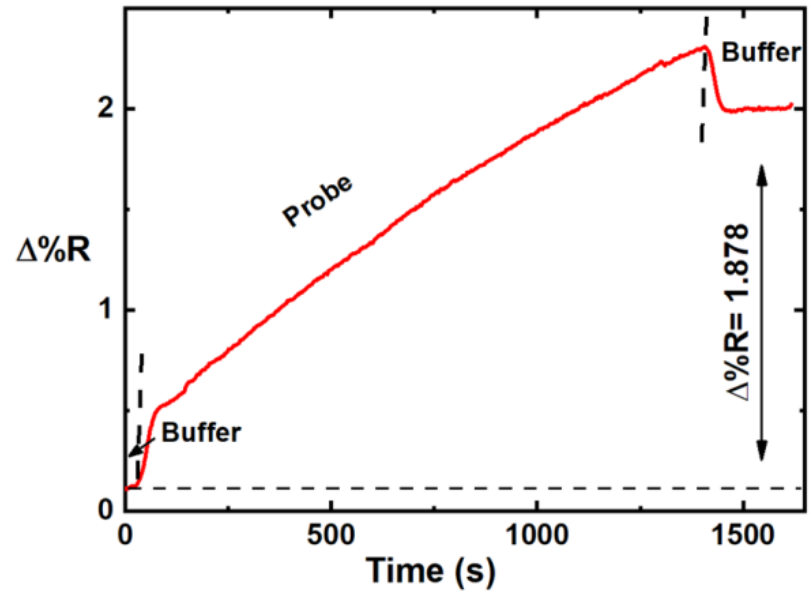

Figure 6.6: Representative changes in per cent reflectivity (Δ%R) over time detected for the immobilization of probe. The probe was immobilized through direct interaction of thiol moiety with the gold surface. The signal detected when the running buffer baseline was established after probe adsorption, allowed us to quantify the surface coverage of probe adsorbed on the surface corresponding to 4.7 10^{12} molecules cm^{-2}.

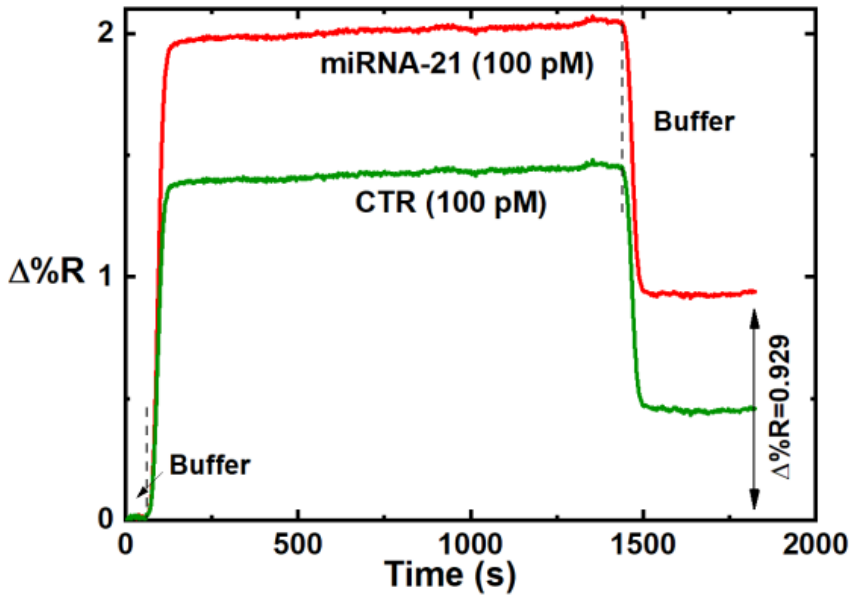

Figure 6.7: Δ%R over time detected for the parallel adsorption of 100 pM solutions of miRNA-21 target analyte and CTR (unrelated control sequence) on the surface immobilized probe.

We quantified the surface coverage of probe adsorbed on the surface (4.7 10-12 molecules cm-2) measuring the variation of the detected signal after the adsorption of probe (Δ%R=1.878). The number of molecules per unit area was estimated on the basis of the theoretical model described by *Shumaker-Parry et al.* [30].

Figure 6.7 shows representative sensograms detected for the hybridization of miR-21-3p and the interaction of the control unrelated sequence (CTR). Both experiments were conducted using 100 pM solutions. The larger SPR shift detected for the interaction between miR-21-3p and provided an evidence of the capacity of the probe to interact with the miRNA-21 target sequence preferentially.

SPR data referring to the probe immobilization and target hybridization allowed us to calculate the hybridization efficiency (HE) as $HE = (\Delta\%R_{hybridization} \cdot MW_{Probe} / \Delta\%R_{immobilization} \cdot MW_{miRNA\text{-}21})$ where MW_{Probe} and $MW_{miRNA\text{-}21}$ correspond to the molecular weight of the probe and miRNA-21, respectively. HE represents the ratio of probes immobilized on the gold surface that formed a duplex with the target sequence [31]. HE=0.69 was obtained for the interaction of the probe with 100pM miRNA-21 target analyte, thus demonstrating the capacity of the surface-immobilized probe to catch low concentrated miRNA-21 target molecules.

6.2.6 Impedance spectroscopy

Electrochemical experiments were performed to further validate the presence of probe on the G2 gate after the functionalization and to monitor the stability of the biorecognition layer after the incubation with blocking agent mercaptoethanol. The response of the functionalized gate towards electron transfer (between gold electrode and the redox couple $[Fe(CN)_6]^{3-/4-}$) was measured using KCl as support electrolyte (see Experimental section). Impedance spectra in faradaic regime is reported in Figure 6.8 for G2. From the fit relative to the Nyquist plot, the charge transfer resistance undergoes an increase after functionalization with thiolated probe nucleotide equal to approximately 1.3 kΩ and a further increase of 2kΩ after incubation with mercaptoethanol. Impedance was capable of detecting the presence of a hybridized probe-target system for a concentration of 300 pM target miRNA but was not sufficiently sensitive for a lower concentration. The $[Fe(CN)_6]^{3-/4-}$ ions might interfere with the formation and stability of the duplex, therefore the hybridization reaction was performed in a separate incubation volume, and the gate was later transferred to the electrolyte for current/voltage measurement.

More importantly, impedance was used to clarify the stability of the probe functionalization for perturbation of the equilibrium between the probe and blocking agent occurring in the thermal step of hybridization. From the plot reported in Figure 6.9 it is possible to appreciate a slight decrease of the imaginary part of impedance for the probe functionalized G2 after incubation at 37 °C in a solution containing just Tris-EDTA-NaCl buffer. The detached probe might be transferred in solution and be responsible for a competitive target-probe reaction affecting the sensitivity of the biosensor as reported in previous calculation of free energy.

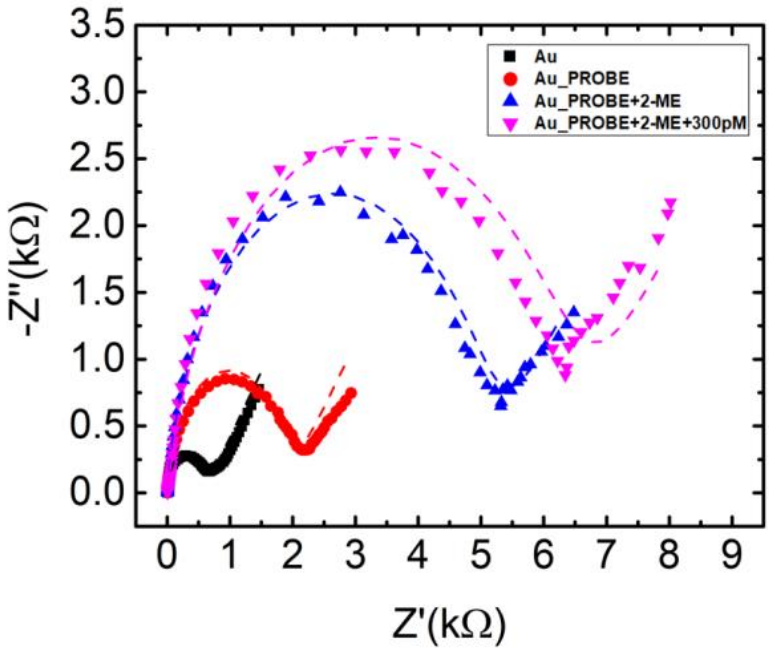

Figure 6.8: Nyquist plot characterizing the impedance of gate G2 taken on a clean gold surface (black), after the immobilization of the probe sequence obtained with thiol bonding (red), after the reaction with mercaptoethanol (blue) which is filling the available site left uncovered by the probe. The incubation with complementary miRNA-21 (300pM) derived sequence is further increasing both the real and imaginary part of impedance (pink). Dashed lines are the result of a Randles circuit (inset) fit.

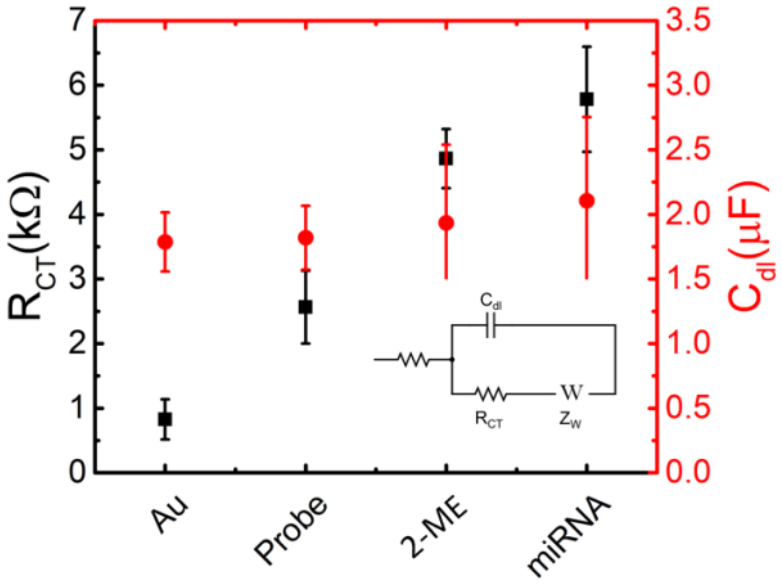

Figure 6.9: Resistance to the charge transfer and Capacitance of the double layer obtained by fitting a classic Randles circuit (shown in the inset) on the Nyquist plots for the consecutive functionalization steps of Gate 2.

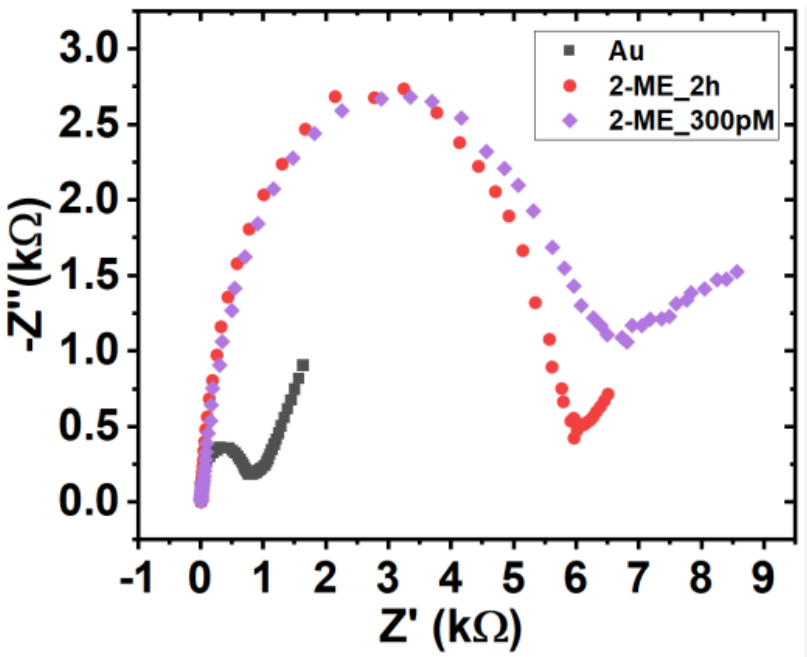

Figure 6.10: Nyquist plot characterizing the impedance of gate G1 taken on a clean gold surface (black), after the functionalization with mercaptoethanol (red). The incubation with complementary miRNA-21-3p (300pM) derived sequence is staying similar in signal with both the real and imaginary part of impedance (pink).

Another stability experiment was performed for the gate electrode (G1). So, the clean gold electrode (G1) was functionalized with 2-Mercaptoethanol for 2 hours and the impedance measurement was taken. Then the gate electrode (G1) covered with 2-ME was incubated in 300pM concentration of the target analyte [miRNA-21-3p] present in the hybridization buffer (Tris-EDTA-NaCl). This incubation process was carried out in an oven at 37˚C for 30 minutes (Figure 6.10). Then the IS measurements was taken, the results obtained show unaffected real and imaginary parts of the impedance, thus, resulting in the same signal obtained before incubation procedure. This proves that the presence of mercaptoethanol (2-ME) compound was unaffected and 300pM concentration of the target analyte [miRNA-21-3p] was hindered by available 2-ME on the gold electrodes. Also with this impedance measurement, one can witness the area coverage for the blocking agent (2-ME) after functionalising it on the clean gold electrode.

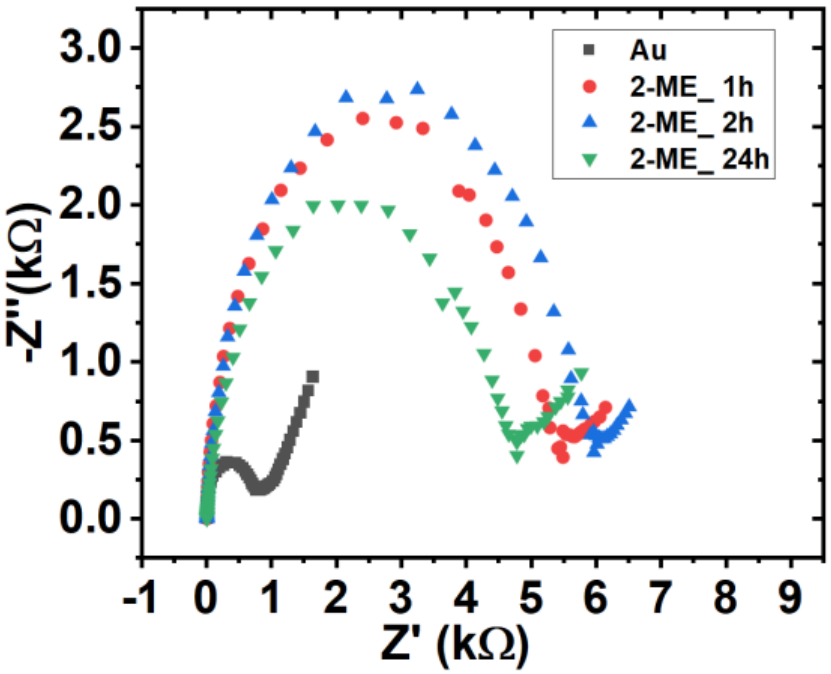

Figure 6.11: Nyquist plot characterizing the impedance of a clean gold surface (black), after the functionalization with mercaptoethanol for 1h (red), 2h (blue) and 24h (green).

An experiment to ensure the area coverage of 2-ME for different period of time (1h, 2h and 24h) was performed. From the impedance measurements obtained, we could see that a maximum area coverage by 2-ME on the clean gold (Au) electrode can be achieved even at 1 hour functionalization. So, the signal obtained after functionalization of 2-ME for 2 hours is similar to that of 1hour. Whereas, 24 hours functionalization of the gold electrode with 2-ME, shows the measurement shifts both in real and imaginary part of the impedance together with the reduction in signal intensity (Figure 6.11). This effect is due to the detachment or dissolving nature of the mercaptoethanol in the buffer with respect to long period of functionalization protocol (24h).

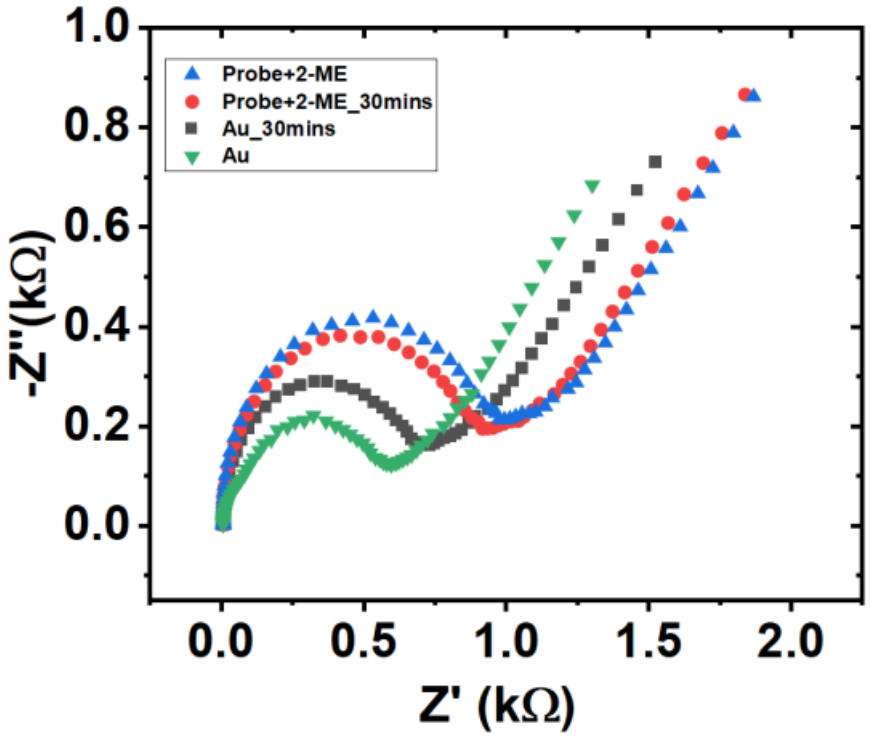

Figure 6.12: Nyquist plot characterizing the impedance of gate(G2) taken on a clean gold surface (green), impedance of the gate G2 has further increased at both real and imaginary parts after the incubation step of G2 in Tris-EDTA-NaCl at 37˚C(black), Gate (G1) taken with the immobilization of the probe sequence obtained with thiol bonding(2µM) and the blocking agent 2-Mercaptoethanol(1mM) (blue),the real and imaginary part of the impedance remains the same after the incubation step for G1 in Tris-EDTA-NaCl at 37˚C(red).

A stability experiment was performed to check the availability of the probe before and after incubation for 30 minutes at 37 ˚C in Tris-EDTA-NaCl buffer without the presence of target analayte. The impedance measurements obtained after incubation in the buffer was similar to the signal, which was measured before incubation in the oven. This clearly shows that there is no influence of the temperature (37˚C) in detaching the probe from the gold surface and the incubation time period of 30 minutes. Perhaps similar experiment was performed for clean bare gold electrode, after 30 minutes of incubation at 37 ˚C with the Tris-EDTA-NaCl buffer, there occurs a change in impedance measurement at both the real and imaginary parts of the impedance. This could be due to the influence of the temperature, incubation time and the salt contaminants available in the buffer, which gets attached to the gold surface (Figure 6.12).

6.2.7 Summary of label-free detection of miRNA-21 with EGOFET

We demonstrate that EGOFET biosensors constitute an ideal candidate for recognition of short sequences of genetic materials in the picomolar region. In particular, miRNA-21 was selected as a model to study the capability of EGOFET to detect the formation of probe-target duplex for almost complementary matching in a buffer suitable for hybridization. The proposed architecture involved for the first time the presence of a second gate electrode working as reference for the calculation of the biosensor signal. The intrinsic shift of response due to semiconductor change of performance in liquid media is now taken into account by dual gate measurement and data analysis. Statistical analysis of the transfer curves allowed us to reconstitute the trend common to different organic transistors fabricated with simple process steps. Gate electrodes functionalized with thiolated oligonucleotide probes are biorecognition interfaces suitable for EGOFET detection scheme since the charges distributed in the oligonucleotide backbone and the stabilizing surrounding media may contribute to signal enhancement and the main mechanism of transduction is based on capacitance. The regeneration of the functionalized gate electrode, although not targeted in the present experiment, will be crucial for transfer of the technology to diagnostic assays.

The free energy of the couple probe-target is estimated by fitting the dependence of dissociation constant with respect to V_{GS} and returns a value sensibly less than the constant extracted by for the homogeneous reaction in solution. This reduction is due to the presence of the probe in solution even at low concentration, and the presence of the surface partially inhibiting the hybridization reaction. The dependence of the signal with respect to square root of target concentration is affecting the overall sensitivity, which is still a palatable one for developing multiplexed electronic biosensors for miRNA panel assays. Impedance spectroscopy measurements of the functionalized gate have been used to validate the stability of the biorecognition layer positively, whereas SPR complementary detection has shown a hybridization efficiency of 69% for the probe-target interaction. Multiplexed EGOFET biosensors may finally represent a sound and viable perspective for integrated devices whose data may be analyzed with good confidence, thanks to the dual gate architecture. This would be very important, for instance, in the label-free detection not only of miRNA biomarkers, but also in the discrimination of point mutations of viruses and microrganisms, as it is very actual in the present epidemics.

6.3 References

[1] Gambari R, Brognara E, Spandidos DA, et al. Targeting oncomiRNAs and mimicking tumor suppressor miRNAs: New trends in the development of miRNA therapeutic strategies in oncology (Review). International Journal of Oncology Spandidos Publications 2016; 49(1):5–32.

[2] Gasparello J, Allegretti M, Tremante E, et al. Liquid biopsy in mice bearing colorectal carcinoma xenografts: gateways regulating the levels of circulating tumor DNA (ctDNA) and miRNA (ctmiRNA). Journal of Experimental & Clinical Cancer Research 2018; 37(1):124.

[3] Khalil S, Fabbri E, Santangelo A, et al. miRNA array screening reveals cooperative MGMTregulation between miR-181d-5p and miR-409-3p in glioblastoma. Oncotarget 2016; 7(19):28195–206.

[4]Giuffrida MC, Zanoli LM, D'Agata R, et al. Isothermal circular-strand-displacement polymerization of DNA and microRNA in digital microfluidic devices. Anal Bioanal Chem 2015; 407(6):1533–43.

[5] Feng Y-H, Tsao C-J. Emerging role of microRNA-21 in cancer (Review). Biomedical Reports Spandidos Publications 2016; 5(4):395–402.

[6] Lu TX, Munitz A, Rothenberg ME. MicroRNA-21 Is Up-Regulated in Allergic Airway Inflammation and Regulates IL-12p35 Expression. The Journal of Immunology American Association of Immunologists 2009; 182(8):4994–5002.

[7] Landgraf P, Rusu M, Sheridan R, et al. A Mammalian microRNA Expression Atlas Based on Small RNA Library Sequencing. Cell Elsevier 2007; 129(7):1401–14.

[8] Fang H, Xie J, Zhang M, et al. miRNA-21 promotes proliferation and invasion of triple negative breast cancer cells through targeting PTEN. Am J Transl Res 2017; 9(3):953–61.

[9] Qu K, Zhang X, Lin T, et al. Circulating miRNA-21-5p as a diagnostic biomarker for pancreatic cancer: evidence from comprehensive miRNA expression profiling analysis and clinical validation. Scientific Reports Nature Publishing Group 2017; 7(1):1692.

[10] Markou A, Zavridou M, Lianidou ES. miRNA-21 as a novel therapeutic target in lung cancer. Lung Cancer (Auckl) 2016; 7:19–27.

[11] Luo G, Luo W, Sun X, et al. MicroRNA-21 promotes migration and invasion of glioma cells via activation of Sox2 and β-catenin signaling. Molecular Medicine Reports Spandidos Publications 2017; 15(1):187–93.

[12] Bellassai N, D'Agata R, Jungbluth V, et al. Surface Plasmon Resonance for Biomarker Detection: Advances in Non-invasive Cancer Diagnosis. Front Chem 2019; 7.

[13] Miao X, Wang W, Kang T, et al. Ultrasensitive electrochemical detection of miRNA-21 by using an iridium(III) complex as catalyst. Biosensors and Bioelectronics 2016; 86:454–58.

[14] Cardoso AR, Moreira FTC, Fernandes R, et al. Novel and simple electrochemical biosensor monitoring attomolar levels of miRNA-155 in breast cancer. Biosensors and Bioelectronics 2016; 80:621–30.

[15] Hakimian F, Ghourchian H, Hashemi A sadat, et al. Ultrasensitive optical biosensor for detection of miRNA-155 using positively charged Au nanoparticles. Scientific Reports Nature Publishing Group 2018; 8(1):2943.

[16] Cadoni E, Manicardi A, Madder A. PNA-Based MicroRNA Detection Methodologies. Molecules Multidisciplinary Digital Publishing Institute 2020; 25(6):1296.

[17] D'Agata R, Spoto G. Advanced methods for microRNA biosensing: a problem-solving perspective. Anal Bioanal Chem 2019; 411(19):4425–44.

[18] Majd SM, Salimi A, Ghasemi F. An ultrasensitive detection of miRNA-155 in breast cancer via direct hybridization assay using two-dimensional molybdenum disulfide field-effect transistor biosensor. Biosensors and Bioelectronics 2018; 105:6–13.

[19] Berto M, Casalini S, Di Lauro M, et al. Biorecognition in Organic Field Effect Transistors Biosensors: The Role of the Density of States of the Organic Semiconductor. Anal Chem American Chemical Society 2016; 88(24):12330–38.

[20] Casalini S, Dumitru AC, Leonardi F, et al. Multiscale Sensing of Antibody–Antigen Interactions by Organic Transistors and Single-Molecule Force Spectroscopy. ACS NanoAmerican Chemical Society 2015; 9(5):5051–62.

[21] Lauro MD, Buscemi G, Bianchi M, et al. Photovoltage generation in enzymatic bio-hybrid architectures. 2019[Online] Zenodo 2019.

[22] Macchia E, Manoli K, Di Franco C, et al. Organic Field-Effect Transistor Platform for LabelFree, Single-Molecule Detection of Genomic Biomarkers. ACS Sens American Chemical Society 2020; 5(6):1822–30.

[23] Sensi M, Berto M, Gentile S, et al. Anti-drug antibody detection with label-free electrolytegated organic field-effect transistors. Chem Commun The Royal Society of Chemistry 2021;57(3):367–70.

[24] Aspermair P, Ramach U, Reiner-Rozman C, et al. Dual Monitoring of Surface Reactions in Real Time by Combined Surface-Plasmon Resonance and Field-Effect Transistor Interrogation. J Am Chem Soc American Chemical Society 2020; 142(27):11709–16.

[25] Parkula V, Berto M, Diacci C, et al. Harnessing Selectivity and Sensitivity in Electronic Biosensing: A Novel Lab-on-Chip Multigate Organic Transistor. Anal Chem American Chemical Society 2020; 92, 13, 9330–9337.

[26]miRbase.org. miRNA Entry for MI0000077. Available at: http://www.mirbase.org/cgi-bin/mirna_entry.pl?acc=MI0000077.

[27] Halperin A, Buhot A, Zhulina EB. On the hybridization isotherms of DNA microarrays: the Langmuir model and its extensions. J Phys: Condens Matter 2006; 18(18):S463–90.

[28] Markham NR, Zuker M. DINAMelt web server for nucleic acid melting prediction. Nucleic Acids Res 2005; 33(Web Server issue):W577–81.

[29] Santa Lucia J, Hicks D. The Thermodynamics of DNA Structural Motifs. Annual Review of Biophysics and Biomolecular Structure 2004; 33(1):415–40.

[30]Shumaker-Parry JS, Campbell CT. Quantitative methods for spatially resolved adsorption/desorption measurements in real time by surface plasmon resonance microscopy. Anal Chem 2004; 76(4):907–17.

[31] Špringer T, Šípová H, Vaisocherová H, et al. Shielding effect of monovalent and divalent cations on solid-phase DNA hybridization: surface plasmon resonance biosensor study. Nucleic Acids Res 2010; 38(20):7343–51.

[32] Selvaraj M. Organic Electronic Transistors and Microfluidics for Cancer Biomarker Sensing [Ph.D dissertation] University of Catania, 2021.

LIST OF FIGURES

LIST OF TABLES

LIST OF PUBLICATIONS

- **Saygin GD** et al. Detection of diffusion gradients with multiple gates electrolyte gated organic transistors. (Ready to Submit)

- Selvaraj M, Greco P, Sensi M, **Saygin GD** et al. Label free detection of miRNA-21 with electrolytegated organic field effect transistors (EGOFETs). Biosensors and Bioelectronics 2021; 182:113144. https://doi.org/10.1016/j.bios.2021.113144

- Ricci S, Casalini S, Parkula V, Selvaraj M, **Saygin GD** et al. Label-free immunodetection of α- synuclein by using a microfluidics coplanar electrolyte-gated organic field-effect transistor. Biosensors and Bioelectronics 2020; 167:112433. https://doi.org/10.1016/j.bios.2020.112433

ACKNOWLEDGEMENTS

It gives me great pleasure to present my PhD thesis. This has been a long and extraordinary journey. This work would be not existed without the contributions of others. I would like to write a few words to acknowledge them and their contributions.

First and fore most, I truly thank and give my deepest gratitude to my supervisor **Prof. Dr. Fabio Biscarini.** Without his constant support and encouragement, this research would be not possible. With his wisdom and guidance made my PhD experience valuable and I gained so much knowledge in the biosensing field.

Another important person to acknowledge is my co- supervisor **Dr. Pierpaolo Greco** at University of Ferrara. I thank bottom of my heart for his constant support and encouragement. He showed me that the patience and not giving up against any obstacles are the most important qualities, which one can have not just in research world, but also in real life. My PhD time under his supervision will be always remembered fondly. It has been absolute an honour.

Last, but not least, I would like to thank my family. They have always been a constant support for me. Their encouragement and constant motivation are what made me through this journey. Lila, you are the brightest colour of my sky and your existence gives me so much support and happiness than you could ever imagine. You made every hard day to a happy one. Your bright smile and kind heart give me strength and make me push myself even more for better future. I promise, that I take you to Pisa Tower soon. Of course, I want to thank my close friends, who are in this journey with me. They carried me through mud and rain with their support and their encouragement. I would like to thank Alice Lunghi, Dilara Eda Gursoy, Denizhan Hanci, Ece Cakar Brem, Kubra Pelin Isgor, Meenu Selvaraj and Seda Kizir. They were constantly there for me and gave me strength to finish my PhD. I am grateful and thankful that I have you guys in my life.